Advances in Laser Slowing, Cooling, and Trapping using Narrow Linewidth Optical Transitions

by

John Patrick Bartolotta

B.S., University of Connecticut, 2014

M.S., University of Connecticut, 2016

A thesis submitted to the

Faculty of the Graduate School of the

University of Colorado in partial fulfillment

of the requirements for the degree of

Doctor of Philosophy

Department of Physics

2021

Bartolotta, John Patrick (Ph.D., Physics)

Advances in Laser Slowing, Cooling, and Trapping using Narrow Linewidth Optical Transitions

Thesis directed by Prof. Murray J. Holland

Laser light in combination with electromagnetic traps has been used ubiquitously throughout the last three decades to control atoms and molecules at the quantum level. Many approaches with varying degrees of reliance on dissipative processes have been discovered, investigated, and implemented in both academic and industrial settings. In this thesis, we theoretically investigate and propose three practical techniques which have the capacity to slow, cool, and trap particles with narrow linewidth optical transitions. Each of these methods emphasizes a high degree of coherent control over quantum states, which lends their operation a reduced reliance on spontaneous emission and thus makes them appealing candidates for application to systems that lack closed cycling transitions. In a more general setting, we also study the transfer of entropy from a quantum system to a classically-behaved coherent light field, and therefore advance our understanding of the role of dissipative processes in optical pumping and laser cooling.

First, we describe theoretically a cooling technique named "sawtooth wave adiabatic passage cooling," or "SWAP cooling," which was discovered experimentally at JILA and has since been implemented elsewhere with various atomic species. Second, we discuss some of the results of an experimental realization of SWAP cooling and connect them to the theoretical model. Third, we propose the extension of the coherent mechanism underlying SWAP cooling to the additional task of trapping in a configuration named the "SWAP magneto-optical trap," or "SWAP MOT." Fourth, we propose a method to fundamentally speed up the adiabatic transfer process required for these techniques by using a shortcut-to-adiabaticity protocol based on Lewis-Riesenfeld invariants. Lastly, we propose and theoretically analyze a simple Gedankenexperiment which can be used to study the potential transfer of entropy from an ensemble of particles to a coherent light source.

Dedication

To my fiancée Kelsey, who knows me more than I know myself.

To my parents, Robert and Karen. Thanks for always believing in me.

To my siblings, Mary and Sarah. I wouldn't be who I am today without you.

To the friends and family who helped to shape me along the way.

Acknowledgements

There has never been a time when I recognized the importance and impact of others on my work more than the years I spent as a graduate student at CU Boulder. My challenging journey toward doctorship would certainly not have been possible without the support, reassurance, and wisdom of my mentors and colleagues.

I would first like to thank Murray for granting me the opportunity to grow as a person and physicist under his advisement. I always felt supported by him in both my studies and extracurricular activities. Thanks to Jinx for teaching me the importance of physical intuition over mathematical formalism. Thanks to Athreya Shankar, Simon Jäger, Jarrod Reilly, Haonan Liu, Liang-Ying Chih, and Victor Colussi for being supportive group mates. Thanks to Graeme Smith, John Bohn, Dana Anderson, Jun Ye, James Thompson, Ana Maria Rey, Shiqian Ding, Yewei Wu, Matthew Norcia, and Julia Cline for countless stimulating and productive discussions.

I am indebted to many people and organizations for balancing my lifestyle with activities separate from my academic pursuits. Thanks to the many local climbing gyms and outdoor crags for challenging me both physically and mentally with fantastic climbing routes. Thanks to William Lewis and Ben Galloway for memorable game nights and career advice. Thanks to the members of CU-Prime for working toward an inclusive and equitable physics community. And many thanks to the staff at JILA and the CU Physics Department.

I would not have continued to pursue a physics career without the mentorship of several motivating physicists at the University of Connecticut. Many thanks to Vasili Kharchenko, Richard T. Jones, and Philip Mannheim for these experiences.

Contents

Chapter

Tables

Table

Figures

Figure

Chapter 1

Context and outline

It is only within the last century that we have discovered ways to create light sources with a high degree of coherence, i.e., light comprised of a multitude of photons with a narrow range of frequencies in lockstep with one another. One such source, the laser, has enabled us to control the dynamics of an ever-growing number of atomic and molecular species with unprecedented precision. By using lasers in parallel with other electromagnetic fields, we have learned how to drastically reduce the speed, temperature, and size of dilute gases consisting of these quantum particles. These techniques are essential to countless studies in both applied and basic science, from Bose-Einstein condensation to condensed matter and quantum computing [9, 43, 97, 102].

The diverse quantum nature of atoms and molecules often requires us to devise laser slowing, cooling, and trapping protocols that are unique to the species. This is especially true for heavier atoms and most molecules since they contain a relatively rich internal quantum structure due to the interactions among their constituent protons, neutrons, and electrons. Therefore, an obvious way to simplify the complexity of a slowing, cooling, or trapping process is to limit the number of internal states the system can occupy. However, this is a difficult task because optical pumping supplies energy to the system, which nature actively dissipates in the form of spontaneous photons. These spontaneous emission events irreversibly transfer the system to a potentially undesired quantum state, which can ultimately lead to a loss of control over its motion. Therefore, methods which reduce these events could allow for previously unachievable experiments on quantum gases.

At the same time, some type of irreversible process is a fundamental ingredient of a cooling

or trapping process, so we can not rely on purely coherent (non-dissipative) techniques. This is because entropy must be removed from a system in order for it to become colder and denser. An ideal mechanism then must have a minimal (but non-negligible) reliance on an irreversible process, which is most often spontaneous emission. As we will show, the recently discovered "sawtooth wave adiabatic passage" (SWAP) cooling technique [13, 141] exhibits reduced reliance on spontaneous emission compared to the oldest and most commonly implemented laser cooling mechanism: Doppler cooling. Starting from this discovery, we dedicate our focus to answering the following questions in this thesis:

(1) How exactly does the SWAP protocol lead to cooling if its underlying mechanism seems to be purely coherent in nature, and therefore not capable of entropy reduction?

(2) Can the SWAP protocol be extended to trap particles in space, as is done with Doppler cooling in a conventional magneto-optical trap?

(3) What are the lowest achievable temperatures and cloud sizes with SWAP-based methods?

(4) Can we speed up these techniques in time, although they are fundamentally adiabatic and consequently slow in nature?

(5) Is there some irreversible process other than spontaneous emission which could be responsible for the reduction in entropy of a quantum gas?

We begin with a survey of relevant background information in Chapter 2 which further contextualizes our contributions. We then answer (1) and the first part of (3) in Chapter 3, in which we present our experimental and theoretical studies of SWAP cooling. Subsequently, we study (2) and (3) in Chapter 5 by combining the SWAP protocol with a magnetic trap to produce an additional trapping force. Next, we apply an adiabatic speedup protocol to the state-transfer process in Chapter 6, thereby addressing (4). From a more general perspective, we then address (5) in Chapter 7 by studying the entropy absorption properties of a classically-behaved coherent light field. We conclude with a brief summary in Chapter 8.

Chapter 2

Introduction

Now that we have laid out the general framework of this thesis, we provide a review of the topics that are essential to understanding its contents. We begin with highlighting the main concepts behind the interaction of matter with light in first and second quantization in Section 2.1. We then turn to a quick overview of the theory of open quantum systems in Section 2.2, which allows us to efficiently study a quantum system that is interacting with its surrounding environment. In our description of open quantum systems, we will introduce the density matrix formulation of quantum mechanics, the quantum master equation, and a stochastic computational tool called the Monte Carlo wave function method, or quantum jump method. We will use these techniques extensively throughout our work. Next, we introduce the semiclassical theories of Doppler cooling and the conventional magneto-optical trap (MOT) in Section 2.3. These widely-used cooling and trapping processes will serve as a benchmark to which we will compare the results of SWAP cooling and the SWAP MOT in Chapters 3 and 5, respectively.

2.1 Coherent models of light-matter interaction

The interaction of quantum matter with light forms the very core of each study we present in the following chapters. There exist many excellent textbooks [71, 127, 174] that comprehensively cover various models developed by the scientific community for this type of interaction. In all cases, these models can be sorted into one of two categories: they treat the light as either a classical or quantum mechanical electromagnetic field. While the latter is unequivocally closer to reality, it

comes with the additional cost of complexity, and in some cases introduces unnecessary detail. Because we are interested in physics involving both models, we derive the Hamiltonian for a two-level quantum particle interacting with light in either case in Sections 2.1.3 and 2.1.4. In the classical case, we include the motional degrees of freedom of the particles, which will be essential to our studies on the mechanical effects of laser light in Chapters 3-6. In the quantum case, we limit our discussion to motionless particles, as done in our study of quantum entropy transfer in Chapter 7. On a related note, we also briefly discuss the manifestation of spontaneous emission and its various models in Section 2.1.5.

Of course, we also need a quantum mechanical description of the matter, which is comprised of individual particles such as atoms or molecules. The light interaction alters both the quantum mechanical "internal" states of the electrons bound to these particles and the motional, or "external," state of the entire particle, so we need to choose a model that incorporates both of these effects. With this in mind, in Section 2.1.1 we derive an interaction Hamiltonian in the case when the particle is explicitly treated quantum mechanically (first quantization), whereas the exact nature of the light field is not yet specified. We then simplify this Hamiltonian for the case of a two-level particle and introduce some common notation in Section 2.1.2.

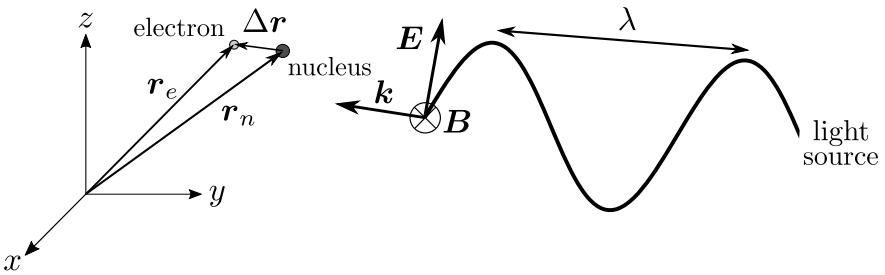

Figure 2.1: Spatial diagram of the light-matter interaction. A neutral quantum particle consisting of a single electron at position $\boldsymbol{r}_e$ and a nucleus with center-of-mass position $\boldsymbol{r}_n$ interacts with a light field with wave vector $\boldsymbol{k}$, wavelength $\lambda = 2\pi/|\boldsymbol{k}|$, electric field $\boldsymbol{E}$, and magnetic field $\boldsymbol{B}$.

2.1.1 First quantization: quantum treatment of matter

We consider the neutral, single-electron particle depicted in Fig. 2.1. The electron has charge $q = -e$, where e is the elementary charge, which means that the rest of the particle, which we simply call the "nucleus," has a net charge $q = e$. We loosely follow the derivations for the light-particle interaction described in Refs. [71] and [127], although we explicitly factor in the nucleus subspace and therefore describe the physics in detail. For clarity, we first provide our conventions for labeling various vectors and operators in Table 2.1.

Table 2.1: Conventions for vector operator quantities. Here we use the short hand "COM" for center-of-mass.

quantity	symbol
electron position	$\hat{\boldsymbol{r}}_e$
nucleus COM position	$\hat{\boldsymbol{r}}_n$
particle COM position	$\hat{\boldsymbol{r}}$
relative electron-nucleus position	$\Delta\hat{\boldsymbol{r}}$
arbitrary position	$\hat{\boldsymbol{R}}$
electron kinetic momentum	$\hat{\boldsymbol{p}}_e$
nucleus kinetic momentum	$\hat{\boldsymbol{p}}_n$
total particle momentum	$\hat{\boldsymbol{p}}$
relative electron-nucleus momentum	$\Delta\hat{\boldsymbol{p}}$

The Hamiltonian $\hat{H}_0$ of the particle in the absence of light is

$$\hat{H}_0 = \frac{\hat{\boldsymbol{p}}_e^2}{2m_e} + \frac{\hat{\boldsymbol{p}}_n^2}{2m_n} + \hat{V}(\hat{\boldsymbol{r}}_e - \hat{\boldsymbol{r}}_n). \tag{2.1}$$

Here, we have labeled quantities related to the electron (nucleus) with the subscript e (n). For $j \in \{e, n\}$, the quantities $\hat{\boldsymbol{p}}_j = -i\hbar\nabla_j = -i\hbar\partial_{\hat{\boldsymbol{r}}_j}$ are kinetic momentum operators, m_j are masses, and $\hat{\boldsymbol{r}}_j$ are position operators. The potential energy $\hat{V}$ encapsulates all electron-nucleus interactions. Notice that Eq. (2.1) looks identical to the classical Hamiltonian of the electron-nucleus system except the position and momentum variables have been replaced with quantum mechanical

operators. These operators satisfy the commutation relations

$$[(\hat{\boldsymbol{r}}_j)_a, (\hat{\boldsymbol{p}}_k)_b] = i\hbar\delta_{ab}\delta_{jk}, \qquad [(\hat{\boldsymbol{r}}_j)_a, (\hat{\boldsymbol{r}}_k)_b] = 0, \qquad [(\hat{\boldsymbol{p}}_j)_a, (\hat{\boldsymbol{p}}_k)_b] = 0 \tag{2.2}$$

for particles $j, k \in \{e, n\}$ and spatial dimensions $a, b \in \{x, y, z\}$.

In the presence of light, the Hamiltonian becomes

$$\hat{H} = \frac{[\hat{\boldsymbol{p}}_e + e\boldsymbol{A}(\hat{\boldsymbol{r}}_e, t)]^2}{2m_e} + \frac{[\hat{\boldsymbol{p}}_n - e\boldsymbol{A}(\hat{\boldsymbol{r}}_n, t)]^2}{2m_n} + e[\Phi(\hat{\boldsymbol{r}}_n, t) - \Phi(\hat{\boldsymbol{r}}_e, t)] + \hat{V}(\hat{\boldsymbol{r}}_e - \hat{\boldsymbol{r}}_n), \tag{2.3}$$

where t is time and $\boldsymbol{A}(\hat{\boldsymbol{r}}, t)$ and $\Phi(\hat{\boldsymbol{r}}, t)$ are the vector and scalar potentials associated with the light field evaluated at the appropriate positions. Note that these potentials are functions of the electron and nucleus position operators and thus can affect their quantum states, but we have not yet specified whether the light itself is classical or quantum mechanical. These potentials are related to the light's (physical) electric and magnetic fields $\boldsymbol{E}(\hat{\boldsymbol{R}}, t)$ and $\boldsymbol{B}(\hat{\boldsymbol{R}}, t)$ by

$$\begin{aligned} \boldsymbol{E}(\hat{\boldsymbol{R}}, t) &= -\nabla\Phi(\hat{\boldsymbol{R}}, t) - \frac{\partial \boldsymbol{A}(\hat{\boldsymbol{R}}, t)}{\partial t}, \\ \boldsymbol{B}(\hat{\boldsymbol{R}}, t) &= \nabla \times \boldsymbol{A}(\hat{\boldsymbol{R}}, t), \end{aligned} \tag{2.4}$$

where $\hat{\boldsymbol{R}}$ is any position vector operator. (We reserve the symbol $\hat{\boldsymbol{r}}$ for the center-of-mass position of the particle, which is introduced later.)

The form of the particle Hamiltonian given in Eq. (2.3) can be simplified through a series of gauge transformations. First, we choose the radiation gauge so that $\Phi = 0$ and $\nabla \cdot \boldsymbol{A} = 0$, which removes the electron-light and nucleus-light electric potential energy terms in Eq. (2.3). Next, we transform the Hamiltonian under the gauge transformation $\hat{U} = \exp[-ie\chi(\hat{\boldsymbol{r}}_n, \hat{\boldsymbol{r}}_e, t)]$, where

$$\chi(\hat{\boldsymbol{r}}_n, \hat{\boldsymbol{r}}_e, t) = \chi_e(\hat{\boldsymbol{r}}_e, t) - \chi_n(\hat{\boldsymbol{r}}_n, t), \tag{2.5}$$

and the χ_j's are undetermined gauge functions. (See Refs. [44] and [45] for a detailed discussion of gauge choice in quantum electrodynamics.) After this operation, the Hamiltonian reads

$$\begin{aligned} \hat{H} = &\frac{\{\hat{\boldsymbol{p}}_e + e[\boldsymbol{A}(\hat{\boldsymbol{r}}_e, t) + \nabla_e\chi_e(\hat{\boldsymbol{r}}_e, t)]\}^2}{2m_e} + \frac{\{\hat{\boldsymbol{p}}_n - e[\boldsymbol{A}(\hat{\boldsymbol{r}}_n, t) + \nabla_n\chi(\hat{\boldsymbol{r}}_n, t)]\}^2}{2m_n} \\ &+ e\left[\frac{\partial\chi_e(\hat{\boldsymbol{r}}_e, t)}{\partial t} - \frac{\partial\chi_n(\hat{\boldsymbol{r}}_n, t)}{\partial t}\right] + \hat{V}(\hat{\boldsymbol{r}}_e - \hat{\boldsymbol{r}}_n). \end{aligned} \tag{2.6}$$

Before we choose the gauge functions χ_j, we apply the "electric dipole approximation," which will drastically simplify the form of the Hamiltonian. From electromagnetic theory, the light field's vector potential $\boldsymbol{A}(\hat{\boldsymbol{R}}, t)$ satisfies the wave equation, which has solution

$$\boldsymbol{A}(\hat{\boldsymbol{R}}, t) = \boldsymbol{A}_0 \exp[i(\boldsymbol{k} \cdot \hat{\boldsymbol{R}} - \omega t)] + \text{c.c.} \tag{2.7}$$

Here, c.c. denotes the complex (or Hermitian) conjugate, $\boldsymbol{A}_0$ is the amplitude of the vector potential, and $\boldsymbol{k}$ and ω are the wave vector and frequency of the light. Because typical atomic dimensions ($|\boldsymbol{r}|_{\text{atom}} \lessapprox 10^{-9}$ m) are much smaller than optical wavelengths ($\lambda \gtrapprox 10^{-7}$ m), it follows that $\boldsymbol{k} \cdot \boldsymbol{r}_{\text{atom}} \propto |\boldsymbol{r}|_{\text{atom}}/\lambda \ll 1$, and thus that the vector potential is approximately uniform over the dimensions of the particle. It is therefore valid to approximate the vector potential as a spatially uniform vector, which we evaluate for convenience at the center-of-mass $\boldsymbol{r}$ of the particle (defined in Eq. (2.11)):

$$\boldsymbol{A}(\hat{\boldsymbol{r}}_j, t) \approx \boldsymbol{A}(\hat{\boldsymbol{r}}, t) = \boldsymbol{A}_0 \exp[i(\boldsymbol{k} \cdot \hat{\boldsymbol{r}} - \omega t)] + \text{c.c.}, \qquad \frac{|\nabla \boldsymbol{A}|}{|\boldsymbol{A}|} \propto |\boldsymbol{k}| \ll 1/|\boldsymbol{r}_{\text{atom}}|. \tag{2.8}$$

Eqns. (2.8) are what is meant by the electric dipole approximation in the field of light-matter interactions, although the exact position at which $\boldsymbol{A}$ is evaluated depends on the context. Equipped with this useful approximation, we now make the clever choice $\chi_j(\hat{\boldsymbol{r}}_j, t) = -\boldsymbol{A}(\hat{\boldsymbol{r}}, t) \cdot \hat{\boldsymbol{r}}_j$ which satisfies

$$\nabla_j \chi_j(\hat{\boldsymbol{r}}_j, t) \approx -\boldsymbol{A}(\hat{\boldsymbol{r}}, t), \qquad \frac{\partial \chi_j(\hat{\boldsymbol{r}}_j, t)}{\partial t} = \boldsymbol{E}(\hat{\boldsymbol{r}}, t) \cdot \hat{\boldsymbol{r}}_j, \tag{2.9}$$

in which we used Eq. (2.4). With these results, the Hamiltonian reduces to

$$\hat{H} = \frac{\hat{\boldsymbol{p}}_e^2}{2m_e} + \frac{\hat{\boldsymbol{p}}_n^2}{2m_n} + e(\hat{\boldsymbol{r}}_e - \hat{\boldsymbol{r}}_n) \cdot \boldsymbol{E}(\hat{\boldsymbol{r}}, t) + \hat{V}(\hat{\boldsymbol{r}}_e - \hat{\boldsymbol{r}}_n). \tag{2.10}$$

Our next alteration is to describe the physics in terms of the center-of-mass of the particle and relative motion of the electron and nucleus. This is motivated by the relative position dependence of the last two terms in Eq. (2.10). The center-of-mass $\hat{\boldsymbol{r}}$ and relative $\Delta\hat{\boldsymbol{r}}$ coordinates are

$$\hat{\boldsymbol{r}} = (m_e \hat{\boldsymbol{r}}_e + m_n \hat{\boldsymbol{r}}_n)/(m_e + m_n), \qquad \Delta\hat{\boldsymbol{r}} = \hat{\boldsymbol{r}}_e - \hat{\boldsymbol{r}}_n, \tag{2.11}$$

and the total $\hat{\boldsymbol{p}}$ and relative $\Delta\hat{\boldsymbol{p}}$ momenta are

$$\hat{\boldsymbol{p}} = \hat{\boldsymbol{p}}_e + \hat{\boldsymbol{p}}_n, \qquad \Delta\hat{\boldsymbol{p}} = (m_e\hat{\boldsymbol{p}}_e - m_n\hat{\boldsymbol{p}}_e)/(m_e + m_n). \tag{2.12}$$

(These coordinates also satisfy the canonical commutation relations [73].) In terms of these coordinates, Eq. (2.10) becomes

$$\hat{H} = \frac{\hat{\boldsymbol{p}}^2}{2m} + \frac{(\Delta\hat{\boldsymbol{p}})^2}{2\mu} - \hat{\boldsymbol{d}} \cdot \boldsymbol{E}(\hat{\boldsymbol{r}}, t) + \hat{V}(\Delta\hat{\boldsymbol{r}}), \tag{2.13}$$

in which $\hat{\boldsymbol{d}} \equiv e\Delta\hat{\boldsymbol{r}}$ is the particle's dipole moment operator. We shall refer to the term in Eq. (2.13) involving $\hat{\boldsymbol{d}}$ as the "dipole term." By inspecting this result, we notice that two of the four terms determine the internal bound states of the electron-nucleus interaction in terms of their relative positions and momenta. This part of the Hamiltonian,

$$\hat{H}_{\text{internal}} = \frac{(\Delta\hat{\boldsymbol{p}})^2}{2\mu} + \hat{V}(\Delta\hat{\boldsymbol{r}}), \tag{2.14}$$

has been characterized to high precision in previous theories and experiments for each atomic and molecular species we study. As such, its spectrum and states are well defined, so we consider it to be "solved" and thus separate it from the rest of our Hamiltonian. Substituting this notation into Eq. (2.13), we at last arrive at the desired form of the Hamiltonian:

$$\hat{H} = \hat{H}_{\text{internal}} + \frac{\hat{\boldsymbol{p}}^2}{2m} - \hat{\boldsymbol{d}} \cdot \boldsymbol{E}(\hat{\boldsymbol{r}}, t). \tag{2.15}$$

Eq. (2.15) is the form of the Hamiltonian we will use to describe all particle-light interactions.

2.1.2 The two-level particle

In the previous section, we did not specify the internal quantum structure of the particle as given by Eq. (2.14). Here, we briefly describe the simplifications made to Eq. (2.15) when the particle can be treated as a two-level system. That is, we suppose that only two of the quantum internal states determined by $\hat{H}_{\text{internal}}$ are relevant during the interaction, and thereby isolate our attention to the idealized, yet rich model of the two-level particle.

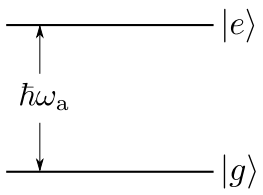

Figure 2.2: Energy level diagram of the internal states of a two-level system, separated by energy $\Delta E = \hbar\omega_{\mathrm{a}}$.

As is customary, we refer to the two internal states of the particle as the "excited" and "ground" state with associated vectors $|e\rangle$ and $|g\rangle$ in the Hilbert space of $\hat{H}_{\mathrm{internal}}$. This terminology reflects the former state's higher relative energy by an amount $\hbar\omega_a$, where ω_a is the angular frequency of a photon containing the same amount of energy (see Fig. 2.2). We refer to these states as the "bare eigenstates" or "bare basis" of $\hat{H}_{\mathrm{internal}}$ because the Hamiltonian is diagonal in this basis in the absence of light. In fact, defining the baseline energy at $\hbar\omega_a/2$ above the ground state, we may write $\hat{H}_{\mathrm{internal}}$, often called the "free particle Hamiltonian," as

$$\hat{H}_{\mathrm{internal}} = \frac{\hbar\omega_a}{2}\left|e\right\rangle\left\langle e\right| - \frac{\hbar\omega_a}{2}\left|g\right\rangle\left\langle g\right| = \frac{\hbar\omega_a}{2}\hat{\sigma}^z, \tag{2.16}$$

in which $\hat{\sigma}^z$ is a Pauli matrix. For this reason, it is said that the excited and ground states $|e\rangle$ and $|g\rangle$ form a pseudo-spin 1/2 system. More generally, the usual raising ($\hat{\sigma}^+ = |e\rangle\langle g|$) and lowering ($\hat{\sigma}^- = |g\rangle\langle e|$) operators, along with the usual Pauli spin operators, $\hat{\sigma}^{x,y,z}$, whose coordinate labels are implicitly understood to refer to the pseudo-spin space, operate on the internal states.

We now shift our attention to the other operator acting on the internal Hilbert space: the particle dipole moment operator $\hat{\boldsymbol{d}}$ [see Eq. (2.13)]. This operator induces transitions between the internal states, which physically corresponds to the absorption and emission of photons from the light field. The polarization $\hat{\epsilon}$ of the light field is chosen based on the magnetic quantum numbers m_e and m_g of the states $|e\rangle$ and $|g\rangle$ (linear if $m_e = m_g$ and circular if $m_e = m_g \pm 1$), so we should also include it in when calculating the matrix elements of $\hat{\boldsymbol{d}}$:

$$\hat{\boldsymbol{d}}\cdot\hat{\epsilon} = \langle g|\hat{\boldsymbol{d}}\cdot\hat{\epsilon}|e\rangle\left|g\right\rangle\left\langle e\right| + \langle e|\hat{\boldsymbol{d}}\cdot\hat{\epsilon}|g\rangle\left|e\right\rangle\left\langle g\right| = \langle g|\hat{\boldsymbol{d}}\cdot\hat{\epsilon}|e\rangle\,(\hat{\sigma}^- + \hat{\sigma}^+). \tag{2.17}$$

In the second step, we (without loss of generality) chose the phase of the off-diagonal dipole matrix

elements to be real. (See Ref. [174] for a derivation of this result from a parity argument.) We note that the extension of these methods to a three (or more) level system, as done in Chapter 5, is straightforward.

2.1.3 Interaction of a moving two-level quantum system with a classical light field

For many purposes in the field of light-matter interactions, a classical treatment of the light is sufficient. In particular, the effects of a light field containing many photons (such as a laser) is often treated as an unperturbed, time-dependent electric potential. That is, the amplitude E_0 of the light's electric field $\boldsymbol{E}(\hat{\boldsymbol{r}}, t)$ is unchanged by the particle interaction, even though the particle absorbs photons. (We address the validity of this treatment to some extent in Chapter 7.) In this case, we can write the electric field as

$$\boldsymbol{E}(\hat{\boldsymbol{r}}, t) = \hat{\epsilon}\, E_0 f(\hat{\boldsymbol{r}}, t), \tag{2.18}$$

where $\hat{\epsilon}$ is the polarization direction, E_0 is the (constant) field amplitude, and the spatiotemporal profile $f(\hat{\boldsymbol{r}}, t)$ depends on the laser setup.

We restrict our studies to laser light propagating along one spatial dimension, which we call the z-direction so that the wave vector is $\boldsymbol{k} = \pm k\, \hat{e}_z$. Here, we have used the notation $\hat{e}_j$ to denote a unit vector pointing along the j-direction. In Chapters 5 and 6, we will consider the effects of traveling waves, for which the function f is [126]

$$f_{\text{traveling}}(\hat{\boldsymbol{r}}, t) = \cos(k\hat{z} - \omega_L t) = \frac{1}{2}\left(e^{i(k\hat{z} - \omega_l t)} + e^{-i(k\hat{z} - \omega_L t)}\right), \tag{2.19}$$

where ω_L is the laser frequency. In Chapter 3, we will consider the effects of a standing wave (the sum of counterpropagating traveling waves), for which the function f is

$$f_{\text{standing}}(\hat{\boldsymbol{r}}, t) = \cos(k\hat{z} - \omega_L t) + \cos(k\hat{z} + \omega_L t) = 2\cos(k\hat{z})\cos(\omega_L t). \tag{2.20}$$

Notice that the amplitude of a standing wave is twice as large as that of a traveling wave. For this reason, care needs to be taken when defining the coupling strength, often called the Rabi frequency, between the light field and the particle.

The next obvious step is to substitute the electric field $\boldsymbol{E}$ [Eq. (2.18)] for the laser setup of interest into the Hamiltonian $\hat{H}$ [Eq. (2.15)]. For the case of the traveling wave [Eq. (2.19)], the dipole term is

$$-\hat{\boldsymbol{d}} \cdot \boldsymbol{E}(\hat{\boldsymbol{r}}, t) = -\frac{\langle g|\hat{\boldsymbol{d}} \cdot \hat{\epsilon}|e\rangle \; E_0}{2}(\hat{\sigma}^- + \hat{\sigma}^+)\left(e^{i(k\hat{z}-\omega_L t)} + e^{-i(k\hat{z}-\omega_L t)}\right), \tag{2.21}$$

in which we used Eq. (2.17) for the dipole moment operator. This expression can be simplified by invoking the "rotating wave approximation," which removes terms that are unlikely to affect the dynamics due to their required energy when the light is quasi-resonant. Inspecting the relative energies of the bare eigenstates [see Fig. 2.2], we learn that the raising $\hat{\sigma}^+ = |e\rangle\langle g|$ and lowering $\hat{\sigma}^- = |g\rangle\langle e|$ operators supply and remove energy from the particle, respectively. This means that their expectation values have a time-dependence that satisfies $\hat{\sigma}^\pm \propto e^{\pm i\omega_a t}$, and hence that each term in Eq. (2.21) (when distributed) oscillates in time with frequencies of magnitude $|\omega_a \pm \omega_L|$. Under the rotating wave approximation, we remove terms oscillating with the sum frequency, as only the terms oscillating with the difference frequency $|\omega_a - \omega_L|$ govern the observable dynamics. Simultaneously defining the Rabi frequency as

$$\Omega \equiv -\frac{\langle g|\hat{\boldsymbol{d}} \cdot \hat{\epsilon}|e\rangle \; E_0}{\hbar}, \tag{2.22}$$

Eq. (2.21) reduces to

$$-\hat{\boldsymbol{d}} \cdot \boldsymbol{E}(\hat{\boldsymbol{r}}, t) = \frac{\hbar\Omega}{2}\left(\hat{\sigma}^- e^{-i(k\hat{z}-\omega_L t)} + \hat{\sigma}^+ e^{i(k\hat{z}-\omega_L t)}\right), \tag{2.23}$$

which is the form often used in the literature. This process is very similar to the standing wave case. We will extensively use Eq. (2.23) and its equivalent standing wave form in our studies of laser slowing, cooling, and trapping.

If the frequency of the light changes in time, we replace the accumulated temporal phase of the light $\omega_L t$ in all above equations with its equivalent integral form:

$$\omega_L t \to \eta(t) \equiv \int_{t_0}^{t} \omega_L(t')\, dt'. \tag{2.24}$$

This replacement is important if the range of the applied light frequencies $\delta\omega_L = \max[\omega_L(t)] - \min[\omega_L(t)]$ is at least on the order of the other relevant frequencies in the interaction, such as the Rabi frequency Ω [Eq. (2.22)], recoil frequency ω_r [Eq. (2.66)], and spontaneous emission rate γ [Eq. (2.35)]. In the following chapters, $\delta\omega_L$ is on the order of MHz, which is often larger than these other frequencies, and hence we make the adjustment. In principle, the wave vector $\boldsymbol{k}$ should also be adjusted in the spatial phase:

$$k = \frac{\omega_L}{c} \to k(t) \equiv \frac{\omega_L(t)}{c}. \tag{2.25}$$

However, the change in wave vector $\delta k = \delta\omega_L/c$ is much smaller than the only other relevant quantity: the particle "wave vector," $p/\hbar$. This is true because the spread in the particle momentum is fundamentally bounded from below by the photon momentum $\hbar k$ in the processes we propose, as we show in Chapter 3. Therefore, we approximate k to remain fixed in all cases.

2.1.4 Second quantization: interaction of motionless two-level quantum system with a quantized light field in a cavity

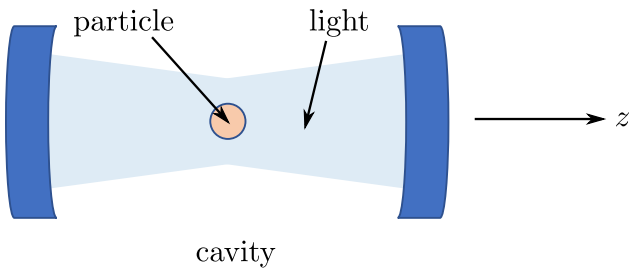

Figure 2.3: A quantum particle is placed in an optical cavity that contains a quantized light field.

When the quantum nature of the light is essential to understanding the physics of interest, then one must quantize the light field through the process of second quantization. This procedure promotes the light's electric and magnetic fields to operators (related to individual quanta, or photons) that evolve according the laws of quantum mechanics. For brevity, we refer the reader

to the second chapter of Ref. [71] for an in-depth derivation of quantized light fields and only derive the interaction Hamiltonian, called the Jaynes-Cummings Hamiltonian, for a single-mode quantum electromagnetic field and a quantum two-level particle in an optical cavity [see Fig. 2.3]. Although it is not strictly necessary, we also remove the atomic motion for simplicity. The resulting interaction is related to what we study in Chapter (7).

Because the boundary conditions of electrodynamics and quantum mechanics play a role in the derivation, it is necessary to quantize the electromagnetic field within a "quantization volume" V. In the case of Chapter (7), this volume will correspond to the optical cavity which contains the quantized field. The single-mode quantized electric field of light with frequency ω propagating along the z-direction in a cavity is found to be

$$\hat{\boldsymbol{E}}(\hat{\boldsymbol{r}},t) = \hat{\epsilon}\left(\frac{\hbar\omega}{\epsilon_0 V}\right)^{1/2}\sin(k\hat{z})(\hat{a}+\hat{a}^\dagger) = \hat{e}\,E_0 f(\hat{\boldsymbol{r}})\,(\hat{a}+\hat{a}^\dagger), \tag{2.26}$$

in which $E_0 = (\hbar\omega/\epsilon_0 V)^{1/2}$ characterizes the maximum vacuum electic field amplitude, and $f(\hat{\boldsymbol{r}}) = \sin(k\hat{z})$ is the spatial profile. (We have written this operator in the Schrödinger picture, so it is time-independent.) Notice that Eq. (2.26) looks very similar to its classical counterpart in Eq. (2.18), except we now include the creation $\hat{a}^\dagger$ and annihilation $\hat{a}$ operators of the quantum harmonic oscillator, which have the basic properties

$$\hat{a}^\dagger\,|n\rangle = \sqrt{n+1}\,|n+1\rangle\,, \quad \hat{a}\,|n\rangle = \sqrt{n}\,|n-1\rangle\,, \quad [\hat{a},\hat{a}^\dagger] = 1. \tag{2.27}$$

In this case, the operators act on a Fock space $\{|n\rangle\}_{n=0}^{\infty}$ which describes the photon occupancy of the cavity. Their inclusion in Eq. (2.26) reflects the dependence of the electric field amplitude on the number of cavity photons.

If the particle is motionless, then we can demote the particle position operator $\hat{z}$ to a classical value z, which is the (fixed) position of the particle in the cavity. With this result, the dipole term in Eq. (2.15) becomes

$$-\hat{\boldsymbol{d}}\cdot\hat{\boldsymbol{E}}(\hat{\boldsymbol{r}},t) = -\,\langle g|\hat{\boldsymbol{d}}\cdot\hat{\epsilon}|e\rangle\;E_0\sin(kz)\,(\hat{\sigma}^- + \hat{\sigma}^+)\,(\hat{a}+\hat{a}^\dagger), \tag{2.28}$$

where we have again used Eq. (2.17). Invoking the rotating wave approximation and defining the vacuum Rabi frequency g as

$$g(z) \equiv -\frac{2\,\langle g|\hat{\boldsymbol{d}}\cdot\hat{\epsilon}|e\rangle\; E_0 \sin(kz)}{\hbar}, \tag{2.29}$$

the dipole term becomes

$$-\hat{\boldsymbol{d}}\cdot\hat{\boldsymbol{E}}(\hat{\boldsymbol{r}},t) = \frac{\hbar g(z)}{2}(\hat{\sigma}^{-}\hat{a}^{\dagger} + \hat{\sigma}^{+}\hat{a}), \tag{2.30}$$

which is the typical form of the Jaynes-Cummings interaction Hamiltonian. Combining this result with the free particle Hamiltonian [Eq. (2.16)] and the free field Hamiltonian

$$\hat{H}_{0,\text{field}} = \hbar\omega\hat{a}^{\dagger}\hat{a} \tag{2.31}$$

(for which we dropped the trivial vacuum energy term), we arrive at the full Jaynes-Cummings Hamiltonian:

$$\hat{H}_{JC} = \frac{\hbar\omega_a}{2}\hat{\sigma}^{z} + \hbar\omega\hat{a}^{\dagger}\hat{a} + \frac{\hbar g}{2}(\hat{\sigma}^{-}\hat{a}^{\dagger} + \hat{\sigma}^{+}\hat{a}). \tag{2.32}$$

Notice that we have absorbed the position dependence into the definition of g. We will study a system very closely related to this result in Chapter 7.

2.1.5 The spontaneous emission process

The last fundamental physical process we need to introduce is spontaneous emission, which causes a quantum system in a state other than the lowest-energy state to eventually "relax" to a lower-energy state. The scientific community has developed many different physical theories to explain this phenomenon over the last century [131, 132]. From a classical perspective, this process is induced by the radiation reaction, i.e., the interaction of the electron with its own electromagnetic field. The theory of quantum electrodynamics, however, elicits a different origin: it is caused by the interaction of the particle with the ground, or "vacuum" states of the universe's electromagnetic field. In other words, the quantum perspective argues that the non-zero energy of the ground state of the free-space electromagnetic field (or "zero-point energy"), which contains no photons, causes an irreversible exponential decay of excited state populations. We provide the reader with the following insightful quote, which connects these two perspectives:

> "Of course we always get the same expression γ for the spontaneous emission rate [when deriving it with different orderings of quantum mechanical operators], because the operators we are reordering do in fact commute, but our *interpretation* of the origin of spontaneous emission may change. Again this is a consequence of the intimate, fluctuation-dissipation connection between radiation reaction and the zero-point, vacuum electromagnetic field."
>
> P. W. Milonni, *Why spontaneous emission?* [130]

Because the classical perspective underestimates the value of γ by a factor of 2, modern authors adopt the quantum perspective [71, 127]. This derivation involves coupling a quantum system to the free-space ("infinite"-volume) quantized electromagnetic field, or "background radiation field," which has a continuum of frequency modes. Generalizing the single-mode formalism discussed in Section 2.1.4, the multi-mode (m.m.) Jaynes Cummings Hamiltonian is

$$\hat{H}_{JC,\text{m.m.}} = \frac{\hbar\omega_a}{2}\hat{\sigma}^z + \hbar\sum_s \omega_s \hat{a}_s^\dagger \hat{a}_s + \sum_s \frac{\hbar g_s}{2}(\hat{\sigma}^- \hat{a}_s^\dagger + \hat{\sigma}^+ \hat{a}_s), \tag{2.33}$$

in which s is a mode index. To gain intuition for why we expect dynamics to occur even in a space devoid of photons, consider the following matrix elements of $\hat{H}_{JC,\text{m.m.}}$:

$$\langle g, 1_s | \hat{H}_{JC,\text{m.m.}} | e, 0_s \rangle = \frac{\hbar g_s}{2}. \tag{2.34}$$

Physically, the fact that the matrix element in Eq. (2.34) is non-zero tells us that a quantum particle can still transition from its excited state to a ground state. More specifically, we should expect a quantum particle prepared in the excited state $|e\rangle$ to undergo vacuum Rabi oscillations with each mode s.

We now introduce an important approximation: the "Weisskopf-Wigner approximation" [127, 189]. Under the assumption that the bandwidth of the background radiation field is large, the correlation time τ_{corr} between any two different modes is correspondingly small. If this correlation time is small compared to the timescales associated with the particle evolution, then we can "coarse-grain" over the evolution of the particle state. (We will revisit this approximation in the derivation of the master equation in Section 2.2.2.) This approximation leads to destructive interference of the vacuum Rabi oscillations, and the net effect is irreversible exponential decay into the ground

state $|g\rangle$. It can be shown that this decay rate, called the free-space spontaneous emission rate γ, is

$$\gamma = \frac{\omega_a^3 \,|\, \langle g|\hat{\boldsymbol{d}}|e\rangle \,|^2}{3\pi\epsilon_0\hbar c^3}. \tag{2.35}$$

In principle, we could accurately evolve the dynamics of our quantum particle by incorporating the background radiation field into all of our calculations. However, the detailed evolution of the this field is generally not of interest, and we have shown that it can be effectively modeled by the inclusion of γ. Therefore, it would be desirable to construct a general theory that accounts for the effects of the background radiation field without its explicit inclusion. This leads us to the theory of open quantum systems, which is discussed in the next section.

2.2 Theory of open quantum systems

In Section 2.1, we derived a mathematical formalism for the interaction of a two-level quantum particle with light under "coherent," i.e., Hamiltonian dynamics. In the following chapters, we will not be interested in the evolution of the background radiation field introduced in Section 2.1.5, or for that matter, any other presence in the universe that could possibly affect the system of interest. However, we have no choice but to incorporate the background field's pervasive effects if we hope to accurately capture the system's dynamics. We therefore study the system through the theory of open quantum systems [25]. In this framework, the universe is split into two subspaces: the "system," which we are interested in studying, and the "environment" (the rest of the universe), which potentially affects the system but is not of interest.

Before we can introduce this theory, we must introduce the density operator $\hat{\rho}$, also called the density matrix. This matrix will take the place of the state vector $|\psi\rangle$ in describing the state of our system, and is described in Section 2.2.1. We will then show how the background radiation field can be formally separated from the dynamics, yielding a quantum master equation that describes the system in Section 2.2.2. We then present a convenient way to incorporate the effects of dissipation on particle motion in Section 2.2.3. In Section 2.2.4, we discuss a useful and experimentally-

motivated calculational tool for simulating the master equation: the Monte Carlo wave function method.

2.2.1 The density matrix formalism

We often find ourselves in situations in which the exact quantum state of a system is unknown, but we do know that it may be in one of several states $|\psi_i\rangle$, each with a probability p_i. The system is then said to be in a statistical ensemble of the states $|\psi_i\rangle$. This is a fundamentally separate notion from a quantum superposition

$$|\Psi\rangle = \sum_i \alpha_i |\psi_i\rangle , \tag{2.36}$$

in which α_i is a probability amplitude and $|\Psi\rangle$ is the quantum state of the system, because Eq. (2.36) assumes that the state $|\Psi\rangle$ is a specific vector sum of the states $|\psi_i\rangle$. In other words, if we were to create many copies of our system, then a randomly chosen copy would be in $|\psi\rangle_i$ with probability p_i. In this sense, the system exists as a classical distribution of quantum states, which has the mathematical representation [127]

$$\hat{\rho} = \sum_i p_i |\psi_i\rangle \langle\psi_i| , \tag{2.37}$$

in which $\hat{\rho}$ is the "density matrix." This type of state may arise due to experimental limitations in state preparation. However, even an initial pure state will evolve into a mixed state if it undergoes some decoherence process, in which the system irreversibly interacts with its environment. In the following chapters, we extensively study systems which may undergo the decoherent spontaneous emission process, and hence we must adopt the density matrix perspective.

We now point out some important properties and terminology for the density matrix formalism. We refer the reader to Ref. [139] for a much more detailed and complete presentation.

Unit trace: We immediately see from Eq. (2.37) that the trace of the density matrix satisfies

$$\mathrm{Tr}[\hat{\rho}] = \sum_j \langle j|\hat{\rho}|j\rangle = \sum_{i,j} p_i \langle j|\psi_i\rangle \langle\psi_i|j\rangle = \sum_{i,j,k,k'} p_i c^*_{k'} c_k \langle j|k\rangle \langle k'|j\rangle = \sum_i p_i \sum_j |c_j|^2 = 1, \tag{2.38}$$

in which the sets $\{|j\rangle\}$, $\{|k\rangle\}$, and $\{|k'\rangle\}$ form a basis for the Hilbert space. This is the equivalent condition for state normalization $\langle\Psi|\Psi\rangle = 1$.

Pure vs. mixed states: Notice that the density matrix reduces to a single outer product state $\hat{\rho} = |\psi_i\rangle \langle\psi_i|$ if the system can only be in the state $|\psi_i\rangle$, i.e., $p_i = 1$ and therefore $p_j = 0$ for $j \neq i$. In this case, there is no classical uncertainty in the state of the system, and the density matrix is therefore said to be in a "pure state." If $\hat{\rho}$ is not pure, then it is said to be in a "mixed state." One way to measure whether a density matrix is pure or mixed (without explicit diagonalization, which may be difficult) is to calculate its "purity" $\mathrm{Tr}[\hat{\rho}^2]$. It can be shown that

$$\frac{1}{d} \leq \mathrm{Tr}[\hat{\rho}^2] \leq 1, \tag{2.39}$$

where d is the dimension of the Hilbert space, and $\mathrm{Tr}[\hat{\rho}^2] = 1$ if and only if $\hat{\rho}$ is pure.

Operator expectation values: For a state $|\Psi\rangle$, the expectation value of an observable $\hat{A}$ is given by the familiar calculation

$$\langle \hat{A} \rangle = \langle \Psi | \hat{A} | \Psi \rangle \,. \tag{2.40}$$

Generalizing this notion to the density matrix case, we see from Eq. (2.37) that

$$\langle \hat{A} \rangle = \sum_i p_i \langle \psi_i | \hat{A} | \psi_i \rangle = \sum_i p_i \langle \psi_i | \hat{A} \left(\sum_j |j\rangle \langle j| \right) |\psi_i\rangle = \sum_j \langle j| \hat{\rho} \hat{A} |j\rangle = \mathrm{Tr}\left[\hat{\rho}\hat{A}\right]. \tag{2.41}$$

Evolution: For a closed quantum system (no interactions with an external entity), the state $\hat{\rho}(t)$ is evolved in time according to the von-Neumann equation

$$\frac{d\hat{\rho}}{dt} = \frac{1}{i\hbar}\left[\hat{H}, \hat{\rho}\right]. \tag{2.42}$$

This result can be easily derived from the fact that each state $|\psi_i\rangle$ evolves under the Schrödinger equation

$$i\hbar \frac{d\,|\psi_i\rangle}{dt} = \hat{H}\,|\psi_i\rangle \,. \tag{2.43}$$

Reduced density matrices: If the density matrix $\hat{\rho}$ describes a bipartite system, i.e, a system comprised of two distinct parts a and b, each of which live in a subspace of the total Hilbert space $\mathcal{H}_a, \mathcal{H}_b \subseteq \mathcal{H}$ respectively, then the "reduced density matrix" $\hat{\rho}_i$ of each subsystem is given by

$$\hat{\rho}_i = \mathrm{Tr}_j[\hat{\rho}], \qquad i \neq j. \tag{2.44}$$

Equipped with these properties, we can now derive the quantum master equation which is used to describe open quantum systems.

2.2.2 The quantum master equation

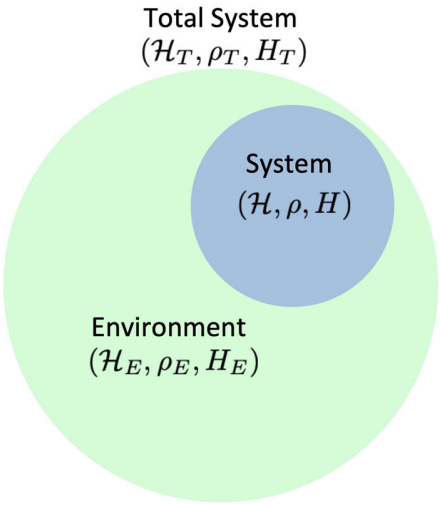

Figure 2.4: Diagram of a bipartite quantum system. The total Hilbert space $\mathcal{H}_T$ is divided into the "system" subspace $\mathcal{H}$ and the "environment" subspace $\mathcal{H}_E$. Image from Ref. [113].

As shown in the previous section, a closed quantum system living in a Hilbert space $\mathcal{H}_T$, where T represents the "total" system, described by a density matrix $\hat{\rho}_T$ is evolved in time by the von-Neumann equation [Eq. (2.42)], which is the density matrix version of the Schrödinger equation. In this section, we discuss the key concepts behind the derivation of the quantum master equation, which evolves states in a subspace of interest $\mathcal{H} \subseteq \mathcal{H}_T$ of $\mathcal{H}_T$, which we call the "system" subspace, potentially interacting with the (uninteresting) remainder of the total system, which we call the "environment" subspace $\mathcal{H}_E$. The various spaces are shown diagrammatically in Fig. 2.4. We refer the reader to Ref. [70] for an excellent formulation of this derivation.

The steps for deriving the master equation is as follows:

(1) Solve the von-Neumann equation [Eq.(2.42)] for the total density matrix $\hat{\rho}_T$ under the effects of the total Hamiltonian $\hat{H}_T$ to second order in perturbation theory (the Born

approximation)

(2) Trace over the environment subspace $\mathcal{H}_E$ using Eq. (2.44)

(3) Simplify the result based on the timescale hierarchy

$$\tau_{\text{corr}} \ll \tau_{\text{sys}} \ll \tau_{\text{band}}, \tag{2.45}$$

where τ_{corr} is the (vanishingly small) correlation time of the background field modes, τ_{sys} is the characteristic timescale of the system of interest, and τ_{band} is the (very large) inverse bandwidth of the background radiation field (the Weisskopf-Wigner, or Markov approximation)

The resulting equation for the system density matrix $\hat{\rho}$ reads [113]

$$\frac{d\hat{\rho}}{dt} = \frac{1}{i\hbar}[\hat{H}, \hat{\rho}] + \hat{\mathcal{L}}\hat{\rho}, \tag{2.46}$$

where $\hat{H}$ is the system Hamiltonian, and

$$\hat{\mathcal{L}}\hat{\rho} = \sum_i \left(\hat{J}_i \hat{\rho} \hat{J}_i^\dagger - \frac{1}{2} \left\{ \hat{J}_i^\dagger \hat{J}_i, \hat{\rho} \right\} \right) \tag{2.47}$$

is the "Lindblad superoperator." The operators $\hat{J}_i$, called "jump operators," incorporate the dissipative effects of the system's interaction with the environment by projecting higher-energy state populations to lower-energy states at the appropriate dissipative rate. In other words, the $\hat{J}_i$'s describe the various decay channels of the system. Eq. (2.46) is the workhorse of our studies in the following chapters.

There are important consequences to introducing a dissipative process into a quantum system. First, it allows for an arbitrarily initialized system to reach a steady-state configuration. This can be seen by setting the time derivative of $\hat{\rho}$ in Eq. (2.46) to zero:

$$0 = \frac{1}{i\hbar}[\hat{H}, \hat{\rho}_{\text{ss}}] + \hat{\mathcal{L}}\hat{\rho}_{\text{ss}} \quad \Rightarrow \quad [\hat{H}, \hat{\rho}_{\text{ss}}] = -i\hbar\hat{\mathcal{L}}\hat{\rho}_{\text{ss}}. \qquad \text{(steady-state)} \tag{2.48}$$

For $\hat{\mathcal{L}}\hat{\rho} \neq 0$, this equation can be solved for the steady-state density matrix $\hat{\rho}_{\text{ss}}$. However, if there were no dissipative processes ($\hat{\mathcal{L}}\hat{\rho} = 0$), then Eq. (2.48) states that $\hat{\rho}$ must commute with $\hat{H}$ to reach

steady-state, which is not true for an arbitrary initial state. Second, a dissipative interaction allows for an irreversible change of the system's entropy. Of course, there would be a corresponding change in the environment's entropy by the second law of thermodynamics. In the following chapters, we will often choose the system Hamiltonian $\hat{H}$ to evolve the system into a relatively low-entropy steady-state configuration.

2.2.3 The Lindblad superoperator in laser slowing, cooling, and trapping

In Chapters 3-6, we will be studying two- and three- level quantum particles that are free to move in one spatial dimension. To determine the Lindblad superoperator $\hat{\mathcal{L}}\hat{\rho}$ for this type of system, we need to characterize the decay channels $\hat{J}$ associated with the spontaneous emission process. For simplicity, we demonstrate the derivation of $\hat{\mathcal{L}}\hat{\rho}$ for a moving two-level particle that may emit linearly polarized light (Chapters 3, 4, and 6) or circularly polarized light (Chapter 5). The extension to the three-level case is straightforward.

Because the particle exists in three-dimensional space, it may emit spontaneous photons with angular momentum $\hbar q$ and wave vector $\boldsymbol{k}_{\mathrm{sp}}$ according to a (normalized) dipole radiation pattern [135]

$$N_{\pm}(u) = \frac{3}{8}\left(1+u^2\right), \qquad N_0(u) = \frac{3}{4}\left(1-u^2\right), \tag{2.49}$$

in which $u = \cos\phi$, and $0 \leq \phi \leq \pi$ is the angle between $\boldsymbol{k}_{\mathrm{sp}}$ and the axis of motion, which we call the z-axis here. The subscripts denote the angular momentum of the emitted photons, which depends on the internal level structure of the system of interest. Notice that Eq. (2.49) is continuous, which means that there is a continuum of decay channels corresponding to the different emission directions. The jump operator corresponding to the variable u is then

$$\hat{J}_u = \sqrt{\gamma N(u)}e^{-ik\hat{z}u}\hat{\sigma}^-, \tag{2.50}$$

where we have used $|\boldsymbol{k}_{\mathrm{sp}}| = k$, and the exponential operator accounts for the associated momentum recoil

$$\Delta p_u = \hbar k u \tag{2.51}$$

of the particle along the z-axis. Generalizing the sum in Eq. (2.47) to an integral, we find that

$$\hat{\mathcal{L}}\hat{\rho} = \gamma \left(\int_{-1}^{1} du\, N(u) e^{-ik\hat{z}u} \hat{\sigma}^- \hat{\rho} \hat{\sigma}^+ e^{ik\hat{z}u} - \frac{1}{2} \left\{ \hat{\sigma}^+ \hat{\sigma}^-, \hat{\rho} \right\} \right). \tag{2.52}$$

We emphasize that we have integrated over u in the anticommutator terms in Eq. (2.52).

For computational simplicity, we now discuss how to perform a coarse discretization of the dipole radiation pattern such that the particle remains on a momentum grid with a spacing defined by the photon momentum $\hbar k$, but the distribution still sufficiently models the momentum diffusion caused by the continuous pattern [Eq. (2.49)]. More specifically, let us define the discretized radiation pattern

$$N_q^{\text{disc}}(u) = A_q \left[\delta(u-1) + \delta(u+1) \right] + B_q\, \delta(u), \tag{2.53}$$

where δ is the Dirac delta function, which allows for the emission of a spontaneous photon with momentum $\hbar q$ along the $\pm\hat{z}$-directions (with equal probability A_q by symmetry) and spontaneous emission perpendicular to the $\hat{z}$-direction with probability B_q. Then, the Lindblad superoperator in Eq. (2.52) can be approximated by

$$\hat{\mathcal{L}}_q\, \hat{\rho} = \gamma \left(A_q\, e^{-ik\hat{z}} \hat{\sigma}^- \hat{\rho} \hat{\sigma}^+ e^{ik\hat{z}} + A_q\, e^{ik\hat{z}} \hat{\sigma}^- \hat{\rho} \hat{\sigma}^+ e^{-ik\hat{z}} + B_q\, \hat{\sigma}^- \hat{\rho} \hat{\sigma}^+ - \frac{1}{2} \left\{ \hat{\sigma}^+ \hat{\sigma}^-, \hat{\rho} \right\} \right). \tag{2.54}$$

We choose A_q and B_q by enforcing that the resulting first and second moments of the momentum recoil [see Eq. (2.51)] match that of the continuous pattern. The first moments are $\langle \Delta p \rangle = 0$ in all cases by symmetry. For the case of linear polarization ($q = 0$), the second moments are

$$\begin{aligned} \langle \Delta p^2 \rangle &= (\hbar k)^2 \int_{-1}^{1} du\, u^2 N_0(u) = \frac{1}{5} (\hbar k)^2, \\ \langle \Delta p^2 \rangle^{\text{disc}} &= (\hbar k)^2 \int_{-1}^{1} du\, u^2 N_0^{\text{disc}}(u) = 2A_0 (\hbar k)^2. \end{aligned} \quad \Rightarrow \quad A_0 = \frac{1}{10}, \quad B_0 = \frac{8}{10}. \tag{2.55}$$

For circular polarization ($q = \pm 1$), the second moments are

$$\begin{aligned} \langle \Delta p^2 \rangle &= (\hbar k)^2 \int_{-1}^{1} du\, u^2 N_{\pm}(u) = \frac{2}{5} (\hbar k)^2, \\ \langle \Delta p^2 \rangle^{\text{disc}} &= (\hbar k)^2 \int_{-1}^{1} du\, u^2 N_{\pm}^{\text{disc}}(u) = 2A_{\pm} (\hbar k)^2. \end{aligned} \quad \Rightarrow \quad A_{\pm} = \frac{1}{5}, \quad B_{\pm} = \frac{3}{5}. \tag{2.56}$$

We will use Eq. (2.54) with the A_q's and B_q's determined in Eqns. (2.55) and (2.56) in each of the following chapters that involve particle motion.

2.2.4 The Monte Carlo wave function method

Armed with the quantum master equation [Eq. (2.46)], we are in principle ready to begin investigating the physics of interest in each of our proposed projects. Our investigations in Chapters 3-6 involve the usage of time-dependent light fields, which makes Eq. (2.46) analytically intractable. We are therefore compelled to adopt a numerical approach. While the dimension of the internal state Hilbert spaces d_{int} of the two- and three-level quantum particles we consider are relatively small and therefore numerically tractable, their external Hilbert space dimension d_{ext} is potentially very large. This means that calculating the density matrix $\hat{\rho}(t)$, which has $(d_{\text{int}}d_{\text{ext}})^2-1$ degrees of freedom, is computationally expensive. Fortunately, there exist various methods of approximating the solution to the quantum master equation, such as mean field theory, quantum and c-number Langevin theory [127], truncated cumulant theory, and the Monte Carlo wave function method [63, 70, 135, 151].

We adopt the last procedure, which involves the stochastic evolution of many state vectors $|\psi\rangle$, which have $2(d_{\text{int}}+d_{\text{ext}})-2$ degrees of freedom. This lower scaling makes their evolution faster computationally at the expense of only approximating the dynamics. This method is based on the assumption that the information gained by continuously monitoring the system for signatures of dissipative events, which yield "quantum jumps" [133] to lower energy states in the system, can be used to infer the state of the system at any given time for a particular experiment iteration. In all of the cases we consider, a quantum jump corresponds to the emission of a spontaneous photon, although there may be multiple "decay channels" depending on the emission pattern and the number of internal states. These experimental iterations can be either physical (performed in a laboratory) or numerical (simulated on a computer); we consider the latter scenario. Each iteration can be roughly understood as a particular (and potentially stochastic) run of the experiment and is accordingly called a "quantum trajectory." It follows that the density matrix, which represents the average state of the system over all possible outcomes, can then be approximated as the average of these individual trajectories [see Eq. (2.61)].

We follow the Monte Carlo wave function approach outlined in Ref. [63]. The algorithm for the evolution of each quantum trajectory, which can performed in parallel, is as follows:

(1) Initialization: If the initial state of the system is pure ($\hat{\rho}(0) = |\phi\rangle\langle\phi|$), then initialize the wave function as the corresponding state vector: $|\psi(0)\rangle = |\phi\rangle$. If the initial state is mixed, then randomly initialize the wave function as one of the $|\psi_i\rangle$'s [Eq. (2.37)] weighted by their probabilities. Generate and store a random number $0 \leq r \leq 1$. Proceed to step (2).

(2) Evolution: Evolve the wave function under the non-Hermitian Hamiltonian

$$\hat{H}_{\text{eff}} = \hat{H} - \frac{i\hbar}{2}\sum_i \hat{J}_i^\dagger \hat{J}_i, \tag{2.57}$$

in which the $\hat{J}_i$'s are the jump operators introduced in the previous section, until either (i) the final desired time is reached, or (ii) the norm of the wave function satisfies

$$\langle\psi(t)|\psi(t)\rangle = r. \tag{2.58}$$

(Note that the norm of the wave function $|\psi(t)\rangle$ may have decreased due to the non-Hermiticity of $\hat{H}_{\text{eff}}$.) In case (i), proceed directly to step (4). In case (ii), proceed to step (3).

(3) Quantum jump: A quantum jump has occurred. Simulate the jump by randomly choosing a decay channel $\hat{J}_i$ weighted by the decay channel probabilities

$$P_i = \frac{\langle\psi(t)|\hat{J}_i^\dagger \hat{J}_i|\psi(t)\rangle}{\sum_j \langle\psi(t)|\hat{J}_j^\dagger \hat{J}_j|\psi(t)\rangle}. \tag{2.59}$$

Once the decay channel has been determined, set the (normalized) state after the jump to be

$$|\psi'(t)\rangle = \frac{\hat{J}_i\,|\psi(t)\rangle}{\langle\psi(t)|\hat{J}_i^\dagger \hat{J}_i|\psi(t)\rangle}. \tag{2.60}$$

Repeat step (2).

(4) Repeat the entire process if another quantum trajectory is desired.

At any time during the evolution, the approximate density matrix can be calculated according to the equation

$$\hat{\rho}(t) \approx \frac{1}{N} \sum_{j=1}^{N} |\psi_j(t)\rangle \langle \psi_j(t)| , \tag{2.61}$$

where j indexes a particular quantum trajectory, and $N \gg 1$ is the total number of quantum trajectories. We would arrive at the exact form of the density matrix in the limit $N \to \infty$. Operator expectation values can then be approximated through Eq. (2.41), although it generally requires less memory to calculate the expectation value on a trajectory-by-trajectory basis with Eq. (2.40) and then average the results.

Eq. (2.61) demonstrates why decoherence processes tend to change an initially pure state to a mixed state. Namely, if there were no decoherence processes, then $\hat{H}_{\text{eff}}$ would be Hermitian. Consequently, the norm of each wave function wouldn't change, and no stochasticity would be introduced into the quantum trajectories. Each quantum trajectory would hence be identical, and Eq. (2.61) would then be pure.

2.3 Doppler-based cooling and trapping processes

At this point, we have presented the essential mathematical and computational tools necessary for calculating the quantities we discuss in the following chapters. In this section, we describe the commonly-implemented methods of two-level Doppler cooling and the conventional magneto-optical trap (MOT), which provide us with a benchmark to which we will compare the laser cooling and trapping techniques we describe in Chapters 3 and 5.

2.3.1 Approximation of classical particle motion

In most theoretical treatments of Doppler cooling and MOTs, the particle is approximated to be a classical point particle, i.e., the position and momentum operators $\hat{\boldsymbol{r}}$ and $\hat{\boldsymbol{p}}$ are replaced with the classical variables $\boldsymbol{r}$ and $\boldsymbol{p}$ which are evaluated at the center-of-mass of the particle. (In the context of laser cooling and trapping, this is often called the "semiclassical approximation," which is not to be confused with the approximation of light as a classical electromagnetic field,

although these approximations are often invoked in tandem.) We showed in Section 2.1 that the electric field $\boldsymbol{E}(\boldsymbol{r}, t)$ of the applied light has a characteristic length determined by the wavelength $\lambda = 2\pi/k$. To treat the motion of the particle classically, then, the spatial width $\sigma_{\hat{\boldsymbol{r}}}$ of the particle's wave function (or wave packet) must be small compared to the wavelength of the light:

$$\sigma_{\hat{\boldsymbol{r}}} \ll \lambda. \tag{2.62}$$

Moreover, the wave packet's momentum spread $\sigma_{\hat{\boldsymbol{p}}}$ must correspond to a spread of Doppler shifts that is small compared to the linewidth γ of the cooling transition [53]:

$$\frac{k\sigma_{\hat{\boldsymbol{p}}}}{m} \ll \gamma, \tag{2.63}$$

where m is once again the particle mass. Together with the Heisenberg uncertainty principle

$$\sigma_{\hat{\boldsymbol{r}}}\sigma_{\hat{\boldsymbol{p}}} \geq \hbar, \tag{2.64}$$

these localization conditions imply that

$$\chi \equiv \frac{\omega_r}{\gamma} \ll 1, \tag{2.65}$$

in which

$$\omega_r = \frac{\hbar k^2}{2m} \tag{2.66}$$

is the "recoil frequency" of the transition. Notice that $\hbar\omega_r$ corresponds to the kinetic energy of a particle with a momentum equal to that of a single photon $p = \hbar k$ and hence sets a frequency scale for the particle motion.

Eq. (2.65) is equivalent to the condition that the timescale of the internal state dynamics (determined by γ) is much faster than the timescale of the particle motion (determined by ω_r), and therefore that we can approximate the internal states to be in steady state at all times. For most laser cooling transitions, ω_r is on the order of kHz and γ is on the order of MHz, so this approximation is valid. However, the systems we consider in the following chapters correspond to $\chi \approx 1$, so we must preserve the quantum mechanical nature of the center-of-mass position and

momentum. Nevertheless, it is still useful to understand the effects of Doppler cooling in this regime for the sake of context and comparison. For the remainder of this chapter, we will consider systems obeying Eq. (2.65). Moreover, we will only study motion along one dimension, which we call the z-direction.

2.3.2 Cooling force

In Section 2.1.1, we derived the following expression [Eq. (2.15)]

$$\hat{H} = \hat{H}_{\text{internal}} + \frac{\hat{\boldsymbol{p}}^2}{2m} - \hat{\boldsymbol{d}} \cdot \boldsymbol{E}(\hat{\boldsymbol{r}}, t). \tag{2.67}$$

for the interaction of a quantum particle with a light field. We now wish to investigate the resulting mechanical effects on the particle, i.e., the evolution of its center-of-mass motion due to the forces induced by the light. Of course, this is described by Newton's second law of motion [127]

$$\hat{\boldsymbol{F}}(t) = \frac{d\hat{\boldsymbol{p}}}{dt} = \frac{i}{\hbar}[\hat{H}, \hat{\boldsymbol{p}}] = -\frac{\partial \hat{H}}{\partial \hat{\boldsymbol{r}}} = \frac{\partial}{\partial \hat{\boldsymbol{r}}} \left(\hat{\boldsymbol{d}} \cdot \boldsymbol{E}(\hat{\boldsymbol{r}}, t) \right). \tag{2.68}$$

Notice that only the dipole term results in a force because $\hat{H}_{\text{internal}}$ involves the particle's relative coordinates (and not the center-of-mass) and the kinetic energy term commutes with $\hat{\boldsymbol{p}}$.

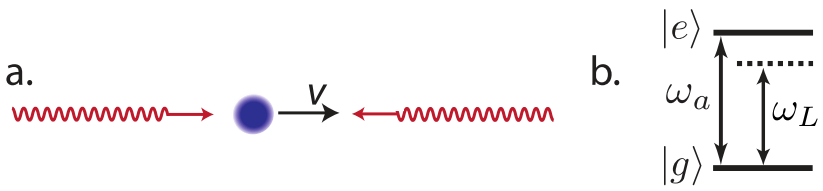

Figure 2.5: (a) Laser setup for Doppler cooling. Counterpropagating beams interact with particles of velocity v. (b) Energy level diagram of the two-level particle with the laser frequency ω_L. Notice that the laser is red detuned, i.e., $\omega_L < \omega_a$ so that $\delta < 0$ [see Eq. (2.70)].

Under the assumptions introduced in Section 2.65 (classical, one-dimensional motion) and the electric dipole approximation of Section 2.1.1 (electric field is uniform over the spatial extent of the particle), the expectation value of the light force operator $\hat{\boldsymbol{F}}(t)$ defined in Eq. (2.68) is

$$F(t) = \langle \hat{\boldsymbol{F}}(t) \rangle = \langle \hat{\boldsymbol{d}} \cdot \hat{\epsilon} \rangle \, E_0 \frac{\partial f(z,t)}{\partial z}, \tag{2.69}$$

in which we used Eq. (2.18). It is necessary to use a standing wave [two counterpropagating laser beams, Fig. 2.5(a)] to realize cooling, which means that function f is given by Eq. (2.20). After the rotating wave approximation, incorporating the steady-state solution of the internal state variables (as given by the optical Bloch equations [126]), and averaging over a wavelength, the resulting force is

$$F_{\text{Doppler}} = -\beta v = \hbar k^2 \frac{8 s_0 (\delta/\gamma)}{\left(1 + (2\delta/\gamma)^2\right)^2} \, v = \hbar k^2 \frac{8 s (\delta/\gamma)}{1 + (2\delta/\gamma)^2} \, v, \tag{2.70}$$

in which $v = p/m$ is the particle velocity,

$$\delta = \omega_L - \omega_a \tag{2.71}$$

is the laser "detuning" from the transition frequency of the two-level particle,

$$s_0 \equiv 2|\Omega|^2/\gamma^2 \tag{2.72}$$

is the on-resonance saturation parameter, and

$$s \equiv \frac{s_0}{1 + (2\delta/\gamma)^2} \tag{2.73}$$

is the saturation parameter. We emphasize that Eq. (2.70) is only valid in the limit of low saturation, $s \ll 1$, so that the steady state excited state population

$$\rho_{ee} = \frac{s}{2(1+s)}, \tag{2.74}$$

is low. This is because a low excited state fraction ensures that spontaneous emission returns particles to the ground state. Otherwise, stimulated emission would occur, which in this case would cancel the average force. Additionally, some nontrivial, velocity-dependent, multiphoton forces (see Sections 3.6.1 and 3.6.2) begin to affect the dynamics if the saturation is not low.

Notice that Eq. (2.70) has the form of a damping force, so it will tend to reduce the speeds of moving particles if the friction coefficient satisfies $\beta > 0$. The reduction of velocities to zero, regardless of the initial velocity, is exactly what is meant by laser "cooling." The cooling condition $\beta > 0$ is equivalent to $\delta < 0$, or $\omega_L < \omega_a$ [see Fig. 2.5(b)]. So, this procedure will tend to cool the

particles if the laser frequency is designed to be lower than the transition frequency of the two-level particle. In analogy to the red color of lower frequency light, this is referred to as a "red detuned" configuration.

Let us now provide an intuitive, microscopic description of the mechanism behind this "Doppler cooling" process. Because both lasers are red detuned in the laboratory frame (by design), they are not "on resonance" with a motionless particle, i.e., the magnitudes of the frequency of the light ω_L and the transition frequency ω_a do not exactly match. However, if the particle is moving along the z-direction, then it will perceive a Doppler shift kv for each laser in its frame of reference. More specifically, the light which is propagating in the opposite direction of its motion (counterpropagating) will be "blue shifted," and the light which is propagating along the same direction as its motion (copropagating) will be further "red shifted." Therefore, the counterpropagating laser is closer to resonance with the particle, and is then more likely to cause the particle to absorb a photon. Because photons have momentum, this absorption will impart an impulse to the particle in the opposite direction of its motion. Soon after, the particle will release a spontaneous photon. (This is much more likely than stimulated emission because $s \ll 1$.) Many iterations of this absorption - spontaneous emission process will result in the cooling of the particle to a zero average velocity, as the absorbed photons always push against its motion, and the effects of the spontaneous photons average to zero due to the random emission direction. This photon picture will prove to be invaluable in understanding the laser cooling and slowing protocols we propose in the following chapters.

2.3.3 Minimum temperature

The previous section elucidated the circumstances under which the laser configuration depicted in Fig. 2.5(a) would apply a viscous optical force to a two-level particle exhibiting classical motion. It seems from what we presented so far that all particles would eventually reach zero velocity and remain motionless. This is of course not what happens because the particles also undergo momentum diffusion due to their continuous interaction with the laser [126]. For example,

near zero velocity, the particles no longer preferentially interact with a single beam, which causes them to randomly absorb a photon from either beam and potentially gain speed. Additionally, the particles have a chance of emitting spontaneous photons if they have a nonzero excited state fraction, which yields a force in a random direction.

It can be shown that the balance between the cooling force and the momentum diffusion results in a Gaussian spread of velocities. This suggests that we can characterize the ensemble of particles by a "temperature" T in a similar fashion to the theory of statistical mechanics. More specifically, it can be shown by modelling the motion as a random walk (or a Fokker-Planck equation) that the momentum distribution $W(p)$ of the particle ensemble equilibrates to the form

$$W(p) \propto e^{-\beta p^2/2mD}, \tag{2.75}$$

in which β is the friction coefficient derived in the previous section [Eq. (2.70)] and D is the diffusion coefficient. While D can be derived in a rigorous way from these models, we instead provide an intuitive, quick derivation [126]. Consider a particle locked to a momentum grid with spacing $\hbar k$. As a consequence, the particle can emit spontaneous photons only along the z-axis. For a single beam, the probability per unit time that the particle emits a spontaneous photon is given by the scattering rate $\gamma_p = \gamma\rho_{ee}$. Multiplying this rate by two (since there are two beams) and incorporating the magnitude of the momentum recoil results in the diffusion coefficient

$$D = \frac{2(\Delta p)^2}{\Delta t} = 4\gamma_p(\hbar k)^2. \tag{2.76}$$

Comparing the form of Eq. (2.75) to that of a 1D Maxwell-Boltzmann momentum distribution, we arrive at the Einstein relation

$$k_B T = \frac{D_0}{\beta}. \tag{2.77}$$

Substituting our results from Eqns. (2.70) and (2.76) into Eq. (2.77) and minimizing the temperature with respect to detuning δ, we arrive at the "Doppler temperature" formula

$$T_D = \frac{\hbar\gamma}{2k_B}. \tag{2.78}$$

This corresponds to a temperature of roughly $25\,\mu$K for a $\gamma = 2\pi \times 1$ MHz linewidth transition. We will compare the Doppler temperature T_D to the temperatures resulting from the methods we propose in the following chapters.

2.3.4 The magneto-optical trap

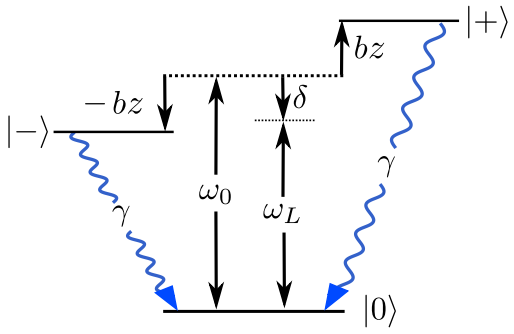

Figure 2.6: Relevant states of a $J_g \to J_e = J_g + 1$ transition for a conventional MOT. Using the notation $|J, m_j\rangle$, the labeled states are $|0\rangle = |0, 0\rangle$, $|\pm\rangle = |1, \pm 1\rangle$. We also provide the Zeeman shifts $\pm bz$ in the case of a nonzero magnetic field.

Now that we have characterized the forces and temperatures achieved with Doppler cooling, we explain its combination with a quadrupole magnetic trap to form a magneto-optical trap (MOT) [126]. Such a configuration is relatively easy and inexpensive to create, robust to experimental errors, and exhibits both cooling and trapping capabilities. We will replace the cooling mechanism of this apparatus to generate higher coherent forces in Chapter 5. We first specify the necessary state structure, magnetic field, and laser configuration, and then we discuss the underlying physics of the MOT.

The trapping force is a consequence of the energy of a magnetic dipole moment $\hat{\boldsymbol{\mu}}$ in an external magnetic field $\boldsymbol{B}$. In analogy with the classical case,

$$\hat{H}_B = -\hat{\boldsymbol{\mu}} \cdot \boldsymbol{B}. \tag{2.79}$$

The magnetic dipole moment of a quantum system is related to its total angular momentum $\hat{\boldsymbol{J}}$

through the relationship

$$\hat{\boldsymbol{\mu}} = -\frac{g_j \mu_B}{\hbar} \hat{\boldsymbol{J}}, \tag{2.80}$$

in which μ_B is the Bohr magneton, and g_j is the Landé g-factor. We consider the simple three level system depicted in Fig. 2.6, which has two excited Zeeman sub-levels $|J_e, M_e = \pm 1\rangle = |\pm\rangle$ and one ground state $|J_g, M_g = 0\rangle = |0\rangle$. Such a system exists as part of a $J_g \to J_e = J_g + 1$ transition, which occurs in many atoms. Notice that we have labeled the states by their magnetic quantum numbers $m_j = 0, \pm 1$. The ground and excited state manifolds are separated by an energy $\hbar\omega_0$, and the magnetic sub-levels decay to the ground at a rate γ. We have omitted the $|J_e, m_e\rangle = |1, 0\rangle$ state from the model because it will not be optically pumped, and hence does not participate in the dynamics.

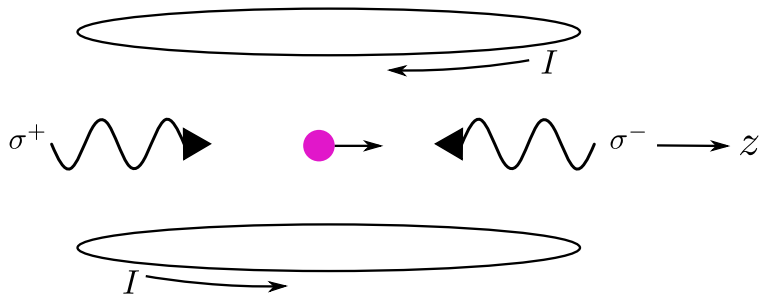

Figure 2.7: The laser ($\sigma^- - \sigma^+$) and current (I) distribution for a 1D conventional MOT. The anti-Helmholtz coils generate a magnetic field $B(z) = |\nabla B| z$, where $|\nabla B|$ is the magnetic field gradient [see Eq. (2.82)].

The magnetic field induced by the anti-Helmholtz coils of a magnetic quadrupole trap [see Fig. 2.7] is given by

$$B(\boldsymbol{r}) = |\nabla B| \sqrt{y^2 + z^2 + 4x^2} \tag{2.81}$$

in which $|\nabla B|$ is the magnetic field gradient, z and y form a plane parallel to the current loops, and x is along the axial direction. Because we consider motion only along the z-direction, the magnetic field becomes

$$\boldsymbol{B}(z) = |\nabla B| z \, \hat{e}_z. \tag{2.82}$$

Using Eqns. (2.82) and 2.80 in Eq. (2.79), we find that

$$\hat{H}_B = \hbar b z \left(|+\rangle \langle +| - |-\rangle \langle -| \right), \tag{2.83}$$

in which $b = g\mu_B |\nabla B|/\hbar$, and g is the g-factor of the transition. The laser configuration consists of counterpropagating lasers of opposite circular polarization σ^- and σ^+, as shown in Fig. 2.7. These lasers can drive the $|0\rangle \rightarrow |-\rangle$ and $|0\rangle \rightarrow |+\rangle$ transitions, respectively. Care must be taken to properly align the currents and laser polarizations into the exact configuration shown in Fig. 2.7 (or the equivalent configuration flipped about an axis pointing out of the paper). Otherwise, the particles will be driven out of the trap.

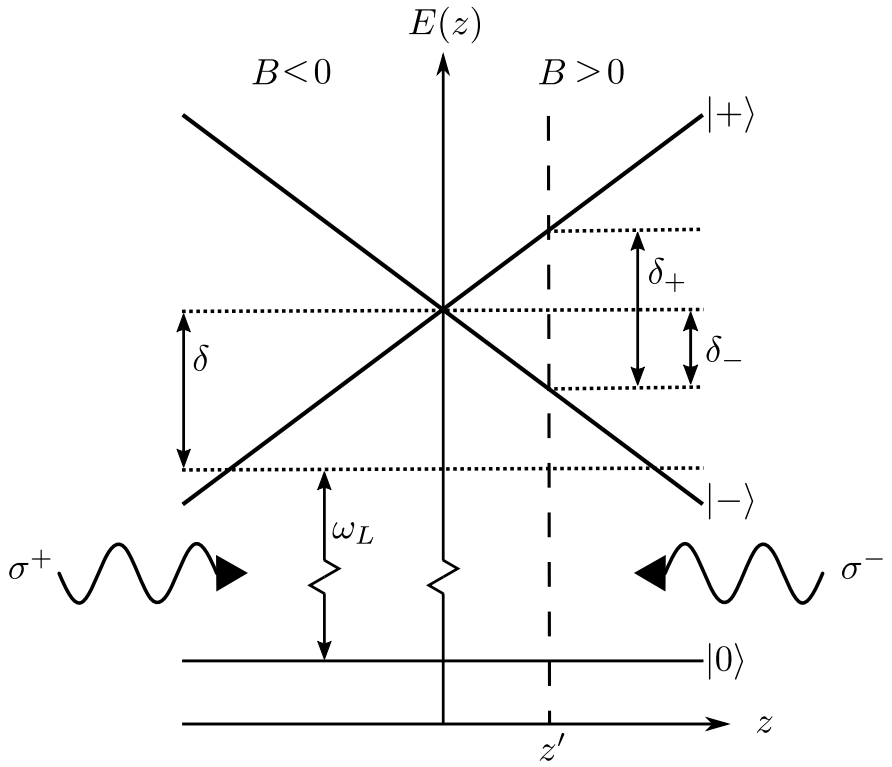

Figure 2.8: Energy diagram and laser configuration for a conventional MOT.

The laser frequency ω_L is tuned below the zero-magnetic field transition frequency ω_0 ($\delta < 0$) so that the Doppler cooling process still operates in a MOT. We now demonstrate the microscopic mechanism for realizing a trapping force. Consider a particle with zero momentum on the right side

of the trap at position z', as shown in Figure 2.8. Because the laser is red detuned and the excited states have a Zeeman shift [Eq. (2.83)], it is closer to resonance with the $|0\rangle \rightarrow |-\rangle$ transition. Therefore, the particle will preferentially absorb from the σ^- beam, which is coming from the right side of the trap. The particle will then experience an impulse that drives it toward the center of the trap. The same process occurs for particles on the left side of the trap with the $|0\rangle \rightarrow |+\rangle$ transition and the σ^+ laser. Just as in Doppler cooling, we operate in the low-saturation limit $s \ll 1$ so the particles emit a spontaneous photon soon after the absorption. (This explains why the coherent Zeeman force $\hat{F}_B = -\partial \hat{H}_B / \partial z$, which tends to pull particles away from the center of the trap with this absorption procedure, does not play a major role in the dynamics.) This cycle is repeated many times, which ultimately leads to both cooling and trapping of the particle ensemble.

The trapping force can also be demonstrated from a macroscopic force perspective. The force imparted to the particles by each of the traveling waves is given by [126]

$$\boldsymbol{F}_{\pm} = \pm \frac{\hbar \boldsymbol{k} \gamma}{2} \frac{s_0}{1 + s_0 + (2\delta_{\pm}/\gamma)^2}, \tag{2.84}$$

in which

$$\delta_{\pm} = \delta \mp \boldsymbol{k} \cdot \boldsymbol{v} \pm bz. \tag{2.85}$$

(We will find that this is very similar to an important, motion-based detuning we define in Chapter 5.) We can find the total force $\boldsymbol{F}$ on the particles through the vector sum of the two forces $\boldsymbol{F}_{\pm}$ due to the circularly polarized traveling waves:

$$\boldsymbol{F} = \boldsymbol{F}_+ + \boldsymbol{F}_- = -\beta \boldsymbol{v} - \kappa \boldsymbol{r}. \tag{2.86}$$

Notice that the first term on the rightmost side of Eq. (2.86) is the same friction force we found in Doppler cooling. This verifies that particles in a MOT are still cooled by the Doppler cooling mechanism. The second term is a restoring force with

$$\kappa = \frac{b}{k} \beta, \tag{2.87}$$

which immediately implies that particles will also experience a conservative trapping force toward the center of the trap.

Chapter 3

SWAP cooling: theoretical investigation

In this chapter, we present our theoretical contributions toward understanding the sawtooth wave adiabatic (SWAP) cooling method. This work resulted in our Physical Review A article (Ref. [13]), which was published in August 2018 and largely constitutes the material presented in this chapter. The experimental realization of SWAP cooling is the subject of Chapter 4. In this cooling method, two-level particles undergo successive adiabatic transfers upon interaction with counter-propagating laser beams that are repeatedly swept over the transition frequency. We explain the basic mechanism behind its operation and characterize the parameter regime in which it is most efficient and practical. We show that particles with narrow linewidth transitions can be cooled to near the recoil limit. We also demonstrate that SWAP cooling has an inherently reduced reliance on spontaneous emission compared to Doppler cooling, which makes it particularly applicable to systems lacking closed cycling transitions, such as molecules.

3.1 Introduction

The use of coherent light to cool the motion of particles such as atoms to sub-Kelvin temperatures has greatly expanded the capabilities of atomic and molecular physics [123]. The earliest and simplest mechanism demonstrated and understood was Doppler cooling [77, 192], which relies on preferential absorption between counterpropagating lasers, followed by spontaneous emission. While Doppler cooling is simple and robust, the large number of spontaneous emissions involved has several drawbacks: spontaneously emitted photons impart random momentum kicks to the

particle that cause diffusion and limit the achievable temperatures. These spontaneous emission events can also result in the particle falling into internal states that are no longer near resonance with the applied light so that the cooling ceases. In the case of atoms, the latter can be mitigated by adding a small number of additional lasers to "repump" into cooled states, but in the case of molecules the number of uncooled states may be so large that this approach becomes a significant challenge [31]. Doppler cooling can reach the recoil temperature (set by the recoil energy from a single emitted photon) for narrow linewidth transitions such that $\gamma < \omega_r$, where γ and ω_r are the optical transition linewidth and recoil frequency respectively. However, the cooling time scale in this parameter regime is long, scaling inversely with γ.

Several approaches to laser cooling have been developed to mitigate the negative effects of spontaneous emission [3]. In sub-Doppler cooling mechanisms such as Sisyphus cooling [54], the energy removed per spontaneously emitted photon is large, allowing lower temperatures to be reached. In Raman sideband cooling [78], tight confinement of the atom can suppress the effect of momentum recoil associated with spontaneous emission, enabling cooling to nearly the ground state of the external potential well. Cavity-cooling techniques [84] can be used to reduce free-space spontaneous emission by causing preferential decay to a desired state via the output coupler of an optical resonator.

Recently, we have experimentally demonstrated a new cooling mechanism, named "SWAP cooling" (sawtooth wave adiabatic passage cooling) in which particles are coherently driven between ground and excited states of a narrow-linewidth optical transition by counterpropagating, frequency-swept lasers. Spontaneous emission is still critical in order to remove entropy from the system to achieve steady-state cooling, but by coherently driving a particle between its ground and excited state multiple times, large amounts of energy can be removed per spontaneous emission. This provides a way to generate significant forces and to reach low temperatures while maintaining a large velocity capture range. The approach is largely insensitive to perturbations such as laser frequency drifts, magnetic fields, and AC Stark shifts. These factors have made SWAP cooling a useful experimental technique for cooling atomic strontium using its 7.5 kHz linewidth, dipole-forbidden

$^1S_0 \rightarrow {}^3P_1$ transition [141]. A related procedure has been used in the generation of a new form of magneto-optical trap [137]. Sub-Doppler cooling of ^{87}Rb was recently observed using SWAP cooling with two-photon Raman transitions between ground hyperfine states [74]. In general, the approach is applicable to any atomic species, especially alkaline-earth-like atoms that possess inter-combination transitions. Further, the reduced reliance on spontaneous emission may make SWAP cooling a useful tool for cooling molecules that have narrow linewidth optical transitions, such as the 160 kHz linewidth $X^2\Sigma \rightarrow A'^2\Delta_{3/2}$ transition in YO [49].

Here, we present a detailed theoretical analysis of SWAP cooling. We explore the minimum achievable temperature as well as the various laser-particle interactions that affect particle dynamics. We investigate its capture range and the forces involved in the cooling process. We show that for appropriate parameters, SWAP cooling can be used to cool to near the recoil limit. We also simulate the rate at which spontaneous photons are emitted during cooling, confirming that the amount of energy removed per spontaneous emission event can greatly exceed the limits of Doppler cooling.

3.2 Basic mechanism

The main mechanism for momentum removal in SWAP cooling is the coherent transfer of a particle toward zero momentum via adiabatic passage. Momentum is removed by time-ordered stimulated absorption and emission of photons caused by interaction with a standing wave formed by counter-propagating laser beams. To describe the cooling, we consider a two-level particle with internal states $|e\rangle$ and $|g\rangle$, separated in energy by $\hbar\omega_{\mathrm{a}}$, and one dimension of motional freedom along the $\hat{z}$-direction (see Figure 3.1). We choose to represent the external degree of freedom in the momentum basis and with label $|p\rangle$, where p denotes a momentum eigenstate such that $\hat{p}\,|p\rangle = p\,|p\rangle$.

As shown in Figure 2, the laser frequencies, $\omega_L(t)$, follow an asymmetric sawtooth waveform with full range Δ_s and period T_s so that the slope of the sawtooth ramp is $\alpha \equiv \Delta_s/T_s$. The sawtooth frequency ramp is centered on the transition frequency, ω_{a}, and the frequency is linearly ramped from below to above ω_{a}. We approximate the wavenumber, k, to be fixed throughout the

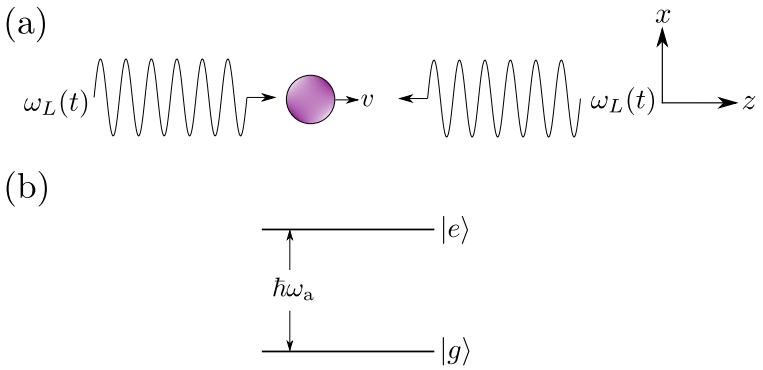

Figure 3.1: (a) Spatial setup of the standing wave (two counterpropagating lasers with frequency $\omega_L(t)$) and particle (circle) with velocity v in the lab frame. (b) Energy level diagram of the bare internal states, separated by energy $\Delta E = \hbar\omega_a$.

sweeping sequence. This also implies that the recoil frequency, $\omega_r = \hbar k^2/2m$, is fixed, where m is the mass.

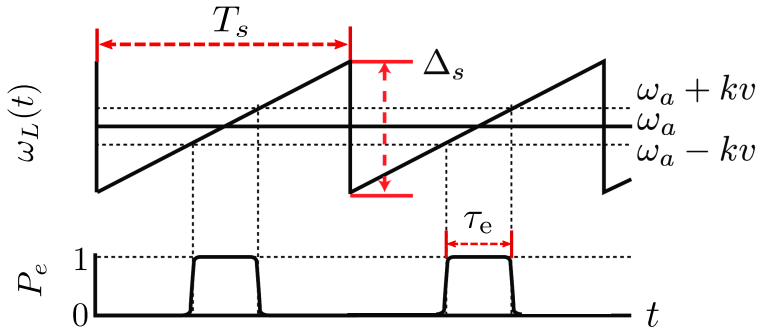

Figure 3.2: Top: The laser frequency, $\omega_L(t)$, as a function of time. The approximate resonance frequencies for a particle with velocity v are labeled. The sweep range is chosen to be large enough such that both beams will become resonant with the particle at some time during the sweep. Bottom: The ideal excited-state fraction, P_e, in the adiabatic regime. The particle remains in the excited state for a time interval τ_e.

The direction of particle motion matters since Doppler shifts set the time-ordering of which beam first interacts with the particle. To understand this time-ordering, consider a particle initially in the state $|g, p_i\rangle$. The Doppler shift ensures that the counter-propagating beam is the first to sweep across the transition frequency. If we first focus on the case with $p_i > 0$, this adiabatically transfers the particle to the state $|e, p_i - \hbar k\rangle$ via stimulated absorption. After some time, the co-

propagating beam will achieve resonance, adiabatically transferring the particle to $|g, p_i - 2\hbar k\rangle$ via stimulated emission. For $p_i < 0$, the mapping is $|g, p_i\rangle \rightarrow |e, p_i + \hbar k\rangle \rightarrow |g, p_i + 2\hbar k\rangle$. In either case, the particle is transferred closer to zero momentum. The net result is the removal $2\hbar k$ of momentum and transfer back to the particle's initial internal state without spontaneous emission. Subsequent sweeps would then continue to remove momentum in units of $2\hbar k$. Figure 3.2 shows this process by illustrating the ideal excited state fraction, P_e, over two sweeps.

The particle's internal state at the beginning of a sweep is a crucial factor in determining the impulse it receives from each laser. If the particle instead begins a sweep in the excited state, it is transferred away from zero momentum. Hence, one of the roles of spontaneous emission is to ensure that the particle begins a sweep in the ground state. This is achieved by requiring an imbalance between the times spent inside and outside of the two resonances, which corresponds to

$$\Delta_s > 4|kv|. \tag{3.1}$$

This condition also enforces the requirement that the sweep range, Δ_s, is large enough for both laser beams to achieve resonance with the particle.

There are several other conditions that must be satisfied in order to realize SWAP cooling. In order to ensure a low probability of decay during the time interval the particle is in the excited state, τ_e, we require the condition

$$\tau_\mathrm{e} \ll \frac{1}{\gamma}. \tag{3.2}$$

Importantly, the Rabi frequency of each laser beam, Ω_0, and the laser frequency sweep rate, α, must satisfy the condition

$$\kappa \equiv \frac{\Omega_0^2}{\alpha} \geq 1, \tag{3.3}$$

so that there is a substantial probability, P_a, for an adiabatic transition at each resonance [194]:

$$P_a = 1 - \exp\left[-\frac{\pi}{2}\frac{\Omega_0^2}{\alpha}\right]. \tag{3.4}$$

We shall refer to κ as the adiabaticity parameter. Any κ that satisfies Eq. (3.3) is said to be within the adiabatic regime, and any κ that does not satisfy Eq. (3.3) is said to be within the diabatic

regime.

3.3 System dynamics

The quantum master equation

$$\frac{d\hat{\rho}}{dt} = \frac{1}{i\hbar}[\hat{H}, \hat{\rho}] + \hat{\mathcal{L}}\hat{\rho} \tag{3.5}$$

governs the time evolution of the density matrix, $\hat{\rho}$, whose Hilbert space includes both the particle's internal and external degrees of freedom. The Hamiltonian, $\hat{H}$, captures the coherent dynamics, while the Lindblad superoperator, $\hat{\mathcal{L}}\hat{\rho}$, captures the incoherent dynamics due to spontaneous emission and the associated recoil.

The operators $\hat{z}$ and $\hat{p}$ describe the particle's position and momentum, respectively. The excited and ground states, $|e\rangle$ and $|g\rangle$, form a pseudo-spin 1/2 system, as discussed in Section 2.1.2. The electric field of the applied lasers is polarized along the quantization axis, $\hat{x}$, (see Figure 3.1) and is described in first quantization by the operator

$$\hat{\boldsymbol{E}}(\hat{z}, t) = \hat{x}E_0\Big[\cos\left(k\hat{z} + \eta(t)\right) + \cos\left(k\hat{z} - \eta(t)\right)\Big]. \tag{3.6}$$

Here, the amplitude of each standing wave is E_0, and the time-dependent accumulated phase of the laser field, $\eta(t)$, from initial time t_0 is

$$\eta(t) \equiv \int_{t_0}^{t} \omega_L(t')\, dt' \,. \tag{3.7}$$

In the interaction picture defined by the free Hamiltonian

$$\hat{H}_0(t) = \frac{\hat{p}^2}{2m} + \frac{\hbar}{2}\omega_{\mathrm{a}}\hat{\sigma}^z, \tag{3.8}$$

the particle's non-dissipative dynamics, under the dipole and rotating wave approximations, is described by the interaction Hamiltonian

$$\hat{H} = \frac{\hbar}{2}\Omega_s \cos\left(k\hat{z} + \frac{k\hat{p}}{m}t\right)\left(\hat{\sigma}^+ e^{-i\theta(t)} + \text{h.c.}\right), \tag{3.9}$$

where

$$\theta(t) \equiv \int_{t_0}^{t} \omega_L(t') - \omega_\mathrm{a}\, dt' = \eta(t) - \omega_\mathrm{a} t \tag{3.10}$$

is the time-dependent phase of the laser field's detuning from resonance. The standing wave's peak Rabi frequency,

$$\Omega_s \equiv 2\Omega_0 = -\frac{2\,\langle e|\hat{\boldsymbol{d}}\cdot\hat{x}|g\rangle\, E_0}{\hbar}, \tag{3.11}$$

characterizes the interaction strength of the electric field with the particle's electric dipole operator $\hat{\boldsymbol{d}}$. We refer the reader to Sections 2.1 and 2.2 for more model details.

In order to keep the momentum distribution on a discretized grid for computational simplicity, we approximate the dipole radiation pattern to produce recoil of magnitudes $-\hbar k, 0$, and $\hbar k$ along $\hat{z}$ with probabilities $\frac{1}{5} : \frac{3}{5} : \frac{1}{5}$, respectively [135]. As discussed in Section 2.2.3, the resulting Lindblad superoperator is

$$\hat{\mathcal{L}}\hat{\rho} = \gamma\left(\frac{1}{5}e^{ik\hat{z}}\hat{\sigma}^-\hat{\rho}\hat{\sigma}^+e^{-ik\hat{z}} + \frac{1}{5}e^{-ik\hat{z}}\hat{\sigma}^-\hat{\rho}\hat{\sigma}^+e^{ik\hat{z}} + \frac{3}{5}\hat{\sigma}^-\hat{\rho}\hat{\sigma}^+ - \frac{1}{2}\left\{\hat{\sigma}^+\hat{\sigma}^-,\hat{\rho}\right\}\right). \tag{3.12}$$

We emphasize that this form of $\hat{\mathcal{L}}\hat{\rho}$ is only valid for states $|e\rangle$ and $|g\rangle$ with magnetic quantum numbers m satisfying $\Delta m = \pm 1$. For states with the selection rule $\Delta m = 0$, such as the dipole-forbidden ${}^1\mathrm{S}_0 \to {}^3\mathrm{P}_1$ transition $\left(|g\rangle \equiv |{}^1\mathrm{S}_0, m=0\rangle \text{ and } |e\rangle \equiv |{}^3\mathrm{P}_1, m=0\rangle\right)$ studied in Chapter 4, one should use recoil probabilities $\frac{1}{10} : \frac{8}{10} : \frac{1}{10}$.

In summary, we consider numerical and theoretical results of Eq. (3.5) with $\hat{H}$ given by Eq. (3.9) and $\hat{\mathcal{L}}\hat{\rho}$ given by Eq. (3.12) in the following sections.

3.4 Dynamics in the high-velocity regime

The core mechanism whereby SWAP cooling removes momentum and energy from a particle's motion is most easily understood in a regime in which one can consider that the particle interacts sequentially with one traveling wave and then the other. We shall henceforth refer to this as the "high-velocity regime." To define it, we must consider the time it takes to adiabatically transfer a particle with initial velocity v_i between its internal states, which we call τ_jump, as well as the time

interval separating the two resonances, which we denote by τ_{res}. In the adiabatic regime, it can be shown that $\tau_{\text{jump}} = 2\Omega_0/\alpha$ (see [185]). We derive τ_{res} in the following subsection.

3.4.1 Resonance times and intervals in the adiabatic limit

In the adiabatic limit ($\Omega_0^2 \gg \alpha$), most of the population transfer for a motionless particle occurs around $t = 0$ for a detuning profile $\delta(t) = \alpha t$, as this is when the laser is in resonance with the particle. By energy conservation (see Eq. (3.24) with $n = 0$), motional degrees of freedom translate this "resonance period" for a particle in the state $|g, p\rangle$ interacting with a right-traveling wave to the time that satisfies

$$\alpha t_{\text{right}} - \omega_r(2\beta + 1) = \alpha t_{\text{right}} - kv - \omega_r = 0, \tag{3.13}$$

where $\beta \equiv p/\hbar k$. For high-velocity particles ($kv \gg \omega_r$), the resonance period agrees with the intuitive Doppler shift result. However, the additional recoil term is important for low velocity ($kv \simeq \omega_r$) particles. A similar result can be found for the interaction of a ground-state particle with a left traveling wave ($\beta \to -\beta$), which translates the resonance period to

$$\alpha t_{\text{left}} - \omega_r(-2\beta + 1) = \alpha t_{\text{left}} + kv - \omega_r = 0. \tag{3.14}$$

The resonance periods for a particle starting in the excited state can be found with the substitution $\omega_r \to -\omega_r$ on the additional recoil term. It is easily shown that adiabatic transfer with motion has the same probability as the motionless case [194].

In the high-velocity regime [see Eq. (3.16)], there is one stimulated absorption and one stimulated emission per sweep in SWAP cooling. From Eqs. (3.13) and (3.14), the time separating these resonant phenomena for a particle with initial velocity v_i, labeled τ_{res}, is

$$\tau_{\text{res}} = \frac{2(kv_i - 2\omega_r)}{\alpha}. \tag{3.15}$$

It should be noted that (3.15) is only valid in the adiabatic limit, since the time associated with the stimulated absorption recoil has been included.

Figure 3.3 shows the time-ordering of these processes, as well as a measure of the total excited time, $\tau_{\rm e}$, defined as the sum of $\tau_{\rm jump}$ and $\tau_{\rm res}$ in this regime. Roughly half of each $\tau_{\rm jump}$ overlaps

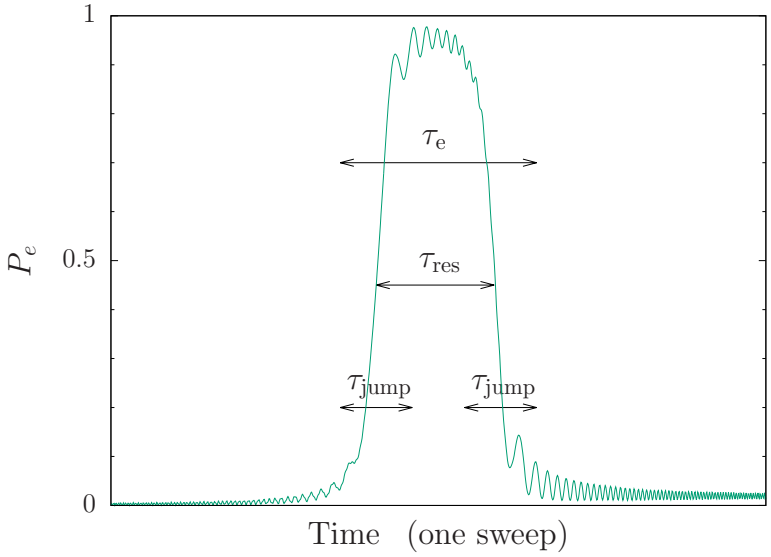

Figure 3.3: The excited state fraction, P_e, of a particle prepared in the state $|g, 10\hbar k\rangle$ over one sweep. Values are: $\Delta_s = 200\omega_r, T_s = 22/\omega_r$, and $\Omega_0 = 5\omega_r$.

with $\tau_{\rm res}$. Therefore, to keep the resonances separated, we define the high-velocity regime to be the range of velocities that satisfy $\tau_{\rm jump} < \tau_{\rm res}$, or

$$|\Omega_0| < |kv_i - 2\omega_r|. \qquad \text{(high-velocity regime)} \tag{3.16}$$

It is important to emphasize that particles outside of the high-velocity regime may still be cooled under the SWAP cooling procedure. However, their dynamics are more difficult to describe and analyze qualitatively.

3.4.2 Dressed state picture

A convenient and intuitive way to understand adiabatic transfer is the dressed state formalism. Working in the laser frame, we diagonalize the Hamiltonian

$$\hat{H}(t) = \frac{\hat{p}^2}{2m} - \frac{\hbar}{2}\delta(t)\hat{\sigma}^z + \frac{\hbar}{2}\Omega_s \cos(k\hat{z})\hat{\sigma}^x, \tag{3.17}$$

at each instant in time. Here, $\delta(t) \equiv \alpha t$ is the laser detuning from resonance, since the detuning is linearly ramped from $-\Delta_s/2$ to $\Delta_s/2$. We track the evolution of the minimal set of eigenstates necessary to demonstrate the evolution of a particle that begins a sweep in the state $|g, p\rangle$ in the high-velocity regime. This set maps to the bare eigenstates

$$\{|g, p\rangle, |e, p - \hbar k\rangle, |g, p - 2\hbar k\rangle, |e, p - 3\hbar k\rangle\} \tag{3.18}$$

in the limit of large detuning ($|\delta(t)| \gg |kv|$). The avoided crossing of a multi-photon process known as a Doppleron resonance, which does not affect the dynamics of a particle in the high-velocity regime, is also present (see Section 3.6.1 for details).

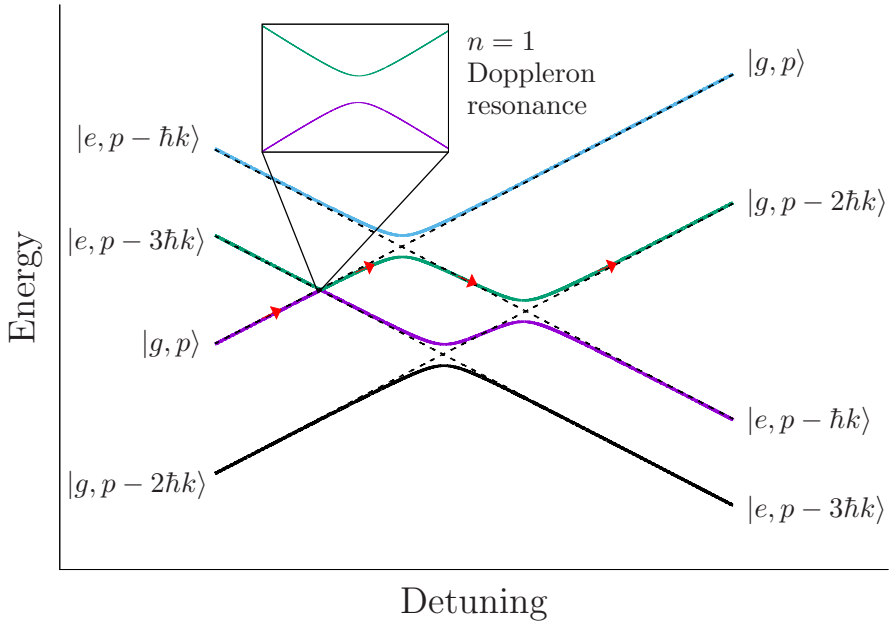

Figure 3.4: Eigenvalue energy vs. detuning for the four coupled states given in Eq. (3.18). The inset shows the splitting of an $n = 1$ Doppleron resonance, which is small in the high-velocity regime. The red arrows identify the physical path being considered. Dashed lines show the evolution of the uncoupled states. Values are: $\Omega_0 = 2\omega_r, \alpha = \omega_r^2, T_s = 50/\omega_r$. $p = 4\hbar k$.

Figure 3.4 shows the instantaneous eigenvalues as the detuning is linearly ramped. Starting in the state $|g, p\rangle$, the particle diabatically crosses the higher-order Doppleron resonance, thus being transferred into a different eigenstate. It then undergoes two adiabatic crossings, which correspond

to the two resonances previously discussed, and ends up in the state $|g, p - 2\hbar k\rangle$, signifying the removal of $2\hbar k$ of momenta. It is important to note that Figure 3.4 only depicts the correct evolution of a particle that follows the red arrows; in reality, the surrounding states would couple to states of higher and lower momenta.

3.4.3 Coherent dynamics

In order to further illustrate the dynamics strictly due to coherent evolution, we numerically calculated the time evolution of the root-mean-square (rms) momentum of the particle, $p_{\text{rms}} = \sqrt{\langle \hat{p}^2 \rangle}$, as it underwent SWAP cooling starting from the initial state $|\psi_i\rangle = |g, 10\hbar k\rangle$ and without spontaneous emission ($\gamma = 0$). The Rabi frequency was chosen such that the simulation operated in the high-velocity regime for all momentum states $|p_i| > \hbar k$.

Figure 3.5 shows the rms momentum, p_{rms}, vs. time, expressed in terms of the number of sweeps. The probability of finding the particle in the excited state, $P_e = |\langle e|\psi\rangle|^2$, is also shown on the right hand axis. One sees that during each sweep the particle was adiabatically transferred to the excited state and then back to the ground state. Each transition was accompanied by a reduction in the particle's momentum by $\hbar k$ for a total of $2\hbar k$ per sweep. As the momentum of the particle was reduced, the time between transitions became shorter (i.e., the width of the pulses became smaller). This is what one would expect since the velocity of the particle and therefore the accompanying Doppler shift is decreased.

By symmetry, and as confirmed by calculation, the rms momentum decreased in an identical manner for the state with opposite initial momentum, $|g, -10\hbar k\rangle$. Course graining over the individual sweeps, the effective force exerted on the particle drives it toward zero velocity, independent of its initial direction of motion. As a result, one should draw an important distinction between the force exhibited here and a "slowing force" that can be understood as applying a uniform translation to the momentum of all particles. Such slowing forces are often implemented in the context of slowing a molecular beam with chirped-frequency light [196] or using rapidly varying electrostatic potentials as is done in Stark decelerators [21], but do not lead to steady-state cooling.

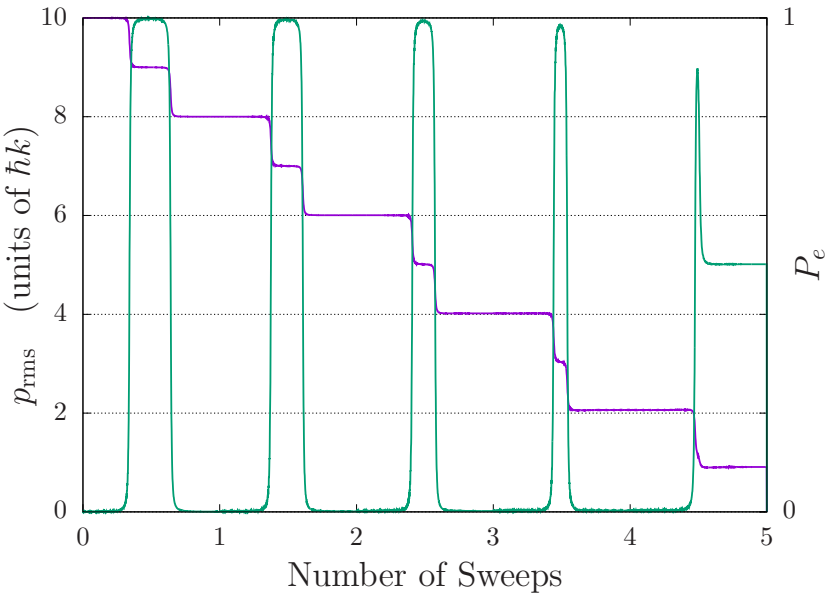

Figure 3.5: Root-mean-square momentum, $p_{\rm rms}$ (step-like curve; magenta), for a particle starting in the state $|g, 10\hbar k\rangle$ over five sweeps. The curve exhibiting rising and falling pulses shows the excited state fraction, P_e (cyan). The particle experiences a significant reduction in $p_{\rm rms}$ and is left in a superposition of the internal states. Values are: $\Delta_s = 120\omega_r, T_s = 1000/\omega_r$, and $\Omega_0 = \omega_r$.

On the final sweep shown in Figure 3.5, the particle approached zero momentum where the dynamics are modified. At the end of the final sweep, the particle had a 50% probability of occupying the $|g, 0\rangle$ state, and a 25% probability of occupying each of the $|e, \hbar k\rangle$ and $|e, -\hbar k\rangle$ states, resulting in a final rms momentum of $p_{\rm rms} = \hbar k/\sqrt{2}$ and a final excited state probability of $P_e = 1/2$. We will see that being left in the excited state at the end of the sweep is an important consideration for understanding the final equilibrium temperature.

3.4.4 High-velocity regime dynamics including dissipation

We have shown that under the influence of purely coherent dynamics, a particle prepared in its internal ground state can be sufficiently transferred to low momentum. In a realistic system, however, the presence of spontaneous emission restricts the amount of time a particle may remain in the excited state, Eq. (3.2), which increases for higher initial momentum. Nevertheless, in the context of the high-velocity regime in the adiabatic limit, it can be shown that there is no

upper bound on the momentum states that can be transferred to lower momentum via the SWAP cooling procedure, contingent that arbitrarily high Rabi frequencies and sweep rates are accessible. However, there exists a fundamental lower bound:

$$\left|\frac{p}{\hbar k}\right| \gtrapprox 1 + \frac{2\kappa\gamma}{\omega_r}. \tag{3.19}$$

This motivates the use of SWAP cooling on a transition for which $\kappa\gamma/\omega_r$ is small. It is a requirement of adiabatic transfer to have κ at least on the order of unity, so the experimentalist only has the freedom to vary the ramp slope α and Rabi frequency Ω_0 accordingly. Regardless of experimental laser parameters, narrow linewidth transitions (on the scale of the recoil frequency) are preferable if the goal is to maximally cool the system.

3.5 Forces and capture range

For analyzing the cooling dynamics, it is useful to investigate the equivalent classical force exerted on a particle as a function of its velocity or momentum. We have chosen to describe this relationship by defining various quantities that provide information about the impulse imparted to the particle over a single sweep.

3.5.1 Conservative forces

One way to describe impulsive momentum kicks applied to the particle is the change in its rms momentum due to a single sweep:

$$\Delta p_{\text{rms}} \equiv \sqrt{\langle\psi_f|\,\hat{p}^2\,|\psi_f\rangle} - \sqrt{\langle\psi_i|\,\hat{p}^2\,|\psi_i\rangle}, \tag{3.20}$$

where $|\psi_i\rangle$ is the state of the particle prior to the sweep and $|\psi_f\rangle$ is the state of the particle after the sweep. We describe the impulse in this way (rather than the average momentum) because the system exhibits Bragg oscillations, which are transitions between resonantly coupled momentum states $|p\rangle \leftrightarrow |-p\rangle$ (see Section 3.6.2). These oscillations yield an additional momentum change that is qualitatively different to the adiabatic transfer dynamics that we are interested in and does not

contribute to the cooling process. The rms momentum is a measure that by construction excludes the effect of such Bragg oscillations.

Figures 3.6 and 3.7 show the computed rms impulse $\Delta p_{\rm rms}$ vs. the initial momentum p_i for a particle initially prepared in $|\psi_i\rangle = |g, p_i\rangle$ and $|\psi_i\rangle = |e, p_i\rangle$, respectively. The values chosen for the adiabaticity parameter, $\kappa = 0.5$ (top rows) and $\kappa = 4$ (bottom rows), demonstrate the system's behavior in the diabatic and adiabatic regimes, respectively, and were varied by changing only the Rabi frequency, Ω_0. The probability of being left in the excited state at the end of the sweep, P_e, is also provided.

To aid in the description of the dynamics, we have labeled specific regions of momentum space with the symbols (0), (1), and (2), where (i) labels the maximum number of lasers the particle substantially interacts with at any time during the sweep. More specifically, a particle with initial velocity v_i lies within the region defined by:

$$\begin{aligned} |kv_i| &> \frac{\Delta_s}{2} \qquad \text{region (0)} \\ |\Omega_0| < |kv_i| &< \frac{\Delta_s}{2} \qquad \text{region (1)} \\ |kv_i| &< |\Omega_0| \qquad \text{region (2).} \end{aligned} \tag{3.21}$$

Note that region (1) roughly corresponds to the high-velocity regime, Eq (3.16). Uninterestingly, particles in region (0) do not significantly interact with the laser field, so we restrict our discussion to regions (1) and (2).

For most states in region (1), the resulting $\Delta p_{\rm rms}$ and P_e after the sweep are roughly constant. The general results of a diabatic sweep in region (1), as seen in both Figures, may be interpreted as giving a low imparted impulse and a failure to return the particle to its initial internal state. In contrast, the general results of an adiabatic sweep in region (1) are an impulse of $|\Delta p_{\rm rms}| \approx 2\hbar k$ and significant return to the initial internal state; these are the ideal coherent dynamics of the high-velocity regime as previously discussed. The highest momentum states within region (1) do not quite undergo this ideal behavior, even in the adiabatic regime, because the particle does not begin the sweep in an eigenstate of the Hamiltonian, Eq. (3.9).

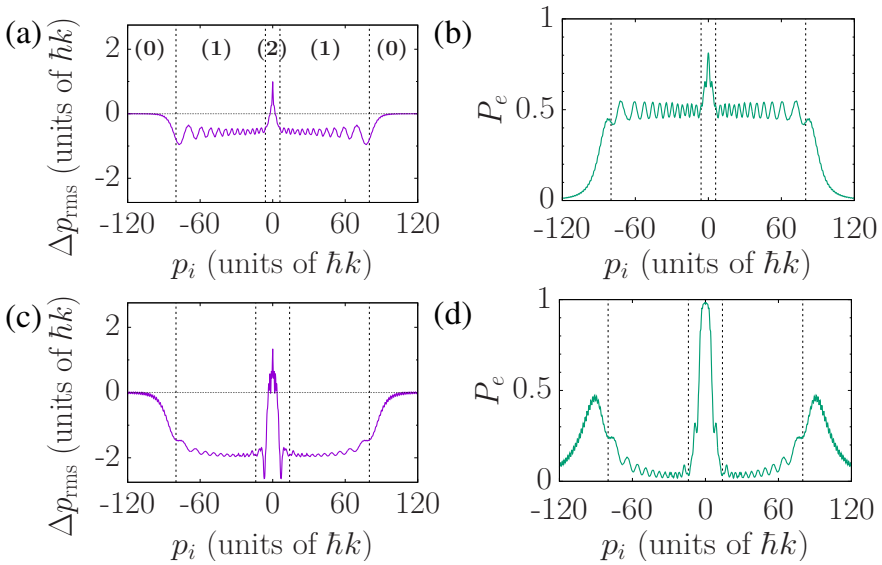

Figure 3.6: $\Delta p_{\rm rms}$ vs. p_i ((a) and (c)) and P_e vs. p_i ((b) and (d)) for a particle that started in the state $|g, p_i\rangle$ at the beginning of a sweep. The various momentum regions in Eqs. (3.21) are labeled in Figure 3.6(a) and are presented in all subplots by vertical, dashed lines. The horizontal, dashed line corresponds to $\Delta p_{\rm rms} = 0$. The adiabaticity parameter κ lies in the diabatic regime for plots (a) and (b) ($\kappa = 0.5, \Omega_0 = 9.5\omega_r$) and in the adiabatic regime for plots (c) and (d) ($\kappa = 4, \Omega_0 = 26.8\omega_r$). Values are: $\Delta_s = 360\omega_r$, $T_s = 2/\omega_r$.

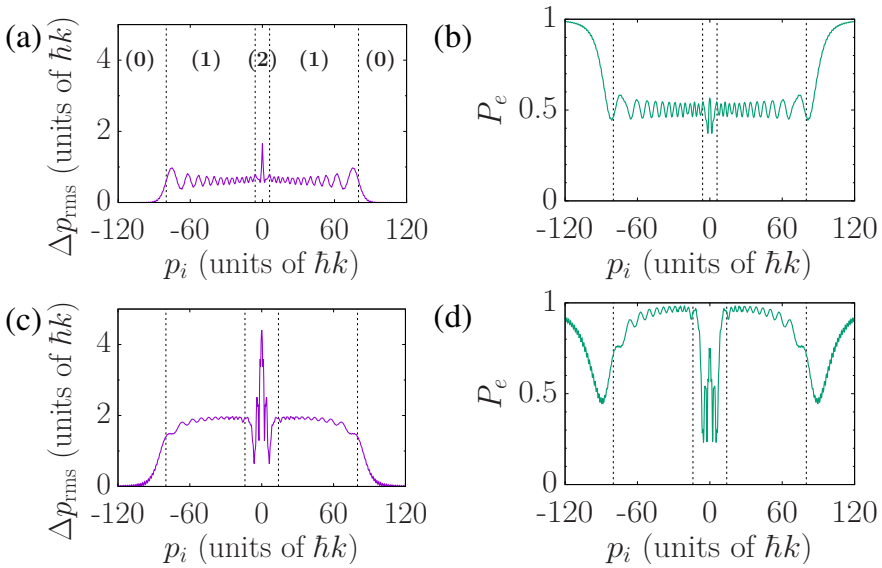

Figure 3.7: $\Delta p_{\rm rms}$ vs. p_i ((a) and (c)) and P_e vs. p_i ((b) and (d)) for a particle that started in state $|e, p_i\rangle$ at the beginning of a sweep. The various momentum regions in Eqs. (3.21) are labeled in Figure 3.7(a) and are presented in all subplots by vertical, dashed lines. The adiabaticity parameter κ lies in the diabatic regime for plots (a) and (b) ($\kappa = 0.5, \Omega_0 = 9.5\omega_r$) and in the adiabatic regime for plots (c) and (d) ($\kappa = 4, \Omega_0 = 26.8\omega_r$). Values common to all plots are: $\Delta_s = 360\omega_r$, $T_s = 2/\omega_r$.

As previously mentioned, Dopplerons and the ambiguous time-ordering of the two laser interactions can significantly modify the force in region (2) such that the physics is more complex. The effect of this complex behavior is clearly visible in Figures 3.6 and 3.7 as $|p_i|$ approaches zero. In particular, a particle within region (2) initially in the internal ground state will be transferred to the excited state after a sweep, which would then send it on a trajectory toward increasingly higher momentum. This motivates the requirement described by Eq. (3.1), which will on average reset the particle to the ground state for the next sweep via spontaneous emission.

3.5.2 Forces including dissipation

While Section 3.5.1 provides insight into the conservative forces in SWAP cooling, it does not include the dissipative features that ultimately lead to phase-space compression and equilibration. Moreover, we enforced specific state preparation at the beginning of each sweep. In order to explore the forces one would expect in the laboratory, i.e., with $\gamma \neq 0$ and no specific state preparation, we define an average impulse as

$$\Delta p_{\text{avg}} \equiv \text{Tr}\left[\hat{p}\hat{\rho}_f\right] - \text{Tr}\left[\hat{p}\hat{\rho}_i\right] \tag{3.22}$$

with the constraint that the internal state populations are the same at the beginning and end of the sweep. The quantities $\hat{\rho}_i$ and $\hat{\rho}_f$ are the density operators associated with the initial and final particle states, respectively. We shall call these internal state populations the "steady-state" populations, P_e^{ss} for each p_i. Note that steady-state here refers only to the internal state populations being equal before and after the sweep cycle; the momentum in general will change. This choice of representing the impulse is motivated by the desire to compare to other cooling methods where the internal populations reach a stationary situation, and to thereby allow investigation of the relationship between force and particle velocity in a more general context.

Figure 3.8(a) displays Δp_{avg} for a large range of initial momentum states p_i. The parameters were chosen such that the time between the two laser interactions, τ_{res}, obeyed $\tau_{\text{res}} \leq 1/\gamma$ for all $|kv_i| < \Delta_s/2$. We see that the overall effect of SWAP cooling yielded an impulse toward zero

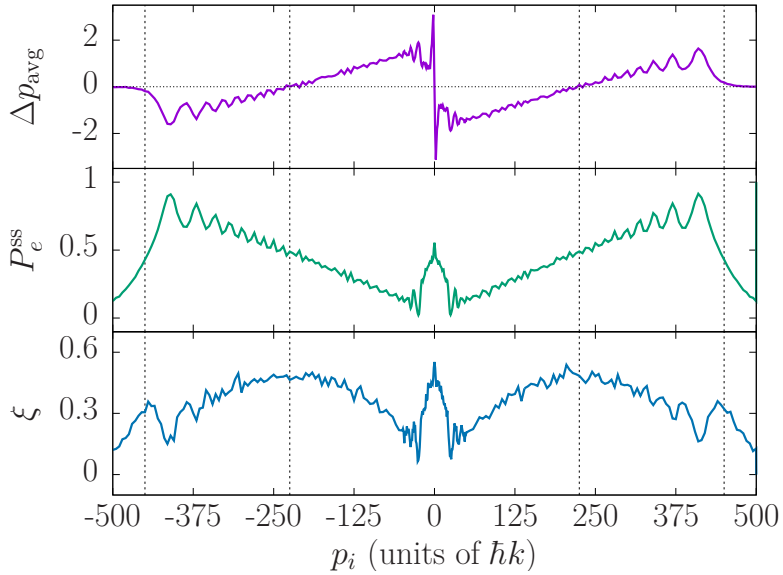

Figure 3.8: Various quantities for a particle that is subject to a single sweep with $\gamma \neq 0$ as a function of its initial momentum, p_i. (a) Δp_{avg} (average impulse, in units of $\hbar k$). (b) P_e^{ss} (steady-state population). (c) ξ (number of scattered photons). The vertical, dashed lines correspond to the four conditions $|kv| < \Delta_s/2$ (where Δp_{rms} falls to zero) and $|kv| < \Delta_s/4$ (the capture range). Each point was averaged over 1000 trajectories. Values are: $\Delta_s = 1800\omega_r$, $T_s = 1.0/\omega_r$, $\Omega_0 = 60\omega_r, \gamma = \omega_r$.

momentum for $|kv_i| < \Delta_s/4$ and an impulse away from zero momentum for $\Delta_s/4 < |kv_i| < \Delta_s/2$. This motivates Eq. (3.1) as a characterization of the momentum capture range of SWAP cooling. For low momentum, the effects of Bragg oscillations, Dopplerons, and the ambiguous time-ordering of laser interactions result in momentum dynamics that differ from those in the high-velocity regime.

Figures 3.8(b) and 3.8(c) present the steady-state excited state fraction, P_e^{ss}, and the average number of incoherent scattering events per sweep, which we call ξ, for the same parameters. We see that impulses with magnitudes of nearly $2\hbar k$ are imparted for $|p_i|$ near $25\hbar k$ with only ~ 0.2 scattering events per sweep. Moreover, the momentum states around $|p_i| = 25\hbar k$ experienced an average force of $|\Delta p_{\text{avg}}/T_s| \approx 2\hbar k\gamma$, which is roughly four times the cooling force that one expects from a radiation pressure force that fully saturates the atomic transition. This means that SWAP cooling can provide large cooling forces with a relatively low scattering rate. We investigate this useful feature in more detail in Section 3.8.

3.6 Effect of higher-order processes

3.6.1 Doppleron resonances

As the laser frequencies are swept, multi-photon transitions often called Dopplerons come to resonance even when single-photon transitions do not. As shown in Figure 3.9(a), an n^{th}-order Doppleron process is characterized by the absorption of $n+1$ photons from one beam and the emission of n photons into the other, resulting in a $(2n+1)\hbar k$ net momentum transfer to the particle, and it being left in the opposite internal state from which it started [134]. In general, Doppleron resonances can occur both before and after the single-photon resonances, and their existence has the potential to substantially affect particle dynamics outside the high-velocity regime.

Doppleron resonances only occur for specific values of laser detuning. For a particle with initial momentum $p_i = \beta_i \hbar k$, the time of an n^{th}-order Doppleron resonance can be found from energy conservation:

$$\beta_i^2 \hbar\omega_r + (n+1)\hbar\omega_L(t) = n\hbar\omega_L(t) + \hbar\omega_{\text{a}} + \beta_f^2 \hbar\omega_r. \tag{3.23}$$

We have neglected the AC Stark shift here for simplicity. In Eq. (3.23), the terms proportional to n are the energies of the photons being absorbed and emitted, $\hbar\omega_{\text{a}}$ is the transition energy, and the terms proportional to ω_r are the initial and final kinetic energies of the particle.

Paired with the momentum condition $\beta_f = \beta_i - (2n+1)$, where β_f is the particle's momentum after the Doppleron process, the time, t_n, of an n^{th}-order Doppleron resonance for a lab-frame laser detuning profile $\delta_n(t) = \alpha t_n$ obeys

$$\alpha t_n = -(2n+1)kv_i + (2n+1)^2\omega_r = -\left(n + \frac{1}{2}\right)(kv_i + kv_f). \tag{3.24}$$

Regardless of the Rabi frequency, multiphoton effects become relevant for low momentum states. From numerical methods, the 1^{st}-order splitting in a dressed state picture (see Figure 3.4) behaves as

$$\Omega^{(1)} \approx \frac{\Omega_0^3}{16(kv_i - 3\omega_r)^2}, \tag{3.25}$$

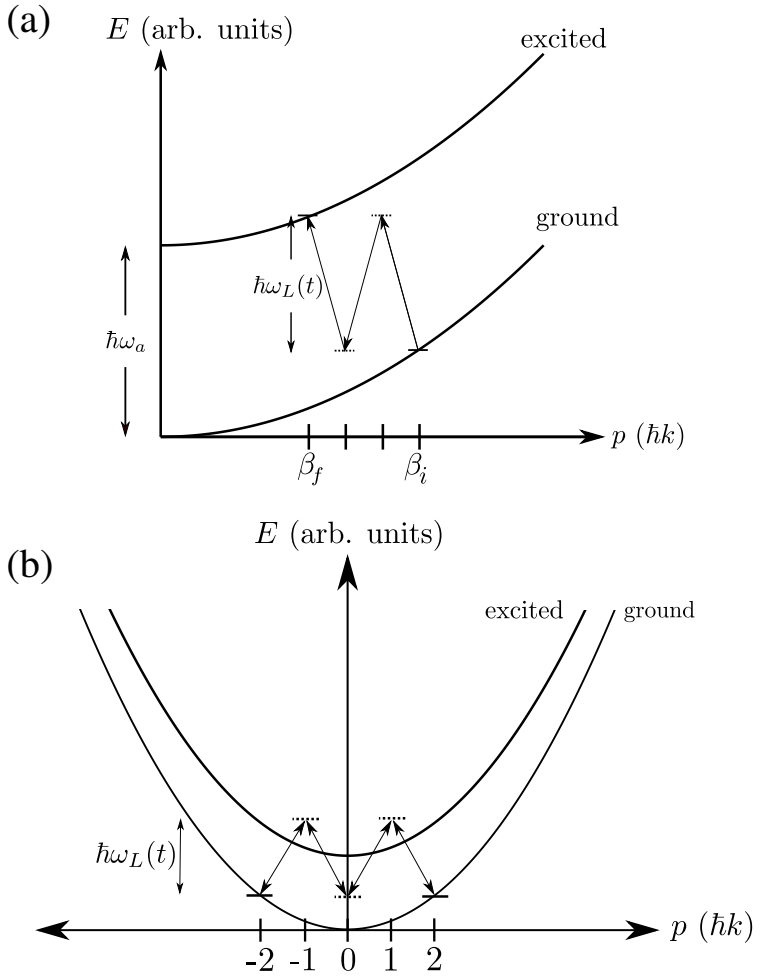

Figure 3.9: (a) A 1st-order Doppleron resonance, characterized by the condition $\beta_f = \beta_i - 3$. (b) A Bragg resonance between the states $|g, \pm 2\hbar k\rangle$.

which suggests that the probability of adiabatically passing through a first-order Doppleron resonance is [194]

$$P_a^{(1)} = 1 - \exp\left[-\frac{\pi}{512}\frac{\Omega_0^6}{\alpha(kv_i - 3\omega_r)^4}\right]. \tag{3.26}$$

The size of the argument in this exponential can be used to define the conditions for which Dopplerons are relevant for a particle with velocity v_i. Because SWAP cooling requires Eq. (3.3) to be satisfied, we choose to define the Doppleron regime as follows:

$$|\Omega_0| > |kv_i - 3\omega_r| \qquad \text{(Doppleron regime)}. \tag{3.27}$$

Comparing this result with Eq. (3.16), we see that the Doppleron regime describes nearly all

remaining states outside the high-velocity regime. Of course, there exist similar conditions for higher-order Doppleron resonances.

Increasing Ω_0, i.e., allowing for more Doppleron resonances, may decrease the amount of time it takes to reach a steady-state temperature, as they allow for more momentum transfer. However, the final temperature increases with Ω_0 (see Figure 3.13). Thus, minimum temperatures with a high capture range may be achieved by dynamically changing the Rabi frequency as the particle is cooled over time.

3.6.2 Bragg oscillations

Momentum states experience nontrivial effects due to Bragg oscillations, i.e., particle scattering from a light grating (the standing wave). These transitions, which are between states with $\pm\beta\hbar k$ momenta where β is an integer, occur at a rate [114]

$$\Omega_{B,\beta}(t) \approx \frac{|\Omega_0|^{2\beta}}{4^{\beta}(8\omega_r)^{\beta-1}[(\beta-1)!]^2\delta(t)^{\beta}}, \tag{3.28}$$

provided that $|\delta(t)| > |\Omega_0| > \gamma$. Figure 3.9(b) displays the energy diagram for a Bragg resonance between the $|g, \pm 2\hbar k\rangle$ states. If there are many oscillations, it is likely that system noise will cause the oscillations for different particles to become out of phase, leaving, on average, half of the atoms in either momentum state. This phenomenon is an important consideration in the analysis of the impulses in Figure 3.10.

Integrating Eq. (3.28) and dividing by 2π gives the total number of β^{th}-order Bragg oscillations between times t_i and t_f:

$$N_{\beta}(t_i, t_f) = \frac{1}{2\pi}\left|\int_{t_i}^{t_f} \Omega_{B,\beta}(t')\,dt'\right| \propto \left|\int_{t_i}^{t_f} \frac{1}{\delta(t')^{\beta}}\,dt'\right|. \tag{3.29}$$

The quantities t_i and t_f are related to the times of stimulated absorption/emission during the sweep process, as these will carry the particle away from the states that are experiencing Bragg oscillations.

To provide a few interesting examples, 1^{st}-order Bragg transitions affect the dynamics of the

initial states $|\psi\rangle_0 = |g, \hbar k\rangle\,, |g, 3\hbar k\rangle$. From Eq. (3.29) and using Eqns. (3.13) and (3.14),

$$N_1 \approx \frac{\kappa}{8\pi} \ln\left|\frac{2\omega_r}{\Delta_s}\right|, \quad |\psi\rangle_0 = |g, \hbar k\rangle\,; \tag{3.30}$$
$$N_1 \approx \frac{\kappa}{8\pi} \ln\left|\frac{\Delta_s}{6\omega_r}\right|, \quad |\psi\rangle_0 = |g, 3\hbar k\rangle\,.$$

The Bragg oscillations occur before the SWAP resonances for $|g, \hbar k\rangle$ and after the SWAP resonances for ($|g, 3\hbar k\rangle$). Although N_1 scales logarithmically with Δ_s in both cases, a sufficiently large sweep range will promote multiple Bragg oscillations.

The effect of Bragg oscillations at low p_i, which manifests as a sharp, linear feature in Figure 3.8(a), is elucidated by considering the effect of switching the sweep direction. Bragg oscillations can mix the particle between the $|\pm p_i\rangle$ states before the particle resonates with the lasers, so the net Δp_{avg} is independent of the sweep direction. To compare Δp_{avg} with and without these oscillations, we define impulses $\Delta p^{\pm}$ in the following way:

$$\Delta p^{\pm} \equiv \frac{(\Delta p_{\text{avg}})_{\text{pos}} \pm (\Delta p_{\text{avg}})_{\text{neg}}}{2} \tag{3.31}$$

in which the subscripts "pos" and "neg" refer to the sign of the ramp, i.e., red to blue or blue to red detuning, respectively. By symmetry, we expect the effect of Bragg oscillations to be present in Δp^+ and to cancel in Δp^-. Figure 3.10 displays $\Delta p^{\pm}$ as a function of the initial momentum, p_i. The substantial effect of Bragg oscillations were seen to be present in Δp^+ for $|p_i| < 7\hbar k$. For p_i nearer to the high-velocity regime, which is $|p_i| > 30.5\hbar k$ for this set of parameters, Bragg oscillations do not play a significant role, and we observe Δp^+ tending to zero, and Δp^- tending to $\pm 1.5\hbar k$.

3.7 Temperature limit as $\gamma \to 0$

We now provide the results of a SWAP cooling simulation that includes the effects of dissipation, but in the limit $\gamma \to 0$. To accomplish this, we modifed the frequency profile to be a series of single sawtooth ramps with period $T_s \ll 1/\gamma$, each separated by a time $T_{\text{wait}} \gg 1/\gamma$, as shown in Figure 3.11. This "sweep-wait" scheme effectively mimics the cooling process for a particle with

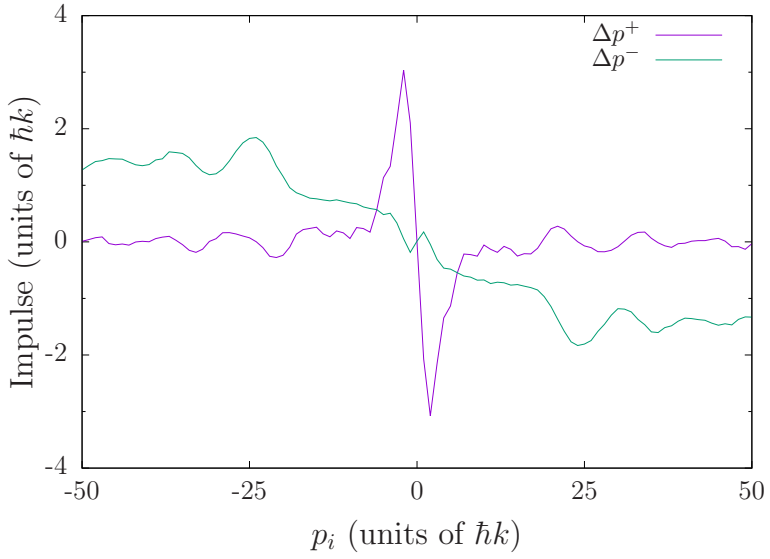

Figure 3.10: $\Delta p^{\pm}$ vs. p_i. The sharp, linear feature in Δp^+ is due to Bragg oscillations, which mix the particle between the $|\pm p_i\rangle$ states before it reaches resonance with the lasers. Each point is averaged over 1000 trajectories. Values are: $\Delta_s = 1800\omega_r$, $T_s = 1.0/\omega_r$, $\Omega_0 = 60\omega_r, \gamma = \omega_r$.

an ultranarrow linewidth. It also reduced the required computation time by allowing (i) Δ_s to be small and (ii) the use of the analytical expression for free-space spontaneous decay. We modeled the limit $T_{\text{wait}} \to \infty$ and $\gamma \to 0$ by setting $\gamma = 0$ and projecting any remaining excited state population to the ground state, along with simulating any accompanying momentum recoil.

Figure 3.12 presents the evolution of a particle that started in the state $|g, 10\hbar k\rangle$ under this cooling scheme. At the end of this simulation, the temperature of the particle was observed to asymptote to a value near the recoil limit, $2T_r$, where

$$k_B T_r \equiv \frac{(\hbar k)^2}{2m} = \hbar\omega_r, \tag{3.32}$$

and k_B is Boltzmann's constant. We use the variance in p as a measurement of the 1D temperature, T, i.e.,

$$\frac{\sigma_p^2}{2m} \approx \frac{\langle p^2 \rangle}{2m} = \frac{1}{2} k_B T. \tag{3.33}$$

It should be noted that not all steady state solutions are Gaussian in nature, but are centered on zero momentum. Thus, the first equality in Eq. (3.33) universally holds once the system has equilibrated.

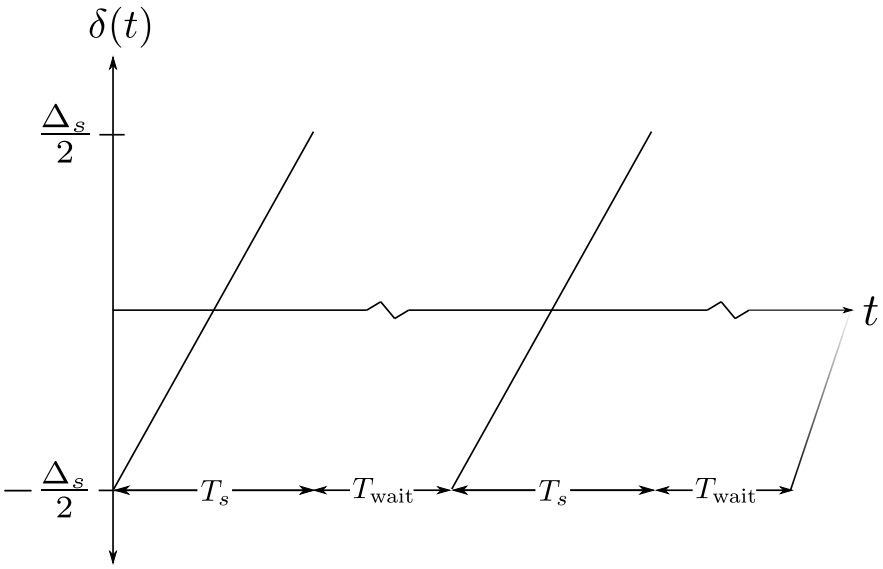

Figure 3.11: Frequency profile for the simplified "sweep-wait" cooling scheme.

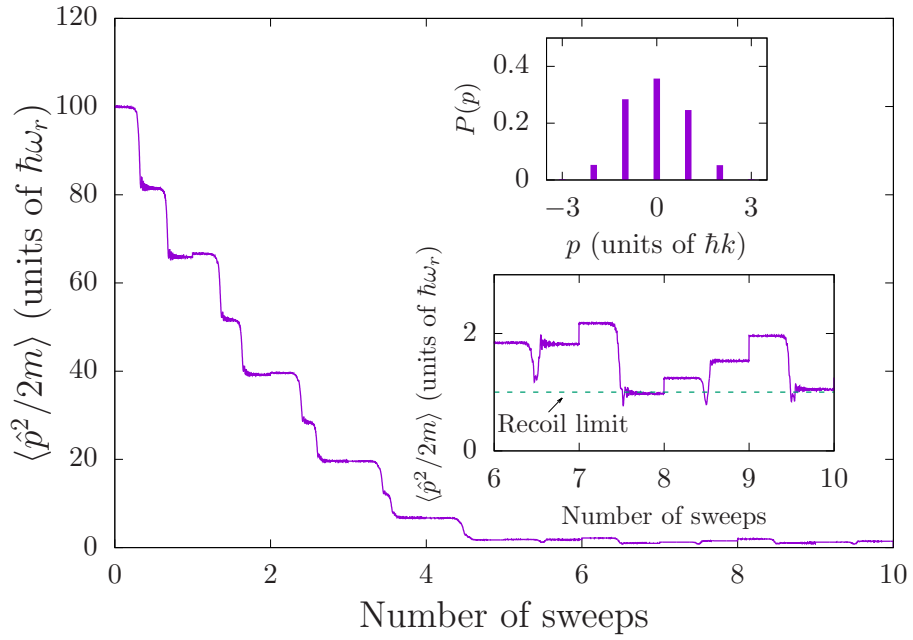

Figure 3.12: Cooling of a particle that begins in the state $|g, 10\hbar k\rangle$ to the recoil limit after 5 sweep-wait cycles. Top inset: A snapshot of the momentum distribution $P(p)$ halfway through the 7^{th} sweep. Bottom inset: A closer look at the cooling trajectory once the system reached equilibration. The recoil limit, $2T_r$, is included as a horizontal, dashed line. This curve is the average of 100 trajectories. Values are: $\Delta_s = 100\omega_r, T_s = 60/\omega_r$, and $\Omega_0 = 2\omega_r$.

It is also interesting to consider how the final temperature scales with Ω_0. Figure 3.13 displays this relationship in both the diabatic and adiabatic regimes. A minimum temperature was found just within the adiabatic regime. From the numerics, the temperature was observed to follow a linear relationship

$$k_B T = \frac{1}{2}\hbar\Omega_0 \tag{3.34}$$

in the adiabatic regime, which we attribute to decreased time ordering between adiabatic transfers and the particle spending more time in the excited state, hence more scattering events. This linear relationship held for at least twice the domain of Figure 3.13. An increase in temperature was observed in the diabatic regime, which we attribute to both a reduction in conservative forces as described in Section 3.5.1, and the presence of a significant excited state fraction at the end of each sweep, leading to more diffusion from spontaneous emission.

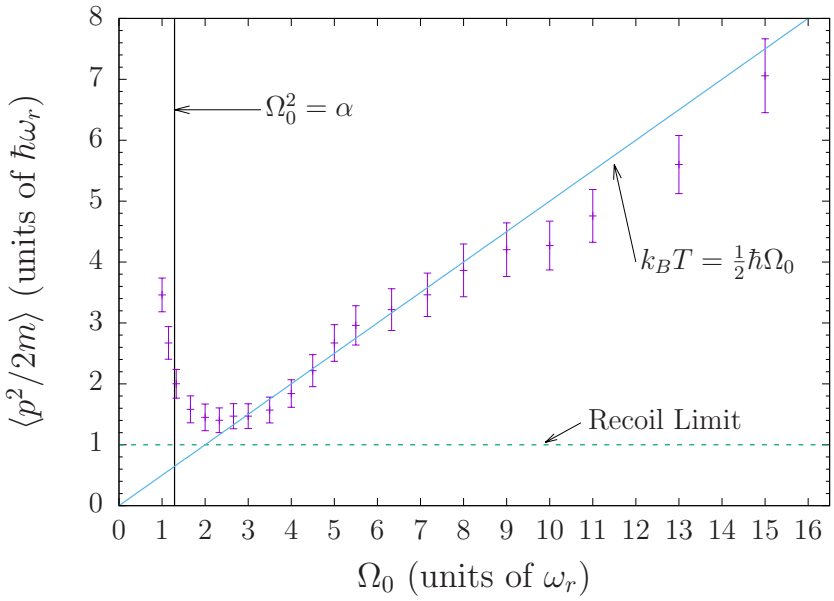

Figure 3.13: Stationary values of $\langle p^2/2m\rangle$ as a function of Ω_0 in the sweep-wait sequence. The vertical, solid line labels the value of Ω_0 that divides the diabatic and adiabatic regimes. The recoil limit is represented as a horizontal, dashed line. Deep within the adiabatic regime, the temperature scales linearly with Ω_0. Values are: $\Delta_s = 100\omega_r, T_s = 60/\omega_r$. Each point is averaged over 500 trajectories.

In Chapter 4, we present a plot which shows the same quantities as in Fig. 3.13, but with

experimental and simulation data for the $\gamma = 2\pi \times 7.5$ kHz linewidth $^1S_0 \rightarrow {}^3P_1$ transition in ^{88}Sr. The simulation data was created by employing the method of Monte Carlo wave functions (see Section 2.2.4) with the SWAP cooling quantum master equation [Eq. (3.5)].

3.8 Cooling efficiency

We now compare the efficiency of SWAP cooling with Doppler cooling. We define "cooling efficiency" here as the energy carried away from the system per scattering event. This choice is motivated in part by the potential application of SWAP cooling to systems where closed cycling transitions may not be accessible and therefore a large number of spontaneous emission events are undesirable. We calculate the cooling efficiency by preparing an ensemble of particles in a specific initial state, $|g, 20\hbar k\rangle$, and subsequently applying both Doppler and SWAP cooling for comparison. Here, we used the SWAP cooling scheme presented in Figure 3.2, in which dissipation is included at all times.

Clearly, many fewer scattered photons are required for SWAP cooling to reduce the energy and to bring the system close to equilibrium. In fact, in the simulation, SWAP cooling was able to remove up to an average of $5\hbar k$ of momentum per scattered photon. As a consequence, in comparison to Doppler cooling's ideal cooling efficiency, we deduce that SWAP cooling promises to be well-suited to cooling particles where the adverse affects of spontaneous emission are significant, such as those that lack closed cycling transitions.

3.9 Conclusion

The SWAP (sawtooth wave adiabatic passage) procedure proves to be a robust and simple cooling mechanism. Our analysis of both the coherent and dissipative dynamics of two-level particles suggests that it has numerous applications, such as to systems with narrow linewidth or no closed cycling transitions. We have shown its ability to cool particles to the recoil limit while simultaneously inducing larger cooling forces and maintaining a higher cooling efficiency than Doppler cooling.

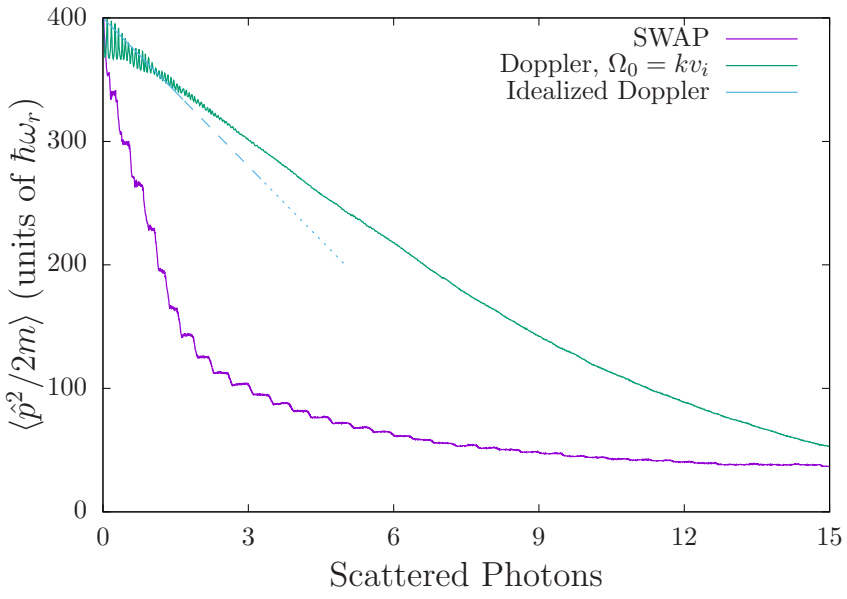

Figure 3.14: $\langle \hat{p}^2 \rangle / 2m$ vs. the average number of scattered photons for SWAP cooling and Doppler cooling. For both methods, $\omega_r = \gamma$. The SWAP parameters are: $\Omega_0 = 28\omega_r, \Delta_s = 391\omega_r, T_s = 1/\omega_r$, and Doppler parameters are: $\Omega = 40\omega_r, \delta = -40\omega_r$. The SWAP cooling data is over 38 sweeps. Each curve is averaged over 1000 trajectories. We extract an average cooling efficiency for SWAP cooling of up to $5\hbar k$ per scattered photon.

The scope of the calculations presented in this paper were limited to two-level atoms moving along one-dimension. It will be interesting to consider more general atomic systems and more general geometries of laser and trapping fields. In particular, SWAP cooling may be applied to magneto-optical trapping [12, 137], to optical lattices, and to general multilevel laser cooling strategies [74, 171]. The realization of the SWAP protocol in a magneto-optical trap is in fact the topic of the next chapter. Furthermore, while it is important to recognize that while our calculations are fully quantum mechanical (consisting of a complete description of the internal and external variables) with the inherent advantages of not having to make approximations, it will also be useful to develop and validate semiclassical methods where many-sweep cycles can be treated with higher efficiency. This will be important to treat more massive systems such as complex molecules.

In the future, it will be interesting to further elaborate on the concept of a cooling efficiency, i.e., the removal of a system's energy and entropy per scattering event, in the general context of laser cooling theory. For example, the information associated with the momentum of a particle

initially in the state $|g, p_i\rangle$ may be encoded in the time record of spontaneously emitted photons. This provides significant motivation for a systematic analysis of entropy dynamics in the various implementations of laser cooling that may prove to be an insightful and useful endeavor for the laser cooling and atomic physics community. We discuss this topic to some extent in Chapter 7.

The protocol we have proposed is inherently limited by the requirement of adiabatic transfer between quantum states. We discuss the relaxation of this requirement by use of an adiabatic speedup protocol in Chapter 6.

Chapter 4

SWAP cooling: experimental results and comparison to theory

Now that we have developed and studied SWAP cooling from a theoretical perspective, we present the results of its first experimental realization as well as a comparison of the experimental results to theory. While we also discuss its basic mechanism, forces, and achievable temperatures in this chapter, we refer the reader to Chapter 3 for a more detailed analysis. The content shown here is mainly from our New Journal of Physics article (Ref. [141]), which was published in February 2018. To put the discovery of SWAP cooling into context, we quote the wise and humbling words of Matthew A. Norcia, who first witnessed its cooling potential in the laboratory as a graduate research assistant in James Thompson's lab at JILA:

> "Basically, I pressed a button on the function generator."
>
> Dr. Matthew Norcia, *A Little Less Spontaneous* [98]

The content shared in the chapter demonstrates that SWAP cooling is a robust cooling mechanism capable of exerting large forces via a weak transition and with reduced reliance on spontaneous emission. We present a simple intuitive model for the resulting frictional force, and directly demonstrate its efficacy for increasing the total phase-space density of an atomic ensemble. We rely on both simulation and experimental studies using the 7.5 kHz linewidth $^1S_0 \rightarrow ^3P_1$ transition in ^{88}Sr. The reduced reliance on spontaneous emission may allow this adiabatic sweep method to be a useful tool for cooling particles that lack closed cycling transitions, such as molecules.

4.1 Introduction

The development of Doppler cooling and sub-Doppler cooling in the 1980's has revolutionized our ability to control neutral atoms, ions, and mechanical resonators [34, 42, 59]. Since then, Doppler cooling techniques have been extended to narrow-linewidth optical transitions to achieve lower temperatures and high phase-space density [62, 86, 91, 110, 176, 186]. Additionally, there is an ongoing effort to use Doppler cooling for molecules [85, 170]. Each of these pursuits face certain persistent limitations. The use of weak transitions limits the forces achievable with Doppler cooling, and the narrow transition linewidth makes the cooling very sensitive to perturbations of the cooling transition frequency [92] and to drifts in the cooling laser frequency. In the case of molecules, the large number of spontaneous emissions required for Doppler cooling is a key obstacle due to the high probability of spontaneous Raman transitions to undesired states.

Here we present a new form of laser cooling that mitigates these issues. Our technique relies on the adiabatic transfer of atoms to and from a long-lived optically excited state to both slow and cool the atoms. Because the role of spontaneous emission is reduced (though not eliminated) relative to standard Doppler cooling techniques, our technique enables large forces to be generated even on weak transitions, and may facilitate the extension of laser cooling techniques to systems that lack closed cycling transitions. Of particular interest, this technique may be applied to the slowing and cooling of molecules with narrow linewidth optical transitions [49, 99].

From a fundamental perspective, this work has important implications for the ongoing discussion of the role of spontaneous emission in dissipating entropy during laser cooling [51, 124]. Our view is that spontaneous emission (or another form of dissipation) is necessary to achieve phase-space compression, but that the total number of spontaneously scattered photons required can be quite low (of order one). Similar conclusions have been reached in the study of optical pumping in high angular momentum states of atoms [159] and cooling with single spontaneous emission events [152].

4.2 Basic mechanism

To understand our cooling mechanism in its simplest form, we consider a two-level atom with a long-lived optically excited state $|e\rangle$ and ground state $|g\rangle$ moving in one dimension with velocity v (Fig. 4.1a). Two counterpropagating laser beams with wave-number k and frequency ω are linearly ramped in frequency from below to above the atomic transition frequency ω_a, with full sweep range Δ_s. This ramp is repeated to form a sawtooth pattern in time (Fig. 4.1c). Each laser interacts with the two-level atom with a Rabi frequency Ω, which is larger than the spontaneous decay rate γ from $|e\rangle$ to $|g\rangle$. The sweep range is adjusted such that $\Delta_s > \Omega, 4kv$. The frequency sweep rate $\alpha = (d\omega/dt)$ fulfills the Landau-Zener condition $\alpha \ll \Omega^2$ for adiabatic transfer of population between ground and excited states. Lastly, the jump in laser frequency at the end of each ramp is treated as perfectly diabatic.

In the reference frame of the atom, both cooling beams start below resonance with the atomic transition. Doppler shifts due to the atomic motion cause the beam counter-propagating to the atom's velocity to appear kv higher in frequency and the co-propagating beam to appear kv lower in frequency. As the laser sweep upward in frequency, the counter-propagating beam sweeps over resonance first, and adiabatically transfers the atom from $|g\rangle$ to $|e\rangle$. Because of the long lifetime of the excited state, the atom remains in $|e\rangle$ until the co-propagating beam sweeps over resonance and adiabatically transfers it back to the ground state. In this process, the atom has absorbed one photon from the beam propagating against its motion, and emitted a photon into the beam propagating along its motion, resulting in a net momentum transfer of $2\hbar k$ against its motion. The laser frequency is then diabatically jumped back to its start frequency such that the atom remains in $|g\rangle$, and then the process is repeated.

Similar principles have been explored [87, 129, 142, 172, 173] to generate large forces. In these works, the time-ordering of the left and right-going pulses is fixed by parameters external to the atom. Here, because the time-ordering of the interaction with the two beams is determined by the atomic velocity, the force always opposes the atom's velocity, and thus causes slowing for

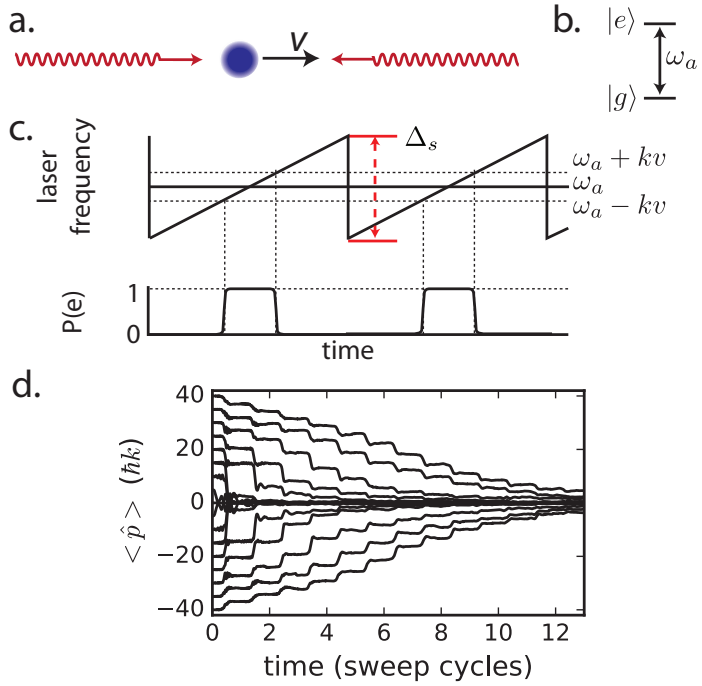

Figure 4.1: (a) A moving atom is illuminated by two counter-propagating laser beams, whose frequencies are modulated with a saw-tooth wave-form. (b) The atom is treated as a two-level system with transition frequency ω_a. (c) Representation of frequencies in lab frame. Because of Doppler shifts resulting from atomic motion, the co-propagating (counter-propagating) laser beams are resonant with $|g\rangle$ to $|e\rangle$ transition when the laser frequency $\omega = \omega_a - kv$ ($\omega_a + kv$). Because ω increases with time, the counter-propagating laser sweeps over the transition before the co-propagating laser. If the atom starts in $|g\rangle$, the counter-propagating laser transfers the atom from $|g\rangle$ to $|e\rangle$ as it sweeps over resonance, and the co-propagating laser transfers the atom back to $|g\rangle$. This results in the transfer of two photon recoils of momenta to the atom in the correct direction to slow the atom. (d) Simulation of trajectories in momentum space. When the atoms have large momenta, each sweep lowers the momentum by $2\hbar k$. At lower momenta, multi-photon processes can transfer larger amounts of momentum.

atoms moving in either direction.

4.3 Numerical demonstration of basic mechanism

Fig. 4.1d shows simulated trajectories for atoms that begin at different initial momenta using a Monte Carlo wave function trajectory method [63], which is further discussed in Section 4.7. Atoms are prepared in a pure quantum state specified by their internal ground state and fixed momentum. The average momentum over 50 trajectories is calculated at each time step. At high

momentum, each sweep lowers the momentum of the atom by roughly $2\hbar k$. At lower momentum, we find that the change in momentum per sweep can greatly exceed $2\hbar k$, as multiple photons are transferred between the two cooling beams.

At low momentum, the role of spontaneous emission becomes more important. As the atom is slowed to near-zero velocity, the Doppler shift becomes small compared to the Rabi frequency, $kv \lesssim \Omega$, and the condition for deterministic time ordering of adiabatic transfers from the two beams no longer holds. When this occurs, the simple picture of sequential adiabatic transfers to and from $|e\rangle$ becomes invalid, and the probability that the atom is found in $|e\rangle$ at the end of the sweep, which ideally should be 0, becomes appreciable. While the sawtooth frequency sweep leads to slowing for an atom that is in the ground state at the beginning of a sweep, it causes an atom that starts in the excited state to increase in velocity. In the absence of spontaneous emission, the atom would find itself on a heating trajectory after initial cooling. The presence of spontaneous emission is therefore critical, as it ensures that the atom preferentially starts in $|g\rangle$ at the beginning of each sweep. This breaks time reversibility, enabling cooling and phase space compression to occur.

We can extract the rate of spontaneous emission events from the simulation. For a trajectory that begins at 100 photon momenta and realistic sweep and atomic properties for ^{88}Sr, the atom's momentum is initially reduced by an average of five photon momenta for each spontaneous emission event. This can be compared to Doppler cooling, which requires at least one scattered photon per photon momentum removed, and in practice typically much more. Once the atom has reached its equilibrium temperature, the average scattering rate is slightly less than one photon per sweep for the same parameters. If applied to a species for which spontaneous emission is problematic (like molecules), it may be useful to apply velocity-selective optical pumping to a dark state to avoid the continued scattering of photons from already cooled particles.

4.4 Demonstration of steady-state cooling and phase space compression

We experimentally verify that our mechanism leads to cooling by applying two counter-propagating beams to an ensemble of ^{88}Sr atoms pre-cooled to roughly 600 μK (Fig. 4.2a). The

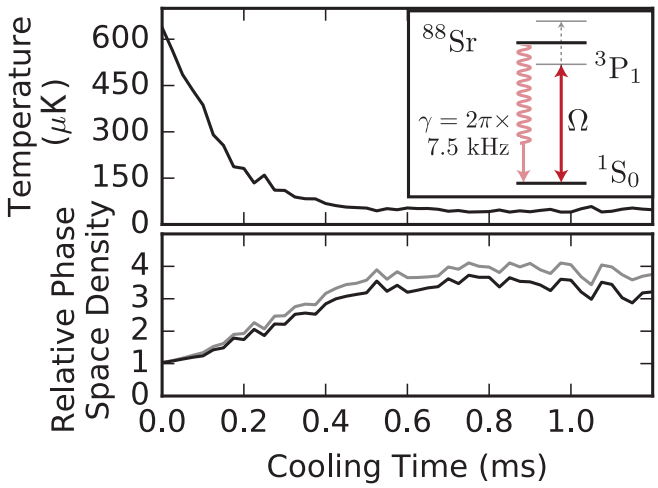

Figure 4.2: Experimental study of an atomic ensemble using one-dimensional cooling by adiabatic transfer. (a) An ensemble of atoms, precooled to around 600 μK, is illuminated by frequency-swept counterpropagating beams for a variable amount of time. The one-dimensional temperature is decreased to a steady-state value of 45 μK by the cooling lasers. (b) The phase-space density in one dimension (grey trace) and three dimensions (black trace) is increased during the cooling process.

frequency of the two beams is swept upwards by $\Delta_s = 2\pi \times 6.6$ MHz every 50 μs. The frequency sweep is centered on the resonance of the dipole-forbidden $^1\mathrm{S}_0 \rightarrow {}^3\mathrm{P}_1$ transition, which has a linewidth of $\gamma = 2\pi \times 7.5$ kHz. The two beams are linearly polarized in the direction of a 3.3 gauss magnetic field, such that the light-atom interaction can be described as a two-level system with $|g\rangle \equiv |^1\mathrm{S}_0, m_j = 0\rangle$ and $|e\rangle \equiv |^3\mathrm{P}_1, m_j = 0\rangle$, where m_j labels the magnetic Zeeman sub-level.

The cooling beams are applied for a time of 50 μs to 1200 μs (i.e. application of 1 to 24 sweeps) after which the beams are turned off. The temperature of the atomic cloud is determined from a fluorescence image of the cloud after free ballistic expansion for 10 ms. In the direction of beam propagation, we find that for these parameters the atoms are cooled from their initial temperature of roughly 600 μK to 45 μK in of order 300 μs or 6 sweeps.

Importantly, we directly observe an increase in phase-space density during the cooling process, and not simply velocity reduction. We measure atom loss during cooling to be negligible and the relative increase in phase space density is $\rho/\rho_\circ = \Delta x_\circ \Delta v_\circ / (\Delta x \Delta v)$, where Δx and Δv ($\Delta x_\circ$ and

$\Delta v_\circ$) are the measured cloud size and velocity spread after (before) cooling. In Fig. 4.2b, this quantity is shown as the grey line. The black line in Fig. 4.2b accounts for measured heating in the orthogonal directions (which for simplicity we have assumed to be equal in the two directions). Note that because the atoms are not confined and the cooling is only applied along one dimension, this increase of phase-space density is much smaller than one would obtain with the same decrease in temperature for three-dimensional cooling in a harmonic trap.

4.5 Comments on entropy removal

The fact that phase-space density increases indicates that entropy is removed during the cooling process. This may seem problematic for a mechanism that relies heavily on unitary dynamics and stimulated emission. However, as discussed above, the presence of even small amounts of spontaneous emission is critical for breaking time reversibility and enabling phase-space compression. In related works [152, 159], it was found that the number of scattered photons required to remove entropy from a system can be quite low (of order one).

In these protocols, the timing of the emitted photons encodes key information about the initial state of the quantum system. In an idealized version of our cooling mechanism, the dynamics are completely unitary as the atom is slowed from a high initial momentum. When it reaches some lower momentum threshold, the simple picture of subsequent adiabatic transfer breaks down and the atom begins to scatter photons. In this way, the initial velocity of the atom is encoded in the time delay before the atom began to scatter photons, and the atom's initial entropy in momentum space is mapped onto entropy contained in the measurement record of when photons are and are not spontaneously emitted. While a detailed analysis of the entropy transfer is beyond the scope of the work here and will be explored more fully in future work, we believe that the above picture captures the essential physics of how phase-space compression is achieved.

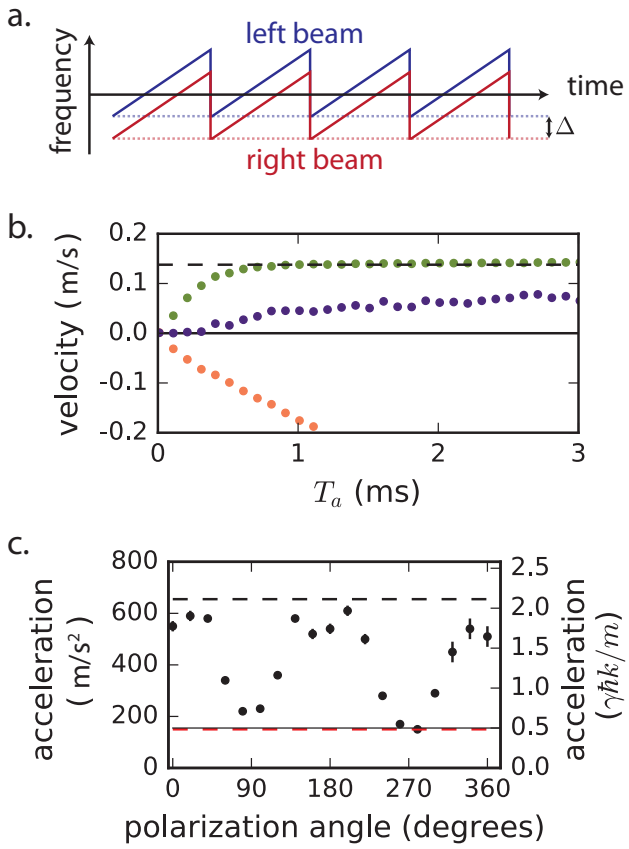

Figure 4.3: Cooling into a moving reference frame. (a) We apply a frequency offset in the lab reference frame between the two beams, which creates a moving reference frame in which the beams have equal frequency. (b) If the laser frequency is swept upwards, (green points) the atoms settle into the moving reference frame, which has a velocity indicated by the dashed black line. If the laser frequency is swept downwards (orange points), the atoms accelerate in the other direction, without cooling. If the frequency sweep is symmetric (purple points), atoms experience a small acceleration due to radiation-pressure imbalance. (c) Acceleration vs. polarization angle between two beams. Acceleration is enhanced when the polarizations of the two beams are aligned. The solid line represents the maximum acceleration for a saturated two-level atom without stimulated emission. The dashed red line represents the measured acceleration with a single beam. Black points represent acceleration with both beams applied. The dashed black line represents the acceleration that two photon recoils per sweep of the laser frequency would produce.

4.6 Cooling forces

We now turn to a more detailed characterization of the forces involved in the cooling process. Previously, we have considered the case where the instantaneous frequencies of the two beams are equal in the lab frame. If, however, we introduce a fixed relative offset frequency between the

counter-propagating beams (as shown in Fig. 4.3a), then atoms that are stationary in the lab frame will be accelerated until their velocity matches that of the frame F moving at velocity $v_F = \Delta/2k$, in which the two beams appear to have equal instantaneous frequencies.

We apply the frequency-swept beams for a variable amount of time T_a, then measure the resulting velocity of the atoms. This is shown in Fig. 4.3b for several sweep configurations. The green points represent the cooling configuration described above, with the laser frequency adiabatically swept from low to high and diabatically jumped from high to low. The two beams are offset by a detuning $\Delta/2\pi = 400$ kHz, and are swept by $\Delta_s/2\pi = 8$ MHz every 33 μs. We observe that the atoms undergo initial acceleration until they reach equilibrium with the velocity of the moving frame $v_F = 0.14$ m/s.

To rule out the interpretation that the atoms are merely being dragged by the moving standing wave formed by the detuned lasers, we reverse the direction of the sawtooth sweep without changing the relative detuning Δ of the two beams. The standing wave still moves in the same direction as before, but now the atoms accelerate in the other direction. While the upwards sweep causes saturation of the atomic velocity at v_F, no such saturation is apparent for a downwards sweep. This confirms that the downwards sweep configuration does not lead to cooling.

Finally, when we apply a symmetric triangle-ramped frequency sweep to the lasers, the atoms undergo a much smaller acceleration, likely due to incidental residual radiation pressure from an intensity imbalance between the two beams.

Because our mechanism relies on stimulated emission, much larger accelerations can be achieved than would be possible with Doppler cooling on such a narrow transition. To quantify this acceleration, we apply the beams for a time much shorter than it takes the atoms to reach equilibrium velocity, and measure the resulting change in velocity. If we apply only one of the two cooling beams, the atoms experience an acceleration consistent with $(\gamma/2)(\hbar k/m) = 155$ m/s^2, the expected value for a maximally saturated atom.

We see a far more dramatic effect when we apply both beams at the same time (Fig. 4.3c). When the polarizations of the two beams are aligned, we observe a maximum acceleration of around

600 m/s^2 for a sweep period of 20 μs, a factor of almost 4 above both the observed acceleration from the leftward beam alone and the maximum expected acceleration for a two-level atom without stimulated emission. This measured acceleration is within ten percent of the value we would expect if each sweep of the laser frequency led to two photon recoils of momentum transfer, though this agreement may partly be due to a cancellation between the effects of imperfect adiabatic transfers and multi-photon processes. When the polarizations are made orthogonal, the acceleration returns to near the single-beam value, as only one of the beams interacts with $|e\rangle$.

4.7 Temperature measurement and comparison to simulation

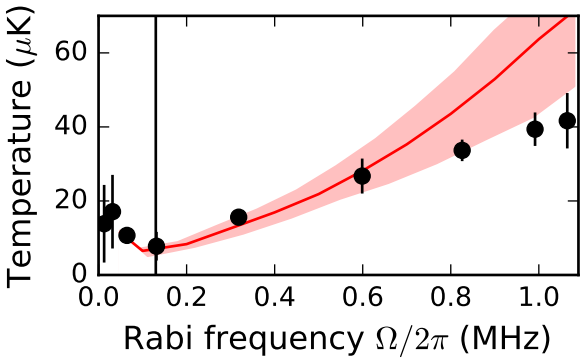

Figure 4.4: Temperature vs. Rabi frequency for a sweep range of 7 MHz and repetition rate of 15 kHz. Red line represents the results of our simulations, and black points are experimental data. The red band indicates uncertainty of prediction due to statistical uncertainty in simulation results, experimental calibration of Ω, and variations in Rabi frequency during the sweep. The vertical line at 130 kHz represents the approximate point at which we expect adiabaticity to break down: $\Omega^2 = \alpha$. We discuss possible sources for the disagreement at high Rabi frequency in the main text.

We now compare our experimentally measured temperature to simulation in Fig. 4.4. This plot presents the same quantities as the idealized $\gamma \to 0$ study in Section 3.7, but for $\gamma \neq 0$.

The simulation used is a Monte Carlo wave function approach, as introduced in Section 2.2.4, which evolves the quantum master equation

$$\frac{d\hat{\rho}}{dt} = \frac{1}{i\hbar}[\hat{H}, \hat{\rho}] + \hat{\mathcal{L}}\hat{\rho} \tag{4.1}$$

described in detail in Section 3.3. While the external electric field associated with the cooling lasers is treated classically, the internal and external atomic degrees of freedom are treated fully quantum mechanically. The wave function contains ground and excited internal states in addition to a discrete family of external momentum states, which are equally spaced in units of $\hbar k$ up to a maximum cutoff. The unitary dynamics are generated by the single-particle Hamiltonian

$$\hat{H} = \frac{\hat{p}^2}{2m} + \frac{1}{2}\hbar\omega_a\hat{\sigma}^z + \hbar\Omega\cos(k\hat{z})\left(\hat{\sigma}^+ e^{-i\eta(t)} + \text{h.c.}\right), \tag{4.2}$$

where the instantaneous phase of the applied coherent field $\eta(t)$ is the time integrated instantaneous frequency, with the frequency ramped in the sawtooth pattern previously described. Because the full atom and field system is an open quantum system due to the presence of spontaneous emission, the Lindblad superoperator proportional to the spontaneous emission rate

$$\hat{\mathcal{L}}\hat{\rho} = \gamma\left(\frac{1}{5}e^{ik\hat{z}}\hat{\sigma}^-\hat{\rho}\hat{\sigma}^+e^{-ik\hat{z}} + \frac{1}{5}e^{-ik\hat{z}}\hat{\sigma}^-\hat{\rho}\hat{\sigma}^+e^{ik\hat{z}} + \frac{3}{5}\hat{\sigma}^-\hat{\rho}\hat{\sigma}^+ - \frac{1}{2}\left\{\hat{\sigma}^+\hat{\sigma}^-,\hat{\rho}\right\}\right) \tag{4.3}$$

is also included to fully simulate the associated quantum master equation.

Both experiment and simulation show a minimum temperature as a function of Rabi frequency. At low Rabi frequency, the Landau-Zener condition $\alpha \ll \Omega^2$ breaks down, leading to inefficient adiabatic transfers. For the parameters used in (Fig. 4.4), $\alpha = \Omega^2$ when $\Omega = 2\pi \times 130$ kHz, roughly the point at which temperature is minimized in both the simulation and experimental results.

At larger Ω, both the experimentally measured and simulated temperatures rise with Ω, though the predicted and observed values appear to disagree at large Ω. This may be explained by the use of an approximate dipole radiation pattern which is better suited for a $\Delta m_j = \pm 1$ transition in the Lindblad superoperator [Eq. (4.3)], which introduces additional momentum diffusion and therefore results in a higher temperature. Moreover, several experimental factors could lead to this discrepancy. Because an acousto-optic modulator (AOM) is used to sweep the frequency of the cooling lasers, there are significant power variations during the sweep. Including this effect in our simulation resulted in lower temperatures at high Rabi frequency, and this effect can explain

much of the disagreement (as indicated by the red band in Fig. 4.4). Furthermore, imperfect laser polarization and finite bias field may lead to cooling on the transitions to $^3\mathrm{P}_1$, $m_j = \pm 1$, especially at high Rabi frequency. Nevertheless, the data roughly obeys the linear relationship

$$k_B T \propto \hbar\Omega, \tag{4.4}$$

for values of Ω in the adiabatic limit, which we discussed in Section 3.7 in the limit $\gamma \to 0$.

These results highlight that obtaining low temperatures requires low Rabi frequencies, and a sufficiently slow sweep such that the Landau-Zener condition $\alpha \lesssim \Omega^2$ is maintained. These conditions indirectly constrain the values of the atomic decay rate γ that are compatible with achieving low temperatures. In order to be in a regime where adiabatic transfer can be performed efficiently, we require that $\Omega \gg \gamma$, which motivates the use of narrow linewidth transitions in order to utilize a low Rabi frequency and obtain a low temperature. The sweep rate α is further constrained by the condition that the atoms should not decay between subsequent adiabatic transfers to and from the excited state, which requires $\alpha/2kv \gtrsim \gamma$. If we take v to be the initial velocity of the particles to be cooled, this condition represents a tradeoff between low final temperatures (which necessitate a small sweep rate α), and a large velocity capture range (which requires large α). This tradeoff becomes more favorable for long-lived excited states, though in principle can be mitigated in certain applications by dynamically adjusting the sweep rate and range as the particles are cooled.

By optimizing the sweep parameters in our simulation to achieve low equilibrium temperatures for ^{88}Sr atoms that begin at low temperature (making capture range a more minor concern), we achieve an equilibrium temperature of 2.3 μK. We find that colder temperatures can be achieved in simulation by using a longer-lived excited state. For comparison, this temperature is roughly an order of magnitude above the Doppler cooling limit for the same transition. Clearly, the key merit of our cooling mechanism is not its ability to achieve the lowest possible temperature, but rather to provide relatively strong forces on weak transitions, a large capture range, and a reduced reliance on spontaneous emission.

4.8 Conclusion

We have demonstrated a novel cooling mechanism in which large accelerations may be achieved even on optical transitions with low scattering rates. This mechanism may find application to the cooling of molecules, and can improve the performance of atomic cooling using dipole-forbidden optical transitions. From a technical perspective, this cooling method has the advantage of low sensitivity to long-term laser frequency drifts and to perturbations of the atomic transition frequency, for example to those encountered while loading into a deep optical dipole trap [92].

After the publication of this study, various extensions and modifications to this cooling mechanism have been realized and proposed, including the theoretical investigation [13] described in the previous chapter, the use of circularly polarized beams and magnetic field gradients to form a magneto-optical trap [12, 137, 171] (which is the subject of the next chapter), the application to ^{87}Rb (which has no narrow-line optical transition) by using Raman transitions [74], and the deceleration of a beam of ^{163}Dy atoms [146]. We also expect that this cooling mechanism can be used to achieve near ground state cooling of tightly confined atoms. To speed up the adiabatic transfers and therefore increase the stimulated forces, we also consider the incorporation of an adiabatic speedup protocol [14] in Chapter 6.

Chapter 5

SWAP MOT

In the previous two chapters, we demonstrated how the SWAP protocol can be used to cool atoms and molecules with narrow linewidth optical transitions. In this chapter, we show theoretically how it can be combined with a magnetic trap to supply an additional trapping force. This work resulted in a publication in Physical Review A (Ref. [12]) in May 2020. As opposed to related methods that have been previously reported [137], our approach utilizes repeated cycles of stimulated absorption and emission processes to achieve both trapping and cooling, thereby reducing the adverse effects that arise from photon scattering. Specifically, we demonstrate this method's ability to cool, slow, and trap particles with fewer spontaneously emitted photons, higher forces and in less time when compared to a traditional MOT scheme that utilizes the same narrow linewidth transition (see Section 2.3.4). We calculate the phase space compression that is achievable and characterize the resulting system equilibrium cloud size and temperature.

5.1 Introduction

Trapping and slowing devices based on the removal of momentum, energy, and entropy via light are ubiquitous and essential in most experiments on quantum gases. Techniques such as the slowing and cooling of particles by preferential absorption from a counterpropagating laser [68, 77], the magneto-optical trap [156], Zeeman decelerators [172], the bichromatic force [191], and sawtooth-wave adiabatic passage (SWAP) cooling [13, 141] all rely on many cycles of an engineered light-matter interaction for this purpose.

It is widely understood that spontaneous emission is a fundamental requirement for the laser cooling and trapping of atoms and molecules. This is due to the fact that the scattered photons irreversibly remove entropy, allowing the system to violate the conditions for Liouville's theorem to apply and to thereby undergo compression in terms of the occupied volume in phase space. While incorporating repeated scattering events is acceptable for systems with a closed cycling transition, this can lead to significant loss for systems with many degrees of freedom, such as molecules, which may have a large number of dynamically decoupled internal states, or "dark states." Protocols such as the optical repumping from uncoupled states to cooled states can mitigate this issue [90, 170], but a more absolute solution would be to significantly reduce the number of spontaneous emissions necessary to achieve slowing, cooling, and trapping.

SWAP cooling can cool a system to equilibrium with fewer spontaneous emissions than Doppler cooling and slow a distribution of particles using purely coherent dynamics [13]. We present the results of combining SWAP cooling with a quadrupole magnetic trap, which we call a SWAP MOT [140]. We show that a SWAP MOT is able to demonstrate slowing, cooling, and trapping with fewer scattered photons, higher conservative forces, and in less time when compared with a traditional MOT scheme.

Our approach differs from other methods of implementing the SWAP procedure in a MOT [137, 171] because we formulate a method to incorporate the stimulated emission process originally envisioned in the first proposals of SWAP cooling [13, 141]. This addition promotes both cooling and trapping and reduces the number of scattered photons required for equilibration. In order to achieve the desired coherent dynamics, we propose that the cooling laser polarizations and magnetic field directions (or, equivalently, the direction of the electron's magnetic moment) should be abruptly switched at the center and end of each sweep (see Fig. 5.1).

In Section 5.2 we explicate the particle dynamics achieved with the SWAP MOT protocol. In Section 5.3 we develop a semiclassical model in which the internal states are treated quantum mechanically and the external states are treated classically. Section 5.4 explains the details of our numerical algorithm. In Section 5.6 we define regimes in phase space that exhibit different types of

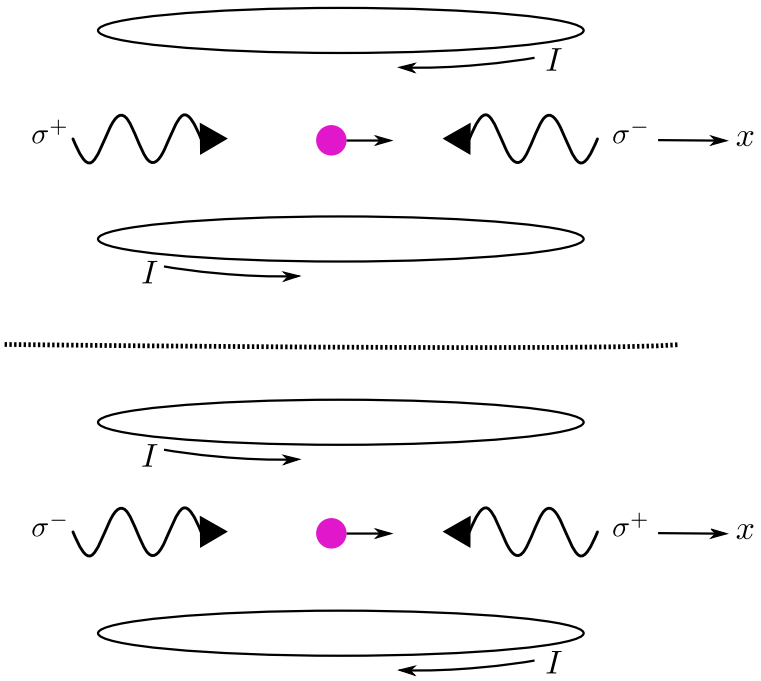

Figure 5.1: A schematic of the two experimental setups for the 1D SWAP MOT (motion only along the x-direction) that operate in alternating periods of the cooling cycle. Anti-Helmholtz coils with current I and counterpropagating lasers of opposite circular polarization σ^+ and σ^- create a magnetic-optical trap for neutral particles (pink circle). The laser polarizations and current directions are (ideally) instantaneously, periodically switched between the two setups as the detuning of each laser, which is linearly ramped from below to above the resonance of the cooling transition, passes through zero.

dynamic behavior under SWAP MOT evolution, define capture range conditions, and demonstrate phase space compression and MOT loading. In Section 5.7 we provide various scaling properties of the procedure over the range of interesting system parameters.

5.2 SWAP MOT mechanism

The SWAP procedure relies on the coherent transfer of a particle between quantum states via adiabatic rapid passage. The internal structure of the simplest quantum system that demonstrates the desired dynamics consists of two excited states with a common ground state, which we label $|+\rangle, |-\rangle$, and $|0\rangle$, respectively. The labels correspond to the values $m = \pm 1$ and 0, where m is the magnetic quantum number, such as that occurs in a system with a $J = 0 \rightarrow J = 1$ transition, where J is an angular momentum quantum number. Due to our choice of laser polarization, omission of

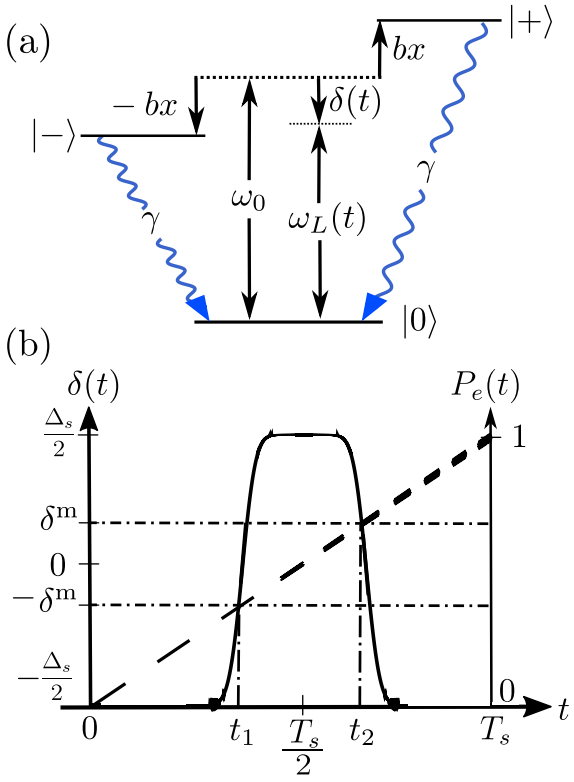

Figure 5.2: (a) The minimum internal state structure necessary for demonstrating SWAP MOT dynamics. The transition frequency ω_0, natural linewidth γ, laser frequency $\omega_L(t)$, detuning $\delta(t)$, and Zeeman shifts $\pm bx$ of the excited states are included. (b) The laser detuning $\delta(t)$ (dashed) and excited state fraction $P_e(t)$ (solid) vs time t over a sweep of period T_s. The particle resonates with the lasers at the times t_1 and t_2 when $\delta(t) = \pm\delta^{\mathrm{m}}$ (dot-dashed), where δ^{m} is the motional detuning [see Eq. (5.2)].

the $|J, m\rangle = |1, 0\rangle$ state is valid, as it is not optically pumped. As shown in Fig. 5.2(a), the excited states are separated in energy from the ground state by $\hbar\omega_0$, where ω_0 is the transition frequency, assumed to be in the optical domain. In the presence of a magnetic field, the excited states are shifted in energy according to the Zeeman shift $\pm\hbar bx$, where $b = g\mu_{\mathrm{B}}(\nabla B)/\hbar$, g is the g-factor of the transition, μ_{B} is the Bohr magneton, and x is the displacement of the particle from the trap center. Both excited states decay to the ground state with a rate given by the linewidth γ. For simplicity, we limit our discussion to one dimension.

As displayed in Fig. 5.1, the experimental setup is nearly identical to that of a type I 1D

MOT [126]. However, instead of fixing the laser detunings

$$\delta(t) = \omega_L(t) - \omega_0 \tag{5.1}$$

below the transition frequency, they are repeatedly swept from below to above the cooling transition in a sawtooth pattern (see the dashed curve in Fig. 5.2(b)) with full period T_s. In Eq. (5.1), $\omega_L(t)$ is the instantaneous laser frequency. Additionally, the directions of the currents I in the anti-Helmholtz coils and the polarizations of the cooling lasers are switched at a rate $2/T_s$. The current directions are chosen such that the magnetic field along the radial direction at the center of the trap, which we call the x-direction (see Fig. 5.1), has the form $B(x) = (\nabla B)x$ during the first half of the sweep, and $B(x) = -(\nabla B)x$ during the second half, where $\nabla B > 0$ is the magnetic field gradient. The laser traveling along the $+x$ ($-x$)-direction has circular polarization σ^+ (σ^-) during the first half, and then these polarizations are exchanged for the second half.

The general desired coherent dynamics over a single cycle of the SWAP procedure is as follows. Let us assume that the particle begins in $|0\rangle$, which is a good assumption due to the effects of spontaneous emission for appropriate system parameters. The particle resonates with one of the lasers when the laser detuning $\delta(t)$ is equal in magnitude to the particle's motional detuning

$$\delta^{\mathrm{m}} \equiv bx + kv, \tag{5.2}$$

which is the sum of its Doppler and Zeeman shifts, as shown in Fig. 5.2(b). Here, k is the wavenumber of the transition and v is the velocity of the particle. More specifically, at the time t_1 during the first half of the sweep defined by $\delta(t_1) = -|\delta^{\mathrm{m}}|$, the particle absorbs a photon from one of the cooling lasers and is transferred into whichever excited state $|e\rangle \in \{|+\rangle, |-\rangle\}$ first comes into resonance. Then, at the time t_2 in the second half of the sweep defined by $\delta(t_2) = |\delta^{\mathrm{m}}|$, the particle emits a photon into the other laser by stimulated emission and is transferred coherently back to $|0\rangle$ [see $P_e(t)$ in Fig. 5.2(b)] with the corresponding momentum shift. It is essential to our method that both the laser polarizations and magnetic field direction are switched between the times t_1 and t_2 so that the particle resonates with the correct laser as to achieve stimulated emission and

the consequent second momentum recoil. This second stimulated process in a sweep is exactly what differentiates our method from other SWAP MOT protocols [137, 171]. Very importantly, this protocol replaces the scattering event required after every absorption in Doppler cooling with a stimulated emission, mitigating the adverse effects of momentum diffusion that would otherwise occur. This feature allows the particle to experience the impulse of many photon momenta while avoiding spontaneous emission.

It is necessary to demonstrate that this protocol inherently generates a force toward the center of the trap (trapping), a force that opposes the particle's motion (slowing), and an overall frictional force (cooling). In order to illustrate its trapping capability, consider a motionless particle with position $x > 0$ [see Fig. 5.3(a)]. The Zeeman shift causes the particle to absorb a σ^- photon from the left-traveling laser during the first half of the cycle and to emit a photon into the right-traveling σ^- laser during the second half, transferring the particle back to $|0\rangle$ with a net impulse of two photon momenta toward the center of the trap. Its slowing capability is elucidated by considering a particle with momentum $p > 0$ near the center of the trap [see Fig. 5.3(b)]. In this case, the Doppler shift causes the particle to absorb a σ^- photon from the left-traveling laser during the first half and to emit a photon into the right-traveling σ^- laser during the second half, transferring the particle back to $|0\rangle$ also with a net impulse of two photon momenta that opposes the particle's motion. Examples with negative x or p similarly would cause trapping and slowing via interaction with the σ^+ laser. The cooling effect is more subtle. To be precise, we define **cooling** as compression of the particle's classical phase space volume, which is achieved through irreversible entropy flow from the particle to free space via the process of spontaneous emission. This most frequently occurs when the Doppler and Zeeman shifts are equal in magnitude but opposite in sign, as the particle resonates with both lasers simultaneously and is left with a significant excited state fraction at the end of a sweep. Spontaneous emission then resets the particle to the ground state for the next sweep, yielding a net drift in phase space toward the phase space origin. Although the discussion so far has been descriptive, we we will elucidate the details of the full dynamics in Section 5.6 through the numerical solutions to follow.

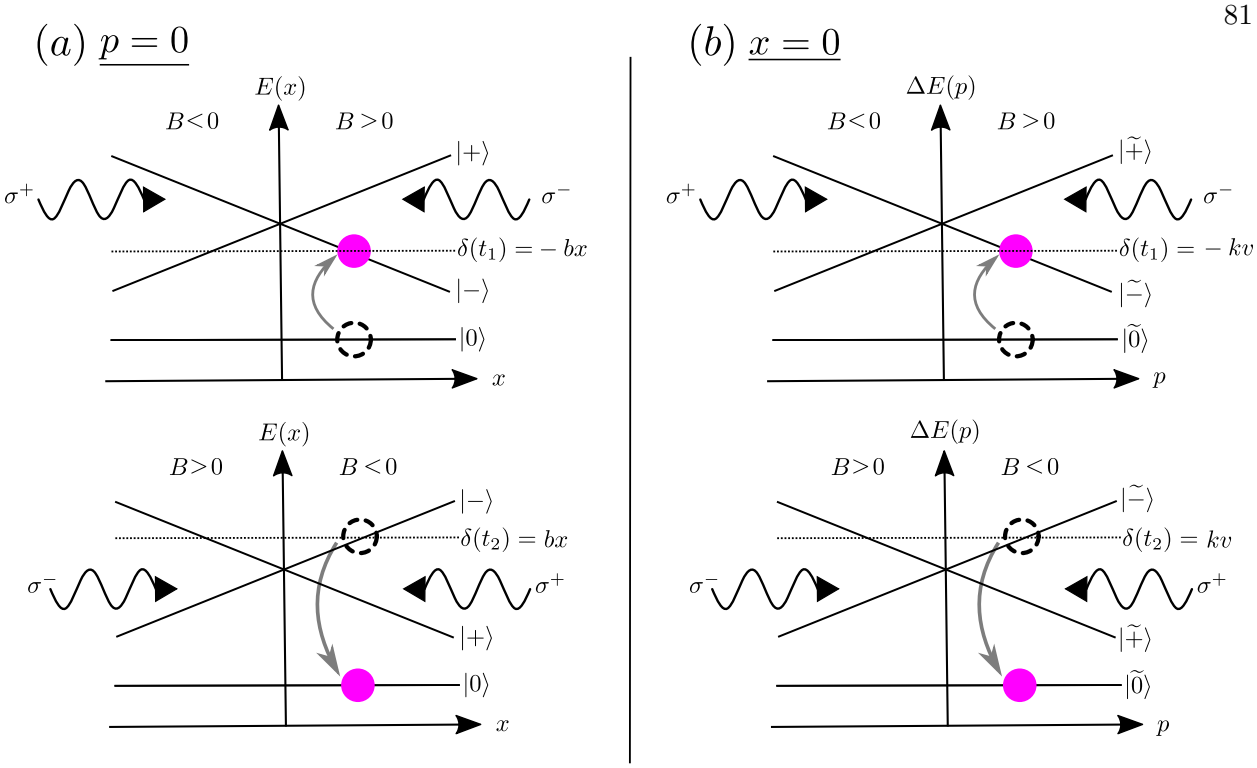

Figure 5.3: A qualitative demonstration of the trapping force (a) and slowing force (b) in a SWAP MOT. The cooling lasers (with circular polarizations $\sigma^{\pm}$) and sign of the magnetic field $B(x)$ setup are included. (a) Top: The energy eigenvalues $E(x)$ of $\hat{H}(t)$ with $\Omega = 0$ of a motionless particle ($p = 0$) as a function of position x during the first half of the sweep. An example system (pink circle) with $x > 0$ in the state $|0\rangle$ absorbs a σ^- photon, yielding an impulse toward $x = 0$ and transferring the particle into the $|-\rangle$ state. This occurs at the time t_1 when the swept laser frequency satisfies $\delta(t_1) = -bx$. Bottom: $E(x)$ vs. x and laser and magnetic field setup during the second half of the sweep. The example system emits a σ^- photon, yielding another impulse toward $x = 0$ and transferring the particle back to the $|0\rangle$ state. This occurs at the time $t_2 > t_1$ when the swept laser frequency satisfies $\delta(t_2) = bx$. (b) Top: The relative energy eigenvalues $\Delta E(p) \equiv E(p) - \frac{p^2}{2m}$ of of $\hat{H}(t)$ with $\Omega = 0$ for the states $W(p)$ [see Eqn. (5.11)] for a particle at the center of the trap ($x = 0$) as a function of momentum p in the first half (top) and second half (bottom) of the sweep. An example system experiences an impulse toward $p = 0$ by undergoing similar dynamics to Fig. 5.3(a) with the substitutions $x \to p$ and $bx \to kv$.

5.3 Model and semiclassical approximations

In order to capture the intricate features of the SWAP procedure, we first develop a fully quantum mechanical model for the particle and then make appropriate semiclassical approximations to create a computationally tractable simulation. We refer the reader to Sections 2.1 and 2.2 for general details on modeling light-matter interactions. As previously described, Fig. 5.2(a) displays

the internal state structure. We track motion along one dimension, for which the particle has momentum and position operators $\hat{p}$ and $\hat{x}$.

The system is subject to counter-propagating lasers of opposite circular polarization (which we denote as σ^+ and σ^-) of instantaneous frequency $\omega_L(t)$ and a magnetic field that depends linearly on the coordinate as $\hat{B}(\hat{x}) = (\nabla B)\hat{x}$. The detunings of the lasers $\delta(t)$ [see Eq. (5.1)] are set to follow a sawtooth waveform pattern centered at zero with range Δ_s and period T_s. In the Schrödinger picture, the coherent dynamics is described by the Hamiltonian

$$\begin{aligned}\hat{H}(t) =& \frac{\hat{p}^2}{2m} + \hbar\omega_0 \left(|+\rangle\langle+| + |-\rangle\langle-|\right) + \hbar b\hat{x}\left(|+\rangle\langle+| - |-\rangle\langle-|\right) \\ &+ \frac{\hbar\Omega}{2}\left(e^{i[k\hat{x}-\eta(t)]}\hat{\sigma}_+^+ + h.c.\right) + \frac{\hbar\Omega}{2}\left(e^{-i[k\hat{x}+\eta(t)]}\hat{\sigma}_-^+ + h.c.\right)\end{aligned} \tag{5.3}$$

during the first half of the sweep, with similar form but substitutions $k \to -k$ and $b \to -b$ during the second half of the sweep. The particle mass is m, the wavenumber of the laser light (which we approximate to be constant) is k, and the magnetic field gradient is characterized by b, which was defined in Section 5.2. The (equal) Rabi frequencies of both of the counterpropagating lasers are Ω, and

$$\eta(t) \equiv \int_0^t \omega_L(t')\,dt' \tag{5.4}$$

is the time-dependent accumulated phase of the laser field. The operators $\hat{\sigma}_i^+ \equiv |i\rangle\langle 0|$ and $\hat{\sigma}_i^- \equiv (\hat{\sigma}_i^+)^\dagger = |0\rangle\langle i|$ are the raising and lowing operators corresponding to transitions between the ground state and the two excited states.

The quantum master equation

$$\frac{d\hat{\rho}}{dt} = \frac{1}{i\hbar}\left[\hat{H}, \hat{\rho}\right] + \hat{\mathcal{L}}\hat{\rho} \tag{5.5}$$

governs the time evolution of the density matrix, $\hat{\rho}$, which fully describes the particle's internal and external states. The Lindblad superoperator captures the incoherent dynamics due to spontaneous emission and its associated recoil. As discussed in Section 2.2.3, we approximate the continuous dipole radiation pattern to produce discrete recoils of magnitudes $-\hbar k, 0$, and $\hbar k$ along the x-direction with probabilities of $\frac{1}{5} : \frac{3}{5} : \frac{1}{5}$, respectively [63, 135]. Although it is not absolutely

necessary to make the simplification that there are only three allowed impulses arising from the direction of the photon emission, the resulting numerical implementation is more straightforward due to the fact that one may take advantage of the presence of uncoupled momentum families. This approximation yields a Lindblad superoperator of the form

$$\hat{\mathcal{L}}\hat{\rho} = \gamma \sum_{i\in\{+,-\}} \left(\frac{3}{5}\hat{\sigma}_i^- \hat{\rho}\hat{\sigma}_i^+ + \frac{1}{5}e^{ik\hat{x}}\hat{\sigma}_i^- \hat{\rho}\hat{\sigma}_i^+ e^{-ik\hat{x}} + \frac{1}{5}e^{-ik\hat{x}}\hat{\sigma}_i^- \hat{\rho}\hat{\sigma}_i^+ e^{ik\hat{x}} - \left\{\hat{\sigma}_i^+\hat{\sigma}_i^-, \hat{\rho}\right\} \right). \tag{5.6}$$

In the interaction picture defined by the free Hamiltonian

$$\hat{H}_0(t) = \hbar\omega_L(t)\left(|+\rangle\langle+| + |-\rangle\langle-|\right), \tag{5.7}$$

the interaction Hamiltonian is

$$\begin{aligned}\hat{H}_{\mathrm{I}}(t) =& \frac{\hat{p}^2}{2m} - \hbar\delta(t)\left(|+\rangle\langle+| + |-\rangle\langle-|\right) + \hbar b\hat{x}\left(|+\rangle\langle+| - |-\rangle\langle-|\right) \\ &+ \frac{\hbar\Omega}{2}\left(e^{ik\hat{x}}\hat{\sigma}_+^+ + h.c.\right) + \frac{\hbar\Omega}{2}\left(e^{-ik\hat{x}}\hat{\sigma}_-^+ + h.c.\right).\end{aligned} \tag{5.8}$$

The corresponding force operator that describes the coherent evolution of the external variables is then

$$\hat{F} \equiv -\frac{\partial\hat{H}_{\mathrm{I}}}{\partial\hat{x}} = \hbar b\left(|-\rangle\langle-| - |+\rangle\langle+|\right) - \frac{i\hbar\Omega k}{2}\left(e^{ik\hat{x}}\hat{\sigma}_+^+ - h.c.\right) + \frac{i\hbar\Omega k}{2}\left(e^{-ik\hat{x}}\hat{\sigma}_-^+ - h.c.\right). \tag{5.9}$$

We now make several approximations to form a tractable, semiclassical model. By the term "semiclassical," we refer to reducing the number of motional degrees of freedom of the particle that need to be tracked, while the laser field is treated classically. The parameter that characterizes the separation of timescales required to treat the motion classically is [53]

$$\chi \equiv \frac{\omega_r}{\gamma} \ll 1, \tag{5.10}$$

where $\omega_r \equiv \hbar k^2/2m$ is the recoil frequency of the transition (see Section 2.3). However, the SWAP procedure causes fewer spontaneous emissions as χ increases [13], so Eq. (5.10) may not necessarily hold. Moreover, the rapid adiabatic passage protocol generates coherences between quantum states, so tracking a single value for the semiclassical momentum p is insufficient. Instead, we simplify our

formalism by limiting the number of quantum states we track at any given time. We retain the term "semiclassical" for this simplification and our consequent treatment of the particle's external variables, and we consider its validity in Section 5.5.

The $\sigma^+ - \sigma^-$ polarization scheme prevents multiphoton processes by angular momentum conservation [53], so a particle in an eigenstate $|\widetilde{0}(p)\rangle \equiv |0, p\rangle$ can only be transferred to the states $|\widetilde{-}(p)\rangle \equiv |-, p - \hbar k\rangle$ and $|\widetilde{+}(p)\rangle \equiv |+, p + \hbar k\rangle$ (and vice versa) during the first half of the sweep. The same statement holds true for the second half of the sweep with $k \to -k$. Therefore, we only track the particle's evolution in the subset of basis states

$$W(p) \equiv \{|\widetilde{0}\rangle, |\widetilde{+}\rangle, |\widetilde{-}\rangle\} \tag{5.11}$$

of the composite Hilbert space, then update p appropriately as the particle absorbs and emits photons.

Next, we treat the particle's external variables in the Hamiltonian $\hat{H}_I(t)$ semiclassically by making the substitutions $\hat{p} \to p$ and $\hat{x} \to x$, where p is a momentum eigenvalue satisfying $\hat{p}\,|p\rangle = p\,|p\rangle$ [which also parameterizes $W(p)$], and x is a c-number that characterizes the particle's spatial position. These classical phase space coordinates will be updated according to a procedure that we develop in Section 5.4. With the state $|\widetilde{0}\rangle$ defining zero energy, the semiclassical Hamiltonian that evolves $W(p)$ is

$$\hat{H}_{\mathrm{s}}(t) = -\hbar(\delta(t) - \delta^{\mathrm{m}})\,|\widetilde{+}\rangle\langle\widetilde{+}| - \hbar(\delta(t) + \delta^{\mathrm{m}})\,|\widetilde{-}\rangle\langle\widetilde{-}| + \frac{\hbar\Omega}{2}\left(\hat{\sigma}^x_{\widetilde{+}} + \hat{\sigma}^x_{\widetilde{-}}\right), \tag{5.12}$$

where $\hat{\sigma}^x_{\widetilde{i}} \equiv \hat{\sigma}^+_{\widetilde{i}} + \hat{\sigma}^-_{\widetilde{i}}$. Note that the motional detuning δ^{m} determines the condition for resonance in Eq. (5.12) as previously discussed. Additionally, we have omitted recoil energy terms $\hbar\omega_r$ under the approximation that they are small in comparison to $\hbar\delta^{\mathrm{m}}$.

The coherent evolution of x and p is typically accounted for via Newton's laws of motion under the classical force

$$F(t) = \left\langle \hat{F}(t) \right\rangle = \hbar b \left[\left| c_{\widetilde{-}}(t) \right|^2 - \left| c_{\widetilde{+}}(t) \right|^2 \right] \quad + \hbar\Omega k \left(\mathrm{Re}\left[i\langle \hat{\sigma}^+_{\widetilde{-}}(t) \rangle \right] - \mathrm{Re}\left[i\langle \hat{\sigma}^+_{\widetilde{+}}(t) \rangle \right] \right), \tag{5.13}$$

where $\left|c_{\widetilde{i}}(t)\right|^2 \equiv \left|\langle\widetilde{i}|\Psi(t)\rangle\right|^2$ are the instantaneous populations of state $|\widetilde{i}\rangle$ determined from the particle's wave function $|\Psi(t)\rangle$ evolved under $\hat{H}_{\rm s}(t)$. As opposed to other semiclassical treatments of laser cooling [126], the effects of $F(t)$ on the particle momentum are intrinsically incorporated into our model due to the p-dependence of the quantum states in $W(p)$. Nevertheless, we provide this force analysis as a consistency check. As we will motivate in Section 5.6, we make the physically reasonable assumption that the coherent force due to photon absorption and emission is much larger than the coherent Zeeman force that arises from the gradient of the magnetic field, **i.e.**, $b \ll \Omega k$, which reduces Eq. (5.13) to

$$F(t) \approx \hbar\Omega k \left(\mathrm{Re}\left[i\langle\hat{\sigma}^+_{\widetilde{-}}(t)\rangle \right] - \mathrm{Re}\left[i\langle\hat{\sigma}^+_{\widetilde{+}}(t)\rangle \right] \right). \tag{5.14}$$

In this limit, the impulse experienced by the particle at any time in the first half of the sweep is

$$\Delta p(t) = \int_{t_0}^{t} F(t')\, dt' \approx \hbar k \left[\Delta P_+(t_0,t) - \Delta P_-(t_0,t) \right], \tag{5.15}$$

where $\Delta P_\pm(t_0,t) \equiv P_\pm(t) - P_\pm(t_0)$ are the changes in population of the states $|\widetilde{\pm}\rangle$ between the times t_0 and t. Eq. (5.15) agrees with the result obtained from calculating

$$\Delta p(t) = \langle\Psi(t)|\hat{p}|\Psi(t)\rangle - \langle\Psi(t_0)|\hat{p}|\Psi(t_0)\rangle . \tag{5.16}$$

Eqns. (5.12) and (5.15) uniquely determine the coherent evolution of a particle during the first half of a sweep. The corresponding equations for the second half of the sweep are found by the substitutions $k \to -k$ and $b \to -b$. The incoherent dynamics are described by the Lindblad superoperator $\mathcal{L}\hat{\rho}$ in Eq. (5.6) with the appropriate substitutions.

5.4 Variant of quantum trajectories

We are now in a position to choose a simulation method for determining the semiclassical evolution of particles in the SWAP MOT. In this section, we develop a variant of the Monte Carlo quantum trajectories method in the time domain [63, 135]. The traditional Monte Carlo wave function method is outlined in Section 2.2.4. This choice is motivated by this method's ability to

create a time record for the emission of spontaneous photons by individual particles, i.e., a quantum jump. We will use this knowledge about the jump time to simulate the motional dynamics as accurately and efficiently as possible within our semiclassical framework.

In the quantum trajectory method, the density matrix $\hat{\rho}(t)$ is obtained by averaging the associated pure states of many "quantum trajectories," each described by a state vector $|\psi\rangle$:

$$\hat{\rho}(t) \approx \frac{1}{N} \sum_{i=1}^{N} |\psi_i(t)\rangle \langle\psi_i(t)| , \tag{5.17}$$

where $N \gg 1$ is the number of simulated trajectories. The state vectors are continuously evolved under a non-Hermitian Hamiltonian defined as

$$\hat{H}_{\text{eff}} \equiv \hat{H} - \frac{i\hbar}{2} \sum_i \hat{J}_i{}^{\dagger} \hat{J}_i \tag{5.18}$$

in addition to discrete quantum jumps that correspond to the various decay channels in the system [63, 135]. As we present below, our method retains these features and introduces fictitious quantum jumps of $|\psi\rangle$ into one of the elements of $W(p)$, directly followed by an update of the coordinates x and p based on the results of the projection. These additional operations allow us to calculate an effective, coarse-grained, single phase space trajectory $\big(x(t), p(t)\big)$ for each quantum trajectory.

In the case of distinguishable spontaneous emission processes, the jump operators $\hat{J}_i$ take the form $\hat{J}_i = \sqrt{\gamma}\hat{\sigma}_i^-$. In our model, the spontaneous photons due to the decay of the the excited states $|\pm\rangle$ to the ground state $|0\rangle$ are distinguishable in principle by their polarization, so our effective semiclassical Hamiltonian is

$$\hat{H}_{\text{eff}}(t) \equiv \hat{H}_{\text{s}}(t) - \frac{i\hbar\gamma}{2} \left(|\widetilde{+}\rangle \langle\widetilde{+}| + |\widetilde{-}\rangle \langle\widetilde{-}| \right) . \tag{5.19}$$

The time evolution protocol for each quantum trajectory is as follows. Note that $k > 0$ ($k < 0$) in the first (second) half of the sweep.

(1) Initialize the classical phase space coordinate (x, p) by sampling from a chosen distribution. Using this choice of p, prepare the quantum state in a state vector that lies in the basis $W(p)$. Record the quantum state as $|\psi_r\rangle$, the time as t_r, and the initial phase space coordinate as (x_r, p_r).

(2) Continuously evolve $|\psi(t)\rangle$ under $\hat{H}_{\text{eff}}(t)$ [Eq. (5.19)] with the external coordinate, (x_r, p_r), held constant. This evolution can be interrupted at at a time t_j when one of two possible discrete quantum jump events occur:

Case A The middle or end of a sweep is reached.

(i) Simulate a fictitious quantum jump of $|\psi(t_j)\rangle$ into one of the basis states in the subspace $W(p_r)$ using populations to determine the relative likelihood, i.e., $|\psi(t)\rangle \to |\psi_P\rangle \in W(p_r)$.

(ii) Calculate the corresponding impulse Δp and displacement Δx according to

$$\begin{aligned} \Delta p &= \langle\psi_P|\hat{p}|\psi_P\rangle - \langle\psi_r|\hat{p}|\psi_r\rangle \in \{0, \hbar k, -\hbar k\}; \\ \Delta x &= \frac{1}{m}\int p(t')\,dt' \approx \frac{1}{m}\frac{p_{\text{avg}}}{2}\Delta t = \frac{1}{m}\left(p_r + \frac{\Delta p}{2}\right)(t_j - t_r) \end{aligned} \tag{5.20}$$

so that the new phase space coordinate is

$$(x, p) = (x_r + \Delta x, p_r + \Delta p). \tag{5.21}$$

(iii) Relabel the basis subset $W(p_r)$ with the updated momentum p.

(iv) Replace $|\psi_r\rangle, t_r$ and (x_r, p_r) with their updated values $|\psi_P\rangle$, t_j, and (x, p).

Case B A spontaneous photon is detected according to the quantum trajectory procedure [63, 135].

(i) Simulate which state $|\widetilde{e}\rangle \in \{|\widetilde{+}\rangle, |\widetilde{-}\rangle\}$ the system occupied and hence decayed from using probabilities weighted by the excited state populations, i.e., project $|\psi(t_j)\rangle \to |\psi_P\rangle = |\widetilde{e}\rangle$.

(ii) Apply Δp and Δx according to Eqns. (5.20) and update (x, p) to correspond to this choice.

(iii) Simulate the spontaneous emission process further by updating p to account for the momentum recoil by selecting one of the three possibilities in the discretely represented dipole radiation pattern. Assign $|\psi(t_j)\rangle = |\widetilde{0}\rangle$.

(iv) Relabel the basis subset $W(p_r)$ with the updated momentum p.

(v) Replace $|\psi_r\rangle, t_r$ and (x_r, p_r) with their updated values $|\widetilde{0}\rangle$, t_j, and (x, p).

(3) Repeat as needed from step 2 until a desired final time is reached.

We choose to perform the operations described in Case A at the middle and end of each sweep because the particle ideally undergoes one adiabatic transfer per half sweep by the design of the SWAP procedure, and hence experiences the impulse of a single photon momentum.

As a framework for comparison and consistency, we have developed an analogous model for a traditional 1D MOT, which we use in Section 5.6. In that case, the phase space variables are only updated whenever a spontaneous event occurs, as this is typically the only mechanism whereby the system can traverse momentum space. The resulting cloud size, temperature, and spontaneous photon record are in close agreement with other models [126]. Moreover, the SWAP MOT algorithm we present agrees well with a fully quantum $\sigma^+ - \sigma^-$ SWAP cooling model with no magnetic trapping (as opposed to the configuration previously developed in [13, 141] with linearly polarized lasers), which can easily be implemented computationally due to its translational invariance. Further investigation of the validity of this three-state model is presented in the following section.

5.5 Validity of three-state basis in SWAP MOT simulation

Here we justify the reduction of the subset to three basis states. Starting the particle in the state $|\psi_0\rangle = |0, p\rangle$, we evolve it according to $\hat{H}_I(t)$ [Eq. (5.8) with $\hat{x} \to x = \text{const}$ for simplicity] over the first half of a sweep in the 7-state basis

$$W_7 \equiv \{|0, p\rangle, |0, p \pm 2\hbar k\rangle, |+, p \pm \hbar k\rangle, |-, p \pm \hbar k\rangle\}. \tag{5.22}$$

For our choice of $|\psi_0\rangle$, these are the only states that can possibly become occupied in one sweep, so it is equivalent to using the full basis set in [13]. At the middle of the sweep, the state is

$$|\psi_{1/2}\rangle = c^0_{1/2}|0, p\rangle + c^-_{1/2}|-, p - \hbar k\rangle + c^+_{1/2}|+, p + \hbar k\rangle, \tag{5.23}$$

where the $c^i_{1/2}$'s are the probability amplitudes of each state. Note that this is the same state we would have calculated had we only tracked the 3-state basis

$$W_3 \equiv \{|0,p\rangle, |+,p+\hbar k\rangle, |-,p-\hbar k\rangle\}. \tag{5.24}$$

Next, we calculate the state at the end of the sweep in two ways. In one case (the "7-state formalism"), we simply propagate $|\psi_{1/2}\rangle$ under $\hat{H}_I(t)$ with $b \to -b$ and $k \to -k$ (i.e., switching the magnetic field and laser polarizations according to our protocol) in W_7 over the second half of a sweep to yield the state $|\psi^7_f\rangle$; this is the final state found by tracking the full 7-state basis throughout the entire sweep. The other case (the "3-state formalism" used in Chapter 5) is more complicated because we must project $|\psi_{1/2}\rangle$ into one of the states in W_3 using probabilities weighted by their populations, which means the final state of the particle will be a mixed state. Here, we propagate three states

$$|\psi^0_{1/2}\rangle = |0,p\rangle; \quad |\psi^-_{1/2}\rangle = |-,p-\hbar k\rangle; \quad |\psi^+_{1/2}\rangle = |+,p+\hbar k\rangle \tag{5.25}$$

according to $\hat{H}_I(t)$ with $b \to -b$ and $k \to -k$ in W_7 over the second half of a sweep. Labeling the results as $|\psi^0_f\rangle, |\psi^-_f\rangle$, and $|\psi^+_f\rangle$, the final state for the 3-state formalism is

$$\hat{\rho}^3_f = |c^0_{1/2}|^2 |\psi^0_f\rangle\langle\psi^0_f| + |c^-_{1/2}|^2 |\psi^-_f\rangle\langle\psi^-_f| + |c^+_{1/2}|^2 |\psi^+_f\rangle\langle\psi^+_f|. \tag{5.26}$$

The state $\hat{\rho}^3_f$ is what is calculated according to our simulation procedure, aside from the additional complexity of updating x at the middle of the sweep.

We now compare the resulting final states $\hat{\rho}^7_f = |\psi^7_f\rangle\langle\psi^7_f|$ and $\hat{\rho}^3_f$ using two metrics. The first is the fidelity of quantum states

$$F(\sigma,\rho) = \mathrm{Tr}\sqrt{\sqrt{\sigma}\rho\sqrt{\sigma}}, \tag{5.27}$$

which reduces to

$$F(\hat{\rho}^3_f, \hat{\rho}^7_f) = \langle\psi^7_f|\hat{\rho}^3_f|\psi^7_f\rangle \tag{5.28}$$

since the final state in the 7-state formalism is pure. The other is a comparison of the final state probability distributions $P^j_i = \langle i|\hat{\rho}^j_f|i\rangle$ according to the chi-squared test. That is, we compare the

chi-squared value

$$\chi^2 = \sum_{i=1}^{7} \frac{(P_i^3 - P_i^7)^2}{P_i^7} \tag{5.29}$$

to the number of degrees of freedom $df = 6$ to quantitatively compare the final probability distributions.

Fig. 5.4a displays F and χ^2 for a region of classical phase space centered on the phase space origin. We refer the reader to Fig. 5.5 and the cited equations therein to gain intuition about the expected dynamics of particles in phase space. The fidelity F of the states $\hat{\rho}_f^3$ and $\hat{\rho}_f^7$ (Fig. 7.3) generally increases with $|\delta^m|$, which implies that the 3-state formalism becomes more accurate in determining both the population and coherences of the particle's quantum state when the stimulated absorption and emission processes are time-resolved. This is expected because the particle becomes distributed over more quantum states when the stimulated processes overlap, which is not captured by the 3-state formalism.

On the other hand, we find that the chi-squared values χ^2 are much smaller than the number of degrees of freedom $df = 6$ in the entire region of phase space (Fig. 5.4b). This suggests that the final population distributions P_i^3 and P_i^7 are nearly identical. For example, at the phase space coordinate $(kx, p/\hbar k) = (2750, 20)$, which has a relatively high χ^2 value of $6 \cdot 10^{-9}$, we find that P_i^3 and P_i^7 are identical to four decimal places. These results imply that the 3-state formalism very accurately captures the final population distribution of a particle over the states W_7 over one sweep, which is promising because these populations directly determine the momentum (and therefore the position) distribution in the SWAP MOT. We expect that this result extends to more than one sweep.

5.6 Phase space dynamics

Now that we have developed and motivated a detailed semiclassical model, we are in a position to simulate and characterize the dynamics in a SWAP MOT. In this section, we first provide general insight for appropriate choices of the many experimental parameters. Then, as a relevant physical

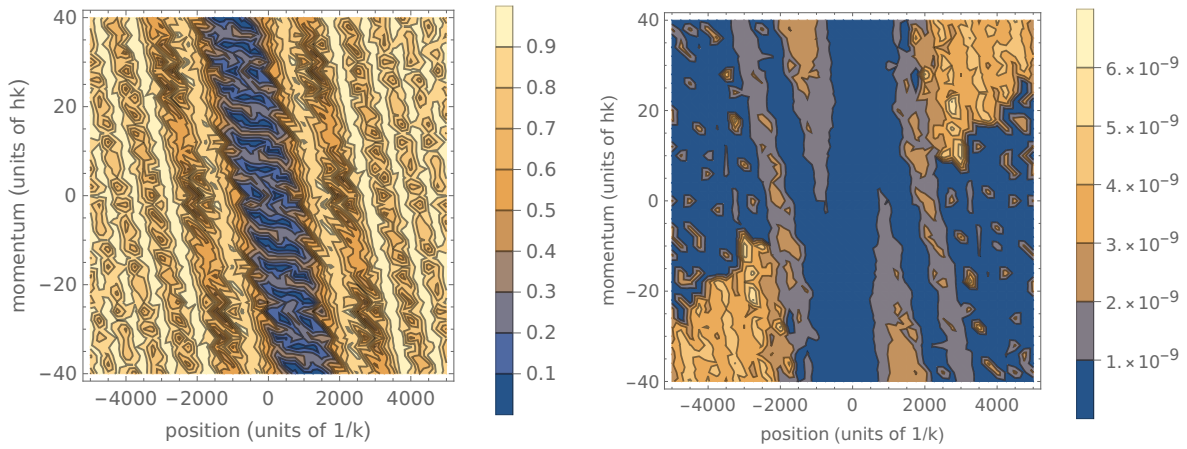

(a) The fidelity F of the final states $\hat{\rho}_f^7$ and $\hat{\rho}_f^3$, which is bounded according to $0 \leq F \leq 1$.

(b) The chi-squared value χ^2 between the final probability distributions P_i^j.

Figure 5.4: Phase space contour plots of various metrics that compare the final states of the 3-state and 7-state formalisms. The relative simulation parameters are identical to those used in Fig. 5.5 except $\gamma \to 0$.

example, we simulate the dynamics of the SWAP MOT procedure as applied to the molecule yttrium monoxide (YO) using parameters for one of its narrow linewidth transitions. We use the simulation results to further elucidate the dynamics in various regions of phase space, which are separated by diagonal lines with slopes determined by the motional detuning (see Fig. 5.5):

$$\delta^{\mathrm{m}} = bx + kv = M\epsilon + 2\beta\omega_r \;\Rightarrow\; \frac{d\beta}{d\epsilon} = -\frac{M}{2\omega_r}. \tag{5.30}$$

Here, $M \equiv b/k$ is the frequency that characterizes the magnetic field gradient, and $\epsilon \equiv kx$ and $\beta \equiv p/\hbar k$ are the position and momentum expressed in the appropriate dimensionless units corresponding to the optical transition. Finally, we compare the results of the trap loading process and phase space compression to those in a traditional MOT.

5.6.1 Choosing appropriate experimental parameters

The essential constraints for the experimental parameters arise from the requirement of rapid adiabatic passage, which forms the foundation of the SWAP method. Landau and Zener proved [194] that population is efficiently transferred between two stable quantum states as long

as the laser frequency is linearly swept over the energy splitting of the states with the following condition satisfied:

$$\kappa \equiv \frac{\Omega^2}{\alpha} > 1, \tag{5.31}$$

where we define κ as the adiabaticity parameter and $\alpha \equiv \Delta_s/T_s$ is the slope of the frequency ramp [194]. Experimental parameters that satisfy Eq. (5.31) are said to operate within the adiabatic regime.

Additionally, it can be shown [185] that the transfer process takes a time $\tau_{\mathrm{j}} = 2\Omega/\alpha$ in the adiabatic regime. Because it is necessary for the system to remain in the excited state without spontaneously decaying for at least a time τ_{j}, it must satisfy $\tau_{\mathrm{j}} \ll 1/\gamma$. Combining this result with Eq. (5.31), we find that the Rabi frequency must satisfy

$$\Omega \gg \gamma. \tag{5.32}$$

This is exactly what is meant by adiabatic *rapid* passage [2].

We now discuss the choice of the sweep range Δ_s. In Section 5.2, we described how a particle can experience a coherent force and a consequent impulse of $2\hbar k$ per sweep if it begins in the internal ground state $|0\rangle$. However, it will still experience an impulse that leads to cooling and trapping, albeit smaller in magnitude, even if it begins with some excited state population. By symmetry, this impulse will aid in cooling and trapping a particle only if its wave function predicts that it is more likely to begin a sweep in $|0\rangle$. One way to guarantee this condition is to enforce an imbalance such that the particle spends more time outside the two photon resonances, allowing spontaneous emission to preferentially optically pump the system to $|0\rangle$ for the next sweep. The most obvious way to do this is to introduce a waiting period in between each sawtooth ramp. However, because it is often desirable to cool and trap as quickly as possible, we only consider situations with no waiting period. In this case, we achieve a time imbalance whenever

$$4|\delta^{\mathrm{m}}| \leq \Delta_s, \tag{5.33}$$

since the resonances are spaced in frequency by $2|\delta^{\mathrm{m}}|$.

Next, we consider restrictions on the sweep period T_s. In the sequence discussed in Section 5.2, the particle spends a time $\tau_{\mathrm{e}} \approx 2|\delta^{\mathrm{m}}|/\alpha$ in one of the excited states in between the two resonances. (This can be seen by writing the detuning during a single sweep as $\delta(t) = \alpha t$ and noting that the lasers resonate with the particle when $\delta(t) = \pm\delta^{\mathrm{m}}$.) Therefore, in order for the particle to maintain a low probability of spontaneous emission in between resonances, τ_{e} must satisfy

$$\tau_{\mathrm{e}} \approx \frac{2|\delta^{\mathrm{m}}|}{\alpha} < 1/\gamma. \quad \Rightarrow \quad 4|\delta^{\mathrm{m}}| < \frac{2\Delta_s}{\gamma T_s}. \tag{5.34}$$

The resetting to the internal ground state enforced by the time imbalance is only useful if the particle does not have a significant chance of decaying between resonances during the next sweep. So, applying Eq. (5.33) and Eq. (5.34), a reasonable restriction on the sweep period T_s is given by

$$\gamma T_s < 2\,, \tag{5.35}$$

in order to obtain fast results. It has been shown experimentally that a cooling force twice as large as the radiation pressure force was achieved in a ^{163}Dy system with the choice $\gamma T_s \approx 0.1$ [146]. However, some experiments may require the much stricter condition of minimal spontaneous events. In these cases, one should instead come close to saturating the bound in Eq. (5.35) so that there is substantial time to reset to the ground state via spontaneous emission in the event of incorrect time-ordering of absorption and emission.

We now derive a condition for the choice of magnetic field gradient. As will be explained in Section 5.6.3.1, there is a specific region of phase space, which we call the "ideal region," where particles generally undergo a change in momentum of $2\hbar k$ per sweep via the coherent dynamics discussed in Section 5.2. Here, it is a good approximation to expand the momentum to first order in time, i.e.,

$$\beta(\tau) \approx \beta_0 + \frac{d\beta}{d\tau}\tau \approx \beta_0 - 2\mathrm{sgn}(\delta_0^{\mathrm{m}})\tau. \tag{5.36}$$

In Eq. (5.36), $\tau \equiv t/T_s$ labels the number of sweeps, and we have made the approximation that the momentum transfer $\Delta\beta = 2$ is uniformly distributed over a sweep instead of localized near photon resonances. Note that the sign function arises because the sign of δ^{m} determines which laser the

system interacts with first, and therefore the direction of the impulse. This family of trajectories has an instantaneous slope of magnitude

$$\left|\frac{d\beta}{d\epsilon}(\tau)\right| = \frac{1}{\omega_r T_s|\beta_0 - 2\mathrm{sgn}(\delta_0^{\mathrm{m}})\tau|} \leq \frac{1}{\omega_r T_s|\beta_0|}, \tag{5.37}$$

which was derived by applying the integral relationship $x = \int v\, dt$, equivalent to $\epsilon = 2\omega_r T_s \int \beta\, d\tau$. Any trajectory with a slope whose magnitude is smaller than Eq. (5.30) has a substantial likelihood of moving out of the ideal region and into an undesirable "heating region," described in Section 5.6.3.3. Therefore, it is reasonable to bound the slope of our trajectories, as given in Eq. (5.37), from below by the the slope of the diagonal lines that define different phase space regions [Eq. (5.30)], which leads to the condition

$$MT_s \leq 2/|\beta_0|. \tag{5.38}$$

Because the minimum achievable temperature in SWAP cooling is the recoil temperature [13], it is safe to assume that the momenta of most of the particles satisfy $|\beta_0| > 1$.

As mentioned earlier, it is necessary to choose a sweep period T_s that comes close to saturating Eq. (5.35) when it is a priority to minimize spontaneous events. Combining Eqns. (5.35) and (5.38) in this limit yields the restriction

$$M \leq \gamma. \tag{5.39}$$

Together, Eqns. (5.32) and (5.39) motivate our omission of the coherent Zeeman force in Section 5.3.

5.6.2 Cooling and trapping of the molecule YO

Figure 5.5 displays simulated phase space trajectories for a cloud of Yttrium Monoxide (YO) particles being cooled and trapped in a SWAP MOT using its 5.9 kHz linewidth $X^2\Sigma^+ \rightarrow A'^2\Delta_{3/2}$ transition [60]. Motivated by recent experimental progress [60], the initial particle distribution was characterized by Gaussians with standard deviations $\sigma_{\epsilon_0} = 9.1 \cdot 10^3$ and $\sigma_{\beta_0} = 11.5$, and is displayed as yellow target symbols "+" in Fig. 5.5. By comparing the initial and final particle distributions, the latter displayed as purple triangles, it is clear that phase space compression was achieved. We quantify this result in Section 5.6.4.

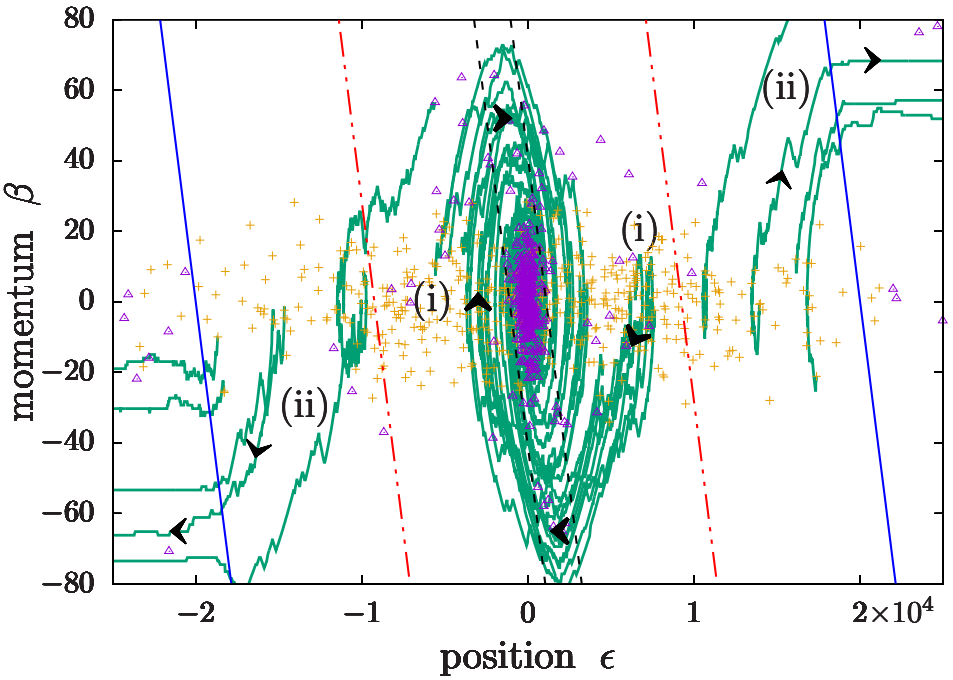

Figure 5.5: Phase space dynamics in a SWAP MOT. The variables β and ϵ label a particle's momentum as a multiple of the number of photon momenta and number of inverse wavenumbers from the center of the trap, respectively. The diagonal lines, which have slopes determined by Eq. (5.30), separate phase space into regions that are labeled above the plot and characterized by Eq. (5.42). Several sample simulated phase space trajectories are displayed as green lines. The black arrows show the flow of time. Particles in the "ideal" region, labeled (i), are generally cooled and trapped, while those outside the "ideal" region, labeled (ii), are heated out of the trap. Each of the particles' initial momenta and positions (yellow targets) were sampled from Gaussian distributions with standard deviations $\sigma_{\beta_0} = 11.5$ and $\sigma_{\epsilon_0} = 9.1 \cdot 10^3$, respectively. Values are: $\omega_r = 0.67\gamma$, $M = 0.05\gamma$, $\Omega = 55\gamma$, $\Delta_s = 2000\gamma$, $T_s = 1.5/\gamma$, and $t_{\max} = 375/\gamma$. For this set of parameters, the particles are slightly cooled and become significantly more trapped (final coordinates are displayed as purple triangles).

The simulation parameters were chosen under the conditions derived in Section 5.6.1. Because we wish to highlight the SWAP MOT's ability to cool and trap with fewer scattered photons, the sweep period was chosen to satisfy $\gamma T_s = 1.5$, which is close to the bound in Eq. (5.35). The magnetic field gradient was consequently chosen to be $M = 0.05\gamma$ in order to yield significant trapping with a capture range roughly corresponding to any particles with momenta smaller in magnitude than $3\sigma_{\beta_0}$ [see Eq. (5.38)]. These choices bounded the motional detuning of most

particles to the interval

$$|\delta^{\mathrm{m}}| \leq M\sigma_{\epsilon_0} + 2\sigma_{\beta_0}\omega_r \approx 470\gamma. \tag{5.40}$$

Therefore, the choice $\Delta_s = 2000\gamma$ guaranteed that most particles underwent the dynamics described in Section 5.2 [Eq. (5.33)] and did not frequently emit spontaneous photons in between the two resonances [Eq. (5.34)]. Finally, to operate in the regime of adiabatic rapid passage, the Rabi frequency was chosen to be $\Omega = 55\gamma$ [see Eqns. (5.31) and (5.32)].

5.6.3 Characteristic dynamics in different phase space regions

The diagonal lines in Fig. 5.5 divide phase space into regions with different characteristic behavior, which we now discuss in the following sections.

5.6.3.1 Region of ideal coherent dynamics

Upon investigation of the coherent dynamics under Eq. (5.12) in the adiabatic limit, we can deduce that a particle initialized in the internal ground state $|0\rangle$ populates a single excited state during a sweep only if $|\delta^{\mathrm{m}}| > |\Omega|$. (In our previous work, we referred to a similar condition as the "high-velocity regime" [13].) Otherwise, power broadening would bring both lasers into resonance with the particle simultaneously, distributing population among all three states. Specifically, a particle with $\delta^{\mathrm{m}} > |\Omega|$ ($\delta^{\mathrm{m}} < -|\Omega|$) first absorbs a photon from the σ^- (σ^+) laser. Then, after the laser polarizations and the magnetic field are abruptly switched, the particle eventually emits a photon into the other laser, which now has the correct polarization (see Fig. 5.3). Thus, the particle experiences a negative (positive) impulse of magnitude $2\hbar k$ after each sweep in the absence of spontaneous emission.

When spontaneous emission is included, the particle must not spend too much in the excited state τ_{e} [see Eq. (5.34)] or else dissipation will occur. In order to retain mostly coherent dynamics, we propose that τ_{e} must be smaller than the time $\log(2)/\gamma$, as half of the particles will decay on average before resonating with the other laser in this time. Combining these results, we expect

coherent dynamics to approximately describe any particles with motional detunings δ^{m} that satisfy

$$|\Omega| < |\delta^{\mathrm{m}}| < \alpha \log(2)/2\gamma. \tag{5.41}$$

We will call this the "ideal" region, as most particles that are initialized in this region are eventually trapped and cooled. As seen in Fig. 5.5, particles in the ideal region, which are labeled (i), follow trajectories that generally exhibit an effective "attraction" to the lines $\delta^{\mathrm{m}} = \pm|\Omega|$. It should be noted that the black arrows display the direction of the flow of time during the simulations.

5.6.3.2 Dynamics near $\delta^{\mathrm{m}} = 0$

In this regime, the Zeeman and Doppler shifts are comparable in magnitude but opposite in sign. Thus, the resonances with each laser are no longer time resolved, resulting in population of both excited states and therefore frequent spontaneous emission events. Nevertheless, we observe an average attraction of the trajectories to the line $\delta^{\mathrm{m}} = 0$ in phase space. This attraction paired with ballistic expansion causes the particle to eventually drift toward the phase space origin in a similar manner to the dynamics within a traditional MOT. After many cycles, the system equilibrates about the phase space origin, as discussed in Section 5.7.

5.6.3.3 Dynamics outside the ideal region

The condition $|\delta^{\mathrm{m}}| < \Delta_s/2$ is necessary to ensure that the particle resonates with both lasers at some point during the sweep. Obviously, particles outside of this regime will undergo purely ballistic expansion, as seen by the trajectories labeled (ii) at later times in Fig. 5.5.

If a particle is in the region defined by $\alpha \log(2)/2\gamma < |\delta^{\mathrm{m}}| < \Delta_s/2$, there is a significant chance of spontaneous emission before resonating with the second laser in a sweep. If the spontaneous emission does occur, the particle will absorb a photon when it resonates with the second laser, directing it even further from the ideal region. In this sense, the particle is heated and will eventually escape the trap, as evidenced by the trajectories labeled (ii) at earlier times in Fig. 5.5. The most extreme case of heating occurs when $|\delta^{\mathrm{m}}| \approx \Delta_s/2$; here, the absorption-emission sequence becomes

centered at the extremes of the sawtooth wave instead of at the center, leading to coherent transfer of the particle away from the phase space origin.

Assembling these considerations together, we arrive at the following complete picture of the phase space regions, labeled in Fig. 5.5:

$$
\begin{aligned}
|\delta^{\mathrm{m}}| &\leq |\Omega| && \text{(overlap, scattering)} \\
|\Omega| < |\delta^{\mathrm{m}}| &< \frac{\alpha \log(2)}{2\gamma} && \text{(ideal coherent dynamics)} \\
\frac{\alpha \log(2)}{2\gamma} < |\delta^{\mathrm{m}}| &< \frac{\Delta_s}{2} && \text{(heating)} \\
\frac{\Delta_s}{2} &< |\delta^{\mathrm{m}}| && \text{(ballistic expansion).}
\end{aligned} \tag{5.42}
$$

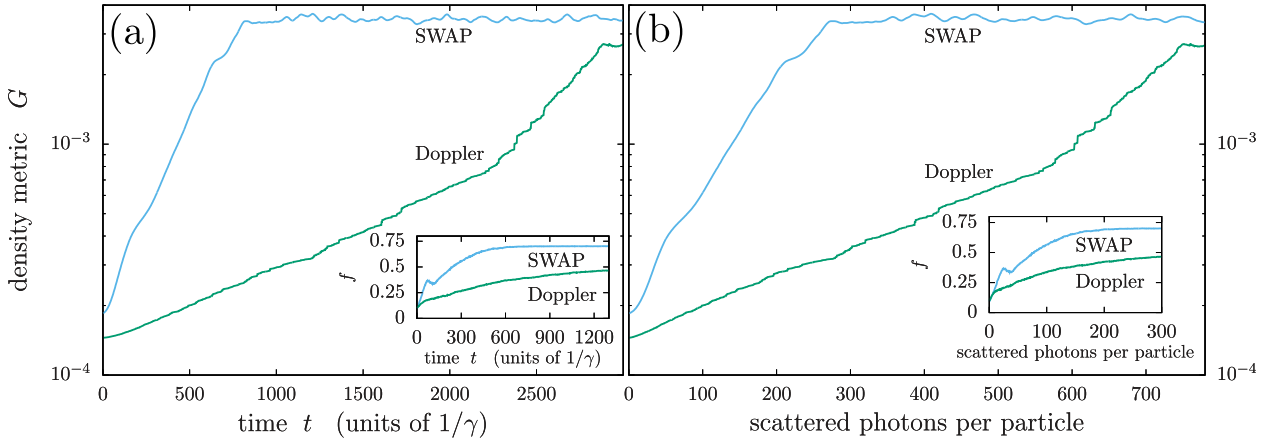

Figure 5.6: Semilog plots of the evolution of the phase space density metric G [see Eq. (5.44)] for the YO system subject to the SWAP MOT and traditional MOT (Doppler). The used SWAP MOT simulation parameters were identical to those in Fig. 5.5. The detunings of the lasers in the traditional MOT simulation were set to $\delta = -\Omega$, and all other parameters were identical to the SWAP MOT simulation. Quantities were averaged over all trajectories that become trapped within the overlap region [see Eq. (5.42)] from $N_{\mathrm{tot}} = 2000$ total trajectories. (a) G vs. time t for all trapped particles. The SWAP MOT equilibrates more quickly than the traditional MOT. Inset: The SWAP MOT captures a higher fraction $f(t)$ of particles. (b) G vs. the average number of spontaneous emissions per particle. Spontaneous emissions of non-trapped particles are not included. The SWAP MOT equilibrates with significantly fewer spontaneous emissions per trapped particle.

In summary, particles that begin in the ideal region are transferred to the overlap region with few scattering events. Once there, the particle frequently scatters photons and the system eventually equilibrates. Any particles that begin outside the ideal region are most likely heated out

of the trap.

5.6.4 Phase space compression

The ultimate signature of a laser cooling method's ability to effectively trap and cool a system is the ability to overcome the limits imposed by Liouville's theorem for Hamiltonian evolution and exhibit compression in terms of occupied phase space volume. One useful metric that can be used to quantify the particle density in phase space is the root-mean-square (rms) interparticle spacing in phase space, l_{rms}. If we label the position of a particle in phase space with the dimensionless vector $\boldsymbol{r} \equiv \{\epsilon, \beta\}$, then l_{rms} is

$$l_{\mathrm{rms}} \equiv \frac{1}{N}\sqrt{\sum_{i>j}^{N} |\boldsymbol{r}_i - \boldsymbol{r}_j|^2}, \tag{5.43}$$

where N is the number of trajectories considered out of the total number N_{tot}. For our purposes, we only need to consider the trajectories that ultimately become trapped within the overlap region. We define a metric G for the particle phase space density as

$$G \equiv 1/l_{\mathrm{rms}}, \tag{5.44}$$

and we label the fraction of trapped particles with $f = N/N_{\mathrm{tot}}$.

In order to gain intuition into the interpretation of G, let us briefly consider its form for a system with a phase space distribution $F(\boldsymbol{r})$ that can be modeled as a product of Gaussian distributions in ϵ and β with standard deviations σ_ϵ and σ_β:

$$F(\boldsymbol{r}) = \frac{N}{2\pi\sigma_\epsilon\sigma_\beta} \exp\left[-\frac{1}{2}\left(\frac{\epsilon^2}{\sigma_\epsilon^2} + \frac{\beta^2}{\sigma_\beta^2}\right)\right]. \tag{5.45}$$

The continuous form of Eq. (5.43) is

$$l_{\mathrm{rms}} = \frac{1}{N}\sqrt{\frac{1}{2}\int dr_1\, dr_2\, F(\boldsymbol{r}_1)F(\boldsymbol{r}_2)|\boldsymbol{r}_1 - \boldsymbol{r}_2|^2}, \tag{5.46}$$

so using Eq. (5.45) in Eq. (5.46) results in

$$G = 1/\sqrt{\sigma_\epsilon^2 + \sigma_\beta^2}. \tag{5.47}$$

Further, let us consider the case when the system is in the Bose-Einstein condensate (BEC) regime. Here, the system would occupy a single volume element of phase space, which corresponds to $\Delta x \Delta p/h = \Delta\epsilon\Delta\beta/2\pi \approx 1$. In the symmetric case $\Delta\epsilon = \Delta\beta$, we find that G is on the order of unity. These results help with interpreting the resulting scale of the calculated values for G in the SWAP MOT, where G will always be considerably below the quantum degenerate value.

Figures 5.6(a) and 5.6(b) show the evolution of G and f for the YO transition introduced in Section 5.6.2 subject to both a traditional MOT and the SWAP MOT as a function of time along with the average number of spontaneous emissions per particle. Only particles that ultimately settle within the overlap region [see Eq. (5.42)] are considered. The insets display the fraction f of particles that are currently within the overlap region. It is evident that both procedures compressed phase space, but the SWAP MOT did so more than three times faster and with roughly a third of the spontaneous emissions required by the traditional MOT for this set of parameters. This result shows that the SWAP MOT can apply higher dissipative forces and remove entropy with a higher photon efficiency, i.e., it removes more energy and momentum per scattered photon than a traditional MOT.

5.6.5 MOT loading

The previous subsection showcases the SWAP MOT's ability to efficiently trap and cool. Here, we demonstrate its ability to coherently translate high momentum states toward zero momentum, which is desirable in, e.g., the loading of molecules from an oven or supersonic nozzle for which a low number of scattered photons is a priority.

Commonly utilized particle loading devices, such as the Zeeman slower, rely on radiation pressure to reduce the particle speed and yield a force that is fundamentally limited by the linewidth of the transition [126]. Consequently, such a process requires roughly one spontaneous photon per absorbed slowing photon. In contrast, the SWAP protocol is fundamentally limited by the rate at which one can can stimulate rapid adiabatic passage. Hence, operating in the regime $\Omega \gg \gamma$ yields significantly higher coherent forces and therefore smaller slowing distances with fewer scattering

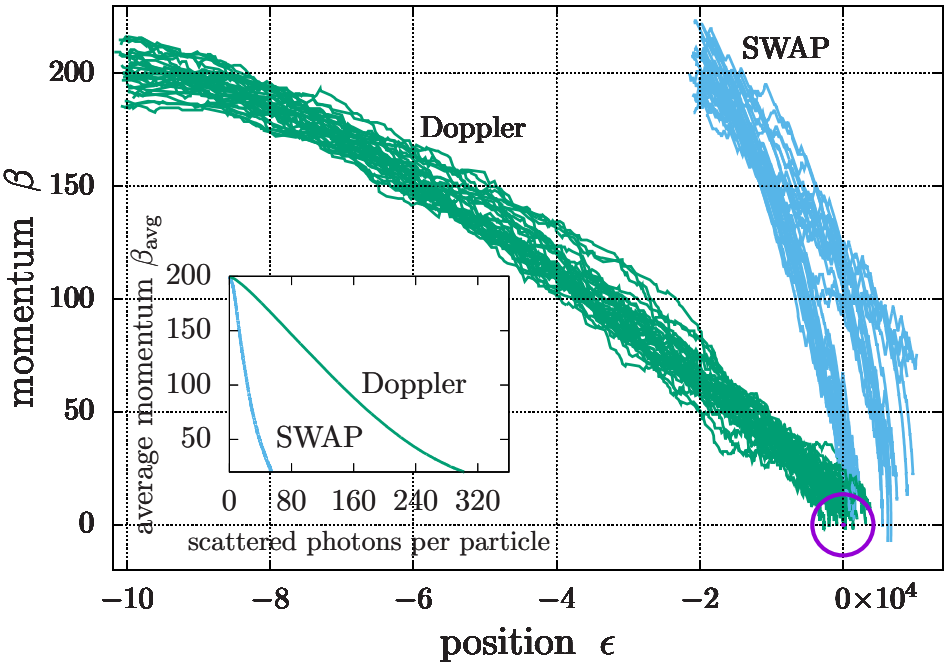

Figure 5.7: Simulated phase space trajectories of particles being loaded into a SWAP MOT and traditional MOT (Doppler). The trajectories generally flow toward the phase space origin, which is labeled by a purple circle. The particles subject to the SWAP MOT experience much higher forces compared to the radiation pressure force intrinsic to the traditional MOT. Common parameters are: $\omega_r = 0.67\gamma$, $\Omega = 60\gamma$, $\beta_0 = 200, \sigma_{\epsilon_0} = 1000, \sigma_{\beta_0} = 10$. SWAP MOT parameters are: $M = 0.012\gamma$, $\Delta_s = 1600\gamma$, $T_s = 1/\gamma$, $t_{\max} = 175/\gamma$, $\epsilon_0 = -2 \cdot 10^4$. Traditional MOT parameters are: $M = 0.0025\gamma$, $\delta = -60\gamma$, $t_{\max} = 1000/\gamma, \epsilon_0 = -10^5$. Inset: The average momentum number β_{avg} vs. the average number of spontaneous emissions per particle. The SWAP MOT is loaded with fewer spontaneous photons and in a shorter distance.

events.

Figure 5.7 shows the results of simulating the slowing of YO on the 5.9 kHz transition using both a traditional MOT and a SWAP MOT. We chose the Rabi frequency $\Omega = 60\gamma$ for both procedures to allow for high coherent forces in the SWAP MOT and rapid absorption in the traditional MOT. The laser detunings in the traditional MOT were set to $\delta = -\Omega$ so that the particles were close to resonance with the counterpropagating laser at the beginning of the simulation. The SWAP magnetic field gradient $M = 0.012\gamma$ was chosen so that the trajectories lay on the border between the overlap and ideal regions for the entire slowing process, which minimized the amount of time the particles spent in the excited states while keeping the resonances sufficiently

separated. It is evident that this procedure applied forces to the particles in the SWAP MOT that were roughly five times larger than the traditional MOT and consequently slowed them in roughly one-fifth of the distance. As shown in the inset of Fig. 5.7, the SWAP procedure produced roughly a fifth of the spontaneous photons required by the traditional MOT in order to reach the region of the phase space origin for this set of parameters. Therefore, the SWAP MOT may potentially be a strong candidate for molecular slowing, as it produces high coherent forces with few spontaneous photons, which may thereby reduce the adverse effect of optical pumping into dark states.

5.7 Equilibrium temperatures and cloud sizes

The simulated phase space diagram shown in Fig. 5.5 and the resulting phase space densities shown in Fig. 5.6 suggest that particles captured in a SWAP MOT eventually equilibrate to a final, fixed phase space distribution. In this section, we describe the associated equilibrium momentum and position distributions by analyzing their dependence on both laser intensity and the ratio ω_r/γ, where the latter quantity characterizes the separation between the external and internal timescales.

The equilibrium momentum and position probability distributions $P(\beta)$ and $P(\epsilon)$ from a YO SWAP MOT simulation are displayed in Figs. 5.8(e) and 5.8(f). The parameters were identical to those in Fig. 5.5, except $\Omega = 60\gamma$ here. Both distributions can approximately be described by a normalized Gaussian function with zero mean, as shown by the fits displayed as blue curves. In this way, we can consider the measured width to the momentum distribution as approximately the standard deviation of a thermal 1D Maxwellian distribution. From the equipartition theorem,

$$\frac{p_{\mathrm{rms}}^2}{2m} = \hbar\omega_r\beta_{\mathrm{rms}}^2 = \frac{1}{2}k_BT, \tag{5.48}$$

thereby defining an effective temperature T. We find this type of fit to be much more accurate for the momentum distribution than is observed for the position distribution. Nevertheless, the points displayed as purple circles in Figs. 5.8(a-d) are extracted by fitting each resulting probability distribution to a Gaussian with zero mean.

Figures 5.8(a) and 5.8(c) display the equilibrium root-mean-square momenta β_{rms} and po-

sitions ϵ_{rms} for various values of Ω/γ using the YO transition introduced in Section 5.6.2. These plots provide information about the effects of the laser intensity I on the equilibrium phase space distribution, since $\Omega/\gamma \propto \sqrt{I}$ [126]. One reason these plots are of interest is because the lowest temperature in other cooling methods is typically achieved in the limit of low saturation, i.e., $\Omega \to 0$ (although in this limit the cooling may take a long time and the trapping effect is reduced), which is not usually experimentally reasonable due to the demands of adiabaticity [Eq. (5.31)] and rapid adiabatic passage [Eq. (5.32)]. The vertical, black dashed line separates the plots into diabatic (left) and adiabatic (right) regimes. We observe that the minimum temperature and cloud size is achieved slightly within the adiabatic region, where particles are efficiently transferred into resonant states with minimal negative effects from power broadening. A similar result for the minimum temperature was previously discovered for SWAP cooling [13, 141].

Figures 5.8(b) and 5.8(d) display the equilibrium root-mean-square momenta β_{rms} and positions ϵ_{rms} for various values of ω_r/γ when $\Omega = 60\gamma$. This ratio is a fundamental property of the cooling transition, so this investigation transcends our focus on the specific YO transition used elsewhere in this work and provides a better understanding of the SWAP protocol's efficacy on an arbitrary transition. As seen in Fig. 5.8(b), β_{rms} decreases as ω_r/γ increases, which provides direct evidence for our claim that SWAP procedures applied to narrow linewidth transitions result in lower temperatures T. On the other hand, we observe an increase in cloud size in Fig. 5.8(d).

In the deeply adiabatic regime, we observe that the root-mean-square values scale as

$$\beta_{\text{rms}} \propto \sqrt{\frac{\Omega}{\omega_r}}; \qquad \epsilon_{\text{rms}} \propto \Omega. \tag{5.49}$$

Numerical fits according to the equation

$$\beta_{\text{rms}} = \sqrt{\frac{\Omega}{C\omega_r}} \tag{5.50}$$

are displayed as green dot-dashed curves in Figs. 5.8(a) and 5.8(b). Figure 5.8(c) is numerically fit to the equation

$$\epsilon_{\text{rms}} = C\Omega. \tag{5.51}$$

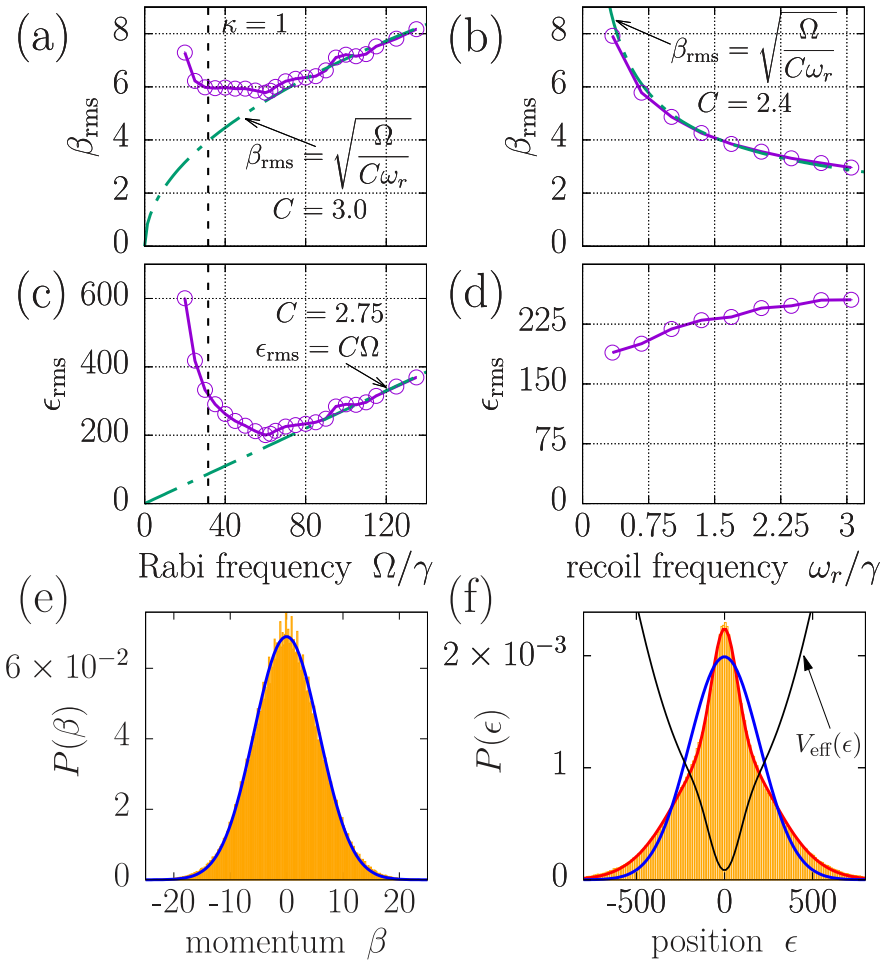

Figure 5.8: (a-d): Equilibrium root mean square momenta $\beta_{\rm rms}$ and positions $\epsilon_{\rm rms}$ as a function of Rabi frequency Ω [(a) and (c)] and recoil frequency ω_r [(b) and (d)], both in units of the linewidth γ. The vertical, dotted black lines in subplots (a) and (c) display the Rabi frequency for which the adiabaticity parameter $\kappa = 1$ [see Eq. (5.31)]. Numerical fits to plots (a-c), which are displayed as green dot-dashed curves, are discussed in the text. Common parameters are: $M = 0.05\gamma$, $\Delta_s = 2000\gamma$, and $T_s = 2/\gamma$. The recoil frequency in plots (a), (c), (e) and (f) is $\omega_r = 0.67\gamma$, and the Rabi frequency in plots (b), (d), (e) and (f) is $\Omega = 60\gamma$. Each point (purple circles) was averaged over data taken from 800 independent trajectories, each being sampled once per sweep over 1,500 sweeps. (e-f): Equilibrium momentum and position probability distributions $P(\beta)$ and $P(\epsilon)$. Gaussian fits (blue curves), which were used to extract root-mean-square values, are discussed further in the text. Histogram data was taken from 800 independent trajectories, each being sampled once per sweep over 1,500 sweeps. In (f), the black curve is the effective potential $V_{\rm eff}(\epsilon)$ [Eq. (5.59)] that generates the non-Gaussian position distribution [Eq. (5.54), red curve].

The scaling constants C for each independent fit are displayed within each plot. Combining Eq. (5.48) with the observed trend in Eq. (5.49), we find that

$$k_B T \propto \hbar\Omega, \tag{5.52}$$

which agrees with previous studies of SWAP cooling (see Ref. [13] and Chapter 3).

In a traditional MOT, the equilibrium temperature T_{trad} scales with the linewidth γ [126]:

$$k_B T_{\text{trad}} \propto \hbar\gamma. \tag{5.53}$$

providing this is larger than the recoil temperature. Comparing this to Eq. (5.52), we find that the temperature reached in a SWAP MOT must be larger since $\Omega \gg \gamma$. As was discussed in the original SWAP cooling papers [13, 141], we again reach the conclusion that the utility of the SWAP MOT is not its low temperatures, but its ability to apply larger forces and reach equilibrium faster and with fewer scattered photons. This is especially applicable to systems with narrow line transitions, i.e., small γ.

5.7.1 SWAP MOT effective potential

As shown by the red curve in Fig. 5.8(f), the position distribution is actually more accurately described by the sum of two Gaussians of different widths:

$$X(x) \approx \frac{w}{\sqrt{2\pi}\sigma_1} \exp\left(-\frac{x^2}{2\sigma_1^2}\right) + \frac{(1-w)}{\sqrt{2\pi}\sigma_2} \exp\left(-\frac{x^2}{2\sigma_2^2}\right), \tag{5.54}$$

where $0 \leq w \leq 1$ describes the relative weight of the two Gaussians, and σ_1 and σ_2 are the widths of the two distributions. Note that we have normalized the distribution for simplicity. This suggests that the effective potential $V_{\text{eff}}(x)$ describing both the conservative and dissipative effects of the SWAP MOT has an exaggerated dip near $x = 0$, similar to that of a dimple trap [188]. Here we derive an effective potential $V_{\text{eff}}(x)$ from the resulting equilibrium position distribution, which we include as a black curve in Fig. 5.8(f).

In a state of thermodynamic equilibrium, the classical phase space distribution ρ of a system is given by [168]

$$\rho(x,p) = Z^{-1} e^{-H(x,p)/k_B T}, \tag{5.55}$$

where Z is the partition function and H is the system Hamiltonian. If we consider a system with a Hamiltonian of the form

$$H(x,p) = \frac{p^2}{2m} + V_{\text{eff}}(x), \tag{5.56}$$

where $V_{\text{eff}}(x)$ is an effective potential, then the position distribution $X(x)$ satisfies

$$X(x) \equiv \int \rho(x,p)\,dp \propto e^{-V_{\text{eff}}(x)/k_B T}. \tag{5.57}$$

Equivalently,

$$V_{\text{eff}}(x) \propto -\log X(x). \tag{5.58}$$

In the case of the SWAP MOT, we find that

$$V_{\text{eff}}(x) \propto -\log\left[\frac{w}{\sqrt{2\pi}\sigma_1}\exp\left(-\frac{x^2}{2\sigma_1^2}\right) + \frac{(1-w)}{\sqrt{2\pi}\sigma_2}\exp\left(-\frac{x^2}{2\sigma_2^2}\right)\right] \tag{5.59}$$

by using Eq (5.54). We plot this effective potential against the simulated position space distribution arising in the SWAP MOT in Fig. 5.8(f).

5.8 Conclusion

We have proposed a novel cooling, trapping, and slowing scheme for neutral particles, which we have termed the SWAP MOT. We have outlined an experimental protocol and developed a simple and efficient semiclassical model and simulation that demonstrates its ability to generate phase space compression. We have also specified a protocol for determining appropriate experimental parameters for application to an arbitrary transition. Our results demonstrate the SWAP MOT's ability to generate large coherent and dissipative forces with fewer scattered photons than traditional MOTs. We provided a discussion of the resulting equilibrium 1D temperature and cloud size scaling properties with Rabi and recoil frequencies and compared the results to those found from our theoretical model of the traditional MOT.

Aside from eventual experimental implementation, there are several topics that could be studied in future work. We have not explicitly simulated 3D dynamics, but we conjecture that applying the SWAP MOT protocol to each dimension successively in time is a viable option [171]. Also, the incorporation of shortcuts to adiabaticity could speed up the protocol with a low energetic cost [75]. We consider one such shortcut to adiabaticity approach in the next chapter. Moreover, there are a number of additions to the simulation that would be required to more accurately

capture the dynamics in the quantum regime (aside from developing a computationally efficient algorithm to simulate the fully quantum model developed in this work), such as spontaneous photon reabsorption, particle collisions, and system loss to states that are not resonant with the cooling laser frequencies.

Furthermore, we identify that the stimulated emission process can be realized in our model via any operation that reverses the sign of the magnetic dipole potential energy

$$\hat{H}_B(\hat{x}) = -\hat{\boldsymbol{\mu}} \cdot \hat{\boldsymbol{B}}(\hat{x}) \tag{5.60}$$

at the middle of the sweep, where

$$\hat{\boldsymbol{\mu}} = -\frac{g_J \mu_\mathrm{B}}{\hbar} \hat{\boldsymbol{J}} \tag{5.61}$$

is the magnetic dipole moment of the particle and $\hat{\boldsymbol{J}}$ is the total electronic angular momentum. We incorporated the sign flip by magnetic field switching, but this is technically difficult in an experimental setting and it is fundamentally impossible to perfectly, diabatically switch the magnetic field direction. Other potentially more experimentally viable options are applying π-pulses at the middle of each sweep in order to transfer the population between the excited Zeeman sublevels, thereby flipping the sign of $\hat{\boldsymbol{J}}$, or optically pumping into a nearby hyperfine manifold with a spin g-factor of opposite sign. Alternatively, it is possible that a vertically-shifted, sinusoidal magnetic field could also achieve similar dynamics.

Chapter 6

Speeding up particle slowing using shortcuts to adiabaticity

The cooling and trapping mechanisms discussed in Chapters 3-5 inherently rely on the dynamics to be adiabatic, and can therefore take a potentially unfeasible amount of time. In this chapter, we propose a method that relaxes the adiabatic condition by applying laser pulses that achieve the same state transfer effects in a shorter amount of time. We focus on the simpler case of particle slowing, i.e., reducing its kinetic energy but not necessarily its temperature, although we anticipate that it can be applied within cooling and trapping protocols. This work resulted in a publication in Physical Review A (Ref. [14]) in October 2020.

More specifically, this method can potentially generate large forces without the associated momentum diffusion that results from the random directions of spontaneously scattered photons. We consider time-resolved laser pulses with periodically modified detunings that address an ultranarrow electronic transition to reduce the particle momentum through repeated absorption and stimulated emission cycles. We implement a shortcut to adiabaticity approach that is based on Lewis-Riesenfeld invariant theory. This affords our scheme the advantages of adiabatic transfer, where there can be an intrinsic insensitivity to the precise strength and detuning characteristics of the applied field, with the advantages of rapid transfer that is necessary for obtaining a short slowing distance. For typical parameters of a thermal oven source that generates a particle beam with a central velocity on the order of meters per second, this could result in slowing the particles to near stationary in less than a millimeter. We compare the slowing scheme to widely-implemented slowing techniques that rely on radiation pressure forces and show the advantages that potentially

arise when the excited state decay rate is small. Thus, this scheme is a particularly promising candidate to slow narrow-linewidth systems that lack closed cycling transitions, such as occurs in certain molecules.

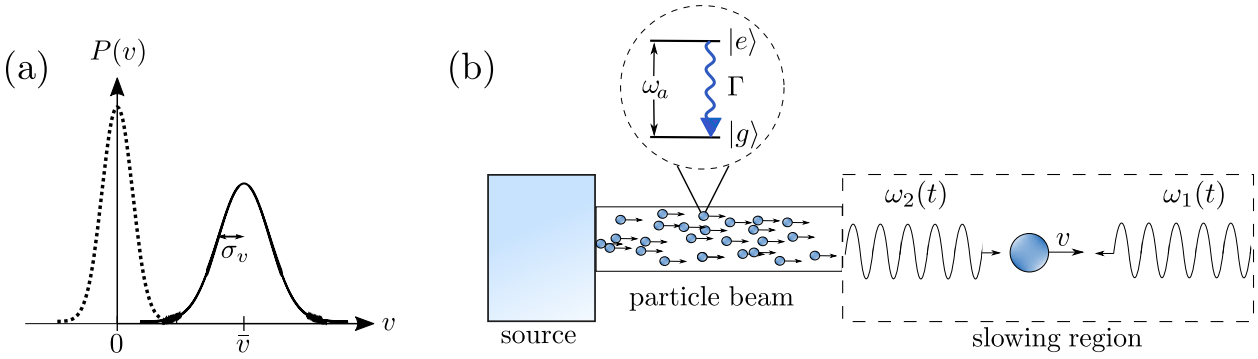

Figure 6.1: (a) Schematic of the normalized velocity distributions $P(v)$ of the particle beam before (solid) and after (dashed) the slowing process. We characterize the initial distribution by a Gaussian function with a standard deviation σ_v and mean velocity $\bar{v}$. (b) Particles exit an atom or molecule source and are collimated into the slowing region. The spatial setup of the sequentially-pulsed counterpropagating lasers, which have time-dependent frequencies $\omega_1(t)$ and $\omega_2(t)$, and a sample particle with velocity v in the laboratory frame are displayed in the slowing region. The circular inset shows the two-level internal structure of each particle.

6.1 Introduction

For decades, laser cooling atoms and molecules to near absolute zero has been at the forefront of research into the interactions of light and matter [41, 46, 123, 149]. Ultracold ensembles provide testbeds for exploring fundamental physics [164], can create low-temperature superfluids such as Bose-Einstein and fermionic condensates [9, 157], and can be used as platforms for quantum simulators [94]. Since atom and molecule sources typically produce particles with high velocities, it is usually necessary to first perform a precursor stage that removes a substantial fraction of the kinetic energy associated with the random thermal motion, as shown in Figure 6.1(a). A specific example is sodium atoms produced in an oven at thermal velocities of a few hundred meters per second that need to be slowed to a few meters per second before being transferred into a magnetic and/or optical trap [150, 160, 193]. An assortment of particle slowing methods have been developed for this precursor stage, including Stark and Zeeman decelerators [7, 81, 138, 148], centrifuge decelerators

[40], electrostatic trapping methods [20], frequency-chirped laser slowing [181], white light slowing [49, 79], and angled slowing [112], among others. Once slowed, the particles may possess sufficiently low kinetic energy that they can be efficiently loaded into a finite-depth electromagnetic trap [126], such as a magneto-optical trap (MOT), and then be cooled using light [176, 183], cooled through evaporation that redistributes energy through two-body collisions [177], or sympathetically cooled with another species [64].

The ability to produce a large number of ultracold particles is made difficult by practical shortcomings of slowing methods, such as a large slowing distance that requires significant physical space, or substantial spread in the final velocities of the particles. Furthermore, the main hindrance to slowing particles that lack closed cycling transitions is that there may be leakage of population to dark electronic states that are not coupled with the fields that perform the laser cooling and slowing, resulting in the loss of the particle from the system. Even if this does not occur, spontaneous emission of many photons creates momentum diffusion due to the random emission direction, and this results in heating and a finite limit on the achievable temperatures. These issues make methods that increase slowing forces and minimize the number of scattering events through enhanced control of tailored coherent dynamics, such as sawtooth-wave adiabatic passage (SWAP) cooling [12, 13, 74, 137, 141, 171], the Allen-Eberly scheme [8], stimulated Raman adiabatic passage (STIRAP), the adiabatic passage force, and the bichromatic force [33, 125, 129, 172, 173, 187] enticing candidates to consider for particle slowing. However, one concern is that in order to satisfy an intrinsic adiabaticity condition, the time evolution should typically be slow and this could result in a long stopping time and associated large stopping distance.

In order to speed up adiabatic processes while still achieving substantial population transfer, there has been a growing interest in so-called "shortcuts to adiabaticity" [75], i.e., processes that are able to transform systems from an initial quantum state to the same final quantum state as an ideal adiabatic process but in much less time. In this chapter, we present a fast, simple, and robust particle slowing scheme that employs one such shortcut method: inverse engineering based on Lewis-Riesenfeld invariants (LRI) [37, 38, 39, 76, 103, 105]. The slowing scheme involves driving sped-up

transitions from a stable ground state to an excited state and back using counter-propagating, pulsed lasers with intensity and detuning profiles prescribed by the LRI shortcut method, as shown schematically in Figure 6.1(b). By applying this protocol many times, the particle can in principle be subject to the impulse of many photon momenta without emitting spontaneous photons. In Section 6.2, we further motivate the use of our slowing scheme. In Section 6.3, we outline the general theory of LRI-based inverse engineering. In Section 6.4, we present our theoretical model and derive the laser intensity and detuning profiles that result from the LRI shortcut method. In Section 6.5, we study the resulting classical forces, slowing times, and slowing distances, demonstrating that we are able to generate higher forces than what is achieved with radiation pressure as employed in methods such as Zeeman slowing. In Section 6.6, we simulate particle slowing dynamics by applying our method to various atomic and molecular species with narrow linewidth transitions. In Section 6.5, we study our slowing scheme's robustness to various systematic errors that one may encounter when implementing the protocol in an experimental setting, and compare these results to slowing with π-pulse transitions and SWAP slowing.

6.2 Motivation for the speed-up protocol

The concept of coherent transfer between quantum states is a ubiquitous component of most quantum control techniques. The most basic way to achieve such a transfer between two electronic quantum states is to apply a resonant, coherent light pulse for a time $t = \pi/\Omega$, where Ω is the Rabi frequency. While this Rabi-flopping "π-pulse" method completely transfers population, at least in principle, it is not robust to small errors in Ω, the frequency ω of the light source, or coupling to other states outside of the two-level manifold. A further detrimental effect arises when applying this method to quantum particles with motion due to the associated Doppler shift kv of the laser light experienced by the particle, where v is the velocity of the particle as measured in the laboratory frame and $k = 2\pi/\lambda$ is the wavenumber of the transition with wavelength λ. This shifts the laser light away from resonance with the particle, which changes both the rate and maximum amount of population transfer between the states. This issue can be remedied by tuning the laser

light back into resonance with the particle, but this is of limited utility when the goal is to transfer population in many particles that possess a distribution of velocities.

A robust solution to these problems is to chirp the laser frequency through the resonance, as was shown by Landau and Zener in their theory of adiabatic passage [194]. However, such a method is limited in the sense that the laser chirping must be adiabatic, i.e., sufficiently slow compared to the strength of the coupling Ω. More specifically, they showed that the population of state $|2\rangle$, P_2, after the laser is chirped from a detuning of minus infinity to positive infinity, is

$$P_2 = 1 - \exp\left(-\frac{\pi}{2}\frac{\Omega^2}{\alpha}\right), \tag{6.1}$$

where α is the frequency chirping rate in rad/s^2. Thus, if the experiment is operated in the limit $\Omega^2 \gg \alpha$, then $P_2 \approx 1$, regardless of the particle's initial velocity, a phenomenon known as adiabatic passage. The requirement of infinite time can be relaxed if the laser frequency is adiabatically chirped over a frequency range larger than 2Ω in the moving frame of every particle, as can be seen in a dressed state picture. The velocity-independent feature of adiabatic passage motivated the development of SWAP cooling [12, 13, 74, 137, 141, 171], which utilizes periodic frequency chirps to coherently transfer a particle between quantum states in such a way that its momentum can be significantly reduced. A natural extension of SWAP cooling is to employ its ability to apply large coherent forces in the process of particle slowing. However, there are several issues that arise in this venture. The obvious issue is the requirement of adiabaticity, which limits the timescale for population transfer and can lead to undesirably large slowing distances and times. Another potentially detrimental problem that arises from this slow evolution is the particle's tendency to relax from the quantum state with higher energy to the quantum state with lower energy through the process of spontaneous emission, which would disturb the coherent slowing process and introduce unwanted momentum diffusion. This motivates transferring as quickly as possible, and thereby satisfying the requirements, i.e., $\Omega \gg \Gamma$, for adiabatic *rapid* passage [27]. Furthermore, in the neighborhood of the resonance, there are significant oscillations in the populations that result from the precession of the Bloch vector as it travels along the Bloch sphere [67, 185], which can

complicate the amount of population transfer. A detailed investigation of these oscillations and other important timescales in Landau-Zener transition theory is presented in [185].

As we will show, our derivation of an alternative scheme for coherent transfer, by use of LRI theory, ameliorates every issue we have discussed thus far. We drive a different path along the Bloch sphere (see Section 6.4.4) in order to speed up the transfer time and remove the high frequency population oscillations while utilizing the same amount of laser power. But perhaps the most appealing feature of our scheme is the ability to **exactly** transfer population between quantum states in a finite time, which in principle permits high-fidelity slowing of a particle with arbitrarily high momentum to near rest.

6.3 Lewis-Riesenfeld Invariant-based inverse engineering

In this section, we present a brief overview of the LRI shortcut method. This approach allows us to derive specific laser intensity and detuning profiles that can be used to generate fast dynamics with the same results as adiabatic processes.

A dynamical invariant $\hat{I}(t)$ is a Hermitian operator with a time-independent expectation value, i.e.,

$$\langle \hat{I} \rangle = \langle \Psi(t) | \, \hat{I}(t) \, | \Psi(t) \rangle = \text{const}, \tag{6.2}$$

where $|\Psi(t)\rangle$ is the state vector evolved by the Hamiltonian $\hat{H}(t)$. It can be shown that the states $|\psi_n(t)\rangle$, defined by a gauge transformation

$$|\psi_n(t)\rangle = e^{i\alpha_n(t)} \, |\phi_n(t)\rangle \tag{6.3}$$

of the eigenbasis $|\phi_n(t)\rangle$ of $\hat{I}(t)$, are each a solution to the time-dependent Schrödinger equation. In Eq. (6.3), the "Lewis-Riesenfeld phases" $\alpha_n(t)$ are defined as

$$\alpha_n(t) = \frac{1}{\hbar} \int_{t_0}^{t} \langle \phi_n(t') | \, i\hbar \frac{\partial}{\partial t'} - \hat{H}(t') \, | \phi_n(t') \rangle \, dt', \tag{6.4}$$

where t_0 is some initial reference time and $\hbar$ is the reduced Planck constant. It follows that a

general solution $|\Psi\rangle$ to the Schrödinger equation can be decomposed as

$$|\Psi(t)\rangle = \sum_n c_n |\psi_n(t)\rangle = \sum_n c_n e^{i\alpha_n(t)} |\phi_n(t)\rangle , \tag{6.5}$$

where c_n are time-independent amplitudes [105]. From Eq. (6.5), the unitary time-evolution operator in the invariant basis is

$$\hat{U}(t) = \sum_n e^{i\alpha_n(t)} |\phi_n(t)\rangle \langle\phi_n(t_0)| , \tag{6.6}$$

which can be used to solve for the Hamiltonian:

$$\hat{H}(t) = i\hbar \frac{\partial \hat{U}(t)}{\partial t} \hat{U}^\dagger(t). \tag{6.7}$$

These results indicate numerous benefits for this method. In particular, if $\hat{H}(t)$ and $\hat{I}(t)$ are designed to commute at t_0 and some final time t_f, i.e.,

$$\left[\hat{H}(t_0), \hat{I}(t_0)\right] = \left[\hat{H}(t_f), \hat{I}(t_f)\right] = 0, \tag{6.8}$$

then the final state $|\Psi(t_f)\rangle$ will maintain the initial populations for each eigenstate [75], and we therefore recover the results of an adiabatic process without the requirement of slow time-evolution. Also, by combining Eqns. (6.6) and (6.7), we can explicitly inverse-engineer the Hamiltonian in the invariant basis:

$$\hat{H}(t) = -\hbar \sum_n \dot{\alpha}_n |\phi_n(t)\rangle \langle\phi_n(t)| + i\hbar \sum_n |\partial_t \phi_n(t)\rangle \langle\phi_n(t)| . \tag{6.9}$$

Eqns. (6.7)-(6.9) define what is meant by invariant-based inverse engineering. Equating the Hamiltonian in the invariant basis to the original Hamiltonian creates a map between the physical parameters and the auxiliary parameters that define the invariant operator. In Section 6.4.3, We will use this procedure to derive the laser intensity and detuning profiles for each single-photon transition in our slowing scheme.

6.4 Model

We consider the experimental setup depicted in Fig. 6.1(b). As shown in the circular inset, we consider each particle to possess two internal electronic states labeled $|g\rangle$ and $|e\rangle$ with an energy

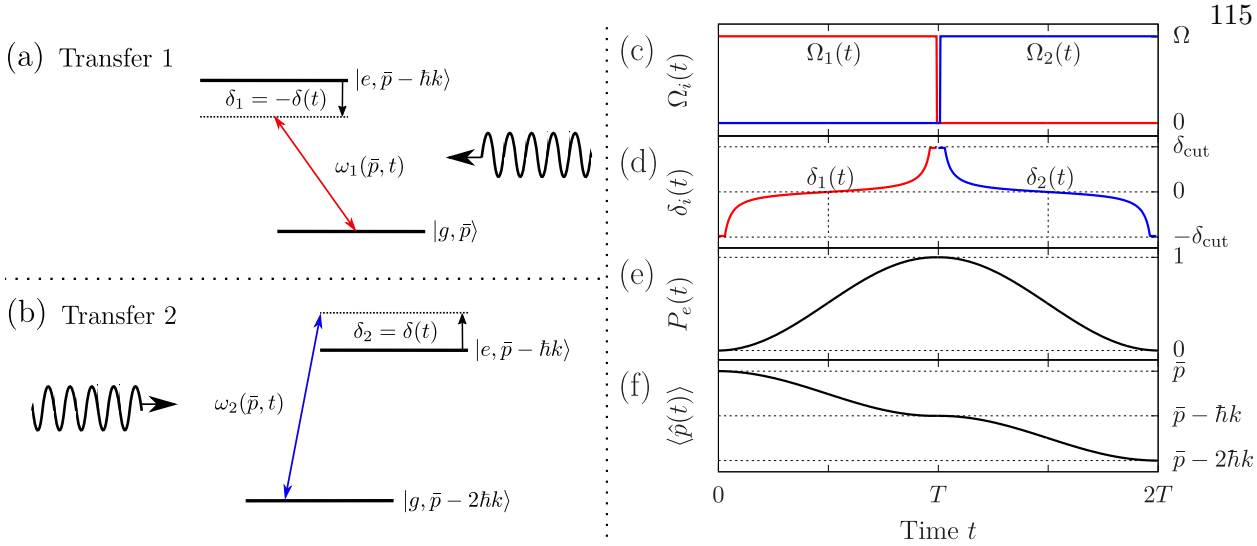

Figure 6.2: **Left**: frequency diagram of an isolated subset of states in the lab frame. The laser frequencies $\omega_i(\bar{p}, t)$ [see Eqns. (6.10)] are dynamically updated according to the solution derived from the Lewis-Riesenfeld invariant shortcut method to promote quick, coherent transfer from (a) $|g, \bar{p}\rangle$ to $|e, \bar{p} - \hbar k\rangle$, followed by (b) $|e, \bar{p} - \hbar k\rangle$ to $|g, \bar{p} - 2\hbar k\rangle$. **Right**: experimental parameters and particle dynamics over a $|\bar{p}\rangle \to |\bar{p} - 2\hbar k\rangle$ sequence of period $2T$. (c) Square-pulse Rabi frequency profiles $\Omega_1(t)$ (red) and $\Omega_2(t)$ (blue) with amplitude Ω [see Eq. (6.37)]. (d) Lewis-Riesenfeld detuning profile $\delta(t)$ [see Eq. (6.38)] with cutoff frequency $\pm\delta_{\text{cut}}$ [see Eq. (6.51)] for each laser. (e) Ideal excited state fraction P_e dynamics. (f) Ideal average momentum $\langle \hat{p} \rangle$ dynamics. Parameters are: $T = 0.032/\omega_r$, $\Omega = 100\omega_r$, $\delta_{\text{cut}} = 250\omega_r$, $\Gamma = 0$, $\bar{p} = 100\hbar k$, and $\beta = 0.85\,\pi/2$.

separation of $\hbar\omega_a$, where ω_a is a frequency assumed to be in the optical domain. The excited state $|e\rangle$ can decay to the ground state $|g\rangle$ at a rate given by the natural linewidth Γ. We track motion along one dimension, for which the particle has position and momentum operators $\hat{z}$ and $\hat{p}$. A thermal beam of particles exits an atom or molecule source (e.g., an oven) at a high average velocity $\bar{v}$ and potentially large velocity spread σ_v. The goal is to quickly remove kinetic energy from the particles such that an appreciable fraction of the final distribution is centered on zero velocity [see Fig. 6.1(a)]. In order to achieve this goal, the particle beam sequentially interacts with pulsed slowing lasers aligned parallel to the beam axis upon entering the slowing region. The essential dynamics are displayed in Fig. 6.2 and are as follows: The counterpropagating laser (laser 1) is switched on, and the particle absorbs a photon and transits to $|e\rangle$. Then, laser 1 is switched off as the copropagating laser (laser 2) is switched on, and the particle emits a photon by stimulated emission, transitioning back to $|g\rangle$. By conservation of momentum, the particle has experienced

an impulse of $2\hbar k$ by the end of the sequence. By repeating many times, we can remove many photon momenta from the particle without the emission of spontaneous photons, contingent that the operation occurs quickly compared to any decoherence processes.

We set the Rabi frequency of each laser $\Omega_i(t)$ (with $i = 1, 2$) to follow a square pulse temporal profile. The peak value Ω [see Fig. 6.2(c)] will be derived from the LRI shortcut method. This choice of waveform relaxes the requirement of exactly aligning the centers of periodic Rabi frequency and laser detuning profiles in time as is needed in other protocols [129, 167, 173], and thus makes the process more robust. We parameterize the instantaneous frequencies $\omega_1(t)$ and $\omega_2(t)$ of each laser field in the form

$$\begin{aligned} \omega_1(\bar{p}, t) &= \omega_a - \delta(t) - k\bar{v} + \omega_r \\ \omega_2(\bar{p}, t) &= \omega_a + \delta(t) + k\bar{v} - 3\omega_r, \end{aligned} \tag{6.10}$$

so that, after accounting for the mean particle velocity $\bar{v} = \bar{p}/m$, each laser is resonant with the transitions displayed in Fig. 6.2(a) and Fig. 6.2(b) when the detuning $\delta(t)$ is zero. We will derive an explicit form for $\delta(t)$ from the LRI shortcut method. Here, $\omega_r \equiv \hbar k^2/2m$ is the recoil frequency of the transition, i.e. $\hbar\omega_r$ is the kinetic energy obtained by an atom at rest from the absorption of a single photon, and m is the particle mass. Also, we have made the typical approximation that the wavenumber $k_i(t)$ of each laser is equal to the constant k at all times, even though the frequency is varying. It should be pointed out that although we have chosen specific signs for $\delta(t)$ in each laser frequency $\omega_i(\bar{p}, t)$ [see Eq. (6.10)], these are not the only conventions that can be employed to result in slowing.

6.4.1 System dynamics

We refer the reader to Sections 2.1 and 2.2 for general details on modeling light-matter interactions. When applied to a system with momentum $\bar{p} = m\bar{v}$, the Hamiltonian takes the general form

$$\hat{H}(\bar{p}, t) = \hat{H}_{\text{self}} + \hat{H}_{\text{int}}(\bar{p}, t), \tag{6.11}$$

where

$$\hat{H}_{\text{self}} = \frac{\hat{p}^2}{2m} + \frac{\hbar\omega_a}{2}\hat{\sigma}^z \tag{6.12}$$

is the particle's free evolution Hamiltonian. The quantity $\hat{\sigma}^z \equiv |e\rangle\langle e| - |g\rangle\langle g|$ is the usual Pauli spin matrix. Under the dipole and rotating wave approximations, the particle-field interaction Hamiltonian $\hat{H}_{\text{int}}(\bar{p}, t)$ in the Schrödinger picture is given by

$$\hat{H}_{\text{int}}(\bar{p}, t) = \frac{\hbar}{2}\hat{\sigma}^-\Big[\Omega_1(t)e^{i[k\hat{z}+\eta_1(\bar{p},t)]} + \Omega_2(t)e^{-i[k\hat{z}-\eta_2(\bar{p},t)]}\Big] + \text{h.c.} \tag{6.13}$$

where $\hat{\sigma}^- \equiv |g\rangle\langle e|$ is the lowering operator. The quantity $\eta_i(\bar{p}, t)$ is the accumulated phase from an initial time t_0 for each laser field [see Eq. (6.10)]:

$$\eta_i(\bar{p}, t) \equiv \int_{t_0}^{t} \omega_i(\bar{p}, t')dt'. \tag{6.14}$$

In order to capture the relevant physics in the first half of the sequence, we omit the second term in Eq. (6.13) (since laser 2 is off) and transform into the interaction picture defined by the Hamiltonian

$$\hat{H}_0(t) = \frac{\hat{p}^2}{2m} + \frac{\hbar}{2}\left[\omega_a - \delta(t)\right]\hat{\sigma}^z. \tag{6.15}$$

The resulting interaction picture Hamiltonian $\hat{H}_1(\bar{p}, t)$ is

$$\hat{H}_1(\bar{p}, t) = \frac{\hbar\delta(t)}{2}\hat{\sigma}^z + \frac{\hbar\Omega_1(t)}{2}\Big(\hat{\sigma}^- \exp\left(i\left[k\hat{z} + k(\hat{v} - \bar{v})t + \omega_r t\right]\right) + \text{h.c.}\Big), \tag{6.16}$$

where $\hat{v} = \hat{p}/m$ is the velocity operator. The interaction picture Hamiltonian for the second half $\hat{H}_2(\bar{p}, t)$ is found by the substitutions $1 \to 2$, $\delta(t) \to -\delta(t)$, $k \to -k$, and $\omega_r \to -3\omega_r$. After the complete evolution with $\hat{H}_1(\bar{p}, t)$ followed by $\hat{H}_2(\bar{p}, t)$, the momentum $\bar{p}$ is updated to $\bar{p} - 2\hbar k$ for the laser detunings [i.e., see Eq. (6.10)] under the assumption that the particle momentum has been changed accordingly, and the process is repeated.

We incorporate the effects of incoherent dynamics due to spontaneous emission and its associated recoil by evolving the density matrix operator $\hat{\rho}$ of the system under the quantum master equation,

$$\frac{d\hat{\rho}}{dt} = \frac{1}{i\hbar}\left[\hat{H}, \hat{\rho}\right] + \hat{\mathcal{L}}\hat{\rho}, \tag{6.17}$$

where the Lindblad superoperator $\hat{\mathcal{L}}$ is

$$\hat{\mathcal{L}}\hat{\rho} = \Gamma\left(\frac{1}{5}e^{ik\hat{z}}\hat{\sigma}^{-}\hat{\rho}\hat{\sigma}^{+}e^{-ik\hat{z}} + \frac{1}{5}e^{-ik\hat{z}}\hat{\sigma}^{-}\hat{\rho}\hat{\sigma}^{+}e^{ik\hat{z}} + \frac{3}{5}\hat{\sigma}^{-}\hat{\rho}\hat{\sigma}^{+} - \frac{1}{2}\left\{\hat{\sigma}^{+}\hat{\sigma}^{-}, \hat{\rho}\right\}\right). \tag{6.18}$$

Here, Γ is the optical transition linewidth (we reserve the symbol γ for an auxiliary variable), and, for convenience, we have approximated the continuous dipole radiation pattern as allowing only the three discrete recoil possibilities that correspond to whole intervals of photon quanta. For states $|e\rangle$ and $|g\rangle$ coupled by a circularly-polarized standing wave, the correct coarse discretization of the radiation pattern yields possible impulses of Δp of $-\hbar k, 0$, and $\hbar k$ along the slowing axis with associated probabilities of $\frac{1}{5}, \frac{3}{5}$, and $\frac{1}{5}$, respectively. We refer the reader to Ref. [135] and Section 2.2.3 for more details on the dicretization procedure.

6.4.2 Eigensystem in a momentum subspace

Our next task is to find appropriate forms for the Rabi frequencies $\Omega_i(t)$ and detuning $\delta(t)$ by following the shortcut protocol. In order to do this, we will perform analytical calculations for transfer 1 in a small, isolated subset $W(\bar{p})$ of the full composite Hilbert space:

$$W(\bar{p}) = \{|g, \bar{p}\rangle, |e, \bar{p} - \hbar k\rangle\} = \{|G\rangle, |E\rangle\}. \tag{6.19}$$

The subset

$$W'(\bar{p}) = \{|e, \bar{p} - \hbar k\rangle, |g, \bar{p} - 2\hbar k\rangle\} \tag{6.20}$$

is used to calculate the corresponding quantities for transfer 2 [see Fig. 6.2(b)], but we do not explicitly show the derivation here as it follows in a straightforward manner. We expect the resulting shortcuts to be useful for application to the entire Hilbert space because the dynamics that result from the interaction with each traveling wave are relatively simple, i.e., there are no multiphoton resonances that would cause population transfer to other quantum states [134]. In Section 6.6, we apply the resulting Rabi frequencies and laser frequencies from this calculation to the entire system in a numerical simulation.

The interaction Hamiltonian $\hat{H}_1(t)$ written in the subspace $W(\bar{p})$ is given by

$$\hat{H}_1^{(W)}(t) = \frac{\hbar\delta(t)}{2}\hat{\sigma}_W^z + \frac{\hbar\Omega_1(t)}{2}\hat{\sigma}_W^x \tag{6.21}$$

where $\hat{\sigma}_W^z \equiv |E\rangle\langle E| - |G\rangle\langle G|$ and $\hat{\sigma}_W^x \equiv |G\rangle\langle E| + |E\rangle\langle G|$. As we will show in subsection 6.4.3, we cast the invariant eigenvectors in a similar form as the eigenvectors of $\hat{H}_1^{(W)}(t)$ to apply the LRI shortcut method. The eigenvalues of $\hat{H}_1^{(W)}(t)$ are

$$E_\pm(t) = \pm\frac{\hbar\tilde{\Omega}_1(t)}{2}, \tag{6.22}$$

where $\tilde{\Omega}_1(t) \equiv \sqrt{\delta(t)^2 + \Omega_1(t)^2}$ is the generalized Rabi frequency. The corresponding instantaneous eigenvectors are

$$\begin{aligned} |+\rangle &= \cos\left(\frac{\chi}{2}\right)|E\rangle + \sin\left(\frac{\chi}{2}\right)|G\rangle, \\ |-\rangle &= \sin\left(\frac{\chi}{2}\right)|E\rangle - \cos\left(\frac{\chi}{2}\right)|G\rangle, \end{aligned} \tag{6.23}$$

with the mixing angle defined by $\cos\chi \equiv \delta(t)/\tilde{\Omega}_1(t)$.

In general, if a system begins in an eigenstate of the Hamiltonian and the time evolution obeys the conditions of the adiabatic approximation, the state of the particle will simply adiabatically follow, only picking up an inconsequential global phase. Therefore, if one chooses experimental parameters such that the particle is initialized in one of the dressed states and the dressed state adiabatically evolves from $|G\rangle$ to $|E\rangle$ (or vice versa), then we can change the particle momentum by $\hbar k$. However, these adiabatic states must evolve slowly to satisfy the adiabatic condition that arises from Landau-Zener theory. We shall now speed up this adiabatic passage by constructing a driving Hamiltonian based on the LRI shortcut method.

6.4.3 Deriving detuning profiles from the auxiliary equations

We are now in a position to design an invariant operator in order to end up with the desired final populations using the formalism established in Section 6.3. Its construction and associated eigenvalue equation can be a difficult process, and various methods have been introduced to overcome this [56, 69, 95, 105]. However, since we have the form of the Hamiltonian and its eigenvectors,

we need only to parameterize $\hat{I}(t)$ and $|\phi_n(t)\rangle$ in the same functional forms. Thus, in a similar manner to [38], we use the inverse engineering approach to parameterize $\delta(t)$ and $\Omega(t)$ as to begin and end the sweep with the desired populations. (Note that this derivation holds for time-dependent $\Omega(t)$ unless noted otherwise.)

We parameterize the eigenvectors of the invariant $\hat{I}(t)$ in parallel to Eq. (6.23):

$$\begin{aligned} |\phi_+(t)\rangle &= \cos\left(\frac{\gamma}{2}\right) e^{i\beta} |E\rangle + \sin\left(\frac{\gamma}{2}\right) |G\rangle, \\ |\phi_-(t)\rangle &= \sin\left(\frac{\gamma}{2}\right) |E\rangle - \cos\left(\frac{\gamma}{2}\right) e^{-i\beta} |G\rangle, \end{aligned} \tag{6.24}$$

where $\gamma = \gamma(t)$ and $\beta = \text{const}$ are auxiliary angles. We have introduced the unitary phase $e^{i\beta}$ parameterized by β as an additional degree of freedom to explore with the shortcut protocol [see Section 6.4.4]. From Eqns. (6.24), it follows that the invariant can be written in the basis of the Hamiltonian as

$$\hat{I}(t) = \frac{\hbar\Omega'}{2} \begin{pmatrix} \cos\gamma & \sin\gamma\, e^{i\beta} \\ \sin\gamma\, e^{-i\beta} & -\cos\gamma \end{pmatrix} \tag{6.25}$$

with eigenvalues $\lambda_\pm = \hbar\Omega'/2$, where Ω' is an arbitrary constant frequency in order to keep $\hat{I}(t)$ with units of energy. Substituting Eqns. (6.21) and (6.24) into Eq. (6.4), we calculate the Lewis-Riesenfeld phases for transfer 1 as

$$\alpha_\pm(t) = \mp\frac{1}{2}\int_0^t (\delta\cos\gamma + \Omega_1 \sin\gamma\cos\beta)\, dt'. \tag{6.26}$$

Substituting these phases into Eq. (6.9), we find that the Hamiltonian is parameterized by

$$\hat{H}_1^{(W)}(t) = \frac{\hbar}{2} \begin{pmatrix} A & Be^{i\beta} \\ B^* e^{-i\beta} & -A \end{pmatrix}, \tag{6.27}$$

where

$$A = \delta(t)\cos^2\gamma + \Omega_1(t)\cos\gamma\sin\gamma\cos\beta, \tag{6.28}$$

$$B = \delta(t)\cos\gamma\sin\gamma + \Omega_1(t)\sin^2\gamma\cos\beta - i\dot{\gamma}. \tag{6.29}$$

Equating the two forms of the Hamiltonian [Eqns. (6.21) and (6.27)], we arrive at the auxiliary equations

$$\dot{\gamma} = \Omega_1(t) \sin\beta, \tag{6.30}$$

$$\delta = \Omega_1(t) \cot\gamma \cos\beta. \tag{6.31}$$

Next, we determine the boundary conditions on the auxiliary variables γ and β required for state transfer from state $|G\rangle$ to $|E\rangle$. As seen from Eq. (6.24), γ must satisfy

$$\gamma(t_0) = \pi n; \qquad \gamma(t_f) = \gamma(t_0) + \pi(2m+1), \tag{6.32}$$

where n and m are integers. For simplicity and without loss of generality, we choose $n = m = 0$ so that γ evolves from 0 to π and causes the state to align with $|\phi_-(t)\rangle$ at $t = t_0, t_f$. Since the commutator between $\hat{H}_1^{(W)}(t)$ and $\hat{I}(t)$ is

$$\begin{aligned}\left[\hat{H}_1^{(W)}(t), \hat{I}(t)\right] = \frac{\hbar^2\Omega'}{2}\Big[&- i\Omega \sin\gamma \sin\beta \hat{\sigma}_W^z + (\delta \sin\gamma e^{i\beta} - \Omega\cos\gamma)\hat{\sigma}_W^\dagger \\ &+ (\Omega\cos\gamma - \delta \sin\gamma e^{-i\beta})\hat{\sigma}_W\Big],\end{aligned} \tag{6.33}$$

where $\hat{\sigma}_W \equiv |G\rangle\langle E|$, we should also impose

$$\Omega(t^*) \sin\gamma(t^*) \sin\beta = 0, \tag{6.34}$$

$$\beta = q\pi \tag{6.35}$$

for $t^* = t_0$ and $t^* = t_f$ and integer q to align the eigenbases of $\hat{H}_1^{(W)}(t)$ and $\hat{I}(t)$ at the beginning and end of the shortcut process [see Eq. (6.8)]. The condition (6.34) is automatically satisfied by (6.32), whereas the condition (6.35) is not necessary to enforce in the case of complete state transfer because it only affects non-physical, global phases.

We have now parameterized the Hamiltonian in terms of the auxiliary angles and found boundary conditions for these angles for the interaction with laser 1. The corresponding quantities for the subsequent interaction with laser 2 are derived in a similar manner.

Together Eqns. (6.30)-(6.32) directly determine the experimental parameters $\delta(t)$ and $\Omega_1(t)$. In the general case of $\Omega_1(t) \neq$ const, we would be faced with the task of choosing, from an infinite set

of Hamiltonians, a particular form of $\gamma(t)$ and $\beta(t)$ that satisfies Eqns. (6.30)-(6.32) [38]. However, we will now simplify the discussion by restricting the solution to the form $\Omega_1(t) = \Omega = \text{const}$, whereby the auxiliary equations (6.30) and (6.31) can be solved analytically, which we now show. Let us label the time required to perform the shortcut as T. Defining $t_0 = 0$ (and therefore $t_f = T$), the auxiliary equation for γ using $\gamma(0) = 0$ yields

$$\gamma(t) = (\Omega \sin\beta)t. \tag{6.36}$$

The other boundary condition $\gamma(T) = \pi$ [see Eq. (6.32)] requires that

$$\pi = \Omega T \sin\beta. \tag{6.37}$$

Combining Eqns. (6.36) and (6.37) and substituting the result into Eq. (6.31), we find that

$$\delta(t) = \frac{\pi \cot\beta}{T} \cot\left(\frac{\pi t}{T}\right). \tag{6.38}$$

We provide a plot of $\delta(t)$ for a particular choice of β and T in Fig. 6.2(d).

We have now found a particular Hamiltonian that will drive the transition $|G\rangle \to |E\rangle$ with dynamics that need not be adiabatic. The analogous solution can be used for laser 2 to drive the transition $|e, \bar{p} - \hbar k\rangle \to |g, \bar{p} - 2\hbar k\rangle$ using precisely the same theoretical formalism. The method may be optimized further with respect to different cost functions (e.g., see Ref. [175]).

6.4.4 Bloch sphere trajectories

Different choices of the auxiliary angle β [see Eq. (6.24)] can result in very distinct dynamics as the particle is transferred from $|G\rangle$ to $|E\rangle$, which can be seen by investigating the associated Bloch sphere trajectories. The resulting trajectories under the interaction Hamiltonian $\hat{H}_1(t)$ [see Eq. (6.21)] are purely longitudinal and are parameterized by the azimuthal angle $\phi(\beta) = \pi + \beta$. For a more appropriate comparison, we instead work in the time-independent interaction picture defined by the self-energy of the particle [see Eq. (6.12)], which results in the interaction picture Hamiltonian

$$\hat{H}_I(t) = \frac{\hbar\Omega}{2}\left(e^{i\theta(t)} |E\rangle\langle G| + \text{h.c.}\right) \tag{6.39}$$

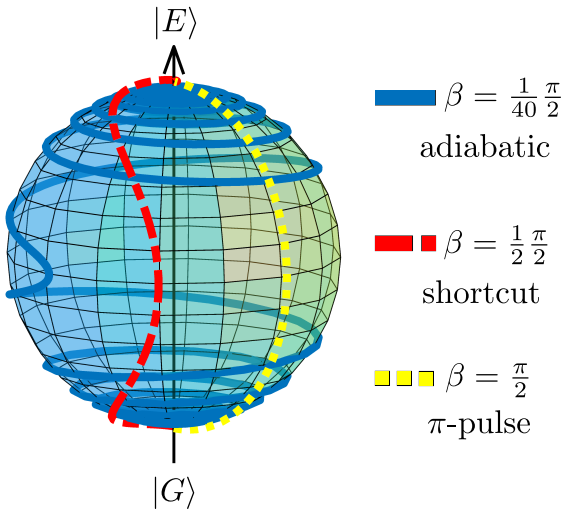

Figure 6.3: Bloch sphere trajectories (thick curves) between the initial state $|G\rangle$ and final state $|E\rangle$ parameterized by the auxiliary angle β [see Eq. (6.24)] in the free-energy interaction picture [see Eq. (6.39)]. We set the Rabi frequency Ω to be equal for all trajectories, and the slowing periods T are given by Eq. (6.37). The cutoff detunings for $\beta = \frac{1}{40}\frac{\pi}{2}$ and $\beta = \frac{1}{2}\frac{\pi}{2}$ are $\delta_{\text{cut}} = 318\Omega$ and $\delta_{\text{cut}} = 225\Omega$, respectively [see Eq. (6.51)].

in the subspace $W(p)$ [see Eq. (6.19)], where

$$\theta(t) \equiv \int_{t_0}^{t} \delta(t')\, dt' \tag{6.40}$$

is the accumulated phase of the detuning $\delta(t)$ derived from the LRI shortcut method [see Eq. (6.38)].

Bloch sphere trajectories for three choices of β are displayed in Figure 6.3. For the sake of comparison, we chose to fix the Rabi frequency Ω across all trajectories so that the slowing periods T are completely determined by β [see Eq. (6.37)]. A choice of auxiliary angle satisfying $\beta = (r + \frac{1}{2})\pi$ for integer r minimizes the slowing period T; this is simply resonant Rabi-flopping ($\delta(t) = 0$). For $r = 0$, i.e., a resonant π-pulse, the system follows the purely longitudinal Bloch sphere trajectory (yellow, dotted curve). This choice of β can lead to experimental challenges, such as inefficient transfer due to sensitivity to errors in Ω (see Section 6.5). On the other hand, a choice of auxiliary angle satisfying $\beta \approx s\pi$ for integer s causes T to tend to infinity, as in an adiabatic process. We approximate the choice $s = 0$ by using the very small auxiliary angle $\beta = \frac{1}{40}\frac{\pi}{2}$, which results in a trajectory that precesses significantly (blue, solid curve). This choice also comes with complications, such as a high chance of spontaneous emission and a large slowing distance. We

take all of these considerations into account and choose from the range $0 \ll \beta < \pi/2$ in our slowing simulations in Section 6.6, which results in an intermediate trajectory (red, dash-dotted curve).

6.5 Slowing dynamics in classical phase space

The usefulness of the LRI shortcut method is ultimately determined by whether or not it can achieve a practical device that is competitive with the current state of the art. With this in mind, we calculate the resulting classical force, slowing time, slowing distance, scattering rate, and number of scattered photons of this method and compare the results to commonly-implemented processes that rely on radiation pressure (RP), such as a Zeeman or Stark decelerator. These quantities are derived below and collected in Table 6.1.

We use Eq. (6.37) in order to calculate the classical force F_{LRI} exerted on the particle during each sweep:

$$F_{\mathrm{LRI}} = \frac{\hbar k}{T} = \frac{\Omega \hbar k \sin\beta}{\pi}. \tag{6.41}$$

The classical force from RP is given by

$$F_{\mathrm{RP}} = \Gamma \hbar k \rho_{\mathrm{ee}} \leq \frac{\Gamma \hbar k}{2}, \tag{6.42}$$

where ρ_{ee} is the excited state fraction, and the inequality is saturated at infinite laser power [126].

Next, we consider the time required to transfer the particle to zero momentum. We assume the particle begins the slowing process in the state $|g, \bar{p}_0\rangle$. It receives an impulse of $\hbar k$ against its motion after every sweep for a total time

$$\Delta t_{\mathrm{LRI}} = T\bar{p}_0/\hbar k = \frac{\pi \zeta_0}{\Omega \sin\beta}, \tag{6.43}$$

where $\zeta_0 \equiv \bar{p}_0/\hbar k$. Assuming that the force F_{RP} remains constant, the slowing time for RP is

$$\Delta t_{\mathrm{RP}} = \frac{\zeta_0}{\Gamma \rho_{\mathrm{ee}}}, \tag{6.44}$$

since approximately one scattered photon is required per slowing photon.

Table 6.1: Comparison of slowing dynamics between the shortcut slowing scheme based on Lewis-Riesenfeld invariants and radiation-pressure slowing. If $\Omega \sin\beta \gg \pi\Gamma\rho_{ee}$, the shortcut slowing scheme results in larger forces, shorter slowing times, shorter slowing distances, and fewer scattered photons than RP.

slowing method	force F	slowing time Δt	slowing distance Δx	scattering rate R^s	number of scattered photons N
Lewis-Riesenfeld	$\frac{\Omega\hbar k \sin\beta}{\pi}$	$\frac{\pi\zeta_0}{\Omega\sin\beta}$	$\frac{\omega_r\zeta_0^2}{2\Omega\sin\beta}\lambda$	$\frac{\Gamma}{2}$	$\frac{\Gamma}{\Omega}\frac{\pi}{2\sin\beta}\zeta_0$
Radiation pressure	$\Gamma\hbar k\rho_{ee}$	$\frac{\zeta_0}{\Gamma\rho_{ee}}$	$\frac{\omega_r\zeta_0^2}{2\pi\rho_{ee}\Gamma}\lambda$	$\Gamma\rho_{ee}$	ζ_0

We now calculate the distance a particle in the final momentum wave packet travels in physical space throughout the slowing process in order to reach zero momentum. We approximate $p(t)$ to be linear:

$$p(t) \approx \bar{p}_0 - \hbar k t/T \tag{6.45}$$

so we may write the slowing distance as

$$\Delta x_{\mathrm{LRI}} = \frac{p_{\mathrm{avg}}}{m}\Delta t = \frac{\omega_r T \zeta_0^2}{2\pi}\lambda, \tag{6.46}$$

where $p_{\mathrm{avg}} = \bar{p}_0/2$ is the time-averaged momentum and λ is the wavelength of the transition. Because laser power is typically the limiting experimental factor, we use Eq. (6.37) to rewrite Eq. (6.46) as

$$\Delta x_{\mathrm{LRI}} = \frac{\omega_r \zeta_0^2}{2\Omega \sin\beta}\lambda. \tag{6.47}$$

Using Eq. (6.42), we can obtain a similar expression for the RP slowing distance:

$$\Delta x_{\mathrm{RP}} = \frac{\omega_r \zeta_0^2}{2\pi\rho_{\mathrm{ee}}\Gamma}\lambda. \tag{6.48}$$

Comparing the LRI and RP results, we find that our scheme is able to exert higher forces, and therefore slow particles in less time and in a shorter distance, with fewer scattered photons when $\Omega \sin\beta \gg \pi\Gamma\rho_{\mathrm{ee}}$. For choices of $\sin\beta$ and ρ_{ee} on the order of unity, this amounts to the limit $\Omega \gg \Gamma$.

In the LRI analysis, we have not incorporated any effects due to dissipation. Since the slowing mechanism is purely coherent in nature, it would be ideal if there were no spontaneous emission events. This can be achieved in several ways: the use of ultra-narrow linewidth transitions, applying the entire slowing protocol in a time shorter than the lifetime of the excited state (which typically requires extremely high laser power but also results in very small slowing distances), or applying the shortcut protocol on a Raman transition between internal ground states. The last method is beyond the scope of this work, but may extend the application of this protocol to other atomic and molecular species. Nevertheless, the scattering rate R^s of each slowing technique is approximately

$$R^s_{\mathrm{LRI}} \approx \frac{\Gamma}{2}; \quad R^s_{\mathrm{RP}} \approx \Gamma\rho_{\mathrm{ee}} \leq \frac{\Gamma}{2}, \tag{6.49}$$

since the particles in the LRI scheme are in the excited state for roughly half of the time, suggesting that the scattering rates are on the same order. However, the expected number of scattered photons, $N = R^s \Delta t$, for each technique is

$$N_{\mathrm{LRI}} \approx \frac{\Gamma}{\Omega} \frac{\pi}{2 \sin \beta} \zeta_0; \quad N_{\mathrm{RP}} \approx \zeta_0, \tag{6.50}$$

which means that the LRI scheme generates fewer scattered photons when $\Omega \sin \beta \gg \Gamma$.

6.6 Slowing Examples

By repeatedly driving the transition $|g, \bar{p}\rangle \rightarrow |e, \bar{p} - \hbar k\rangle$ followed by $|e, \bar{p} - \hbar k\rangle \rightarrow |g, \bar{p} - 2\hbar k\rangle$ according to our shortcut solution, we now show that we are able to slow a significant number of particles when the full composite Hilbert space is taken into account. After each pair of transitions, we update the momentum $\bar{p}$ to $\bar{p} - 2\hbar k$ in the laser frequencies [see Eq. (6.10)], as we assume that the initial population in $|g, \bar{p}\rangle$ has moved to $|g, \bar{p} - 2\hbar k\rangle$. Note that this procedure results in the slowing of a pulse, as opposed to a steady-state ensemble, of particles. We assume that the jump in laser frequency at the end of each ramp is perfectly diabatic. Since there is very little population transfer when $\delta(t) \gg \Omega$, we do not track the detuning profile's asymptotic behavior, as this can cause numerical errors. We thus take $\delta(t)$ to be equal to a constant $\pm\delta_{\mathrm{cut}}$ in these regions, defined by

$$\delta(t < t_0 + t_{\mathrm{cut}}) = -\delta(t > t_f - t_{\mathrm{cut}}) = \delta_{\mathrm{cut}} \tag{6.51}$$

for some cutoff time t_{cut}, as shown in Fig. 6.2(d). We evolve the master equation [Eq. (6.17)] using the method of quantum Monte Carlo wave functions [135]. This involves unraveling the master equation into trajectories based on stochastic simulation of spontaneously emitted photons.

Fig. 6.4 presents the momentum distribution of an ensemble of particles before (blue) and after (orange) application of our slowing scheme over 100 sweeps in the case of purely coherent (left column) and dissipative (right column) dynamics. In the dissipative case, we chose $\Gamma = \omega_r$ as an order-of-magnitude estimate for a narrow-linewidth transition. We chose to initialize the momentum distribution as either a momentum eigenstate at $100\hbar k$ (top row) or a Gaussian profile

with an average momentum $\langle\hat{p}\rangle = 100\hbar k$ and a standard deviation of $\sigma_{p,0} = 10\hbar k$ (bottom row), which typically corresponds to an initial average particle speed on the order of 1 m/s. While actual physical systems may have much higher initial particle beam speeds, this choice sufficiently demonstrates the slowing effects of our protocol. We have chosen to use the average momentum of the Gaussian as the initial momentum used in the laser frequencies ($\bar{p}_0 = \langle\hat{p}\rangle$) because it results in the largest fraction of slowed particles. For experimental accessibility and robustness, we chose $\beta = 0.85\,\pi/2$ and $\Omega = 100\Gamma$, which results in a shortcut time $T = 0.032/\Gamma$ [see Eq. (6.37)] typically on the order of microseconds, much shorter than the associated timescale of radiation pressure slowing on the transition. This choice of Ω also sets the expected number of scattered photons N to be on the order of unity [see Eq. (6.50)].

As seen in Fig. 6.4, a substantial fraction of the distribution is slowed to near zero momentum. We first discuss the results in the case of purely coherent dynamics (left column). If the system begins in the eigenstate $|g, 100\hbar k\rangle$ [Fig. 6.4(a)], about 99.3% of the population ends in the zero momentum eigenstate. (We attribute the lack of 100% transfer to our use of a cutoff frequency $\delta_{\text{cut}} = 244\omega_r$.) If the system begins in a Gaussian state [Fig. 6.4(c)], about 35% of the population ends with momentum $|p| \leq 10\hbar k$, which corresponds to about half of the population within one standard deviation of the average momentum in the initial distribution.

In the case of dissipative dynamics, 29% of the population ends with momentum $|p| \leq \hbar k$ if the system is initialized in the eigenstate $|g, 100\hbar k\rangle$ [Fig. 6.4(b)], and 13% of the population ends with momentum $|p| \leq 10\hbar k$ if the system is initialized in the Gaussian state [Fig. 6.4(d)]. In both cases, there was an average of 1.6 scattered photons per particle, which agrees with the predicted scattering rate given in Table 6.1. These results demonstrate that our protocol can potentially slow a significant fraction of particles to zero momentum in a very short distance and with few spontaneous emission events. An appealing feature of our protocol is its ability to apply high slowing forces with a virtually negligible reliance on spontaneous emission.

As a more realistic demonstration, we present several atomic and molecular species that are reasonable candidates for our slowing protocol in Table 6.2. We simulated the slowing of each

Table 6.2: Fundamental properties for various atomic and molecular candidates for shortcut slowing on a narrow transition.

Species	Transition	Wavelength (nm)	Linewidth (kHz)	Recoil frequency (kHz)	Saturation intensity (W/cm^2)
^{40}Ca	$^1S_0 \rightarrow {}^3P_1$	657	0.4	11.5	1.8×10^{-7}
^{88}Sr	$^1S_0 \rightarrow {}^3P_1$	689	7.5	4.8	3.0×10^{-6}
YO	$X^2\Sigma^+ \rightarrow A'^2\Delta_{3/2}$	690	5.9	4.0	2.3×10^{-6}
^{174}Yb	$^1S_0 \rightarrow {}^3P_1$	556	180	3.7	1.4×10^{-4}
BaH	$X^2\Sigma^+ \rightarrow A^2\Pi$	1061	1200	1.3	1.3×10^{-4}

Table 6.3: Slowing results for various atomic and molecular candidates using a 0.1 W/cm^2 laser intensity and starting from a momentum of $200\hbar k$. The Rabi frequency, slowing time, and slowing distance follow from Eqns. (6.52), (6.43), and (6.47) respectively, with $\beta = 0.85\,\pi/2$. The simulated capture fraction, defined as the fraction of particles with momentum $|p| \leq 3\hbar k$ after the slowing process, was calculated over 1,000 trajectories for Ca, Sr, and YO, and 10,000 trajectories for Yb and BaH.

Species	Rabi frequency (MHz)	Initial speed at $200\hbar k$ (m/s)	Slowing time (μs)	Slowing distance (μm)	Capture fraction
^{40}Ca	0.2	3.0	494	746	5.6×10^{-1}
^{88}Sr	1.0	1.3	106	70	1.5×10^{-1}
YO	0.9	1.1	119	66	2.1×10^{-1}
^{174}Yb	3.4	0.82	30	12	6.8×10^{-6}
BaH	23.6	0.54	4	1	1.6×10^{-5}

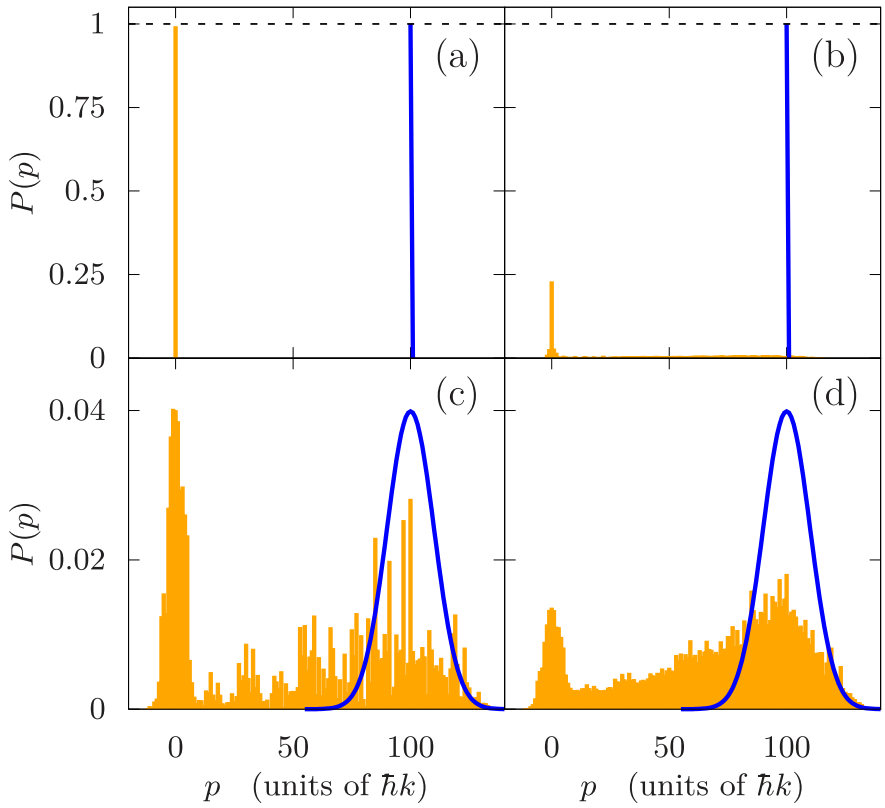

Figure 6.4: Initial (blue) and final (orange) momentum distributions $P(p)$ of a system subject to the slowing protocol. The system is initialized in the internal ground state $|g\rangle$ and with a momentum distribution of either the $100\hbar k$ eigenstate (top row) or a Gaussian state with average momentum $\langle\hat{p}\rangle = 100\hbar k$ and width $\sigma_p = 10\hbar k$ (bottom row). The excited state linewidth is $\Gamma = 0$ in (a) and (c), and $\Gamma = \omega_r$ in (b) and (d). Further details are discussed in text. Other parameters are: $\Omega = 100\omega_r$, $T = 0.032/\omega_r$, $t_{\text{tot}} = 1.6/\omega_r$, and $\delta_{\text{cut}} = 244\omega_r$, $\beta = 0.85\,\pi/2$, and $\bar{p}_0 = 100\hbar k$. Subplots (b) and (d) are averaged over 1,000 trajectories.

species with an initial momentum of $200\hbar k$ using a 0.1 W/cm^2 laser intensity, and provide the expected slowing times Δt, slowing distances Δx, and capture fractions C in Table 6.3. The saturation intensity I_{sat}, laser intensity I, and Rabi frequency Ω can be calculated according to [126]

$$2\left(\frac{\Omega}{\Gamma}\right)^2 = \frac{I}{I_{\text{sat}}}; \quad I_{\text{sat}} \equiv \frac{\pi h c \Gamma}{3\lambda^3}, \tag{6.52}$$

where h is Planck's constant and c is the speed of light. The calculated slowing times and distances become smaller as the transition dipole matrix element increases, as can be seen for the species with larger linewidths. However, the required temporal control of the Rabi frequency and detuning

profiles in these cases may be an experimental challenge. One solution is to simply reduce the laser power, but this can quickly move the parameters away from the regime $\Omega \gg \Gamma$, which increases the chance of spontaneous emission and hence reduces the capture fraction C.

Due to our method's sensitivity to spontaneous emission, a rough estimate for the capture fraction C is given by the fraction of particles that do not emit a single spontaneous photon throughout the slowing process. Using Eq. (6.50), this is approximately

$$C \approx \exp\left(-N_{\mathrm{LRI}}\right) = \exp\left(-\frac{\Gamma}{\Omega}\frac{\pi}{2\sin\beta}\zeta_0\right). \tag{6.53}$$

This formula is on the same order as the simulated capture fractions given in Table 6.3 for Ca, Sr, and YO, but it underestimates the results for Yb and BaH, suggesting that particles can still be slowed after emitting spontaneous photons. Eq. (6.53) is not a fundamental limit, as it can be improved with a more sophisticated implementation of the shortcut process, such as introducing occasional waiting periods so that the particles return to the internal ground state (as is done in other methods [129]), allowing the laser pulses to overlap in time (see Fig. 6.6), or repeating the slowing protocol over a range of momentum states. For example, we were able to increase the simulated ^{174}Yb capture fraction by over an order of magnitude to $C = 1.7 \times 10^{-4}$ by introducing a laser pulse overlap fraction $f = 0.2$ as discussed in Section 6.7.

6.7 Robustness

We now study the robustness of the shortcut slowing scheme to various systematic errors that may arise in an experimental setting. Specifically, we modify the Rabi frequency amplitude, then separately consider the result of slowing a particle with a momentum p that is not equal to the momentum accounted for in the laser frequencies $\bar{p}$ (Fig. 6.5). We also consider the scheme's robustness to the temporal overlap f of the square pulses (Fig. 6.6), which may minimize scattering events since it potentially reduces the amount of time the particle remains in the internal excited state. For simplicity, we focus on a single $|g\rangle \to |e\rangle \to |g\rangle$ process and calculate the resulting impulse Δp experienced by the particle. Moreover, we employ a phase relation between the laser

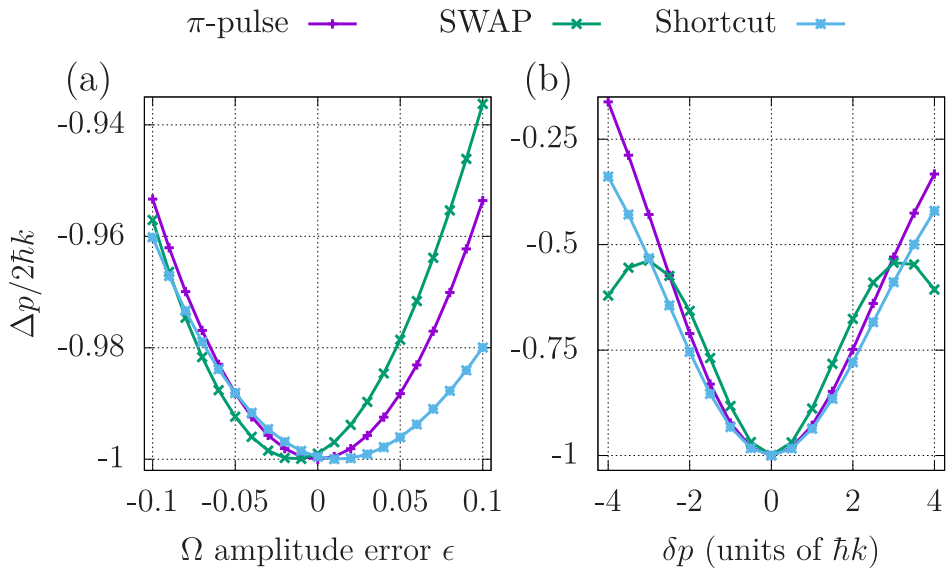

Figure 6.5: Robustness comparison of π-pulse slowing (purple, plus), SWAP slowing (green, cross), and the shortcut scheme (blue, circle with cross) over a $\bar{p} \to \bar{p} - 2\hbar k$ transfer process. Ideally, the resulting impulse Δp satisfies $\Delta p/2\hbar k = -1$. The evolution is purely coherent ($\Gamma = 0$), the momentum of the particle (which is addressed by the laser frequencies) is $\bar{p} = 2\hbar k$, and the Rabi frequency is $\Omega = 10\omega_r$ for all processes. (a) Impulse Δp experienced by the particle, in units of the ideal impulse magnitude $2\hbar k$, as a function of the error in the Rabi frequency amplitude ϵ [see Eq. (6.55)]. The shortcut scheme is the most robust protocol when $\epsilon > 0$. (b) $\Delta p/2\hbar k$ as a function of the relative momentum of the particle δp with respect to the momentum $\bar{p} = 2\hbar k$ used in the laser frequencies [see Eqns. (6.10) and (6.56)]. For this set of parameters, the shortcut and π-pulse scheme are generally more robust than SWAP slowing. π-pulse parameters are: $T = 0.314/\omega_r$ and $\beta = \pi/2$. SWAP slowing parameters are: $T = 1/\omega_r$ and $\Delta = 50\omega_r$. Shortcut parameters are: $T = 0.44/\omega_r$, $\delta_{\text{cut}} = 230\omega_r$, and $\beta = 0.5\,\pi/2$.

pulses such that the Rabi frequency of each pulse is purely real. The correct detuning profiles are employed throughout this section. We set the Rabi frequency to $\Omega = 10\omega_r$ across all slowing methods, but necessarily allow for different slowing times.

Using the auxiliary variable $\beta = 0.5\,\pi/2$, we compare the robustness of our scheme to both π-pulse and SWAP slowing. As discussed in Section 6.4.4, The π-pulse solution is a special case of our slowing method with the choice $\beta = \pi/2$, which results in a fixed detuning [see Eq. (6.38)]. SWAP slowing is simulated by using a sawtooth-wave detuning profile with full range Δ and period T for each single-photon transfer. Unlike SWAP cooling, the lasers are sequentially pulsed as in Fig. 6.2(a) and 6.2(b), and the laser detunings are centered on the momentum $\bar{p}$.

While there is not a unique way to choose the SWAP slowing parameters, we used the following method. Landau and Zener showed [194] that the population of the second (initially unoccupied) state P_2 if the laser is linearly chirped from a detuning of minus infinity to positive infinity, is given by Eq. (6.1). Therefore, to obtain a transfer probability of at least 95%, we chose to set $\Omega^2/\alpha = 2$. Next, we increased the chance of population transfer by setting the shortcut period to be several times larger than the approximate time τ_j required to transfer population between quantum states in the adiabatic regime [185]:

$$\tau_j = \frac{2\Omega}{\alpha} = \frac{0.4}{\omega_r} \quad \Rightarrow \quad T = \frac{1}{\omega_r} > \tau_j. \tag{6.54}$$

These choices constrained the sweep range to be $\Delta = 50\omega_r$. Note that the resulting SWAP slowing period $T = 1/\omega_r$ is significantly longer than the π-pulse ($T \approx 0.3/\omega_r$) and shortcut slowing ($T \approx 0.4/\omega_r$) periods [see Eq. (6.37)].

Fig. 6.5(a) presents the resulting particle impulse Δp as a function of the error in the Rabi frequency amplitude, which is characterized by the small parameter ϵ:

$$\Omega \to \Omega(1+\epsilon). \tag{6.55}$$

While the shortcut scheme applies a similar impulse Δp compared to the π-pulse method for $\epsilon < 0$, it is the most robust method for $\epsilon > 0$. The SWAP slowing result, while being the most robust method for $\epsilon < 0$, can change significantly with small changes to the parameters. This instability is as a result of high-frequency population oscillations [185]. Moreover, when dissipation is included, the much longer SWAP slowing period increases the chance of spontaneous emission, which can disrupt the slowing process. These results demonstrate the utility of the shortcut scheme, as it is robust to small errors ϵ and takes much less time than SWAP slowing. Note that intensity modulators typically have errors less than approximately 5%.

Fig. 6.5(b) presents the effects of applying each slowing method to a particle with a momentum p which is not equal to the momentum $\bar{p}$ accounted for in the laser frequencies [see Eq. (6.10)]. Such an error occurs when slowing a cloud of particles with a distribution of momenta. We param-

eterize this difference in momentum with the variable δp as:

$$p = \bar{p} + \delta p. \tag{6.56}$$

In this case, we find that the shortcut scheme is most robust for small δp, but SWAP slowing becomes more robust for $|\delta p| > 3\hbar k$. This change in the trend for SWAP slowing near the particular values $\delta p = \pm 3\hbar k$ is due to population oscillations, and the results can again change significantly with small changes in the parameters. In the limit of adiabatic dynamics and time-resolved transfers (which necessarily takes a long time), SWAP slowing is generally most robust to this error since the rate of change of the detuning profile in SWAP slowing is constant, thereby removing the need to align the center of the laser detuning profile with the Doppler shift of the particle. It should be noted that it is not necessarily a problem that the shortcut scheme is less robust to large deviations of δp from zero because we scan through values of $p/\hbar k$ in integer steps by design. What is more important is that the shortcut scheme is more robust when $|\delta p| < \hbar k$ than SWAP slowing, as particles will not necessarily have integer momentum.

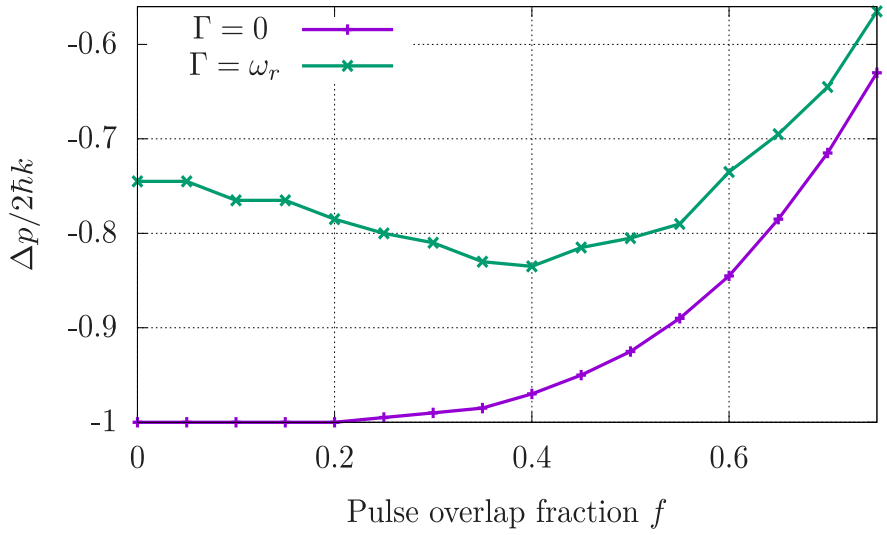

Figure 6.6: Impulse Δp experienced by the particle, in units of the ideal impulse magnitude $2\hbar k$, as a function of the laser pulse overlap fraction f. The impulse is calculated under both coherent ($\Gamma = 0$) and dissipative ($\Gamma = \omega_r$) dynamics. Other parameters are: $T = 0.44/\omega_r$, $\delta_{\text{cut}} = 230\omega_r$, $\Omega = 10\omega_r$, $\bar{p} = 2\hbar k$, and $\beta = 0.5\,\pi/2$. All points are averaged over 1,000 trajectories.

Fig. 6.6 presents the effects of allowing the laser pulses to overlap in time. We define the

overlap fraction of the square pulses f such that $f = 0$ when the pulses are completely time-resolved but occur sequentially with no delay, and $f = 1$ when the pulses occur at the same time for the entire pulse duration. We find, in the case of purely coherent dynamics ($\Gamma = 0$), that a pulse overlap fraction as large as $f = 0.2$ does not change the impulse experienced by the particle. In the case of dissipative dynamics, we find that there is an optimal f that maximizes the impulse Δp. This optimal f, which depends on system specifics, must be small enough to allow transfer to $|e\rangle$ before the transfer back to $|g\rangle$, but large enough to minimize the time the particle spends in the excited state, thereby minimizing the chance of spontaneous emission. It should be noted that a pulse overlap introduces the possibility of multiphoton, or Doppleron, resonances [134] which may interfere with the single-photon slowing dynamics.

When slowing a particle with a large initial momentum $p \gg \hbar k$ to rest, we emphasize that the slowing efficiency is significantly affected by even a small deviation from the ideal impulse $\Delta p = -2\hbar k$ since the error compounds exponentially with the number of transfer processes, and the particle is generally not transferred back to $|g\rangle$ for the next pulse sequence. It may be possible to further enhance the robustness of the slowing protocol to the rapidly changing detuning profile at the beginning and end of the transfers by using a Rabi frequency profile that satisfies $\Omega(t_0) = \Omega(t_f) \to 0$, such as a Gaussian or a sinusoidal function [129, 167, 173]. However, in order to satisfy the auxiliary equations and boundary conditions [see Eqns. (6.30)-(6.32)], the peak Rabi frequency may need to be larger than what we consider here.

6.8 Conclusion and Outlook

In this work, we proposed a purely coherent particle slowing scheme. By utilizing the method of inverse-engineering based on Lewis-Riesenfeld invariant theory, we demonstrated that these slowing designs are able to achieve effective adiabatic dynamics but with a short slowing time. We illustrated how to design Rabi frequency and detuning profiles that achieve the desired dynamics and demonstrated that our slowing blueprint is a promising alternative to conventional slowing schemes that rely on radiation pressure for narrow linewidth systems or systems that lack a closed

cycling transition. We theoretically examined the effective classical forces exerted on the particles during the slowing processes and demonstrated that, when the Rabi frequency is large compared to the excited state decay rate, our scheme is able to exert significantly higher forces than radiation pressure while maintaining a very low number of scattered photons. We also showed that our proposed slowing scheme is robust to various systematic errors.

A possible practical implementation of our scheme is to directly apply it to a particle beam exiting a supersonic nozzle or buffer gas cell. Our scheme may also be utilized as a second slowing stage after particles exiting an effusive oven have been slowed in a precursor stage to the order of 10 m/s and the initial spread in velocity has been greatly reduced. Additionally, it may be possible to implement our protocol as a steady-state slowing procedure by compensating for the changing particle velocity with a magnetic field gradient instead of the time-dependent laser frequencies, in a similar approach to a Stark or Zeeman decelerator.

A natural next step would be to optimize our shortcut solutions with respect to different criteria. Time-optimization of different adiabatic shortcuts has been studied previously for two-level systems [161, 162], STIRAP [136], and frictionless cooling in harmonic traps [175]. Another optimization criterion comes from the fact that adiabatic shortcuts cannot be implemented without an energetic cost, an intrinsic relationship that has been rigorously studied for Berry's transitionless quantum driving algorithm [28], various other shortcuts [1], and in its applications to quantum computing [52]. Thus, minimizing the energetic cost for a fixed sweep period is, in effect, finding the most efficient shortcut. Additionally, quantum optical control based protocols could be implemented to derive further solutions [72].

Another appealing scheme is a similar shortcut protocol applied to a system with an internal state structure comprised of two stable ground states coupled to an excited state, such as found in a $J = 1 \rightarrow J' = 1$ transition, where J is the total electronic angular momentum quantum number. Speeding up a Raman transition between the ground states could remove twice as much momentum per transition. This model, while generally requiring more laser power, has the additional benefit of an engineered excited state linewidth, which can be made arbitrarily small if the lasers are

sufficiently detuned from the excited state. Moreover, applying anti-symmetric detuning sweeps could allow for control of the slowed velocity range, potentially resulting in a slowed distribution with a low temperature.

There are similarities between our results and others [111, 129, 167, 173] in the sense that two-level inversion is achieved in the diabatic limit. A more thorough investigation could further our understanding of the connection between these solutions and adiabatic shortcuts.

Furthermore, it is impossible to implement the LRI scheme to the entire momentum Hilbert space by hand. An intriguing possible solution to this problem is to employ advanced optimization techniques, such as quantum optimal control and reinforcement learning, to find a solution that maximizes the slowing scheme's capture range or minimizes the energetic cost of implementing the shortcut for a given sweep period.

Chapter 7

Entropy transfer from a quantum particle to a classical coherent light field

In the previous chapters, we studied various laser cooling (Chapters 3 and 4), trapping (Chapter 5), and slowing (Chapter 6) techniques. In the cases involving cooling, we saw that the ensemble of quantum particles eventually equilibrated to some temperature and cloud size. As discussed in Section 2.2.2, this was a consequence of the dissipative spontaneous emission process, which irreversibly carried away entropy from the ensemble by its interaction with the environment and allowed the system to reach a steady-state configuration. We can also ask the question as to whether the degrees of freedom of the laser light could also remove entropy from the particle ensemble. However, this would require a quantized model of the laser light (see Section 2.26) and a relaxation of the assumption that the laser light is unperturbed by the particle-laser interaction. We adopt this perspective and investigate its consequences in this chapter.

In this chapter, we develop and theoretically analyze a simple Gedankenexperiment which involves the interaction of a coherent state with a quantum particle in an optical cavity. We quantify the resulting alteration of the light field by measuring the fidelity of its initial and equilibrium states. Using Bayesian inference, we demonstrate the information transfer through photon measurements. In addition, we employ the concepts of quantum entropy and mutual information to quantify the entropy transfer from the particle to the light field. In the weak coupling limit, we validate the usually assumed negligible alteration of the light field and entropy transfer. In the strong coupling limit, however, we observe that the information of the initial particle state can be fully encoded in the light field even for large photon numbers. Nevertheless, we show that spontaneous emission is a

sufficient mechanism for removing the entropy initially stored in the particle. Our analysis provides a deeper understanding of the entropy exchange between quantum matter and classical light.

7.1 Introduction

When studying a quantum system, it is generally desirable for it to be prepared in a low-entropy configuration. Such systems can populate a relatively small number of quantum states, which makes their dynamics more controllable, predictable, and comprehensible [22, 195]. If the system of interest is a gas consisting of atoms or molecules, its entropy is typically reduced by utilizing laser cooling and optical pumping techniques. In these processes, the particles absorb light from an applied laser field and incoherently scatter the light into free space [126]. While these methods can irreversibly remove entropy from the gas, the second law of thermodynamics requires that the total entropy of the universe does not decrease, and therefore that the entropy of the gas must have been absorbed by some other system. In this context, the most common explanation is that the entropy of the gas is absorbed by the vacuum modes of the quantized electromagnetic field [190]. This process is often cast in the framework of open quantum systems whereby the quantized electromagnetic field is treated as an external reservoir, allowing for an irreversible reduction of the gas's entropy through the process of spontaneous emission [24, 65, 155].

It is typically explained that the reservoir can absorb a substantial amount of entropy due to the large number of possible emission configurations [93, 126]. Moreover, it is often stated that the coherent light field is not perturbed, and hence does not absorb entropy, because the quantum counterpart to the laser field, the coherent state, is unaffected by the absorption of photons by the gas. However, there are some studies that predict entropy removal from the gas via interaction with the laser field [35, 50, 100, 124, 128]. In an effort to further understand the underlying physics of laser cooling and optical pumping, we propose a simple Gedankenexperiment that probes the change of a light field that coherently interacts with a particle containing nonzero initial entropy. Our results conclude that the entropy initially possessed by the particle can be imprinted on the applied light field, but the same information is also encoded in the spontaneous photons emitted

by the particle.

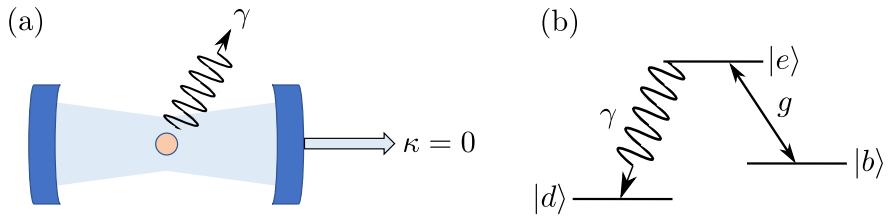

Figure 7.1: (a) A schematic of the experimental setup. A particle (circle) is placed in a lossless ($\kappa = 0$) optical cavity that contains a coherent light field. The particle can undergo spontaneous emission into free space at rate γ. (b) Energy diagram of the particle's internal state structure. It is coupled to the cavity with strength g on the bright transition ($|e\rangle \leftrightarrow |b\rangle$) and has a linewidth γ on the dark transition ($|e\rangle \rightarrow |d\rangle$).

7.2 Motivation

We first consider the level of complexity necessary to demonstrate the state alteration and entropy transfer processes with the goal of removing complications or details of any particular cooling or pumping scheme that might obscure the core physics of interest. While other candidates may exist, we model the initial state of the laser field as a coherent state, as this is the quantum state that shares the most similarities with a classical coherent laser field [6]. The coherent state is prepared in a lossless optical cavity, after which any external driving fields are turned off. The cavity is an efficient way to incorporate quantization, and we anticipate that many of our findings also apply to free-space coherent light fields. Because the essential physics of interest is the same, we focus only on the effects of optical pumping on the evolution of the particles' internal states. To this end, we model the gas as a single, motionless particle that exists at an anti-node of the optical cavity. With these considerations in mind, we construct the minimal experimental setup depicted in Fig 7.1(a). The particle possesses two ground states and a single excited state, as shown in Fig 7.1(b). The $|b\rangle \leftrightarrow |e\rangle$ (bright) transition is resonant with the optical cavity, which encapsulates the coherent interaction between the cavity field and the particle, while the $|e\rangle \rightarrow |d\rangle$ (dark) transition is mediated only by the spontaneous emission process, which models the incoherent interaction between the background radiation field and the particle. The particle always transitions

to the dark state $|d\rangle$ upon emission of a spontaneous photon so that the cavity isn't trivially depleted of photons.

By studying this model, we aim to quantify the alteration of the cavity field due to its interaction with the particle and to determine if entropy is transferred from the particle subspace to the cavity subspace through their resulting correlations. To achieve these goals, we employ both statistical and information theoretic techniques. We first calculate the final cavity field state and quantify its distinguishability from the initial cavity state through their quantum fidelity. Then, we demonstrate that information about the particle becomes encoded in the cavity field by using Bayesian inference. Lastly, we quantify the amount of entropy transferred from the particle to the cavity field by calculating the quantum mutual information shared between the initial particle state and final cavity state.

7.3 Model

We refer the reader to Sections 2.1 and 2.2 for details on modeling light-matter interactions. The system of interest [Fig. 7.1(a)] consists of a three-level particle [Fig. 7.1(b)] coupled to a light field in a lossless ($\kappa = 0$) optical single-mode cavity. Let us denote the Hilbert space of each subspace as A and L, respectively. In the time-independent interaction picture, the system is evolved according to the quantum master equation

$$\frac{d\hat{\rho}_{AL}}{dt} = \frac{1}{i\hbar}\left[\hat{H}_{AL}, \hat{\rho}_{AL}\right] + \hat{\mathcal{L}}\hat{\rho}_{AL}. \tag{7.1}$$

Here, the coherent cavity-particle interaction is described by the Jaynes-Cummings Hamiltonian

$$\hat{H}_{AL} = \frac{\hbar g}{2}\Big(|b\rangle\langle e|\,\hat{a}^\dagger + |e\rangle\langle b|\,\hat{a}\Big), \tag{7.2}$$

where g is the coupling strength, and $\hat{a}$ is the annihilation operator for the cavity field. As is achieved in the moving frame of a particle in Doppler cooling, we have set the cavity to be resonant with the particle's bright state transition. The environment surrounding the system, which we model as an infinite bandwidth bosonic bath that is coupled to the particle's dark transition, has

been traced out under the Born-Markov approximation [109, 127]. Its effects are incorporated through the Lindblad superoperator

$$\hat{\mathcal{L}}\hat{\rho} = \gamma\left(\hat{L}\hat{\rho}\hat{L}^{\dagger} - \frac{1}{2}\left\{\hat{L}^{\dagger}\hat{L},\hat{\rho}\right\}\right), \tag{7.3}$$

i.e., the only jump operator is $\hat{J} = \sqrt{\gamma}\hat{L} = \sqrt{\gamma}\,|d\rangle\langle e|$. This term describes the spontaneous emission of photons into free space by the particle that occurs at a rate γ. We consider both analytical and numerical solutions to Equation (7.1) in the sections that follow. We use both MATLAB and the QuantumOptics package in the Julia programming language for numerical calculations [101, 120].

To model the entropy initially possessed by the particle, it is prepared in the mixed state

$$\hat{\rho}_A(0) = x\,|b\rangle\langle b| + (1-x)\,|d\rangle\langle d|\,, \tag{7.4}$$

where $0 \leq x \leq 1$ is the probability that the particle begins in the bright state $|b\rangle$. As already mentioned, the cavity field is initialized in a coherent state

$$|\alpha\rangle = e^{-|\alpha|^2/2}\sum_{n=0}^{\infty}\frac{\alpha^n}{\sqrt{n!}}\,|n\rangle\,, \tag{7.5}$$

where $|n\rangle$ is the n-photon Fock state, so that its initial density matrix reads

$$\hat{\rho}_L(0) = |\alpha\rangle\langle\alpha|\,. \tag{7.6}$$

7.4 Calculating the final cavity field state

In order to derive an analytic form of the cavity field state in the limit $t \to \infty$, we separate the density matrix into Jordan blocks:

$$\begin{gathered}\hat{\rho}_b = \langle b|\hat{\rho}|b\rangle\,|b\rangle\langle b| + \langle b|\hat{\rho}|e\rangle\,|b\rangle\langle e| + \langle e|\hat{\rho}|b\rangle\,|e\rangle\langle b| + \langle e|\hat{\rho}|e\rangle\,|e\rangle\langle e|\,,\\ \hat{\rho}_d = \langle d|\hat{\rho}|d\rangle\,|d\rangle\langle d|\,,\end{gathered} \tag{7.7}$$

in which we momentarily drop the AL subscript for notational simplicity. This simplifies the formalism because the initial particle-cavity state

$$\hat{\rho}(0) = [x\,|b\rangle\langle b| + (1-x)\,|d\rangle\langle d|] \otimes |\alpha\rangle\langle\alpha| \tag{7.8}$$

explicitly assumes there are no coherences between the three internal states. Taking a time derivative and using the master equation Eq. (7.1) in the form

$$\frac{\partial\hat{\rho}}{\partial t} = \frac{1}{i\hbar}\left(\hat{H}_{\text{eff}}\hat{\rho} - \hat{\rho}\hat{H}_{\text{eff}}^{\dagger}\right) + \hat{\mathcal{L}}_{\text{jump}}\,\hat{\rho}, \tag{7.9}$$

we find

$$\dot{\hat{\rho}}_d = \gamma\,\langle e|\hat{\rho}|e\rangle\,|d\rangle\,\langle d|\,, \qquad \dot{\hat{\rho}}_b = \frac{1}{i\hbar}\left[\hat{H}_{\text{eff}}\hat{\rho}_b - \hat{\rho}_b\hat{H}_{\text{eff}}^{\dagger}\right]. \tag{7.10}$$

Here, we used $\langle i|\,\hat{\mathcal{L}}_{\text{jump}}\,|j\rangle = 0$ for $i,j \in \{b,e\}$ and defined

$$\hat{H}_{\text{eff}} = \hat{H} - \frac{i\hbar\gamma}{2}\,|e\rangle\,\langle e|\,, \qquad \hat{\mathcal{L}}_{\text{jump}}\,\hat{\rho} = \gamma\,\langle e|\hat{\rho}|e\rangle\,|d\rangle\,\langle d|\,. \tag{7.11}$$

We first diagonalize the non-Hermitian matrix $\hat{H}_{\text{eff}}$ in the subspace $\{|e,n-1\rangle\,,|b,n\rangle\}$

$$\hat{H}_n = \frac{\hbar}{2}\begin{pmatrix} -i\gamma & g\sqrt{n} \\ g\sqrt{n} & 0 \end{pmatrix} \tag{7.12}$$

for $n>0$. The eigenvalues are $\lambda_{\pm}^{(n)} = -i\hbar\Lambda_{\pm}^{(n)}$, with

$$\Lambda_{\pm}^{(n)} \equiv \frac{\gamma}{4} \pm \frac{i}{2}\sqrt{ng^2 - \frac{\gamma^2}{4}}, \tag{7.13}$$

and the kernel of the matrix $\hat{H}_n - \lambda_{\pm}^{(n)}\hat{\mathbb{I}}_n$ is spanned by

$$\hat{V}_n = \frac{\hbar}{c_n}\begin{pmatrix} -i\Lambda_{+}^{(n)} & -\frac{g\sqrt{n}}{2} \\ \frac{g\sqrt{n}}{2} & -i\Lambda_{+}^{(n)} \end{pmatrix} \tag{7.14}$$

with normalization factor $c_n^2 = \left(-i\hbar\Lambda_{+}^{(n)}\right)^2 + \hbar^2 g^2 n/4$. We now define $\hat{V} = \sum_n \hat{V}_n \otimes \hat{\mathbb{I}}_n$ so that the bright manifold matrix can be written as $\hat{\rho}_b = \hat{V}\hat{\rho}_V\hat{V}^{\dagger}$.

We can use the method of Laplace transforms, $L[\hat{A}](s) = \int_0^{\infty} dt e^{-st}\hat{A}$, to solve for the transformed density matrix:

$$sL[\hat{\rho}] = L[\dot{\hat{\rho}}](s) + \hat{\rho}(0), \tag{7.15}$$

which we then can solve for steady-state:

$$\hat{\rho}(t\to\infty) = \lim_{s\to 0} L[\dot{\hat{\rho}}](s) + \hat{\rho}(0). \tag{7.16}$$

Projecting with $\langle d|$ and $|d\rangle$ and using the master equation Eq. (7.1), $\langle d|\hat{\rho}_b|d\rangle = 0$, and $\langle e|\hat{\rho}_d|e\rangle = 0$, we find

$$\hat{\rho}_d(t \to \infty) = \gamma \lim_{s\to 0} \langle e|L[\hat{\rho}_b](s)|e\rangle + \langle d|\hat{\rho}_d(0)|d\rangle \,. \tag{7.17}$$

To solve for the first term on the right-hand side of Eq. (7.17), we find

$$L[\hat{\rho}_V](s) = L\left[\hat{V}^{-1}\hat{\rho}_b(\hat{V}^\dagger)^{-1}\right](s) = \sum_{n,n'\geq 1} \hat{R}_{n',n} \otimes \hat{I}_{n',n}, \tag{7.18}$$

where $\hat{I}_{n',n}$ is a matrix with 1 at position n', n and zeros everywhere else, and

$$\hat{R}_{n',n} = \frac{\hbar^2}{c_{n'}c_n^*} \begin{pmatrix} \frac{g^2\sqrt{nn'}}{4(s+\Lambda_+^{(n')}+\Lambda_+^{(n)*})} & \frac{ig\sqrt{n'}\Lambda_+^{(n)*}}{2(s+\Lambda_+^{(n')}+\Lambda_-^{(n)*})} \\ -\frac{ig\sqrt{n}\Lambda_+^{(n')}}{2(s+\Lambda_-^{(n')}+\Lambda_+^{(n)*})} & \frac{\Lambda_+^{(n')}\Lambda_+^{(n)}}{(s+\Lambda_-^{(n')}+\Lambda_-^{(n)*})} \end{pmatrix} \langle n'|\alpha\rangle \langle\alpha|n\rangle \,. \tag{7.19}$$

We next calculate

$$L[\hat{\rho}_b](s) = \sum_{n,n'\geq 1} \hat{V}_{n'}\hat{R}_{n',n}\hat{V}_n^\dagger \otimes \hat{I}_{n',n}, \tag{7.20}$$

and project with $\langle e|$ and $|e\rangle$. Since the excited state in our basis in Eq. (7.12) is $|e, n-1\rangle$, Eq. (7.17) becomes

$$\hat{\rho}_d(\infty) = |d\rangle\langle d| \otimes \left[(1-x)\,|\alpha\rangle\langle\alpha| + x|\alpha^2| \sum_{l,l'\geq 0} K_{l,l'} \langle l'|\alpha\rangle\langle\alpha|l\rangle\,|l'\rangle\langle l|\right], \tag{7.21}$$

with

$$K_{l,l'} \equiv \left(1 + \frac{l+l'}{2} + \frac{(l-l')^2}{8m}\right)^{-1}, \tag{7.22}$$

in which

$$m = \frac{1}{2}\left(\frac{\gamma}{g}\right)^2 \tag{7.23}$$

is the particle-cavity critical photon number. The quantity m characterizes the nonlinearity of the particle-cavity interaction in the sense that the particle will undergo many (few) Rabi oscillations before emitting a spontaneous photon in the strong (weak)-coupling regime $m \ll 1$ ($m \gg 1$) [96].

Projecting $\langle b|$ and $|b\rangle$ on Eq. (7.16) and noting that the steady-state bright state population results from the cavity being in the vacuum state $|0\rangle$, we have

$$\hat{\rho}_b(\infty) = xe^{-|\alpha|^2}\,|b\rangle\langle b| \otimes |0\rangle\langle 0| \,. \tag{7.24}$$

Tracing over the atomic states, we find that the final cavity field state is

$$\hat{\rho}_L(\infty) = (1-x)\,|\alpha\rangle\,\langle\alpha| + x\hat{\rho}_c, \tag{7.25}$$

in which

$$\hat{\rho}_c = e^{-|\alpha|^2}\,|0\rangle\,\langle 0| + |\alpha|^2 \sum_{l,l'\geq 0} K_{l,l'}\,\langle l'|\alpha\rangle\,\langle\alpha|l\rangle\,|l'\rangle\,\langle l| \tag{7.26}$$

characterizes the effects of the interaction.

7.5 Q-function for the final cavity field state

To gain intuition for the differences between the initial and final cavity states, we calculate their Husimi Q-functions, which are defined as

$$Q(\beta) \equiv \frac{\langle\beta|\hat{\rho}|\beta\rangle}{\pi}. \tag{7.27}$$

Here, the coherent states $|\beta\rangle$ form a basis for the 2-dimensional optical phase space $(\mathrm{Re}(\beta), \mathrm{Im}(\beta))$. The initial cavity state has Q-function

$$Q_0(\beta) = \frac{\langle\beta|\hat{\rho}_L(0)|\beta\rangle}{\pi} = \frac{|\,\langle\alpha|\beta\rangle\,|^2}{\pi} = \frac{1}{\pi}e^{-|\alpha-\beta|^2}, \tag{7.28}$$

while the Q-function for the final cavity state is

$$Q_\infty(\beta) = \frac{\langle\beta|\hat{\rho}_L(\infty)|\beta\rangle}{\pi}. \tag{7.29}$$

The latter has a more complicated form since it is generally no longer a coherent state. Fig. 7.2 presents numerical plots of $Q_\infty(\beta)$ for various m. To focus on the effects of the interaction, we choose $x = 1$. We also choose $\alpha = 10$ so that $Q_0(\beta)$ is localized and centered on the coordinate $(\mathrm{Re}(\beta), \mathrm{Im}(\beta)) = (10, 0)$ with a spread on the order of unity.

Fig. 7.2(a) displays $Q_\infty(\beta)$ for the intermediate-coupling case $m = 1$. We find that $Q_\infty(\beta)$ does not differ significantly from $Q_0(\beta)$, which indicates that the cavity field nearly remains in a coherent state. In the case of stronger coupling [$m = 10^{-2}$, Fig. 7.2(b)], however, $Q_\infty(\beta)$ remains localized near $|\beta| = |\alpha|$, but is spread over a larger phase range $\Delta\phi$. In the infinite-coupling limit

$m \to 0$ [Fig. 7.2(c)], we find that $Q_\infty(\beta)$ has a uniform phase distribution, and therefore differs substantially from $Q_0(\beta)$.

Let us now interpret these results. The function $Q_\infty(\beta)$ always remains localized near the circle defined by $|\beta| = |\alpha| = 10$ because the average number of photons in the cavity

$$\bar{n} = \langle \hat{a}^\dagger \hat{a} \rangle \tag{7.30}$$

doesn't significantly change. This is a consequence of the particle's internal state structure [see Fig. 7.1(b)], which prevents a reduction of $\bar{n}$ by more than one, and our choice of a large initial intracavity photon number: $\bar{n}_0 \equiv \bar{n}(0) = 100 = |\alpha|^2$. On the other hand, we observe diffusion of the phase ϕ as m decreases because the particle undergoes more Rabi oscillations with each Fock state before emitting a spontaneous photon, thereby scrambling the cavity field's phase coherence. The coherences vanish completely in the limit $m \to 0$ (as can be seen from the m-dependence of $K_{l,l'}$ [Eq. (7.22)]), resulting in the uniform phase distribution shown in Fig. 7.2(c). This potentially extreme change in the phase distribution is largely responsible for the distinguishability of the initial and final cavity states, which we quantify in terms of their fidelity in the next section.

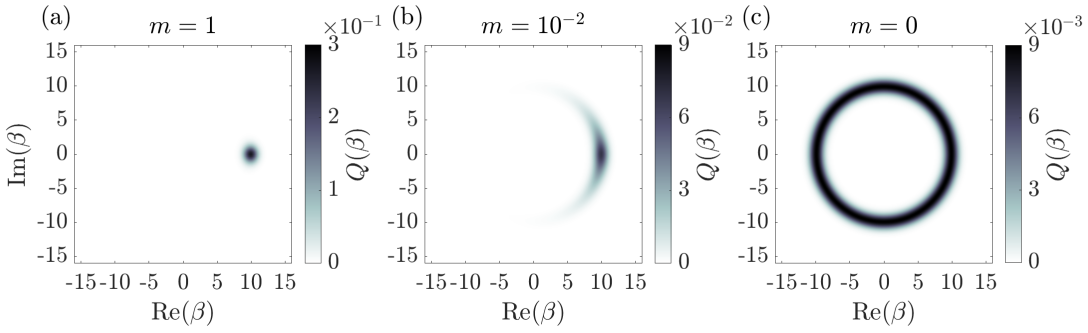

Figure 7.2: The Q-function $Q_\infty(\beta)$ for the final cavity state $\hat{\rho}_L(\infty)$ [see Eq. (7.29)] for various m. We set $x = 1$ and $\alpha = \sqrt{\bar{n}_0} = 10$. Although the amplitude of the state remains localized near $|\beta| = \sqrt{\bar{n}_0} = 10$, the spread in phase ϕ increases as m decreases.

7.6 Calculating the fidelity between the initial and final cavity field states

We now quantify the alteration of the cavity field by calculating the Uhlmann-Jozsa fidelity

$$F(\hat{\rho},\hat{\sigma}) = \left(\mathrm{Tr}\sqrt{\sqrt{\hat{\rho}}\hat{\sigma}\sqrt{\hat{\rho}}}\right)^2 \tag{7.31}$$

between its initial and final states, which is a generalization of the transition probability for pure states [89, 182]. The fidelity satisfies $0 \leq F(\hat{\rho},\hat{\sigma}) \leq 1$ for any two density matrices $\hat{\rho}$ and $\hat{\sigma}$, with $F(\hat{\rho},\hat{\sigma}) = 1$ if and only if $\hat{\rho} = \hat{\sigma}$, and $F(\hat{\rho},\hat{\sigma}) = 0$ if $\hat{\rho}$ and $\hat{\sigma}$ have support on orthogonal subspaces. In particular, if we find that $F(\hat{\rho},\hat{\sigma}) \neq 1$, then the cavity field is no longer in the coherent state $|\alpha\rangle$.

Because the cavity field is initially in a pure state, its fidelity with the final cavity state $\hat{\rho}_L(\infty)$ is simply

$$F \equiv F[\hat{\rho}_L(0),\hat{\rho}_L(\infty)] = \langle\alpha|\hat{\rho}_L(\infty)|\alpha\rangle\,. \tag{7.32}$$

We point out that $F = \pi Q_\infty(\alpha)$, i.e., the fidelity is (up to a factor of π) the Q-function of the final cavity state evaluated at $\beta = \alpha$. We can therefore qualitatively predict features of the fidelity F through the plots in Fig. 7.2. For example, we expect F to decrease as m decreases due to the associated diffusion of the Q-function.

As seen from Eq. (7.25),

$$F = 1 - x\left[1 - f(\bar{n}_0, m)\right], \tag{7.33}$$

in which

$$f(\bar{n}_0, m) \equiv e^{-2\bar{n}_0}\left(1 + \bar{n}_0 \sum_{l,l'\geq 0} K_{l,l'}\frac{\bar{n}_0^{l+l'}}{l!l'!}\right) \tag{7.34}$$

is the fidelity conditioned on the particle beginning in the bright state. We discuss this result in Section 7.7.

7.6.1 Fidelity in the thermodynamic limit

We now calculate an analytic expression for F in the thermodynamic limit $\bar{n}_0 \to \infty$, which is of interest if there are many photons in the cavity (as in laser cooling and optical pumping). Using

the Laplace transform of $K_{l,l'}$ [see Eq. (7.22)] and the Fourier transform of the resulting Gaussian term to reduce its order, we find that the sum in Eq. (7.34) can be rewritten as

$$\sum_{l,l'\geq 0} K_{l,l'} \frac{\bar{n}_0^{l+l'}}{l!l'!} = \int_{-\infty}^{\infty} du \int_0^{\infty} ds \sqrt{\frac{2m}{\pi s}} e^{-s} e^{2\bar{n}_0 e^{-s/2}\cos u} e^{-2mu^2/s}. \tag{7.35}$$

In the limit $\bar{n}_0 \gg 1$, the integrand in Eq. (7.35) is localized around $s = 0$ and $u = 2\pi p$, where p is an integer. This can be seen from the dominating term $\exp\left(2\bar{n}_0 e^{-s/2}\cos u\right)$. Expanding the argument of this term to lowest order in s and u, we find that

$$e^{2\bar{n}_0 e^{-s/2}\cos u} \approx e^{2\bar{n}_0} e^{-s\bar{n}_0} \sum_{p\in\mathbb{Z}} e^{-\bar{n}_0(u-2\pi p)^2}. \qquad (\bar{n}_0 \gg 1) \tag{7.36}$$

From this result, we see that the relevant domains are $0 < s < 1/\bar{n}_0$ and $|u - 2\pi p| < 1/\sqrt{\bar{n}_0}$.

Let us now consider the size of the integrand in Eq. (7.35) for fixed s. The Gaussian term $e^{-2mu^2/s}$ dampens the integrand for increasing u. Along with the term in Eq. (7.36), the integrand is maximized when $u = 0$, and the next largest maxima occur when $u = \pm 2\pi$. Therefore, we can neglect all the components other than $p = 0$ in Eq. (7.36) if the Gaussian term $e^{-2mu^2/s}$ is sufficiently small for all $p \neq 0$. This is true when

$$1 \gg e^{-8\pi^2 m/s} \quad \Longrightarrow \quad m > \frac{s}{8\pi^2}. \tag{7.37}$$

Because the largest relevant value is $s = 1/\bar{n}_0$, this condition is strictest when

$$m > m_{min} \equiv \frac{1}{8\pi^2 \bar{n}_0}. \tag{7.38}$$

Because we are interested in the thermodynamic limit $\bar{n}_0 \to \infty$, we can safely approximate Eq. (7.36) with only the $p = 0$ component, and our result will be valid for all m. Using these results, the sum in Eq. (7.35) becomes

$$\begin{aligned} \sum_{l,l'\geq 0} K_{l,l'} \frac{\bar{n}_0^{l+l'}}{l!l'!} &\approx e^{2\bar{n}_0} \int_{-\infty}^{\infty} du \int_0^{\infty} ds \sqrt{\frac{2m}{\pi s}} e^{-\bar{n}_0 s} e^{-(\bar{n}_0 + \frac{2m}{s})u^2} \\ &= \frac{e^{2\bar{n}_0}}{\bar{n}_0} \sqrt{2\pi m} e^{2m} \mathrm{erfc}(\sqrt{2m}). \end{aligned} \qquad (m > m_{min};\ \bar{n}_0 \gg 1) \tag{7.39}$$

Substituting the result into Eq. (7.33) and applying the thermodynamic limit $\bar{n}_0 \to \infty$, we find that

$$\lim_{\bar{n}_0\to\infty} F = 1 - x\left[1 - \sqrt{2\pi m} e^{2m} \mathrm{erfc}(\sqrt{2m})\right]. \tag{7.40}$$

7.7 Analyzing the fidelity result

We now analyze the fidelity F between the initial and final cavity states after its interaction with the particle, which was calculated in the previous section. But first, we address a common argument that claims that the cavity state should be unchanged ($F = 1$). It is often argued that a coherent state is unaffected by the interaction because it is an eigenstate of the annihilation operator $\hat{a}$ by definition: $\hat{a}\,|\alpha\rangle = \alpha\,|\alpha\rangle$, and therefore is unperturbed by photon absorption. However, what this argument fails to consider is the stimulated emission of a photon back into the cavity, which can occur if the particle-cavity coupling rate is sufficiently large. With this additional process in mind, we emphasize that a change of the cavity state is expected since it implies the action of the creation operator $\hat{a}^\dagger$ [see Eq. (7.2)] on the coherent state, which yields nontrivial dynamics [5].

Nevertheless, we have calculated the fidelity F between the initial and final cavity states [see Eq. (7.33)], and provide a numerical contour plot for the case $x = 1$ (so that $F = f$) in Fig. 7.3(a). We find that $f \ll 1$, and therefore that the cavity state is significantly altered, when $\bar{n}_0 \geq 1$ and $m < 1$. This region of parameter space corresponds to a cavity containing at least one photon (on average) and a strong cavity-particle coupling, respectively.

Because a cooling laser field contains many photons, we focus on the thermodynamic limit $\bar{n}_0 \to \infty$ for the remainder of our investigation, although we include some interesting results for finite $\bar{n}_0$ towards the end of the chapter in Section 7.11. Fig. 7.3(b) displays the corresponding fidelity [Eq. (7.40)], again for the choice $x = 1$, and a numerical result for $\bar{n}_0 = 10$, which agree very well when m is sufficiently large, i.e., it satisfies Eq. (7.38).

We now consider the strong ($m \ll 1$) and weak ($m \gg 1$) coupling limits. From Eqns. (7.33) and (7.40),

$$F \approx \begin{cases} 1 - x(1 - \sqrt{2\pi m}), & m \ll 1 \\ 1 - \dfrac{x}{4m}, & m \gg 1 \end{cases}. \tag{7.41}$$

Therefore, in the infinite-coupling limit $m \to 0$, the fidelity becomes $F = 1 - x$. This shows that the cavity field can be altered by the interaction provided that the particle has a chance of starting

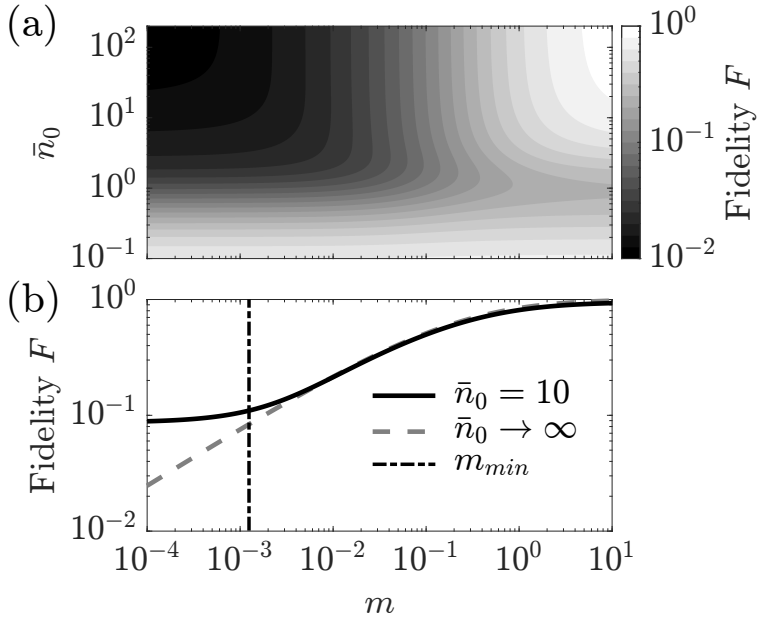

Figure 7.3: Fidelity F between the initial and final cavity states $\hat{\rho}_L(0)$ and $\hat{\rho}_L(\infty)$ [Eq. (7.31)] when the particle begins in the bright state [$x = 1$, see Eqns. (7.33) and (7.34)] as a function of the initial intracavity photon number $\bar{n}_0$ and the critical photon number m. (a) Contour plot of F. When $m < 1$ and $\bar{n}_0 > 1$, we find that $F \ll 1$, signaling a significant change in the cavity state. (b) Numerical (solid, $\bar{n}_0 = 10$) and analytical [dashed, Eq. (7.40)] results for F as a function of m. For $m < m_{min}$ [dot-dashed, Eq. (7.38)], the results diverge.

in the bright state ($0 \ll x \leq 1$). However, in the zero-coupling limit $m \to \infty$, we find that $F = 1$, and the field is not altered.

It is also interesting to consider how small the critical photon number must be for the initial and final cavity states to be substantially distinguishable, e.g., for their fidelity to be $F = \frac{1}{2}$. For simplicity and to achieve the greatest effect, we define such a critical photon number $m_{1/2}$ in the case when the particle is prepared in the bright state. From Eq. (7.40), we find that this occurs when

$$m = m_{1/2} \approx 0.0936. \tag{7.42}$$

One can therefore observe a substantial alteration of the cavity state in an experimental setting by studying a system satisfying $m \leq m_{1/2}$, or more generally, $g \geq 2.3\gamma \gg \kappa$.

These results are direct evidence that the cavity state can be altered by interaction with a particle, even in the limit of infinitely many photons, if the particle-cavity coupling is sufficiently

large. We interpret the deviation from $F = 1$ as result of the development of correlations between the particle and cavity states through the coherent interaction $\hat{H}_{AL}$ [see Eq. (7.2)].

7.8 Bayesian analysis

Now that we have demonstrated an alteration of the cavity state after interaction with the particle, we consider if any information about the particle is imprinted on the cavity field. As discussed in Section 7.5, the change of the cavity state manifests primarily in its phase. This suggests that simply measuring the field intensity

$$\langle \hat{a}^\dagger \hat{a}(\infty) \rangle = \bar{n}_0 - x(1 - e^{-\bar{n}_0}) \tag{7.43}$$

would not provide an effective way to extract this information, as it does not access the phase of the state. Moreover, the potentially broad photon number distribution could introduce photon shot noise. To create a measurement with which we can distinguish differences in both amplitude and phase, we construct a noise-reduced method that can in principle measure the information encoded in the cavity after a single experimental iteration. We first reduce the number of cavity photons by applying the inverse of the displacement operator defined by the initial coherent state:

$$\hat{\eta}_L \equiv \hat{D}(-\alpha)\hat{\rho}_L(\infty)\hat{D}^\dagger(-\alpha), \tag{7.44}$$

which can be done, e.g., by removing a cavity mirror at $t \to \infty$ and feeding the cavity state and a coherent state $|\alpha\rangle$ into separate ports of a beam splitter [144]. (We emphasize that any information about the particle contained in the cavity state is unaltered because this operation is unitary.)

Consider a situation wherein the particle is prepared in some diagonal mixed state [Eq. (7.4)], and we are tasked with determining the initial particle state ("start in $|b\rangle$" or "start in $|d\rangle$") for a given experimental run by performing measurements exclusively on the displaced cavity state $\hat{\eta}_L$. For simplicity, we calculate the results for the maximally mixed state ($x = \frac{1}{2}$), but our results can be generalized to any x. By symmetry, the most successful approach without performing any measurements would be to sample from a flat probability distribution (the "prior"):

$P(\text{start in } |b\rangle) = P(\text{start in } |d\rangle) = \frac{1}{2}$, for which the probability that we would be correct is $P_{\text{prior}}(\text{correct}) = \frac{1}{2}$. What we show here is that a more accurate probability distribution can be constructed by incorporating the results from a single measurement of the displaced cavity photon number distribution $\langle n|\hat{\eta}_L|n\rangle$, thereby proving that information about the particle is present in the cavity field.

For our purposes, it is sufficient to reduce the outcome space to a binary scenario: either we detect (i) zero photons ($n = 0$, "no click") or (ii) one or more photons ($n \geq 1$, "click(s)"). This simplification is appropriate because we gain no additional information about the particle's initial state by distinguishing between nonzero numbers of clicks. With this approach, we only need to calculate the vacuum state population $\langle 0|\hat{\eta}_L|0\rangle$, which is conveniently equivalent to the fidelity F [see Eq. (7.33)]. Notice that one can experimentally probe F by measuring this population. The probability distribution in the event of "no clicks" is then

$$P(\text{no click}|\text{start in } |i\rangle) = \begin{cases} 1, & i = d \\ f(\bar{n}_0, m), & i = b \end{cases}, \tag{7.45}$$

where $f(\bar{n}_0, m)$ is the conditional fidelity. The "click(s)" conditional probability distribution is complementary to Eq. (7.45). With these results, we can use Bayesian inference to construct a posterior probability distribution for the initial particle state conditioned on the cavity measurement:

$$\begin{gathered} P(\text{start in } |i\rangle\,|C) \propto P(C|\text{start in } |i\rangle)P(\text{start in } |i\rangle); \\ i \in \{b, d\}; \quad C \in \{\text{click(s)}, \text{no click}\}. \end{gathered} \tag{7.46}$$

Here, $P(\text{start in } |i\rangle)$ is the (initially flat) prior distribution for the initial particle state [83]. The posterior probability distribution is

$$\begin{aligned} P(\text{start in } |d\rangle \,|\, \text{click(s)}) &= 0; \\ P(\text{start in } |b\rangle \,|\, \text{click(s)}) &= 1; \\ P(\text{start in } |d\rangle \,|\, \text{no click}) &= \frac{1}{1 + f(\bar{n}_0, m)}; \\ P(\text{start in } |b\rangle \,|\, \text{no click}) &= \frac{f(\bar{n}_0, m)}{1 + f(\bar{n}_0, m)}. \end{aligned} \tag{7.47}$$

It is only left to demonstrate that the posterior probability distribution predicts the initial particle state more accurately than the prior probability distribution, i.e., that we would correctly predict the initial particle state with a probability satisfying $P_{\text{post}}(\text{correct}) > P_{\text{prior}}(\text{correct}) = \frac{1}{2}$, by sampling from Eqns. (7.47). Using the posterior probability distribution, the probability that we correctly predict the initial particle state is

$$P_{\text{post}}(\text{correct}) = \frac{1}{1 + f(\bar{n}_0, m)}. \tag{7.48}$$

Since $0 < f(\bar{n}_0, m) < 1$, we find that $P_{\text{post}}(\text{correct}) \geq \frac{1}{2}$, and therefore conclude that information about the particle is present in the cavity field. We emphasize that we have increased our chance of predicting the initial particle state with a single measurement of the cavity state.

We now focus on the thermodynamic limit $\bar{n}_0 \to \infty$, as often occurs in laser cooling and optical pumping. In this limit, the conditional fidelity f is given by Eq. (7.40). Using this form of f in Eq. (7.48), we find that

$$P_{\text{post}}(\text{correct}) \approx \begin{cases} 1 - \sqrt{2\pi m}, & m \ll 1 \\ \dfrac{1}{2}\left(1 + \dfrac{1}{8m}\right), & m \gg 1 \end{cases}. \tag{7.49}$$

In the infinite-coupling limit $m \to 0$, $P_{\text{post}}(\text{correct}) = 1$. Therefore, a single measurement of the cavity state can in principle predict the initial particle state with 100% accuracy, regardless of the high-noise photon statistics. This is possible because in this limit the equilibrium cavity states resulting from the particle starting in $|b\rangle$ and $|d\rangle$ have orthogonal support, as evidenced by their vanishing fidelity {see Eq. (7.33) and Ref. [108]}. In the zero-coupling limit $m \to \infty$, however, $P_{\text{post}}(\text{correct}) = \frac{1}{2} = P_{\text{prior}}(\text{correct})$, so the cavity measurement does not increase our chance of predicting the initial particle state.

7.9 Calculating entropies and mutual information

In the next two sections, we switch gears and investigate the particle-field interaction through the lens of information theory, which provides us with a way to quantify the entropy transfer process. This perspective is appropriate because because we posit that the amount of transferred

entropy is characterized by the mutual information [139] shared between the initial particle state and the equilibrium cavity state. To connect the formalism of this section with the Bayesian inference approach of the previous section, we first calculate the amount of mutual information shared between the initial particle state and final cavity field as determined by the classical conditional probability distribution we derived through the photon number measurements [Eqns. (7.47)]. Then, we calculate their quantum mutual information from a density matrix approach, which incorporates all particle-cavity correlations. We reserve the analysis of these results for Section 7.10.

We briefly reminder the reader of some essential concepts from information theory. In general, mutual information is defined as

$$I(Y:Z) = S(Y) + S(Z) - S(YZ) = S(Y) - S(Y|Z), \tag{7.50}$$

in which Y and Z are probability distributions, $\{S(Y), S(Z)\}$ are their information entropies, $S(YZ)$ is their joint entropy, and $S(Y|Z)$ is the conditional entropy of Y given Z. The entropy S is given by the Shannon entropy

$$S(Y_{\rm cl}) = -\sum_y P(y) \ln P(y) \tag{7.51}$$

for a classical probability distribution $Y_{\rm cl}$ with events y and probabilities $P(y)$, whereas it is given by the von Neumann entropy

$$S(\hat{\rho}_Y) \equiv -{\rm Tr}\left[\hat{\rho}_Y \ln \hat{\rho}_Y\right]. \tag{7.52}$$

for a quantum probability distribution, which is described by a density matrix $\hat{\rho}_Y$. Intuitively, $I(Y:Z)$ is equal to zero in the absence of any correlations between the two distributions, and is maximized if the higher-entropy distribution contains all of the information of the lower-entropy distribution:

$$\begin{aligned} 0 \leq I(Y_{\rm cl}:Z_{\rm cl}) &\leq \min[S(Y_{\rm cl}), S(Z_{\rm cl})], \\ 0 \leq I(\hat{\rho}_Y:\hat{\rho}_Z) &\leq 2\min[S(\hat{\rho}_Y), S(\hat{\rho}_Z)]. \end{aligned} \tag{7.53}$$

Notice that the upper bound of quantum mutual information is twice as large as its classical counterpart [106].

7.9.1 Mutual information from cavity measurements

Here we calculate the (classical) mutual information [Eq. (7.50)] between the initial particle state and equilibrium cavity state as determined by the cavity measurements introduced in Section 7.8. Using the click probabilities from Eq. (7.33), the notation of Eq. (7.46), and generalizing the conditional probability distribution in Eqns. (7.47) to any x, the conditional entropy of the initial particle state given the cavity measurements is

$$\begin{aligned} S[A(0)|L(\infty)] &= -\sum_{C,i} P(C)P(\text{start in } |i\rangle\,|C)\ln[P(\text{start in } |i\rangle\,|C)] \\ &= -xf\ln\left[\frac{fx}{1-x(1-f)}\right] - (1-x)\ln\left[\frac{1-x}{1-x(1-f)}\right]. \end{aligned} \tag{7.54}$$

From the classical mixture in Eq. (7.4), the Shannon entropy of the initial state is

$$S[A(0)] \equiv S_0 = -x\ln x - (1-x)\ln(1-x). \tag{7.55}$$

Together, Eqns. (7.54) and (7.55) can be used to calculate the mutual information [Eq. (7.50)] between the initial particle state and equilibrium cavity state as determined by the cavity measurements:

$$I[A(0) : L(\infty)] = S[A(0)] - S[A(0)|L(\infty)]. \tag{7.56}$$

7.9.2 Quantum mutual information

Let us now explain how to calculate the quantum mutual information between the initial particle state and final cavity state. As seen from Eq. (7.50), this calculation requires knowing the joint distribution of these two states. Because these states are defined at different times, we calculate their joint distribution by incorporating an non-interacting auxiliary Hilbert space R which purifies $\hat{\rho}_A(0)$ and hence contains the entropy of $\hat{\rho}_A(0)$ at all times. We purify the initial particle state through its Schmidt decomposition. That is, we view the particle ensemble as the reduced density matrix of a pure state, $\hat{\rho}_A(0) = \mathrm{Tr}_R\,|u\rangle\,\langle u|_{AR}$, where

$$|u\rangle_{AR} = \sum_i \sqrt{\beta_i}\,|\psi_i\rangle_A \otimes |\phi_i\rangle_R\,. \tag{7.57}$$

Here, $|\psi_n\rangle_A$ is an eigenvector of $\hat{\rho}_A(0)$ with eigenvalue β_n and $|\phi_n\rangle_R \in R$ for an auxiliary Hilbert space R. It can be shown that the reduced density matrices $\hat{\rho}_A(0)$ and $\hat{\rho}_R$ have the same eigenvalues [139], which motivates the interpretation of $\hat{\rho}_R = \mathrm{Tr}_A\,|u\rangle\langle u|_{AR}$ as an identically prepared ensemble to $\hat{\rho}_A(0)$, but with particles that are not interacting with the field. The total system's density matrix becomes $\hat{\rho}_{ARL}$, and the master equation [Eq. (7.1)] is edited by incorporating the identity operator of R:

$$\hat{H}_{AL} \to \hat{H}_{AL} \otimes \hat{\mathbb{I}}_R; \qquad \hat{J} \to \hat{J} \otimes \hat{\mathbb{I}}_R. \tag{7.58}$$

This updated master equation is then used to evolve the initial pure state

$$\hat{\rho}_{ARL}(0) = |u\rangle\langle u|_{AR} \otimes |\alpha\rangle\langle\alpha|_L\,. \tag{7.59}$$

We can then calculate the entropy of any subset of the ARL composite Hilbert space by performing the appropriate trace operations.

Using this formalism, the quantum mutual information

$$I(\hat{\rho}_R : \hat{\rho}_L) = S(\hat{\rho}_R) + S(\hat{\rho}_L) - S(\hat{\rho}_{RL}), \tag{7.60}$$

can then be calculated as follows. Because we prepare the initial particle state as

$$\hat{\rho}_A(0) = x\,|b\rangle\langle b| + (1-x)\,|d\rangle\langle d|\,, \tag{7.61}$$

then it follows that an appropriate Schmidt decomposition is

$$|u\rangle_{AR} = \sqrt{x}\,|b,b\rangle + \sqrt{1-x}\,|d,d\rangle\,. \tag{7.62}$$

The corresponding initial (pure) state of the entire ARL (particle + auxiliary particle + cavity) system is then

$$\begin{aligned}\hat{\rho}_{ARL}(0) &= |u\rangle\langle u|_{AR} \otimes |\alpha\rangle\langle\alpha| \\ &= \Big\{x\,|b,b\rangle\langle b,b| + (1-x)\,|d,d\rangle\langle d,d| + \sqrt{x(1-x)}\,[|b,b\rangle\langle d,d| + \text{h.c.}]\Big\} \otimes |\alpha\rangle\langle\alpha|\,.\end{aligned} \tag{7.63}$$

We now evolve each term in Eq. (7.63) to its corresponding equilibrium state by using Eqns. (7.21) and (7.24):

$$\begin{aligned}\hat{\rho}_{ARL}(\infty) = \\ x\left|b\right\rangle\left\langle b\right|_R \otimes \left(e^{-\bar{n}_0}\left|b\right\rangle\left\langle b\right|_A \otimes \left|0\right\rangle\left\langle 0\right|_L + \bar{n}_0\left|d\right\rangle\left\langle d\right|_A \otimes \sum_{l,l'\geq 0} K_{l,l'}\left\langle l'|\alpha\right\rangle\left\langle \alpha|l\right\rangle\left|l'\right\rangle\left\langle l\right|_L \right) \\ + (1-x)\left|d,d\right\rangle\left\langle d,d\right| \otimes \left|\alpha\right\rangle\left\langle\alpha\right| + \sqrt{x(1-x)}e^{-\bar{n}_0/2}\left(\left|b,b\right\rangle\left\langle d,d\right| \otimes \left|0\right\rangle\left\langle\alpha\right|_L + \text{h.c.}\right).\end{aligned} \tag{7.64}$$

From this result, the reduced density matrices in the RL, R, and L subspaces are

$$\begin{aligned}\hat{\rho}_{RL}(\infty) &= x\left|b\right\rangle\left\langle b\right| \otimes \hat{\rho}_c + (1-x)\left|d\right\rangle\left\langle d\right| \otimes \left|\alpha\right\rangle\left\langle\alpha\right|; \\ \hat{\rho}_R(\infty) &= x\left|b\right\rangle\left\langle b\right| + (1-x)\left|d\right\rangle\left\langle d\right|; \\ \hat{\rho}_L(\infty) &= x\hat{\rho}_c + (1-x)\left|\alpha\right\rangle\left\langle\alpha\right|,\end{aligned} \tag{7.65}$$

where $\hat{\rho}_c$ is given in Eq. (7.26). Notice that $\hat{\rho}_{RL}(\infty)$ is separable, and is therefore not an entangled state. The quantum mutual information $I(\hat{\rho}_R : \hat{\rho}_L)$ [Eq. (7.60)] can be calculated (at least numerically) directly from this result. We can simplify the result, however, since some of the von Neumann entropies can be expressed in terms of the quantity $S(\hat{\rho}_c)$:

$$\begin{aligned}S[\hat{\rho}_{RL}(\infty)] &= S_0 + xS(\hat{\rho}_c); \\ S[\hat{\rho}_R(\infty)] &= S_0,\end{aligned} \tag{7.66}$$

in which $S_0 \equiv S[\hat{\rho}_A(0)]$. We do not investigate the behavior of $S(\hat{\rho}_c)$, but we emphasize that $\hat{\rho}_c$ is generally not pure, and hence has nonzero entropy. The von Neumann entropy of the L subspace $S[\hat{\rho}_L(\infty)]$ is harder to calculate analytically because $\hat{\rho}_c$ and $\left|\alpha\right\rangle\left\langle\alpha\right|$ do not always have orthogonal support. We can, however, use the identity [139]

$$\sum_i p_i S(\hat{\rho}_i) \leq S\left(\sum_i p_i\hat{\rho}_i\right) \leq \sum_i p_i S(\hat{\rho}_i) - \sum_i p_i \ln p_i \tag{7.67}$$

to place an upper and lower bound on the cavity field entropy. From Eqns. (7.65) and (7.67),

$$xS(\hat{\rho}_c) \leq S[\hat{\rho}_L(\infty)] \leq S_0 + xS(\hat{\rho}_c). \tag{7.68}$$

The upper bound is saturated only if $\hat{\rho}_c$ and $\left|\alpha\right\rangle\left\langle\alpha\right|$ have orthogonal support.

7.10 Analyzing the entropies and mutual information

We now analyze the results of the entropic perspective introduced in the previous section. Because the cavity state is inherently quantum, the photon click measurements (which correspond to the diagonal elements of the cavity density matrix) may not reveal all of the information contained in the light field. Consequently, Eq. (7.56) underestimates the amount of mutual information shared between the particle and cavity, so we will mostly use the results from the quantum calculation. However, Eq. (7.56) is useful for approximating the quantum mutual information in the thermodynamic limit $\bar{n}_0 \to \infty$, for which numerical calculations are intractable due to the infinite dimension of the cavity Hilbert space.

It is useful to first consider the upper and lower bounds of the quantum mutual information. Because $\hat{\rho}_{RL}$ is separable [see Eq. (7.65)], the quantum mutual information satisfies Eq. (7.53) without the factor of 2 [139]:

$$0 \leq I[\hat{\rho}_R(\infty) : \hat{\rho}_L(\infty)] \leq \min\{S_0, S[\hat{\rho}_L(\infty)]\} \leq S_0, \tag{7.69}$$

in which $S_0 \equiv S[\hat{\rho}_A(0)]$. In other words, somewhere between none [$I(\hat{\rho}_R : \hat{\rho}_L) = 0$] or all [$I(\hat{\rho}_R : \hat{\rho}_L) = S_0$] of the entropy initially contained in the particle becomes encoded in the cavity field. An important consequence of the classicality of Eq. (7.69) is that the spontaneous photons escaping the system contain all of the information that becomes imprinted on the final cavity state, which we demonstrate in Section 7.10.1.

Fig. 7.4(a) presents various quantum entropic quantities as a function of time t for the choices $x = m = \frac{1}{2}$ and $\alpha = \sqrt{\bar{n}_0} = \sqrt{5}$. These results were calculated by numerically evolving the quantum master equation [Eq. (7.1)] with the aforementioned adjustments [Eqns. (7.58) and (7.59)], and then calculating the von Neumann entropies [Eq. (7.52)] and quantum mutual information [Eq. (7.60)] of the various subspaces. For convenience, we have scaled all quantities by the initial particle entropy S_0. As expected, the particle entropy $S[\hat{\rho}_A(t)]$ decreases (as occurs in laser cooling and optical pumping), the cavity state entropy $S[\hat{\rho}_L(t)]$ increases, and the entire ARL space entropy increases as it evolves under the non-unitary dynamics. Importantly, the quantum mutual information

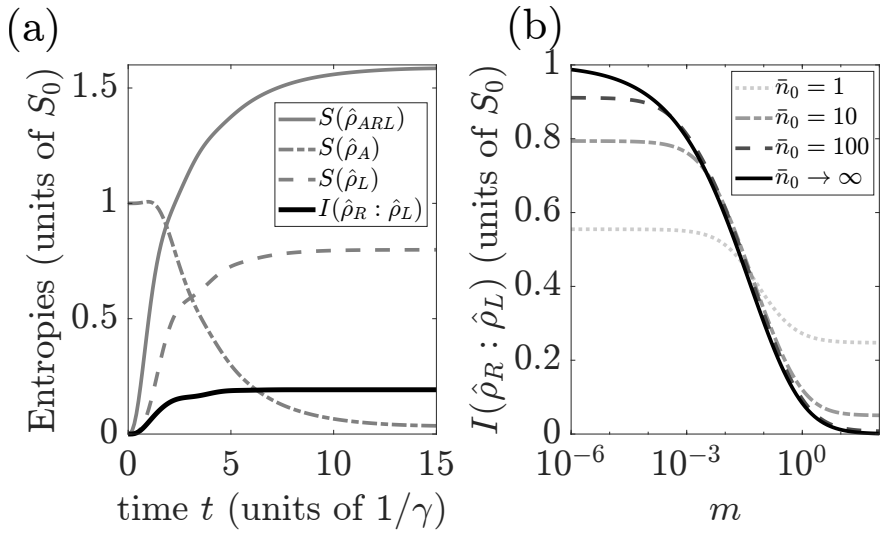

Figure 7.4: Entropic quantities scaled by the initial particle entropy $S_0 \equiv S[\hat{\rho}_A(0)]$. (a) von Neumann entropies $S[\hat{\rho}_M(t)]$ [see Eq. (7.52)] of various subspaces M and quantum mutual information between the field and auxiliary particle $I(\hat{\rho}_R : \hat{\rho}_L)$ [see Eq. (7.60)] as a function of time t. Parameters: $x = 0.5$, $m = 0.5$, and $\bar{n}_0 = 5$. (b) Equilibrium $I(\hat{\rho}_R : \hat{\rho}_L)$ as a function of m for various $\bar{n}_0$ with $x = 0.5$. The $\bar{n}_0 \to \infty$ curve is given by Eq. (7.56). The quantum mutual information reaches its maximum value $I(\hat{\rho}_R : \hat{\rho}_L) = S_0$ [see Eq. (7.69)] in the thermodynamic, infinite-coupling limit: $(\bar{n}_0, m) \to (\infty, 0)$.

$I(\hat{\rho}_R : \hat{\rho}_L)$ increases and equilibrates to a nonzero value, which indicates the imprinting of the particle's initial entropy onto the cavity field.

We present numerical results for the equilibrium value of $I(\hat{\rho}_R : \hat{\rho}_L)$, scaled by S_0, as a function of m for various $\bar{n}_0$ in Fig. 7.4(b) (non-solid curves). These are calculated from the equilibrium density matrices [Eq. (7.65)]. We find that $I(\hat{\rho}_R : \hat{\rho}_L)$ can be as large as $S_0/2$, and hence that a significant amount of information about the initial particle state can be imprinted on the cavity field, for $\bar{n}_0 \geq 1$, provided that m is sufficiently small. As $\bar{n}_0$ increases, we find numerically that the equilibrium quantum mutual information [Eq. (7.60) with the density matrices given by Eq. (7.65)] and mutual information as determined by the cavity measurements [Eq. (7.56)] converge. Therefore, we use Eq. (7.56) to analytically calculate the equilibrium value of $I(\hat{\rho}_R : \hat{\rho}_L)$ in the thermodynamic

limit $\bar{n}_0 \to \infty$ (solid curve). In the strong and weak-coupling limits, this simplifies to

$$I(\hat{\rho}_R : \hat{\rho}_L) \approx \begin{cases} S_0 - \epsilon(x,m), & m \ll \min\left[1, \frac{1}{2\pi}\left(\frac{1-x}{x}\right)^2\right] \\ -\frac{x \ln x}{4m}, & m \gg 1 \end{cases}, \tag{7.70}$$

in which

$$\epsilon(x,m) = -\sqrt{2\pi m}\left[\ln\sqrt{2\pi m} + \ln\left(\frac{x}{1-x}\right) - 1\right] \tag{7.71}$$

is a small positive number. The additional constraint on m in the strong-coupling limit is a consequence of the highly nonlinear behavior of $I(\hat{\rho}_R : \hat{\rho}_L)$ for small m. In the zero-coupling limit $m \to \infty$, we find that $I(\hat{\rho}_R : \hat{\rho}_L) = 0$, so the cavity field does not contain the information entropy of the initial particle state, as expected. However, in the infinite-coupling limit $m \to 0$, we find that $I(\hat{\rho}_R : \hat{\rho}_L) = S_0$, which means that the cavity field contains complete information about the initial particle state. This agrees with our Bayesian inference result in Section 7.8.

Let us now prove analytically that the cavity contains complete information about the particle only in the thermodynamic, high-coupling limit, i.e., that $I(\hat{\rho}_R : \hat{\rho}_L) = S_0$ if $\bar{n}_0 \to \infty$ and $m \to 0$. From Eq. (7.68), this occurs only if the density matrices $\hat{\rho}_c$ and $|\alpha\rangle\langle\alpha|$ have orthogonal support [139]. This condition is equivalent to

$$F(\hat{\rho}_c, |\alpha\rangle\langle\alpha|) = 0, \tag{7.72}$$

where F is the fidelity [see Eq. (7.31)]. Using Eq. (7.25), this can be rewritten as

$$e^{-2\bar{n}_0}\left(1 + \bar{n}_0 \sum_{l,l' \geq 0} K_{l,l'} \frac{\bar{n}_0^{l+l'}}{l!l'!}\right) = 0. \tag{7.73}$$

Because the term in parentheses is positive, the only way to satisfy Eq. (7.73) is to consider the thermodynamic limit $\bar{n}_0 \to \infty$, for which the exponential tends to zero. In this limit, we can then use Eq. (7.39) to simplify Eq. (7.73) to

$$\sqrt{2\pi m} e^{2m} \mathrm{erfc}(\sqrt{2m}) = 0, \tag{7.74}$$

which is true only when $m \to 0$. Therefore, we come to the conclusion that $I(\hat{\rho}_R : \hat{\rho}_L) = S_0$, and therefore that the cavity state contains all of the information about the initial particle state, only in the high-coupling ($m \to 0$), thermodynamic ($\bar{n}_0 \to \infty$) limit.

7.10.1 Entropy of the spontaneous photon

We previously claimed that the spontaneous photon emitted by the particle contains all of the information that becomes encoded in the cavity state. We prove this claim here.

Consider the quantum state describing the particle A, cavity field L, and environment P (which we modeled as an infinite bandwidth bosonic bath). We remind the reader that in Section 2.1.5 we discussed how the environment is responsible for the emission of spontaneous photons by the particle. In our Gedankenexperiment, these three subspaces constitute the entire universe, i.e., they form a closed system and undergo unitary evolution. If we purify the particle state (as done previously) with the auxiliary Hilbert space R, then the density matrix of the entire system at any time t is

$$\hat{\rho}_{ARLP}(t) = |\Psi_{ARLP}(t)\rangle \langle \Psi_{ARLP}(t)| , \tag{7.75}$$

which is obviously pure. It follows that the entanglement entropy between the ARL and P subsystems satisfies

$$S[\hat{\rho}_{ARL}(t)] = S[\hat{\rho}_P(t)]. \tag{7.76}$$

Suppose we propagate the entire $ARLP$ system to equilibrium. For $\bar{n}_0 \gg 1$, the equilibrium particle state $\hat{\rho}_A(\infty)$ is approximately pure (or completely pure for $\bar{n}_0 \to \infty$) because the particle almost certainly ends in the dark state $|d\rangle$:

$$\hat{\rho}_A(\infty) = xe^{-\bar{n}_0} |b\rangle \langle b| + (1 - xe^{-\bar{n}_0}) |d\rangle \langle d| \approx |d\rangle \langle d| . \tag{7.77}$$

It immediately follows that

$$\hat{\rho}_{ARL}(\infty) \approx |d\rangle \langle d| \otimes \hat{\rho}_{RL}(\infty). \tag{7.78}$$

The entanglement entropy is then

$$S[\hat{\rho}_{ARL}(\infty)] \approx S[\hat{\rho}_{RL}(\infty)] = S_0 + xS(\hat{\rho}_c), \tag{7.79}$$

in which we used Eq. (7.66). Combining this result with Eqns. (7.68) and (7.76),

$$S[\hat{\rho}_L(\infty)] \leq S_0 + xS(\hat{\rho}_c) = S[\hat{\rho}_{RL}(\infty)] \approx S[\hat{\rho}_{ARL}(\infty)] = S[\hat{\rho}_P(\infty)], \tag{7.80}$$

or

$$S[\hat{\rho}_L(\infty)] \leq S[\hat{\rho}_P(\infty)]. \tag{7.81}$$

Eq. (7.81) states that the environment $S[\hat{\rho}_P(\infty)]$ always absorbs at least as much information entropy as the equilibrium cavity state. Therefore, spontaneous emission is always a sufficient mechanism for the removal of entropy from the system.

7.11 Additional calculations

In this section, we provide some additional calculations that may be of interest in future work. First, we calculate the complete photon number distribution of the displaced cavity state $\langle n|\hat{\eta}_L|n\rangle$ in the large (but not necessarily infinite) $\bar{n}_0$ limit for arbitrary m, and then in the infinite-coupling limit $m \to 0$ with arbitrary $\bar{n}_0$. We then calculate the fidelity F in the infinite-coupling limit for arbitrary $\bar{n}_0$, which may be particularly interesting for studies of cavity QED interactions between low-photon states and single particles.

Two useful equations in the infinite-coupling limit are the simplification of Eq. (7.22) to

$$K_{l,l'} = \delta_{l,l'} \frac{1}{1+l}, \qquad (m = 0) \tag{7.82}$$

where $\delta_{l,l'}$ is the Kronecker delta, and the simplification of Eq. (7.25) to

$$\hat{\rho}_L(\infty) = (1-x)\,|\alpha\rangle\langle\alpha| + xe^{-\bar{n}_0}\left(|0\rangle\langle 0| + \sum_{n\geq 0} \frac{\bar{n}_0^{n+1}}{(n+1)!}\,|n\rangle\langle n|\right). \qquad (m = 0) \tag{7.83}$$

7.11.1 Displaced final cavity field photon distribution

Here we calculate the photon number distribution of the final cavity field state after action of the displacement operator $\hat{D}(-\alpha)$:

$$\hat{\eta}_L \equiv \hat{D}(-\alpha)\hat{\rho}_L(\infty)\hat{D}(\alpha). \tag{7.84}$$

As seen from Eq. (7.25),

$$\langle n|\hat{\eta}_L|n\rangle = (1-x)\delta_{n,0} + x\left(\frac{e^{-2\bar{n}_0}\bar{n}_0^n}{n!} + \bar{n}_0 T_n\right), \tag{7.85}$$

in which

$$T_n \equiv \sum_{l,l' \geq 0} K_{l,l'} \langle l'|\alpha\rangle \langle \alpha|l\rangle \langle n|\hat{D}(-\alpha)|l'\rangle \langle l|\hat{D}(\alpha)|n\rangle \,. \tag{7.86}$$

Using the ladder operations

$$\hat{a}^\dagger |l\rangle = \sqrt{l+1}\,|l+1\rangle\,; \qquad \hat{a}\,|l\rangle = \sqrt{l}\,|l-1\rangle \tag{7.87}$$

and displacement operator identities

$$\hat{D}^\dagger(\alpha)\hat{a}\hat{D}(\alpha) = \hat{a} + \alpha; \qquad \hat{D}(\alpha)\hat{a}\hat{D}^\dagger(\alpha) = \hat{a} - \alpha; \qquad \hat{D}(-\alpha) = \hat{D}^\dagger(\alpha), \tag{7.88}$$

we find that

$$T_n = \frac{e^{-2\bar{n}_0}\bar{n}_0^n}{n!} \sum_{p,q=0}^{n} \binom{n}{p}\binom{n}{q}(-1)^{q+p} \sum_{l,l' \geq 0} K_{l+p,l'+q} \frac{\bar{n}_0^{l+l'}}{l!l'!} \tag{7.89}$$

Using the Laplace transform of $K_{j+p,j'+q}$ [see Eq. (7.22)] and the Fourier transform of the resulting Gaussian term to reduce its order, we find that

$$T_n = \frac{e^{-2\bar{n}_0}\bar{n}_0^n}{n!} \int_{-\infty}^{\infty} du \int_0^\infty ds \sqrt{\frac{2m}{\pi s}} e^{-s} \left(1 + e^{-s} - 2e^{-s/2}\cos u\right)^n e^{2\bar{n}_0 e^{-s/2}\cos u} e^{-2mu^2/s}. \tag{7.90}$$

In the following two subsections, we compute $\langle n|\hat{\eta}_L|n\rangle$ under approximations which depend on the values of m and $\bar{n}_0$.

7.11.1.1 $\bar{n}_0 \gg 1, m > m_{min}$

If we are interested in the regime $\bar{n}_0 \gg 1$, we can use the same argument as in Section 7.6.1 to simplify T_n. Using Eq. (7.36) with only the $l = 0$ term in Eq. (7.90), we find that we can approximate T_n as

$$T_n \approx \frac{\bar{n}_0^n}{n!} \int_{-\infty}^{\infty} du \int_0^\infty ds \sqrt{\frac{2m}{\pi s}} e^{-\bar{n}_0 s} u^{2n} e^{-(\bar{n}_0 + \frac{2m}{s})u^2}. \qquad (m > m_{min};\, \bar{n}_0 \gg 1, m, n) \tag{7.91}$$

Integrating over u and using Tricomi's confluent hypergeometric function [154], which has integral representation

$$U(a,b,z) = \frac{1}{\Gamma(a)} \int_0^\infty dt\, e^{-zt} t^{a-1}(1+t)^{b-a-1}, \qquad (\mathrm{Re}\, a > 0) \tag{7.92}$$

we can write the approximate form of T_n as

$$T_n \approx \frac{2(2n)!m}{4^n n!\bar{n}_0} U\left(n+1, \frac{3}{2}, 2m\right). \qquad (\bar{n}_0 \gg 1, n;\ m > m_{min}) \tag{7.93}$$

Substituting this result into Eq. (7.86) and taking the thermodynamic limit $\bar{n}_0 \to \infty$, we find that

$$\lim_{\bar{n}_0\to\infty} \langle n|\hat{\eta}_L|n\rangle = (1-x)\delta_{n,0} + x\,\frac{2(2n)!m}{4^n n!} U\left(n+1, \frac{3}{2}, 2m\right). \tag{7.94}$$

Invoking Stirling's approximation, this can be further simplified for $n \geq 1$ to

$$\lim_{\bar{n}_0\to\infty} \langle n|\hat{\eta}_L|n\rangle \approx x\, 2\sqrt{2} e^{-n} n^n m\, U\left(n+1, \frac{3}{2}, 2m\right). \qquad (n \geq 1) \tag{7.95}$$

7.11.1.2 $m \to 0$ and finite $\bar{n}_0$

When $m \to 0$, we can no longer neglect the $l \neq 0$ terms in Eq. (7.36). In this case, we instead use Eq. (7.83) and find that

$$\langle n|\hat{\eta}_L|n\rangle = (1-x)\delta_{n,0} + xe^{-\bar{n}_0}\left(\left|\langle n|\hat{D}(-\alpha)|0\rangle\right|^2 + \sum_{k\geq 0}\frac{\bar{n}_0^{k+1}}{(k+1)!}\left|\langle k|\hat{D}(\alpha)|n\rangle\right|^2\right). \qquad (m=0) \tag{7.96}$$

Using the identity

$$\langle k|\hat{D}(\alpha)|n\rangle = \sqrt{\frac{n!}{k!}}\alpha^{k-n} e^{-|\alpha|^2/2} L_n^{(k-n)}(|\alpha|^2) \tag{7.97}$$

when $k \geq n$ [26, 55], Eq. (7.96) simplifies to

$$\begin{aligned}\langle n|\hat{\eta}_L|n\rangle = (1-x)\delta_{n,0} + xe^{-2\bar{n}_0}\Bigg\{ &\frac{\bar{n}_0^n}{n!} + \frac{\bar{n}_0^{n+1}}{n!}\sum_{k=0}^{n-1}\frac{1}{1+k}\left[L_k^{(n-k)}(\bar{n}_0)\right]^2 \\ &+ \frac{n!}{\bar{n}_0^{n-1}}\sum_{k\geq n}\frac{1}{1+k}\left[\frac{\bar{n}_0^k}{k!}L_n^{(k-n)}(\bar{n}_0)\right]^2\Bigg\},\end{aligned} \qquad (m=0) \tag{7.98}$$

where $L_p^{(q)}(r)$ are the generalized Laguerre polynomials. Using the identity

$$\frac{(-x)^n}{n!}L_k^{(n-k)}(x) = \frac{(-x)^k}{k!}L_n^{(k-n)}(x) \tag{7.99}$$

which is valid for all integer n and k, we can simplify Eq. (7.98) to

$$\langle n|\hat{\eta}_L|n\rangle = (1-x)\delta_{n,0} + x\frac{\bar{n}_0^n e^{-2\bar{n}_0}}{n!}\left[1 + \bar{n}_0 S_n(\bar{n}_0)\right], \qquad (m=0) \tag{7.100}$$

in which

$$S_n(\bar{n}_0) = \sum_{k\geq 0} \frac{1}{1+k}\left[L_k^{(n-k)}(\bar{n}_0)\right]^2 \approx \frac{e^{2\bar{n}_0}}{\bar{n}_0^{n+1}}\frac{(2n)!}{n!}\frac{1}{4^n}\frac{1}{2\sqrt{\pi\bar{n}_0}}. \tag{7.101}$$

The last equality, which is valid when $\bar{n}_0 \gg n$, is demonstrated in Section 7.11.1.3. Using this result in Eq. (7.100), we arrive at the displaced final cavity photon distribution:

$$\langle n|\hat{\eta}_L|n\rangle \approx (1-x)\delta_{n,0} + \binom{2n}{n}\frac{1}{4^n}\frac{x}{2\sqrt{\pi\bar{n}_0}}. \qquad (m=0;\ \bar{n}_0 \gg n) \tag{7.102}$$

For the Fock state populations $1 \ll n \ll \bar{n}_0$, we can expand the n-dependent terms Equation (7.102):

$$\langle n|\hat{\eta}_L|n\rangle \approx \frac{x}{2\pi\sqrt{n\bar{n}_0}}. \qquad (m=0;\ 1 \ll n \ll \bar{n}_0) \tag{7.103}$$

7.11.1.3 Evaluating the Laguerre polynomial sum $S_n(\bar{n}_0)$

To derive the asymptotic limit of the sum in Eq. (7.101), we first introduce the following identity [30]:

$$\sum_{k=0}^{\infty} L_k^{(n-k)}(\bar{n}_0)t^k = (1+t)^n e^{-\bar{n}_0 t}. \tag{7.104}$$

The choice $t = e^x$ leads to

$$g(x) \equiv \sum_{k=0}^{\infty} L_k^{(n-k)}(\bar{n}_0)e^{(k+1)x} = e^x(1+e^x)^n e^{-\bar{n}_0 e^x}. \tag{7.105}$$

We next calculate the antiderivative $G(x)$ of $g(x)$ with the ansatz

$$G(x) = \sum_{l=0}^{n} c_l (1+e^x)^l e^{-\bar{n}_0 e^x}. \tag{7.106}$$

By enforcing $G'(x) = g(x)$, we obtain

$$G(x) = -\frac{1}{\bar{n}_0}\frac{n!}{\bar{n}_0^n}\sum_{l=0}^{n}\frac{\bar{n}_0^l}{l!}(1+e^x)^l e^{-\bar{n}_0 e^x}. \tag{7.107}$$

From the series representation of $g(x)$ in Eq. (7.105) we find

$$G(x) = \sum_{k=0}^{\infty}\frac{L_k^{(n-k)}(\bar{n}_0)e^{(k+1)x}}{k+1} - \frac{1}{\bar{n}_0}\frac{n!}{\bar{n}_0^n}\sum_{l=0}^{n}\frac{\bar{n}_0^l}{l!} \tag{7.108}$$

as a series for G. From Eqns. (7.105) and (7.108), we can write down the following Fourier series

$$\sum_{k=0}^{\infty} \frac{L_k^{(n-k)}(\bar{n}_0)e^{ikx}}{k+1} = \frac{e^{-ix}}{\bar{n}_0} \frac{n!}{\bar{n}_0^n} \sum_{l=0}^{n} \frac{\bar{n}_0^l}{l!} \left[1 - (1+e^{ix})^l e^{-\bar{n}_0 e^{ix}}\right], \tag{7.109}$$

$$\sum_{k=0}^{\infty} L_k^{(n-k)}(\bar{n}_0)e^{ikx} = (1+e^{ix})^n e^{-\bar{n}_0 e^{ix}}. \tag{7.110}$$

By the orthogonality of complex exponentials, we can write

$$\begin{aligned} S_n(\bar{n}_0) &= \sum_{k=0}^{\infty} \frac{1}{k+1} \left[L_k^{(n-k)}(\bar{n}_0)\right]^2 \\ &= \frac{1}{2\pi} \int_0^{2\pi} dx (1+e^{-ix})^n e^{-\bar{n}_0 e^{-ix}} \frac{e^{-ix}}{\bar{n}_0} \frac{n!}{\bar{n}_0^n} \sum_{l=0}^{n} \frac{\bar{n}_0^l}{l!} \left[1 - (1+e^{ix})^l e^{-\bar{n}_0 e^{ix}}\right]. \end{aligned} \tag{7.111}$$

In the large $\bar{n}_0 \gg n$ limit we only need to consider highest order term $l = n$. This is appropriate because we increase $\bar{n}_0$ without increasing n. With this we can approximate

$$S_n(\bar{n}_0) \approx -\frac{1}{2\pi\bar{n}_0} \int_0^{2\pi} dx\, e^{-ix}(1+e^{-ix})^n (1+e^{ix})^n e^{-2\bar{n}_0 \cos(x)}. \tag{7.112}$$

We now use a saddle point method. In the large $\bar{n}_0$ limit the measure will concentrate around $x = \pi$. In that case we can use

$$e^{-2\bar{n}_0 \cos(x)} \approx e^{2\bar{n}_0 - \bar{n}_0 (x-\pi)^2}. \tag{7.113}$$

Consequently we obtain

$$\begin{aligned} S_n(\bar{n}_0) &\approx \frac{e^{2\bar{n}_0}}{2\pi\bar{n}_0} \int_{-\infty}^{\infty} du\, e^{-iu}(1-e^{-iu})^n (1-e^{iu})^n e^{-\bar{n}_0 u^2} \\ &\approx \frac{e^{2\bar{n}_0}}{2\pi\bar{n}_0} \int_{-\infty}^{\infty} du\, u^{2n} e^{-\bar{n}_0 u^2} \\ &\approx \frac{e^{2\bar{n}_0}}{\bar{n}_0^{n+1}} \frac{(2n)!}{n!} \frac{1}{4^n} \frac{1}{2\sqrt{\pi\bar{n}_0}}, \end{aligned} \tag{7.114}$$

which we use in Eq. (7.101).

7.11.2 Fidelity in the infinite coupling limit $m \to 0$

If we are instead interested in the case $m \to 0$ with finite $\bar{n}_0$, we can use Eq. (7.82) to simplify Eq. (7.33) to

$$F = 1 - x \left\{1 - e^{-2\bar{n}_0} \left[1 + \bar{n}_0 \sum_{n \geq 0} \frac{1}{1+n} \left(\frac{\bar{n}_0^n}{n!}\right)^2\right]\right\}. \qquad (m = 0) \tag{7.115}$$

Using the modified Bessel function of the first kind,

$$I_1(2y) = y \sum_{n\geq 0} \frac{1}{1+n} \left(\frac{y^n}{n!}\right)^2, \tag{7.116}$$

Eq. (7.115) becomes

$$F = 1 - x\left\{1 - e^{-2\bar{n}_0}\left[1 + I_1(2\bar{n}_0)\right]\right\}. \qquad (m=0) \tag{7.117}$$

We now consider two cases for $\bar{n}_0$: (i) the thermodynamic limit $\bar{n}_0 \to \infty$, and (ii) the quantum limit $\bar{n}_0 \to 0$, for which we can use the asymptotic expansions

$$I_1(2\bar{n}_0) \approx \frac{e^{2\bar{n}_0}}{2\sqrt{\pi\bar{n}_0}} \qquad (\bar{n}_0 \gg 1); \qquad I_1(2\bar{n}_0) \approx \bar{n}_0 \qquad (\bar{n}_0 \ll 1) \tag{7.118}$$

respectively. Therefore, to leading order in $\bar{n}_0$, we conclude that the fidelity is given by

$$F \approx \begin{cases} 1 - x\bar{n}_0, & \bar{n}_0 \to 0 \\ 1 - x\left(1 - \frac{1}{2\sqrt{\pi\bar{n}_0}}\right), & \bar{n}_0 \to \infty. \end{cases} \qquad (m=0) \tag{7.119}$$

We also consider the limit $m \to \infty$, for which

$$\lim_{m\to\infty} K_{n,n'} = \left(1 + \frac{n+n'}{2}\right)^{-1}. \tag{7.120}$$

In this case the double sum in Eq. (7.33) simplifies and

$$\lim_{m\to\infty} F = 1 - x\left\{1 - e^{-2\bar{n}_0}\left[1 + \frac{1 - e^{2\bar{n}_0}(1-2\bar{n}_0)}{2\bar{n}_0}\right]\right\}. \tag{7.121}$$

To leading order, the fidelity is then

$$\lim_{m\to\infty} F = \begin{cases} 1 - x\bar{n}_0, & \bar{n}_0 \to 0 \\ 1 - \frac{x}{2\bar{n}_0}, & \bar{n}_0 \to \infty. \end{cases} \tag{7.122}$$

7.12 Conclusion

We have demonstrated through a simple Gedankenexperiment under what conditions the entropy of a quantum system can be imprinted on a classical coherent light field, which we model

as a coherent state in a lossless cavity. We have quantified the cavity state's alteration due to the particle-cavity interaction through the measurement of fidelity and proved that the cavity field contains information about the initial state of the particle by the method of Bayesian inference and using quantum information theoretic techniques. Our results demand reconsideration of the underlying physics of laser cooling and optical pumping in the strong particle-light coupling regime, as it suggests that the assumption of an unperturbed light field is not necessarily accurate.

The entropy transfer from the particle to the light field could be realized in an experimental setting by studying a system that satisfies $\kappa \ll \gamma, g$. Although we have mainly focused on the high-$\bar{n}_0$ limit, we believe that there is also interesting physics in the low-$\bar{n}_0$ regime. Our model could also be generalized to further understand some cavity-based quantum memories [4, 88, 163] by, e.g., incorporating cavity pumping and loss ($\kappa \neq 0$) or initializing the cavity field in a different quantum state. We also anticipate that this system can be used as a platform to generate and study novel photon-subtracted states [6].

There are many ways to extend this study for the purpose of modeling the laser cooling process more accurately. Most notably, the incorporation of cavity pumping and loss could permit a nontrivial equilibrium solution even when the particle can relax back to the bright state, which would bring the particle's internal state structure closer to that of typical two-level models. In this case, one could even remove the background radiation field altogether to further investigate the entropy dynamics of the laser-particle system [121]. Of course, particle motion could also be incorporated, potentially allowing for another Hilbert space to absorb or emit entropy.

One could also study this system in the framework of phase space compression. However, the rich correlations generated by quantum mechanical processes preclude a clear phase space approach for quantum systems [17, 18, 143]. This would require, for example, a deeper understanding of the connection between Wigner trajectories and Liouville's theorem [165]. On a related note, one could consider the use of quantum discord as a measurement of quantum correlation [66] as opposed to von Neumann entropy.

Chapter 8

Conclusion

In this thesis, we investigated three novel techniques for manipulating the motion of atoms and molecules with laser light and electromagnetic traps, as well as the transfer of entropy from a quantum system to a classically-behaved yet inherently quantum light field. To contextualize and formalize our approach, we provided the essential background material. We began with building up the physical model for the interaction of quantum particles with light as determined from quantum theory. This required constructing the Hamiltonian for an isolated atom or molecule, demonstrating the emergence of its internal state quantum structure, and then coupling it to an electromagnetic field. We outlined the classical and quantum descriptions of the light field, including the background radiation field which is responsible for spontaneous emission. A discussion of the theory of open quantum systems naturally followed, in which we recast the Schrödinger equation into a quantum master equation which efficiently models the system of interest and its interaction with the environment. Next, we presented an algorithm for simulating the master equation called the Monte Carlo wave function method, which we extensively used for approximating the dynamics in studies involving particle motion. To further contextualize the proposed laser cooling and trapping process, we also provided a brief description of the commonly-implemented Doppler cooling and conventional magneto-optical trap methods.

Our first contribution was the theoretical description of SWAP cooling, a technique which has the capability to cool atoms and molecules with narrow optical transitions. We explained its basic mechanism, outlined its operating regime, and demonstrated its ability to generate large slowing

forces without the need of spontaneous emission. Through numerical simulations, we demonstrated its capacity to cool and characterized its minimum achievable temperature. To benchmark its effectiveness, we compared it to Doppler cooling on the same transition and showed that it requires fewer spontaneous photons to reach thermodynamic equilibrium. We then connected the theory to an experimental realization of SWAP cooling on a narrow linewidth transition in ^{88}Sr. Our numerical simulations agreed with the experimental data, which corroborated our explanation of SWAP cooling's underlying physics. Next, we combined the SWAP cooling protocol with a quadrupole magnetic trap to realize a novel magneto-optical trap, which we named the "SWAP MOT." We explained the necessary alterations to the cooling protocol and developed an efficient semiclassical model. We described its effects on particle motion from a phase space trajectory perspective and proved its potential to exhibit phase space compression with a higher efficiency than a conventional MOT. Our numerical simulations showed that the minimum achievable temperatures agreed with the SWAP cooling result and that the particles can become tightly confined in space. We then relaxed the condition of adiabatic evolution by formulating a speedup protocol based on Lewis-Riesenfeld invariants. We applied it in the context of laser slowing and characterized the parameter regime in which it displays superiority over other common slowing methods. Our final investigation involved tracking the transfer of information entropy from a quantum particle to a classically-behaved coherent light field in a lossless optical cavity. We quantified the alteration of the light field, corroborated many of the typical assumptions regarding the interaction of quantum matter with laser light, and demonstrated that that in some extreme cases, information about the quantum particle can become encoded in the light field.

We are optimistic that our proposed techniques will prove useful in advancing the scientific community's ability to control the motion of atoms and molecules. In particular, we hope that these procedures will increase the catalog of molecules that can be captured in an optical trap for use in basic science and quantum computing experiments. Also, we anticipate that our study on entropy transfer from quantum particles will motivate further investigation into the underlying physics of (and possibly be used to propose new methods of) optical pumping and laser cooling.

Bibliography

[1] Obinna Abah, Ricardo Puebla, Anthony Kiely, Gabriele De Chiara, Mauro Paternostro, and Steve Campbell. Energetic cost of quantum control protocols. New Journal of Physics, 21(10):103048, oct 2019.

[2] A. Abragam. The principles of nuclear magnetism. Clarendon Press, 1961.

[3] C.S. Adams and E. Riis. Laser cooling and trapping of neutral atoms. Progress in Quantum Electronics, 21(1):1 – 79, 1997.

[4] Mikael Afzelius and Christoph Simon. Impedance-matched cavity quantum memory. Phys. Rev. A, 82:022310, Aug 2010.

[5] G. S. Agarwal and K. Tara. Nonclassical properties of states generated by the excitations on a coherent state. Phys. Rev. A, 43:492–497, Jan 1991.

[6] G.S. Agarwal. Quantum Optics. Quantum Optics. Cambridge University Press, 2013.

[7] Nitzan Akerman, Michael Karpov, Liron David, Etay Lavert-Ofir, Julia Narevicius, and Edvardas Narevicius. Simultaneous deceleration of atoms and molecules in a supersonic beam. New Journal of Physics, 17(6):065015, jun 2015.

[8] Leslie Allen and Joseph H. Eberly. Optical Resonance and Two-level Atoms. Dover, 1987.

[9] M. H. Anderson, J. R. Ensher, M. R. Matthews, C. E. Wieman, and E. A. Cornell. Observation of bose-einstein condensation in a dilute atomic vapor. Science, 269(5221):198–201, 1995.

[10] M. Arnal, V. Brunaud, G. Chatelain, C. Cabrera-Gutiérrez, E. Michon, P. Cheiney, J. Billy, and D. Guéry-Odelin. Evidence for cooling in an optical lattice by amplitude modulation. Phys. Rev. A, 100:013416, Jul 2019.

[11] S. Balasubramanian, Shuyang Han, B. T. Yoshimura, and J. K. Freericks. Bang-bang shortcut to adiabaticity in trapped-ion quantum simulators. Phys. Rev. A, 97:022313, Feb 2018.

[12] John P. Bartolotta and Murray J. Holland. Sawtooth-wave adiabatic passage in a magneto-optical trap. Phys. Rev. A, 101:053434, May 2020.

[13] John P. Bartolotta, Matthew A. Norcia, Julia R. K. Cline, James K. Thompson, and Murray J. Holland. Laser cooling by sawtooth-wave adiabatic passage. Phys. Rev. A, 98:023404, Aug 2018.

[14] John P. Bartolotta, Jarrod T. Reilly, and Murray J. Holland. Speeding up particle slowing using shortcuts to adiabaticity. Phys. Rev. A, 102:043107, Oct 2020.

[15] Mark G. Bason, Matthieu Viteau, Nicola Malossi, Paul Huillery, Ennio Arimondo, Donatella Ciampini, Rosario Fazio, Vittorio Giovannetti, Riccardo Mannella, and Oliver Morsch. High-fidelity quantum driving. Nature Physics, 8(2):147–152, Feb 2012.

[16] Peter G. Bergmann and Joel L. Lebowitz. New approach to nonequilibrium processes. Phys. Rev., 99:578–587, Jul 1955.

[17] Alex E. Bernardini and Orfeu Bertolami. Phase-space continuity equations for quantum decoherence, purity, von neumann and renyi entropies. Journal of Physics: Conference Series, 1275:012032, sep 2019.

[18] Alex E Bernardini and Caio Fernando e Silva. Anharmonic effects on phase-space quantum profiles: an exact approach. Journal of Physics: Conference Series, 1612:012002, aug 2020.

[19] M V Berry. Transitionless quantum driving. Journal of Physics A: Mathematical and Theoretical, 42(36):365303, 2009.

[20] Hendrick L. Bethlem, Giel Berden, Floris M. H. Crompvoets, Rienk T. Jongma, André J. A. van Roij, and Gerard Meijer. Electrostatic trapping of ammonia molecules. Nature, 406(6795):491–494, August 2000.

[21] Hendrick L. Bethlem, André J. A. van Roij, Rienk T. Jongma, and Gerard Meijer. Alternate gradient focusing and deceleration of a molecular beam. Phys. Rev. Lett., 88:133003, Mar 2002.

[22] Immanuel Bloch, Jean Dalibard, and Sylvain Nascimbène. Quantum simulations with ultracold quantum gases. Nature Physics, 8(4):267–276, 2012.

[23] E. Boukobza and D. J. Tannor. Entropy exchange and entanglement in the jaynes-cummings model. Phys. Rev. A, 71:063821, Jun 2005.

[24] Samuel L. Braunstein and Arun K. Pati. Quantum information cannot be completely hidden in correlations: Implications for the black-hole information paradox. Phys. Rev. Lett., 98:080502, Feb 2007.

[25] Heinz-Peter Breuer and Francesco Petruccione. The theory of open quantum systems. Oxford Univ. Press, 2010.

[26] K. E. Cahill and R. J. Glauber. Ordered expansions in boson amplitude operators. Phys. Rev., 177:1857–1881, Jan 1969.

[27] J C Camparo and R P Frueholz. A dressed atom interpretation of adiabatic rapid passage. Journal of Physics B: Atomic and Molecular Physics, 17(20):4169–4178, oct 1984.

[28] Steve Campbell and Sebastian Deffner. Trade-off between speed and cost in shortcuts to adiabaticity. Phys. Rev. Lett., 118:100601, Mar 2017.

[29] T. Caneva, M. Murphy, T. Calarco, R. Fazio, S. Montangero, V. Giovannetti, and G. E. Santoro. Optimal control at the quantum speed limit. Phys. Rev. Lett., 103:240501, Dec 2009.

[30] L. Carlitz. On the product of two laguerre polynomials. Journal of the London Mathematical Society, s1-36(1):399–402, 1961.

[31] Lincoln D Carr, David DeMille, Roman V Krems, and Jun Ye. Cold and ultracold molecules: science, technology and applications. New Journal of Physics, 11(5):055049, 2009.

[32] William B. Case. Wigner functions and weyl transforms for pedestrians. American Journal of Physics, 76(10):937–946, 2008.

[33] M. T. Cashen and H. Metcalf. Bichromatic force on helium. Phys. Rev. A, 63:025406, Jan 2001.

[34] Jasper Chan, TP Mayer Alegre, Amir H Safavi-Naeini, Jeff T Hill, Alex Krause, Simon Gröblacher, Markus Aspelmeyer, and Oskar Painter. Laser cooling of a nanomechanical oscillator into its quantum ground state. Nature, 478(7367):89–92, 2011.

[35] Thierry Chanelière, Daniel Comparat, and Hans Lignier. Phase-space-density limitation in laser cooling without spontaneous emission. Phys. Rev. A, 98:063432, Dec 2018.

[36] Xi Chen, I. Lizuain, A. Ruschhaupt, D. Guéry-Odelin, and J. G. Muga. Shortcut to adiabatic passage in two- and three-level atoms. Phys. Rev. Lett., 105:123003, Sep 2010.

[37] Xi Chen, A. Ruschhaupt, S. Schmidt, A. del Campo, D. Guéry-Odelin, and J. G. Muga. Fast optimal frictionless atom cooling in harmonic traps: Shortcut to adiabaticity. Phys. Rev. Lett., 104:063002, Feb 2010.

[38] Xi Chen, E. Torrontegui, and J. G. Muga. Lewis-riesenfeld invariants and transitionless quantum driving. Phys. Rev. A, 83:062116, Jun 2011.

[39] Ye-Hong Chen, Yan Xia, Qing-Qin Chen, and Jie Song. Shortcuts to adiabatic passage for multiparticles in distant cavities: applications to fast and noise-resistant quantum population transfer, entangled states' preparation and transition. Laser Physics Letters, 11(11):115201, sep 2014.

[40] S. Chervenkov, X. Wu, J. Bayerl, A. Rohlfes, T. Gantner, M. Zeppenfeld, and G. Rempe. Continuous centrifuge decelerator for polar molecules. Phys. Rev. Lett., 112:013001, Jan 2014.

[41] Steven Chu. Nobel lecture: The manipulation of neutral particles. Rev. Mod. Phys., 70:685–706, Jul 1998.

[42] Steven Chu, JE Bjorkholm, A Ashkin, and Alex Cable. Experimental observation of optically trapped atoms. Physical Review Letters, 57(3):314, 1986.

[43] Marvin L. Cohen. Essay: Fifty years of condensed matter physics. Phys. Rev. Lett., 101:250001, Dec 2008.

[44] Claude Cohen-Tannoudji, Jacques Dupont-Roc, and Gilbert Grynberg. Lagrangian and Hamiltonian Approach to Electrodynamics, The Standard Lagrangian and the Coulomb Gauge, chapter 2, pages 79–168. John Wiley & Sons, Ltd, 1997.

[45] Claude Cohen-Tannoudji, Jacques Dupont-Roc, and Gilbert Grynberg. Quantum Electrodynamics in the Coulomb Gauge, chapter 3, pages 169–252. John Wiley & Sons, Ltd, 1997.

[46] Claude N. Cohen-Tannoudji. Nobel lecture: Manipulating atoms with photons. Rev. Mod. Phys., 70:707–719, Jul 1998.

[47] J Cohn, A Safavi-Naini, R J Lewis-Swan, J G Bohnet, M Gärttner, K A Gilmore, J E Jordan, A M Rey, J J Bollinger, and J K Freericks. Bang-bang shortcut to adiabaticity in the dicke model as realized in a penning trap experiment. New Journal of Physics, 20(5):055013, May 2018.

[48] Alejandra L. Collopy, Shiqian Ding, Yewei Wu, Ian A. Finneran, Loïc Anderegg, Benjamin L. Augenbraun, John M. Doyle, and Jun Ye. 3d magneto-optical trap of yttrium monoxide. Phys. Rev. Lett., 121:213201, Nov 2018.

[49] Alejandra L Collopy, Matthew T Hummon, Mark Yeo, Bo Yan, and Jun Ye. Prospects for a narrow line mot in yo. New Journal of Physics, 17(5):055008, 2015.

[50] Christopher Corder, Brian Arnold, Xiang Hua, and Harold Metcalf. Laser cooling without spontaneous emission using the bichromatic force. J. Opt. Soc. Am. B, 32(5):B75–B83, May 2015.

[51] Christopher Corder, Brian Arnold, and Harold Metcalf. Laser cooling without spontaneous emission. Physical Review Letters, 114(4):043002, 2015.

[52] Ivan B. Coulamy, Alan C. Santos, Itay Hen, and Marcelo S. Sarandy. Energetic Cost of Superadiabatic Quantum Computation. Frontiers in ICT, 3, 2016.

[53] J Dalibard and C Cohen-Tannoudji. Atomic motion in laser light: connection between semi-classical and quantum descriptions. Journal of Physics B: Atomic and Molecular Physics, 18(8):1661–1683, apr 1985.

[54] J. Dalibard and C. Cohen-Tannoudji. Dressed-atom approach to atomic motion in laser light: the dipole force revisited. J. Opt. Soc. Am. B, 2(11):1707–1720, Nov 1985.

[55] F. A. M. de Oliveira, M. S. Kim, P. L. Knight, and V. Buek. Properties of displaced number states. Phys. Rev. A, 41:2645–2652, Mar 1990.

[56] M. A. de Ponte, P. M. Cônsoli, and M. H. Y. Moussa. Method for the construction of the lewis-riesenfeld time-dependent invariants and their eigenvalue equations. Phys. Rev. A, 98:032102, Sep 2018.

[57] Sebastian Deffner. Shortcuts to adiabaticity: suppression of pair production in driven dirac dynamics. New Journal of Physics, 18(1):012001, Dec 2015.

[58] Luigi Delle Site. Formulation of liouville's theorem for grand ensemble molecular simulations. Phys. Rev. E, 93:022130, Feb 2016.

[59] F Diedrich, JC Bergquist, Wayne M Itano, and DJ Wineland. Laser cooling to the zero-point energy of motion. Physical Review Letters, 62(4):403, 1989.

[60] Shiqian Ding and Jun Ye. Private communication, 2019.

[61] Yan-Xiong Du, Xian-Xian Yue, Zhen-Tao Liang, Jia-Zhen Li, Hui Yan, and Shi-Liang Zhu. Geometric atom interferometry with shortcuts to adiabaticity. Phys. Rev. A, 95:043608, Apr 2017.

[62] P. M. Duarte, R. A. Hart, J. M. Hitchcock, T. A. Corcovilos, T.-L. Yang, A. Reed, and R. G. Hulet. All-optical production of a lithium quantum gas using narrow-line laser cooling. Phys. Rev. A, 84:061406, Dec 2011.

[63] R. Dum, P. Zoller, and H. Ritsch. Monte carlo simulation of the atomic master equation for spontaneous emission. Phys. Rev. A, 45:4879–4887, Apr 1992.

[64] Ethan R. Elliott, Markus C. Krutzik, Jason R. Williams, Robert J. Thompson, and David C. Aveline. NASA's Cold Atom Lab (CAL): system development and ground test status. npj Microgravity, 4(1):16, August 2018.

[65] Massimiliano Esposito, Katja Lindenberg, and Christian Van den Broeck. Entropy production as correlation between system and reservoir. New Journal of Physics, 12(1):013013, jan 2010.

[66] Alessandro Ferraro and Matteo G. A. Paris. Nonclassicality criteria from phase-space representations and information-theoretical constraints are maximally inequivalent. Phys. Rev. Lett., 108:260403, Jun 2012.

[67] Richard P. Feynman, Frank L. Vernon, and Robert W. Hellwarth. Geometrical representation of the schrödinger equation for solving maser problems. Journal of Applied Physics, 28(1):49–52, 1957.

[68] R. Frisch. Experimenteller Nachweis des Einsteinschen Strahlungsrückstoßes. Zeitschrift fur Physik, 86:42–48, January 1933.

[69] Xiao-Chun Gao, Jing-Bo Xu, and Tie-Zheng Qian. Geometric phase and the generalized invariant formulation. Phys. Rev. A, 44:7016–7021, Dec 1991.

[70] Crispin W. Gardiner and Peter Zoller. Quantum noise: a handbook of Markovian and non-Markovian quantum stochastic methods with applications to quantum optics. Springer, 2010.

[71] Christopher Gerry and Peter Knight. Introductory Quantum Optics. Cambridge University Press, 2004.

[72] Steffen J. Glaser, Ugo Boscain, Tommaso Calarco, Christiane P. Koch, Walter Köckenberger, Ronnie Kosloff, Ilya Kuprov, Burkhard Luy, Sophie Schirmer, Thomas Schulte-Herbrüggen, Dominique Sugny, and Frank K. Wilhelm. Training Schrödinger's cat: quantum optimal control. Strategic report on current status, visions and goals for research in Europe. European Physical Journal D, 69(12):279, December 2015.

[73] Kurt Gottfried and Tung-Mow Yan. Quantum mechanics: fundamentals. Springer Science Business Media, 2005.

[74] G P Greve, B Wu, and J K Thompson. Laser cooling with adiabatic transfer on a raman transition. New Journal of Physics, 21(7):073045, jul 2019.

[75] D. Guéry-Odelin, A. Ruschhaupt, A. Kiely, E. Torrontegui, S. Martínez-Garaot, and J. G. Muga. Shortcuts to adiabaticity: Concepts, methods, and applications. Rev. Mod. Phys., 91:045001, Oct 2019.

[76] Utkan Güngördü, Yidun Wan, Mohammad Ali Fasihi, and Mikio Nakahara. Dynamical invariants for quantum control of four-level systems. Phys. Rev. A, 86:062312, Dec 2012.

[77] T. W. Hansch and A. L. Schawlow. Cooling of gases by laser radiation. Optics Communications, 13:68, January 1975.

[78] D. J. Heinzen and D. J. Wineland. Quantum-limited cooling and detection of radio-frequency oscillations by laser-cooled ions. Phys. Rev. A, 42:2977–2994, Sep 1990.

[79] Boerge Hemmerling, Eunmi Chae, Aakash Ravi, Loic Anderegg, Garrett K Drayna, Nicholas R Hutzler, Alejandra L Collopy, Jun Ye, Wolfgang Ketterle, and John M Doyle. Laser slowing of CaF molecules to near the capture velocity of a molecular MOT. Journal of Physics B: Atomic, Molecular and Optical Physics, 49(17):174001, aug 2016.

[80] L Henderson and V Vedral. Classical, quantum and total correlations. Journal of Physics A: Mathematical and General, 34(35):6899–6905, aug 2001.

[81] S. D. Hogan, A. W. Wiederkehr, H. Schmutz, and F. Merkt. Magnetic trapping of hydrogen after multistage zeeman deceleration. Phys. Rev. Lett., 101:143001, Sep 2008.

[82] Alexander S. Holevo. Quantum Systems, Channels, Information: A Mathematical Introduction. De Gruyter, 2 edition, 2019.

[83] M. J. Holland and K. Burnett. Interferometric detection of optical phase shifts at the heisenberg limit. Phys. Rev. Lett., 71:1355–1358, Aug 1993.

[84] Peter Horak, Gerald Hechenblaikner, Klaus M. Gheri, Herwig Stecher, and Helmut Ritsch. Cavity-induced atom cooling in the strong coupling regime. Phys. Rev. Lett., 79:4974–4977, Dec 1997.

[85] Matthew T Hummon, Mark Yeo, Benjamin K Stuhl, Alejandra L Collopy, Yong Xia, and Jun Ye. 2d magneto-optical trapping of diatomic molecules. Physical Review Letters, 110(14):143001, 2013.

[86] Tetsuya Ido, Yoshitomo Isoya, and Hidetoshi Katori. Optical-dipole trapping of sr atoms at a high phase-space density. Phys. Rev. A, 61:061403, May 2000.

[87] A. M. Jayich, A. C. Vutha, M. T. Hummon, J. V. Porto, and W. C. Campbell. Continuous all-optical deceleration and single-photon cooling of molecular beams. Phys. Rev. A, 89:023425, Feb 2014.

[88] P Jobez, I Usmani, N Timoney, C Laplane, N Gisin, and M Afzelius. Cavity-enhanced storage in an optical spin-wave memory. New Journal of Physics, 16(8):083005, aug 2014.

[89] Richard Jozsa. Fidelity for mixed quantum states. Journal of Modern Optics, 41(12):2315–2323, 1994.

[90] Alfred Kastler. Quelques suggestions concernant la production optique et la détection optique d'une inégalité de population des niveaux de quantifigation spatiale des atomes. application à l'expérience de stern et gerlach et à la résonance magnétique. Journal de Physique et le Radium, 11(6):255–265, 1950.

[91] Hidetoshi Katori, Tetsuya Ido, Yoshitomo Isoya, and Makoto Kuwata-Gonokami. Magneto-optical trapping and cooling of strontium atoms down to the photon recoil temperature. Phys. Rev. Lett., 82:1116–1119, Feb 1999.

[92] Hidetoshi Katori, Tetsuya Ido, and Makoto Kuwata-Gonokami. Optimal design of dipole potentials for efficient loading of sr atoms. Journal of the Physical Society of Japan, 68(8):2479–2482, 1999.

[93] Wolfgang Ketterle. Nobel lecture: When atoms behave as waves: Bose-einstein condensation and the atom laser. Rev. Mod. Phys., 74:1131–1151, Nov 2002.

[94] K. Kim, M.-S. Chang, S. Korenblit, R. Islam, E. E. Edwards, J. K. Freericks, G.-D. Lin, L.-M. Duan, and C. Monroe. Quantum simulation of frustrated ising spins with trapped ions. Nature, 465(7298):590–593, Jun 2010.

[95] S.P Kim, A.E Santana, and F.C Khanna. Generalized invariants and quantum evolution of open fermionic systems. Physics Letters A, 272(1):46 – 52, 2000.

[96] H. J. Kimble. Strong interactions of single atoms and photons in cavity QED. Physica Scripta, T76(1):127, 1998.

[97] Vladimir V. Kiselev. Collective effects in condensed matter physics. De Gruyter, 2018.

[98] Catherine Klauss. A little less spontaneous, 2018.

[99] J Kobayashi, K Aikawa, K Oasa, and S Inouye. Prospects for narrow-line cooling of krb molecules in the rovibrational ground state. Physical Review A, 89(2):021401, 2014.

[100] E. Korsunsky. Laser cooling during velocity-selective adiabatic population transfer. Phys. Rev. A, 54:R1773–R1776, Sep 1996.

[101] Sebastian Krämer, David Plankensteiner, Laurin Ostermann, and Helmut Ritsch. Quantumoptics.jl: A julia framework for simulating open quantum systems. Computer Physics Communications, 227:109 – 116, 2018.

[102] T. D. Ladd, F. Jelezko, R. Laflamme, Y. Nakamura, C. Monroe, and J. L. O'Brien. Quantum computers. Nature, 464(7285):45–53, 2010.

[103] Y.-Z. Lai, J.-Q. Liang, H. J. W. Müller-Kirsten, and J.-G. Zhou. Time-dependent quantum systems and the invariant hermitian operator. Phys. Rev. A, 53:3691–3693, May 1996.

[104] Joel L. Lebowitz and Abner Shimony. Statistical mechanics of open systems. Phys. Rev., 128:1945–1958, Nov 1962.

[105] H. R. Lewis and W. B. Riesenfeld. An exact quantum theory of the time-dependent harmonic oscillator and of a charged particle in a time-dependent electromagnetic field. Journal of Mathematical Physics, 10(8):1458–1473, 1969.

[106] Nan Li and Shunlong Luo. Classical and quantum correlative capacities of quantum systems. Phys. Rev. A, 84:042124, Oct 2011.

[107] Yi-Chao Li and Xi Chen. Shortcut to adiabatic population transfer in quantum three-level systems: Effective two-level problems and feasible counterdiabatic driving. Phys. Rev. A, 94:063411, Dec 2016.

[108] Yeong-Cherng Liang, Yu-Hao Yeh, Paulo E M F Mendonça, Run Yan Teh, Margaret D Reid, and Peter D Drummond. Quantum fidelity measures for mixed states. Reports on Progress in Physics, 82(7):076001, jun 2019.

[109] G. Lindblad. On the generators of quantum dynamical semigroups. Communications in Mathematical Physics, 48(2):119–130, 1976.

[110] Thomas H. Loftus, Tetsuya Ido, Andrew D. Ludlow, Martin M. Boyd, and Jun Ye. Narrow line cooling: Finite photon recoil dynamics. Phys. Rev. Lett., 93:073003, Aug 2004.

[111] T. Lu, X. Miao, and H. Metcalf. Nonadiabatic transitions in finite-time adiabatic rapid passage. Phys. Rev. A, 75:063422, Jun 2007.

[112] William Lunden, Li Du, Michael Cantara, Pierre Barral, Alan O. Jamison, and Wolfgang Ketterle. Enhancing the capture velocity of a Dy magneto-optical trap with two-stage slowing. arXiv e-prints, page arXiv:1908.10433, Aug 2019.

[113] Daniel Manzano. A short introduction to the lindblad master equation. AIP Advances, 10(2):025106, 2020.

[114] Peter J. Martin, Bruce G. Oldaker, Andrew H. Miklich, and David E. Pritchard. Bragg scattering of atoms from a standing light wave. Phys. Rev. Lett., 60:515–518, Feb 1988.

[115] S. Martínez-Garaot, A. Ruschhaupt, J. Gillet, Th. Busch, and J. G. Muga. Fast quasiadiabatic dynamics. Phys. Rev. A, 92:043406, Oct 2015.

[116] S. Martínez-Garaot, E. Torrontegui, Xi Chen, and J. G. Muga. Shortcuts to adiabaticity in three-level systems using lie transforms. Phys. Rev. A, 89:053408, May 2014.

[117] Shumpei Masuda and Katsuhiro Nakamura. Fast-forward problem in quantum mechanics. Phys. Rev. A, 78:062108, Dec 2008.

[118] Shumpei Masuda and Katsuhiro Nakamura. Fast-forward of adiabatic dynamics in quantum mechanics. Proceedings of the Royal Society A: Mathematical, Physical and Engineering Sciences, 466(2116):1135–1154, 2010.

[119] Shumpei Masuda and Stuart A. Rice. Fast-forward assisted stirap. The Journal of Physical Chemistry A, 119(14):3479–3487, 2015. PMID: 25775133.

[120] The Mathworks, Inc., Natick, Massachusetts. MATLAB version 9.9.0.1467703 (R2020b), 2017.

[121] P. Maunz, T. Puppe, I. Schuster, N. Syassen, P. W. H. Pinkse, and G. Rempe. Cavity cooling of a single atom. Nature, 428(6978):50–52, Mar 2004.

[122] Gerard McCaul, Alexander Pechen, and Denys I. Bondar. Entropy nonconservation and boundary conditions for hamiltonian dynamical systems. Phys. Rev. E, 99:062121, Jun 2019.

[123] H. J. Metcalf and P. van der Straten. Laser cooling and trapping of atoms. J. Opt. Soc. Am. B, 20(5):887–908, May 2003.

[124] Harold Metcalf. Entropy exchange in laser cooling. Phys. Rev. A, 77:061401, Jun 2008.

[125] Harold Metcalf. Colloquium: Strong optical forces on atoms in multifrequency light. Rev. Mod. Phys., 89:041001, Oct 2017.

[126] Harold J. Metcalf and Peter van der. Straten. Laser cooling and trapping. Springer, 2002.

[127] Pierre Meystre and Murray Sargent. Elements of Quantum Optics. Springer, 2007.

[128] Jian-Guo Miao, Chun-Wang Wu, Wei Wu, and Ping-Xing Chen. Entropy exchange and thermodynamic properties of the single ion cooling process. Entropy, 21(7):650, Jul 2019.

[129] X. Miao, E. Wertz, M. G. Cohen, and H. Metcalf. Strong optical forces from adiabatic rapid passage. Phys. Rev. A, 75:011402, Jan 2007.

[130] P. W. Milonni. Why spontaneous emission? American Journal of Physics, 52(4):340–343, 1984.

[131] Peter W. Milonni, Jay R. Ackerhalt, and Wallace Arden Smith. Interpretation of radiative corrections in spontaneous emission. Phys. Rev. Lett., 31:958–960, Oct 1973.

[132] Peter W. Milonni and Wallace Arden Smith. Radiation reaction and vacuum fluctuations in spontaneous emission. Phys. Rev. A, 11:814–824, Mar 1975.

[133] Z. K. Minev, S. O. Mundhada, S. Shankar, P. Reinhold, R. Gutiérrez-Jáuregui, R. J. Schoelkopf, M. Mirrahimi, H. J. Carmichael, and M. H. Devoret. To catch and reverse a quantum jump mid-flight. Nature, 570(7760):200–204, 2019.

[134] V.G. Minogin and O.T. Serimaa. Resonant light pressure forces in a strong standing laser wave. Optics Communications, 30(3):373 – 379, 1979.

[135] Klaus Mølmer, Yvan Castin, and Jean Dalibard. Monte carlo wave-function method in quantum optics. J. Opt. Soc. Am. B, 10(3):524–538, Mar 1993.

[136] Henrik Lund Mortensen, Jens Jakob W. H. Sørensen, Klaus Mølmer, and Jacob Friis Sherson. Fast state transfer in a λ-system: a shortcut-to-adiabaticity approach to robust and resource optimized control. New Journal of Physics, 20(2):025009, feb 2018.

[137] Juan A. Muniz, Matthew A. Norcia, Julia R. K. Cline, and James K. Thompson. A Robust Narrow-Line Magneto-Optical Trap using Adiabatic Transfer. arXiv e-prints, page arXiv:1806.00838, Jun 2018.

[138] Edvardas Narevicius, Adam Libson, Christian G. Parthey, Isaac Chavez, Julia Narevicius, Uzi Even, and Mark G. Raizen. Stopping supersonic beams with a series of pulsed electromagnetic coils: An atomic coilgun. Phys. Rev. Lett., 100:093003, Mar 2008.

[139] Michael A. Nielsen and Isaac L. Chuang. Quantum Computation and Quantum Information: 10th Anniversary Edition. Cambridge University Press, USA, 10th edition, 2011.

[140] Matthew A. Norcia. New tools for precision measurement and quantum science with narrow linewidth optical transitions. PhD thesis, University of Colorado, Boulder, 8 2018.

[141] Matthew A Norcia, Julia R K Cline, John P Bartolotta, Murray J Holland, and James K Thompson. Narrow-line laser cooling by adiabatic transfer. New Journal of Physics, 20(2):023021, 2018.

[142] B. Nölle, H. Nölle, J. Schmand, and H. J. Andrä. Atomic-beam deflection by double-π-pulse laser technique. EPL (Europhysics Letters), 33(4):261, 1996.

[143] Maxime Oliva, Dimitris Kakofengitis, and Ole Steuernagel. Anharmonic quantum mechanical systems do not feature phase space trajectories. Physica A: Statistical Mechanics and its Applications, 502:201 – 210, 2018.

[144] Matteo G.A. Paris. Displacement operator by beam splitter. Physics Letters A, 217(2):78 – 80, 1996.

[145] O Penrose. Foundations of statistical mechanics. Reports on Progress in Physics, 42(12):1937–2006, dec 1979.

[146] N. Petersen, F. Mühlbauer, L. Bougas, A. Sharma, D. Budker, and P. Windpassinger. Sawtooth-wave adiabatic-passage slowing of dysprosium. Phys. Rev. A, 99:063414, Jun 2019.

[147] Francesco Petiziol, Benjamin Dive, Florian Mintert, and Sandro Wimberger. Fast adiabatic evolution by oscillating initial hamiltonians. Phys. Rev. A, 98:043436, Oct 2018.

[148] M Petzold, P Kaebert, P Gersema, M Siercke, and S Ospelkaus. A zeeman slower for diatomic molecules. New Journal of Physics, 20(4):042001, apr 2018.

[149] William D. Phillips. Nobel lecture: Laser cooling and trapping of neutral atoms. Rev. Mod. Phys., 70:721–741, Jul 1998.

[150] William D. Phillips and Harold Metcalf. Laser deceleration of an atomic beam. Phys. Rev. Lett., 48:596–599, Mar 1982.

[151] M. B. Plenio and P. L. Knight. The quantum-jump approach to dissipative dynamics in quantum optics. Rev. Mod. Phys., 70:101–144, Jan 1998.

[152] Gabriel N Price, S Travis Bannerman, Kirsten Viering, Edvardas Narevicius, and Mark G Raizen. Single-photon atomic cooling. Physical Review Letters, 100(9):093004, 2008.

[153] David E. Pritchard and Phillip L. Gould. Experimental possibilities for observation of unidirectional momentum transfer to atoms from standing-wave light. J. Opt. Soc. Am. B, 2(11):1799–1804, Nov 1985.

[154] A. P. Prudnikov, Yu. A. Brychkov, and O. I. Marichev. Integrals and Series, Volume 3: More Special Functions, volume 3, chapter 7, page 439. Gordon and Breach, 1990.

[155] Krzysztof Ptaszyński and Massimiliano Esposito. Entropy production in open systems: The predominant role of intraenvironment correlations. Phys. Rev. Lett., 123:200603, Nov 2019.

[156] E. L. Raab, M. Prentiss, Alex Cable, Steven Chu, and D. E. Pritchard. Trapping of neutral sodium atoms with radiation pressure. Phys. Rev. Lett., 59:2631–2634, Dec 1987.

[157] C. A. Regal, M. Greiner, and D. S. Jin. Observation of resonance condensation of fermionic atom pairs. Phys. Rev. Lett., 92:040403, Jan 2004.

[158] Florentin Reiter and Anders S. Sørensen. Effective operator formalism for open quantum systems. Phys. Rev. A, 85:032111, Mar 2012.

[159] Simon M. Rochester, Konrad Szymański, Mark Raizen, Szymon Pustelny, Marcis Auzinsh, and Dmitry Budker. Efficient polarization of high-angular-momentum systems. Phys. Rev. A, 94:043416, Oct 2016.

[160] K. J. Ross and B. Sonntag. High temperature metal atom beam sources. Review of Scientific Instruments, 66(9):4409–4433, 1995.

[161] A Ruschhaupt, Xi Chen, D Alonso, and J G Muga. Optimally robust shortcuts to population inversion in two-level quantum systems. New Journal of Physics, 14(9):093040, sep 2012.

[162] A. Ruschhaupt and J.G. Muga. Shortcuts to adiabaticity in two-level systems: control and optimization. Journal of Modern Optics, 61(10):828–832, 2014.

[163] M Sabooni, S Tornibue Kometa, A Thuresson, S Kröll, and L Rippe. Cavity-enhanced storage—preparing for high-efficiency quantum memories. New Journal of Physics, 15(3):035025, mar 2013.

[164] M. S. Safronova, D. Budker, D. DeMille, Derek F. Jackson Kimball, A. Derevianko, and Charles W. Clark. Search for new physics with atoms and molecules. Rev. Mod. Phys., 90:025008, Jun 2018.

[165] R. Sala, S. Brouard, and J. G. Muga. Wigner trajectories and liouville's theorem. The Journal of Chemical Physics, 99(4):2708–2714, 1993.

[166] M. S. Sarandy, E. I. Duzzioni, and R. M. Serra. Quantum computation in continuous time using dynamic invariants. Physics Letters A, 375(38):3343–3347, Sep 2011.

[167] Denise Sawicki and J.H. Eberly. Perfect following in the diabatic limit. Opt. Express, 4(7):217–222, Mar 1999.

[168] F. Schwabl. Statistical Mechanics. Springer Berlin Heidelberg, 2006.

[169] Dries Sels. Stochastic gradient ascent outperforms gamers in the quantum moves game. Phys. Rev. A, 97:040302, Apr 2018.

[170] E. S. Shuman, J. F. Barry, and D. Demille. Laser cooling of a diatomic molecule. Nature, 467(7317):820–823, 2010.

[171] S. Snigirev, A. J. Park, A. Heinz, I. Bloch, and S. Blatt. Fast and dense magneto-optical traps for strontium. Phys. Rev. A, 99:063421, Jun 2019.

[172] J. Söding, R. Grimm, Yu. B. Ovchinnikov, Ph. Bouyer, and Ch. Salomon. Short-distance atomic beam deceleration with a stimulated light force. Phys. Rev. Lett., 78:1420–1423, Feb 1997.

[173] Daniel Stack, John Elgin, Petr M. Anisimov, and Harold Metcalf. Numerical studies of optical forces from adiabatic rapid passage. Phys. Rev. A, 84:013420, Jul 2011.

[174] Daniel A. Steck. Quantum and atom optics, 2007.

[175] Dionisis Stefanatos, Justin Ruths, and Jr-Shin Li. Frictionless atom cooling in harmonic traps: A time-optimal approach. Phys. Rev. A, 82:063422, Dec 2010.

[176] Simon Stellmer, Benjamin Pasquiou, Rudolf Grimm, and Florian Schreck. Laser cooling to quantum degeneracy. Phys. Rev. Lett., 110:263003, Jun 2013.

[177] Benjamin K. Stuhl, Matthew T. Hummon, Mark Yeo, Goulven Quéméner, John L. Bohn, and Jun Ye. Evaporative cooling of the dipolar hydroxyl radical. Nature, 492(7429):396–400, December 2012.

[178] Kazutaka Takahashi. Hamiltonian engineering for adiabatic quantum computation: Lessons from shortcuts to adiabaticity. Journal of the Physical Society of Japan, 88(6):061002, 2019.

[179] E. Torrontegui, S. Martínez-Garaot, and J. G. Muga. Hamiltonian engineering via invariants and dynamical algebra. Phys. Rev. A, 89:043408, Apr 2014.

[180] E. Torrontegui, S. Martínez-Garaot, A. Ruschhaupt, and J. G. Muga. Shortcuts to adiabaticity: Fast-forward approach. Phys. Rev. A, 86:013601, Jul 2012.

[181] S Truppe, H J Williams, N J Fitch, M Hambach, T E Wall, E A Hinds, B E Sauer, and M R Tarbutt. An intense, cold, velocity-controlled molecular beam by frequency-chirped laser slowing. New Journal of Physics, 19(2):022001, Feb 2017.

[182] A. Uhlmann. The "transition probability" in the state space of a $*$-algebra. Reports on Mathematical Physics, 9(2):273 – 279, 1976.

[183] Alban Urvoy, Zachary Vendeiro, Joshua Ramette, Albert Adiyatullin, and Vladan Vuletić. Direct laser cooling to bose-einstein condensation in a dipole trap. Phys. Rev. Lett., 122:203202, May 2019.

[184] Lorenza Viola and Seth Lloyd. Dynamical suppression of decoherence in two-state quantum systems. Phys. Rev. A, 58:2733–2744, Oct 1998.

[185] N. V. Vitanov. Transition times in the Landau-Zener model. Physical Review A, 59:988–994, February 1999.

[186] Kurt R Vogel, Timothy P Dinneen, Alan Gallagher, and John L Hall. Narrow-line doppler cooling of strontium to the recoil limit. IEEE Transactions on Instrumentation and Measurement, 48(2):618–621, 1999.

[187] V.S. Voitsekhovich, M.V. Danileiko, A.M Negriiko, V.I Romanenko, and L.P. Yatsenko. Stimulated light pressure on atoms in counterpropagating amplitude-modulated waves. JETP, 72:219–227, Feb 1991.

[188] Tino Weber, Jens Herbig, Michael Mark, Hanns-Christoph Nägerl, and Rudolf Grimm. Bose-einstein condensation of cesium. Science (New York, N.Y.), 299(5604):232—235, January 2003.

[189] V. Weisskopf and E. Wigner. Berechnung der natürlichen linienbreite auf grund der diracschen lichttheorie. Zeitschrift für Physik, 63(1-2):54–73, 1930.

[190] Viktor Weisskopf. Probleme der neueren quantentheorie des elektrons. Die Naturwissenschaften, 23(37):631–637, 1935.

[191] M. R. Williams, F. Chi, M. T. Cashen, and H. Metcalf. Measurement of the bichromatic optical force on rb atoms. Phys. Rev. A, 60:R1763–R1766, Sep 1999.

[192] D. Wineland and H. Dehmelt. Proposed $10^{14}\,\Delta\nu < \nu$ laser fluorescence spectroscopy on TI^{+} mono-ion oscillator III. Bull. Am. Phys. Soc., 20:637, 1975.

[193] Tao Yang, Kanhaiya Pandey, Mysore Srinivas Pramod, Frederic Leroux, Chang Chi Kwong, Elnur Hajiyev, Zhong Yi Chia, Bess Fang, and David Wilkowski. A high flux source of cold strontium atoms. The European Physical Journal D, 69(10), 2015.

[194] C. Zener. Non-Adiabatic Crossing of Energy Levels. Proceedings of the Royal Society of London Series A, 137:696–702, September 1932.

[195] Xibo Zhang and Jun Ye. Precision measurement and frequency metrology with ultracold atoms. National Science Review, 3(2):189–200, 03 2016.

[196] V. Zhelyazkova, A. Cournol, T. E. Wall, A. Matsushima, J. J. Hudson, E. A. Hinds, M. R. Tarbutt, and B. E. Sauer. Laser cooling and slowing of caf molecules. Phys. Rev. A, 89:053416, May 2014.

[197] Yuanjian Zheng, Steve Campbell, Gabriele De Chiara, and Dario Poletti. Cost of counter-diabatic driving and work output. Phys. Rev. A, 94:042132, Oct 2016.